

AFOSR-TR-95

0608

Approved for public release,
distribution unlimited

Annual Technical Report

on

RESEARCH ON

SUPERSONIC REACTING FLOWS

Grant AFOSR F49620-94-1-0152

Prepared for

AIR FORCE OFFICE OF SCIENTIFIC RESEARCH



For the Period

15 February 1994 to 14 February 1995

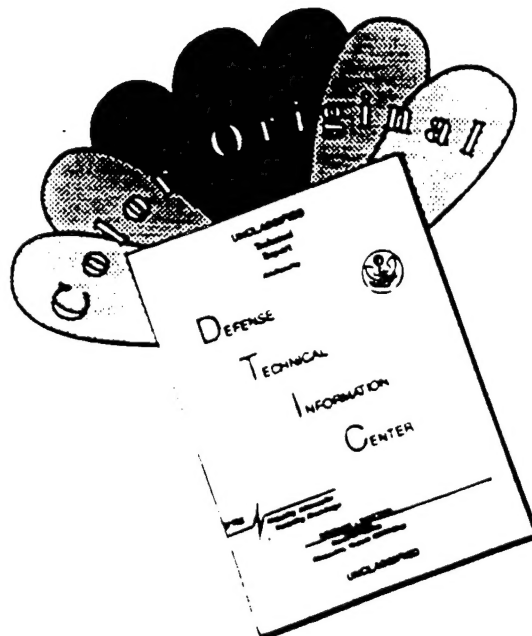
Submitted by

C.T. Bowman
R.K. Hanson
M.G. Mungal
W.C. Reynolds

19951004 151

HIGH TEMPERATURE GASDYNAMICS LABORATORY
Mechanical Engineering Department
Stanford University

DISCLAIMER NOTICE



**THIS DOCUMENT IS BEST
QUALITY AVAILABLE. THE COPY
FURNISHED TO DTIC CONTAINED
A SIGNIFICANT NUMBER OF
COLOR PAGES WHICH DO NOT
REPRODUCE LEGIBLY ON BLACK
AND WHITE MICROFICHE.**

REPORT DOCUMENTATION PAGE

Form Approved
OMB No. 0704-0188

Public reporting burden for this collection of information is estimated to average 1 hour per response, including the time for reviewing instructions, searching existing data sources, gathering and maintaining the data needed, and completing and reviewing the collection of information. Send comments regarding this burden estimate or any other aspect of this collection of information, including suggestions for reducing this burden, to Washington Headquarters Services, Directorate for Information Operations and Reports, 1215 Jefferson Davis Highway, Suite 1200, Arlington, VA 22202-4302, and to the Office of Management and Budget, Paperwork Reduction Project (0704-0188), Washington, DC 20503.

1. AGENCY USE ONLY (Leave blank)		2. REPORT DATE 15 March 1995	3. REPORT TYPE AND DATES COVERED Annual 2/15/94-2/14/95
4. TITLE AND SUBTITLE (U) Research on Supersonic Reacting Flows		5. FUNDING NUMBERS PE - 61102F PR - 2308 SA - BS G - F49620-94-1-0152	
6. AUTHOR(S) C.T. Bowman, R.K. Hanson, M.G. Mungal, W.C. Reynolds		8. PERFORMING ORGANIZATION REPORT NUMBER	
7. PERFORMING ORGANIZATION NAME(S) AND ADDRESS(ES) Department of Mechanical Engineering Stanford University Stanford, CA 94305		10. SPONSORING/MONITORING AGENCY REPORT NUMBER	
9. SPONSORING/MONITORING AGENCY NAME(S) AND ADDRESS(ES) AFOSR/NA 110 Duncan Avenue, Suite B115 Bolling AFB DC 20332-0001			
11. SUPPLEMENTARY NOTES			
12a. DISTRIBUTION/AVAILABILITY STATEMENT Approved for public release; distribution is unlimited		12b. DISTRIBUTION CODE	
13. ABSTRACT (Maximum 200 words) An experimental and computational investigation of supersonic reacting flows, with the objective of gaining a fundamental understanding of the flow physics and chemistry interactions, is in progress. During the past year, experiments were conducted in a supersonic shear flow facility to visualize the instantaneous, three-dimensional structure of the compressible mixing layer and to measure the mixing efficiency. The mixing efficiency was measured by applying a new planar laser-induced fluorescence (PLIF) technique, termed "cold chemistry." The PLIF techniques, developed previously in our laboratory, were refined to allow measurements of temperature, velocity and multiple species in transient high-speed flows. Current codes for direct numerical simulation of time-developing, three-dimensional, reacting, compressible mixing layers were adapted for a new generation of supercomputers. Previously-developed stability analyses were extended to the range of conditions being investigated in the supersonic reacting flow experiments.			
DTIC QUALITY INSPECTED 8			
14. SUBJECT TERMS Turbulent reacting flow, supersonic combustion		15. NUMBER OF PAGES 91	
		16. PRICE CODE	
17. SECURITY CLASSIFICATION OF REPORT Unclassified	18. SECURITY CLASSIFICATION OF THIS PAGE Unclassified	19. SECURITY CLASSIFICATION OF ABSTRACT Unclassified	20. LIMITATION OF ABSTRACT UL

TABLE OF CONTENTS

	<u>Page</u>
1.0 SUMMARY.....	1
2.0 INTRODUCTION	1
3.0 MIXING AND COMBUSTION STUDIES	2
3.1 Objectives	2
3.2 Status of the Research.....	2
3.3 Future Work.....	5
4.0 DIAGNOSTICS IN SUPERSONIC FLOWS.....	6
4.1 Objectives	6
4.2 Status of the Research.....	7
4.3 Future Work.....	8
5.0 ANALYSIS AND SIMULATION	10
5.1 Objectives	10
5.2 Status of the Research.....	10
5.3 Future Work.....	11
6.0 PUBLICATIONS PRODUCED ON THIS GRANT	11
7.0 REFERENCES	12
8.0 PERSONNEL	12
9.0 Ph.D. DEGREES AWARDED.....	13
10.0 PRESENTATIONS	13
11.0 INTERACTIONS RELATED TO THE RESEARCH	13
12.0 INVENTIONS	13

Accession For	
NTIS	CRA&I
DTIC	TAB
Unannounced	
Justification _____	
By _____	
Distribution / _____	
Availability Codes	
Dist	Avail and/or Special

A-1

**Annual Technical Report
Research on Supersonic Reacting Flows**

AFOSR Grant F49620-94-1-0152

February 15, 1994 to February 14, 1995

C. T. Bowman, R. K. Hanson, M. G. Mungal and W. C. Reynolds
Department of Mechanical Engineering
Stanford University
Stanford, CA 94305-3032

1.0 Summary

An experimental and computational investigation of supersonic reacting flows is in progress. The principal objective of the research is to gain a more fundamental understanding of the flow physics and chemistry interactions in compressible turbulent reacting flows that will lead to improved descriptions of these flows. The project comprises two interrelated efforts: (1) an experimental study of mixing and combustion in supersonic flows that utilizes recent advances in laser-based diagnostics, and (2) simulation and modeling of compressible reacting flows using advanced analytical and numerical techniques. A close coupling of these efforts is being maintained in order to gain greater insights into the flow physics and chemistry interactions than could be obtained by either effort alone.

2.0 Introduction

A major technological challenge in achieving sustained hypersonic flight is development of advanced air-breathing propulsion systems in which combustion takes place in supersonic flow. Combustion in supersonic flow is fundamentally different from combustion in the subsonic flow regime employed in existing air-breathing propulsion systems. The current understanding of fundamental aspects of supersonic combustion is inadequate to support development of these advanced propulsion systems.

Recent advances in diagnostics capabilities and significant improvements in our abilities to compute complex flows offer new opportunities to obtain needed fundamental understanding of flow physics and chemistry interactions in compressible reacting flows.

To achieve this understanding, a closely-coordinated experimental and computational investigation of supersonic flows is in progress.

The primary elements of the investigation are mixing and combustion studies, refinement of previously-developed laser-based diagnostics for application in the reacting flow experiments, and analysis and simulation. The specific objectives, status of the research and future plans for each of the program elements are described in the following sections.

3.0 Mixing and Combustion Studies

3.1 Objectives

The objective of this part of the research program is to develop a fundamental understanding of the flow physics and chemistry interaction in compressible reacting flows.

3.2 Status of the Research

A detailed description of results from our previous reacting studies is contained in the Final Technical report on our previous AFOSR grant, Bowman et al. (1993), and a complete report is contained in the Ph.D. thesis of M. F. Miller (1994). Here, we summarize the main accomplishments and findings:

1. A combined OH/acetone Planar Laser-Induced Fluorescence (PLIF) imaging technique was developed to visualize the structure of supersonic reacting mixing layers. This technique is described in detail in Yip et al. (1994).
2. The instantaneous OH/acetone images show that reacting mixing layers have structural features consistent with those observed in nonreacting mixing layers at similar compressibilities.
3. The OH PLIF images and time-averaged OH emission images indicate that combustion intensity in compressible mixing layers is comparable to incompressible layers and that compressibility may, in fact, enhance combustion intensity.
4. The combined OH/acetone PLIF imaging technique was extended to a double-pulse mode to examine the evolution of the mixing layer structure. This technique is described in detail in Seitzman et al. (1994).

Following completion of the reacting flow studies, the supersonic flow facility was reconfigured for non-reacting (mixing) studies. Previous mixing studies performed

in the facility are reported in the Ph.D. thesis of N. T. Clemens (1991). During the past year, experiments were conducted to visualize the instantaneous, three-dimensional (3-D) structure of the compressible mixing layer and to measure its mixing efficiency.

The objective of the 3-D visualizations was to qualitatively investigate the effects of compressibility on large-scale scalar structure. Since the mixing layer transitions from 2-D to 3-D with increasing compressibility, a 3-D diagnostic is particularly well-suited to studying the shape and orientation of such structure. Additionally, with 3-D visualizations the top and bottom of the structures can be seen simultaneously, allowing comparison between the high-and low-speed sides of the layer. These measurements represent the first time-resolved, 3-D visualizations of a supersonic flow.

A schematic of the imaging system is shown in Fig. 1. The 3-D planar imaging system uses a custom high-speed camera to acquire 10 successive planar cuts through the mixing layer at a rate of 107 frames per second. Mixed fluid in the layer is indicated by Mie scattering from condensed alcohol droplets. The resulting planar images are corrected for distortions and volume-rendered on an image processing computer to provide a 3-D volume that can be viewed and sliced from any angle. Example renderings at low and moderate compressibility are shown in Fig. 2.

The low compressibility image sets were found to be dominated by 2-D coherent structures previously seen for low compressibility and lower Reynolds number layers. At moderate compressibility, the mixing layer is primarily comprised of either highly 3-D or oblique structure as has been predicted by stability analysis and direct numerical simulations. The angle of obliquity varies greatly in this transitional compressibility regime. Additionally, cross-linking between structures is evident in some images, resulting in a hatched appearance similar to that seen in numerical simulations. Direct comparison between the high- and low-speed edges of the mixing layer shows the high-speed interface to be smoother than its low-speed counterpart.

Following the 3-D visualizations, efforts centered on verifying and applying a recently-reported PLIF technique (Clemens & Paul, 1993) to perform quantitative mixing measurements. This “cold chemistry” technique mimics a chemical reaction by quenching nitric oxide fluorescence with oxygen to provide a measurement of fluid unmixedness. From the unmixedness measurement, the fraction of the mixing layer consisting of mixed fluid can be determined. Unlike passive scalar measurements, the cold chemistry technique is independent of the resolution of the image recording device and, thus, can provide an accurate measure of the effect of compressibility on mixing efficiency, as well as allowing quantitative comparisons between different mixing enhancements.

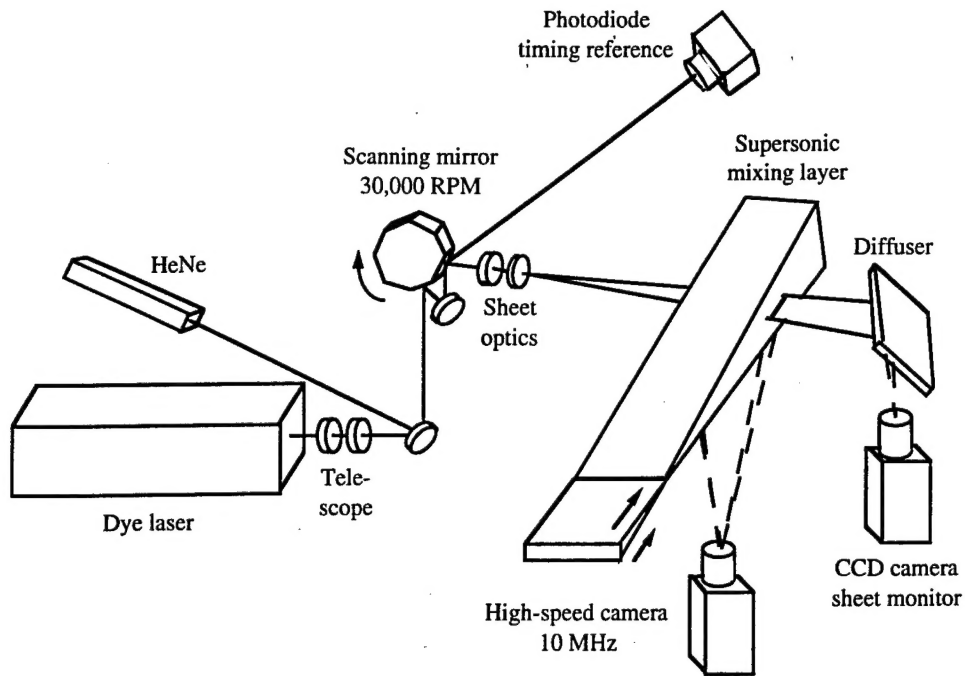


Fig. 1: Experimental setup for instantaneous 3-D imaging of a supersonic mixing layer. A single, 1 μs pulse from the dye laser is formed into a sheet and scanned across the mixing layer by a rotating mirror. Mie scattering in the layer is collected at 10 scan positions by a high-speed framing camera.

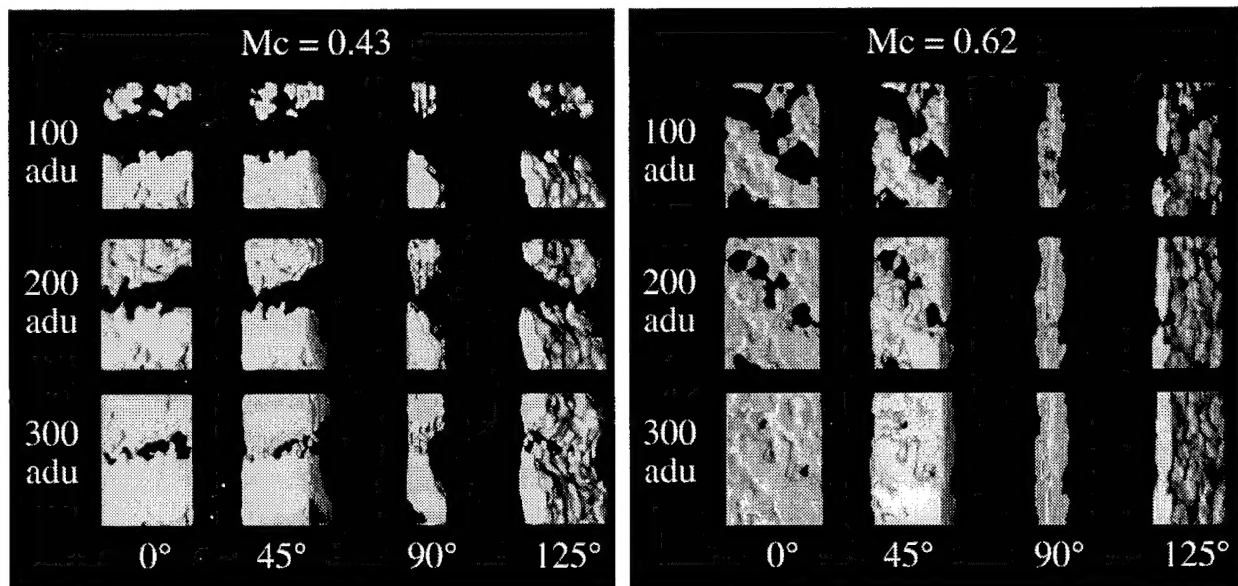


Fig. 2: Volume renderings of a low (left) and moderate (right) compressibility image set, presented as a matrix of isosignal level (arb. density units) on the vertical axis and viewing angle on the horizontal axis. 0° corresponds to a plan view from the low-speed side of the layer.

The accuracy of the diagnostic was verified through extensive static cell experiments. The fluorescence signal was collected from controlled gas mixtures for temperatures and pressure ranges spanning the conditions found in the supersonic mixing layer. Good agreement between fluorescence models and the measured signal was found.

Preliminary passive scalar and cold chemistry PLIF measurements have been made for low and high compressibility mixing layers. Example images are shown in Fig. 3. In the passive scalar case, the nitric oxide tracer was diluted with pure nitrogen streams to provide a largely unquenched fluorescence environment, yielding significantly higher signal-to-noise images than previously available for the compressible mixing layer. For the cold chemistry technique, the tracer stream mixes with an oxygen-bearing stream which effectively quenches the fluorescence and results in a sharp interface between pure fluid and mixed fluid, as seen in Fig. 3.

3.3 Future Work

During the next year, we plan to continue the passive scalar and cold chemistry PLIF experiments to generate the necessary number of images for statistical analysis. These data will determine the effect of compressibility on the mixing efficiency of the unperturbed supersonic mixing layer. Mie scattering experiments will then be conducted to investigate various proposed mixing enhancement geometries. Finally, the performance of promising enhancements will be quantitatively compared using the cold chemistry PLIF diagnostic.

In addition, we are investigating the application of PLIF to the measurement of static temperature in the mixing layer. In this work, we seek to make planar, non-intrusive measurements of temperature in the reacting mixing layer. This goal will be accomplished by means of the two-line fluorescence diagnostic developed under this program and described by McMillin (1993). Determination of the temperature field in the mixing layer will contribute both structural and quantitative information about the interaction between fluid mechanics and chemical kinetics in the layer. These data will complement the imaging results of Miller (1994), which provided visualizations of fuel-bearing regions and combustion zones in the flow. Furthermore, they have the potential to quantify the effects of fluid-mechanical enhancements to mixing and combustion.

The temperature diagnostic involves imaging of the fluorescence resulting from nearly-simultaneous excitation of two different spectral lines of a fluorescent tracer species seeded into the flow, in this case nitric oxide (NO). The delay between the excitations is long enough to allow the fluorescence events to be independent, yet short

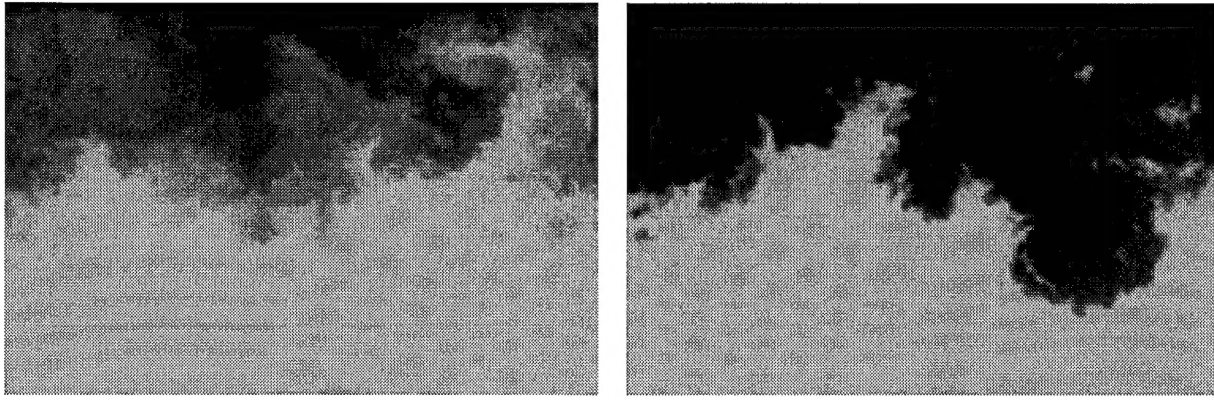


Fig. 3: Passive scalar (left) and cold chemistry (right) PLIF side-view images of a low compressibility mixing layer. The passive scalar image indicates degree of mixing by variation in signal level whereas the cold chemistry image is nearly binary and shows regions of pure fluid.

enough that the collection of both images is instantaneous relative to the convective velocities in the flow. The ratio of signals in the two images at each point is related to the relative populations of the initial (pre-excitation) quantum states of NO, which in turn is a function of temperature through the Boltzmann distribution. Since the temperature depends upon the *ratio* of the signals, the result does not require knowledge of the local number density or collisional quench rate. Since both of these quantities vary widely across the mixing layer, the two-line approach is crucial to obtaining accurate quantitative data in this flow.

Significant phases of the project include planning, calculation, and line selection for the temperature diagnostic, implementation of the optical hardware, and development of systems for tracer seeding, laser tuning, data acquisition, image correction, and interpretation.

4.0 Diagnostics in Supersonic Flows

4.1 Objectives

The goal this aspect of our work has been to develop and demonstrate planar laser-induced fluorescence (PLIF) diagnostics for: thermometry and velocimetry in pulsed flow facilities; and multiple-scalar imaging in reacting flows. PLIF is an attractive technique for studies in a variety of flow environments because it can provide species

and quantum state specific data with high temporal and spatial resolution. This allows radical concentration, temperature (Palmer and Hanson, 1994 and 1995a), and velocity imaging (Palmer and Hanson, 1994), as well as the visualization of turbulent or transient phenomena (Palmer and Hanson, 1995b). The development of multi-laser, multi-camera PLIF approaches has led to important new capabilities for simultaneous monitoring of multiple scalars (Seitzman et al., 1994a) and even the time evolution of flowfield properties (Seitzman et al, 1994b).

4.2 Status of the Research

Here we summarize our most recent work to develop OH PLIF imaging for temperature measurements in a transient hypersonic flowfield created in a shock tunnel. The technique is an extension of a two-line PLIF imaging method used previously in our laboratory to make instantaneous temperature measurements in shock tube flows with nitric oxide and the hydroxyl radical. Application in a supersonic free jet of combustion gases requires several modifications of the experimental technique because of the extreme variations of pressure and temperature and high speed encountered. These include the selection of transitions with sufficient lower state population to ensure reasonable signal level throughout the flowfield; active laser pulse spectral monitoring to eliminate systematic errors associated with large, variable Doppler shifts of the absorption frequency; careful verification of the linearity of the fluorescence signal with input laser energy; and data collection and processing procedures which take into account the long lifetime of the fluorescence signal in the low density portions of the jet.

Figure 4 shows the experimental facility in which the PLIF experiments were carried out. A pressure-driven, reflection-type shock tunnel was used to generate a highly underexpanded, axisymmetric free jet of combustion gases diluted in argon (Ar) from a test gas initially containing 5% hydrogen (H_2) and 5% oxygen (O_2). Sequential fluorescence bursts were induced by broad-band counter-propagating laser sheets directed at an angle through the axis of the jet and tuned to excite an isolated electronic transition in the $A^2\Sigma^+ \leftarrow X^2\Pi(1,0)$ band of OH around 282 nm. A single frequency-doubled dye laser pulse split into two parts formed the sheets, which therefore had identical spectral properties. A 230 ns delay in one of the beams temporally separated the PLIF signals, which were captured by gated, intensified charge coupled device (ICCD) arrays mounted above and below the test section.

Opposite Doppler shifts of the absorption frequency at each point in the flow resulted in a velocity dependence in the resultant image pair. A difference-to-sum combination of the signals induced by the sheets with an analysis of the single-shot laser spectrum and the assumption of flowfield symmetry may be used to infer the instantaneous two-component velocity field of the free jet (Palmer and Hanson, 1994). The rotational temperature field is obtained by taking the ratio of images acquired by exciting two different ro-vibrational transitions with laser pulses having similar lineshapes and relative detuning from their unshifted absorption linecenters. Each image in the ratio is formed by summing images acquired simultaneously with a single laser pulse. Because a single excitation system was used, separate experiments were performed to acquire the images necessary for temperature analysis. Measurements of the fluorescence decay time throughout the jet, obtained using the same imaging system, showed no dependence on the initially excited rotational level, allowing a relatively simple conversion between signal ratio and rotational temperature.

Rotational temperature fields inferred from single-shot images are shown in frames a and c of Fig. 5. Also shown are frame-averaged fields (b and d) obtained by evaluating the temperature from 40 individual image ratios and then averaging the results. The images in a and b of Fig. 5 are from combinations of images with $P_1(1)$ and $R_1(4)$ excitation; while those in c and d are from images with $P_1(1)$ and $Q_1(5)$ excitation. Also shown is the temperature field (e) predicted using a method of characteristics (MOC) simulation of the flowfield, with a white line placed at the location of the edges of the laser sheets in the PLIF images. The measured and predicted temperature fields are generally in excellent agreement, although in the turbulent portions of the flow only the mean temperature measurements are valid. Extension of the thermometry technique to instantaneous measurements would require use of two separately tunable pulsed dye lasers, but is otherwise relatively straightforward.

4.3 Future Work

We are presently engaged in analysis of shock tunnel PLIF data and preparation of archival publications. New work will be aimed at developing PLIF schemes for instantaneous temperature imaging in the supersonic mixing layer facility. Approaches to be studied are based on seeding of NO (in the fuel and/or oxidizer streams) or acetone (fuel stream), and on detection of OH in the flame zone.

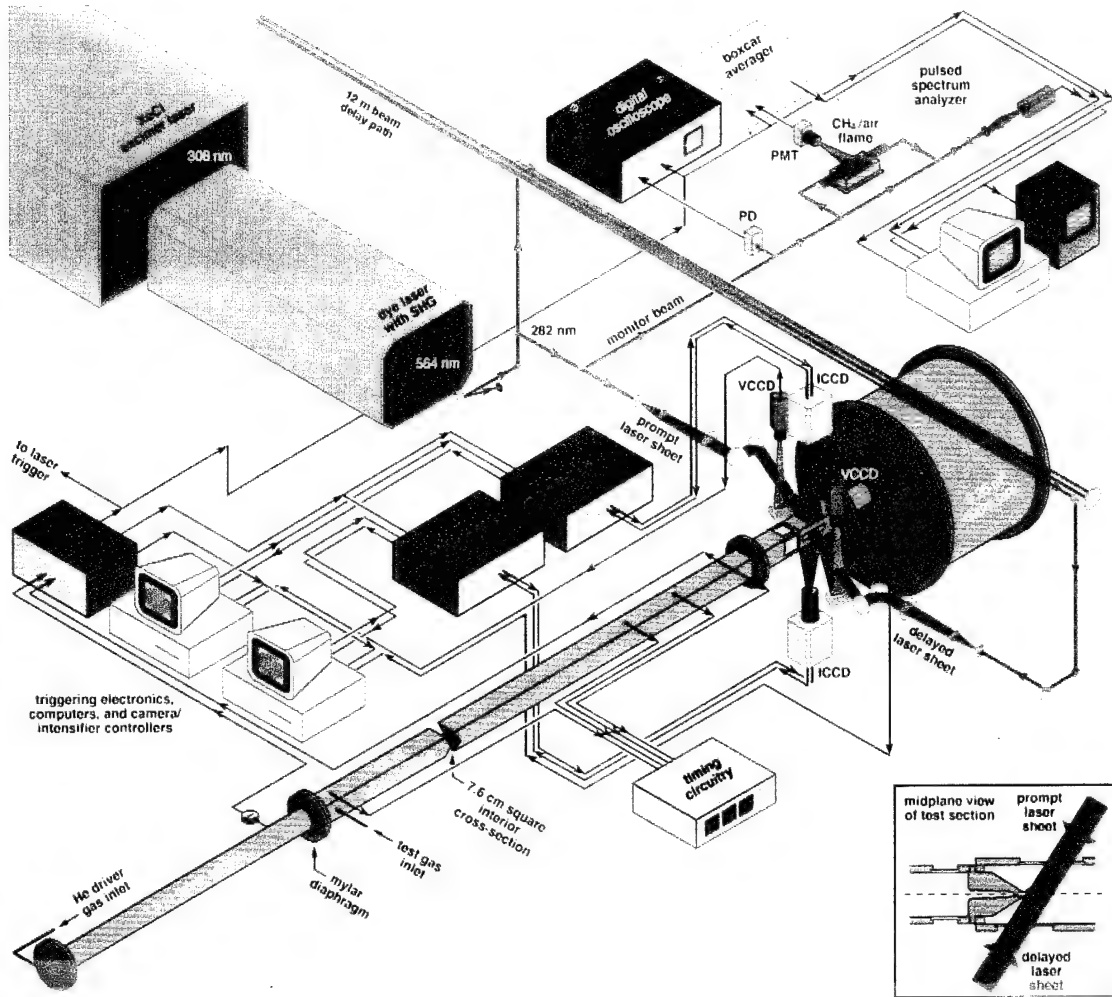


Fig. 4: Schematic of experimental facility with associated optical and electronic components for instantaneous one-laser/ two-camera PLIF imaging.

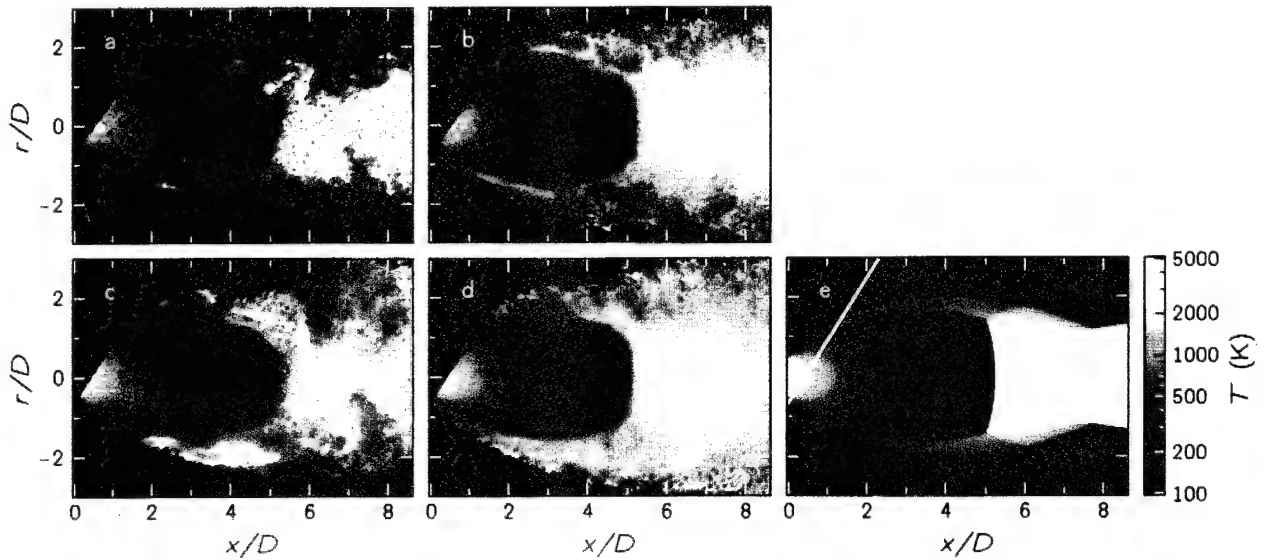


Fig. 5: Single-shot and frame-averaged temperature images, inferred from ratios of $R_1(4):P_1(1)$ (a and b) and $Q_1(5):P_1(1)$ images (c and d). Also shown is the temperature field predicted by the MOC (e). The images are $8.61 \times 5.89 D$ (139×95 pixels) in size. The conditions of the free jet were: $T_s = 3350$ K, $P_s = 3.2$ atm, $P_s/P_a = 61$, with 1.9% OH in Ar and $D = 5$ mm.

5.0 Analysis and Simulation

5.1 Objectives

The objective of this portion of the program is to provide insight for the planning of experiments and to aid in interpretation of the experiments. In particular, the work will explore the ways in which streamwise vortices can be implanted in a two-stream supersonic reacting mixing layer so as to enhance the turbulent mixing and combustion.

5.2 Status of the Research

During the past year, a computer code, developed for the Cray Y-MP serial computer and the Intel Gamma (hypercube) parallel computer on our previous AFOSR grant, was adapted for the Cray C90 serial and Intel Paragon parallel computers now available at the NASA Ames Research Center. Work is currently progressing towards validating these codes, and operational versions are expected shortly. The adaptation to Ames IBM SP-2 massively parallel computer, which has since come into service, is also progressing. It is anticipated that all three machines will be needed for the work under this project, with the SP-2 becoming the primary machine. These codes are in VECTORAL, a local language especially suited to parallel programming that is the primary language used for turbulence simulations at NASA/Ames and Stanford. The new simulations will be of the time-developing compressible mixing layer, with imbedded streamwise vortices, where the heat release is determined by a one-step chemical reaction model. The objective will be to determine the optimal location of the vortices in the mixing layer, and to gain understanding of the way in which these vortices can be used to promote combustion in the laboratory mixing layer.

The stability analysis of Planche and Reynolds (1992b) has been extended to cover more closely the range of the proposed new experiments. This analysis suggests that the dominant modes will be the "slow" modes associated with low-speed mixing layers. In order to reach the range where the "outer modes", which produce the "colayers" found by Planche and Reynolds (1992a,b), will be important, either the heat release or flow Mach number would have to be increased to levels not possible with the present experiment. Hence, we expect that the flow structures observed in the experiment will be similar to those observed previously by Miller et al.(1993).

5.3 Future Work

During the coming year, we will complete the upgrade of the turbulence simulation code for the current generation of NASA/Ames supercomputers. Then, we will begin a series of simulations of the time-developing compressible reacting mixing layer with superposed streamwise vortices, using the simple chemical reaction model. The objective will be to find the positioning of the streamwise vortices, with respect to the primary mixing layer, that gives rise to the most rapid mixing and hence most rapid combustion and energy release. These results will be used to guide the introduction of streamwise vorticity in the laboratory experiments.

6.0 Publications Produced on this Grant

The following publications have been produced on this grant during the reporting period. One copy each of available reprints and preprints are attached to this report.

N.T. Clemens, and M.G. Mungal (1995), "Large-scale Structure and Entrainment in the Supersonic Mixing Layer," *J. Fluid Mech.* **284**, 171-216.

T. C. Island, B. J. Patrie, M. G. Mungal, and R. K. Hanson (1994), "Instantaneous Three-Dimensional Flow Visualization of a Supersonic Mixing Layer", *Experiments in Fluids*, to be published.

J.L. Palmer and R.K. Hanson (1994), "PLIF Measurements of Temperature and Velocity in a Reacting Supersonic Free Jet with OH," AIAA-94-0618.

J.L. Palmer and R.K. Hanson (1995a), "Single-Shot OH PLIF Thermometry in a Reacting, Supersonic Free Jet," AIAA-95-0517.

J.L. Palmer and R.K. Hanson (1995b), "Shock Tunnel Flow Visualization Using Planar Laser-Induced Fluorescence Imaging of NO and OH," *Shock Waves*, in press.

J.M. Seitzman, M.F. Miller, B.K. McMillin, R.K. Hanson, P.A. DeBarber, and C.F. Hess (1994a), "Multiple Scalar Planar Fluorescence Imaging of Reacting Flows," AIAA-94-0228.

J.M. Seitzman, M.F. Miller, T.C. Island, and R.K. Hanson (1994b), "Double-Pulsed Imaging Using Simultaneous Acetone/OH PLIF for Studying the Evolution of High-Speed, Reacting Mixing Layers," *Twenty-Fifth Symposium (International) on Combustion*, in press.

B. Yip, M. F. Miller, A. Lozano and R. K. Hanson (1994), "A combined OH/acetone planar laser-induced fluorescence imaging technique for visualizing combusting flows, Experiments in Fluids **17**, 330-336.

7.0 References

C.T. Bowman, R.K. Hanson, M.G. Mungal and W.C. Reynolds (1993), "Turbulent Reacting Flows and Supersonic Combustion," Final Technical Report, Grant AFOSR-90-0151.

N. T. Clemens and P. H. Paul (1993), "Scalar Measurements in Compressible Axisymmetric Mixing Layers", AIAA Paper 93-0220

B. K. McMillin (1993), "Instantaneous Two-Line PLIF Temperature Imaging of Nitric Oxide in Supersonic Mixing and Combustion Flow Fields," Ph.D. thesis, Report T-287, Dept. of Mechanical Engineering, Stanford University, Stanford, CA.

M. F. Miller, T. C. Island, B. Yip, C. T. Bowman, M. G. Mungal, and R. K. Hanson, (1993), "An experimental study of the structure of a compressible, reacting mixing layer." AIAA Paper 93-0354.

M. F. Miller (1994), "An Experimental Investigation of the Effect of Compressibility on a Turbulent Reacting Mixing Layer," Ph.D. thesis, Report T-299, Dept. of Mechanical Engineering, Stanford University, Stanford, CA.

O. H. Planche and W. C. Reynolds (1992a), "Heat release effect on mixing in supersonic reacting free shear layers." AIAA paper 92-0092.

O. H. Planche and W. C. Reynolds (1992b), "A numerical investigation of the compressible reacting mixing layer." Report TF-56, Thermosciences Division, Department of Mechanical Engineering, Stanford University, October, 1992.

8.0 Personnel

Craig T. Bowman	Professor, Mechanical Engineering
Ronald K. Hanson	Professor Mechanical Engineering
Mark Godfrey Mungal	Associate Professor, Mechanical Engineering
William C. Reynolds	Professor, Mechanical Engineering
Tobin Island	Graduate Research Assistant
Michael Miller	Graduate Research Assistant
Jennifer Palmer	Graduate Research Assistant
William Urban	Graduate Research Assistant

9.0 Ph.D. Degrees Awarded

Michael Miller, June 1994, "An Experimental Investigation of the Effect of Compressibility on a Turbulent Reacting Mixing Layer."

10.0 Presentations

The following presentations were made during the reporting period.

M. F. Miller, J. M. Seitzman, C. T. Bowman and M. G. Mungal, "Evolution of Large-Scale Structures in Reacting Mixing Layers," presented at the 47th Annual Meeting of the APS Division of Fluid Dynamics, Atlanta, GA, Nov. 1994.

J. L. Palmer and R. K. Hanson, "Single-Shot OH PLIF Thermometry in a Reacting Supersonic Free Jet," presented at the 33rd Aerospace Sciences Meeting, Reno, NV, Jan. 1995.

J. M. Seitzman, M. F. Miller, T. C. Island and R. K. Hanson, "Double-Pulsed Imaging Using Simultaneous Acetone/OH PLIF for Studying the Evolution of High-Speed Reacting Mixing Layers," presented at the 25th International Symposium on Combustion, Irvine, CA, Aug. 1994.

11.0 Interactions Related to the Research

There have been no significant interactions with DoD laboratories during the reporting period. Professor F. Houwing from the Australian National University spent his sabbatical leave working in our laboratory on diagnostics for high-speed reacting flows.

12.0 Inventions

No inventions were made during the reporting period.

(Paper submitted December 1993)

DOUBLE-PULSED IMAGING USING SIMULTANEOUS ACETONE/OH PLIF FOR STUDYING THE EVOLUTION OF HIGH-SPEED, REACTING MIXING LAYERS

Jerry M. Seitzman, Michael F. Miller, Tobin C. Island and Ronald K. Hanson

Stanford University
High Temperature Gasdynamics Laboratory
Department of Mechanical Engineering

Twenty-Fifth International Symposium on Combustion
University of California, Irvine, California, USA
July 31-August 5, 1994

Subject Matter Headings: D. Experimental Methodologies
(9.4) Diagnostics,
(2.6) Supersonic Combustion

Corresponding Author: Dr. Jerry M. Seitzman
Mechanical Engineering
HTGL, Building 520
Stanford University
Stanford CA 94305 USA
Phone: (415) 723-2188
FAX: (415) 723-1748
email: jms@navier.stanford.edu

Total Word Count: 5604
3804 words using Microsoft Word's word count
+ 1800 words for 6 figures

Introduction

For high-speed combustion devices in which the fuel and oxidizer are supplied in separate streams, successful operation will often be limited by the rate of mixing between the two streams. In turbulent free shear flows, large-scale motions are responsible for the first step in the mixing process, the entrainment of fuel and oxidizer into the mixing region. Therefore, measurements which shed light on the evolution, e.g., convection, deformation, and chemistry, of the large-scale structures should provide insight into the dynamics of entrainment and mixing, and their coupling to the combustion process.

A logical approach for acquiring these measurements employs high-speed planar imaging of the instantaneous spatial structure of the flow. With such data, a number of digital image processing algorithms could be employed to quantify the evolution of the flow structures [1]. Among the possible planar imaging techniques, planar laser-induced fluorescence (PLIF) is well-suited for combustion measurements. Since PLIF imaging is a resonant technique, it can provide high signal-to-noise records of a number of interesting combustion species [2].

Here, we describe and demonstrate a double-pulse PLIF visualization technique which requires only a single laser to record the structure of a mixing region at two instants in time separated by tens of microseconds. By tuning the laser to simultaneously excite fluorescence from two molecular species, acetone and OH, and using four detectors, we separately record regions containing unburned fuel and those containing combustion gases at both instants in time. The high-speed measurements presented were obtained in a nominally two-dimensional, supersonic, reacting mixing layer consisting of an ambient temperature, low-speed hydrogen-containing fuel stream and a high temperature, supersonic oxidizing stream. The accuracy of the measurements, with respect to correlations between time-delayed image pairs, is experimentally investigated in a low-speed, laminar flame. We believe that this is the first time that a single laser system has been used to provide the necessary pulse delays and energies sufficient to characterize the evolution of a high-speed flow with PLIF imaging of combustion species.

Description of Experiment

Simultaneous Acetone/OH Imaging

As stated above, our approach for studying large-scale structures requires simultaneous PLIF imaging of two species, one marking the unburned fuel gases and the other marking the combustion gases. The ability to acquire both these quantities with a single laser system greatly

reduces the complexity (and cost) of the measurement system. One such technique, recently demonstrated, is based on the simultaneous excitation of OH, as the combustion gas marker, and acetone vapor, seeded into the fuel stream [3-5]. In this approach, a laser is tuned to simultaneously excite both species, while the fluorescence from the two is captured on separate cameras. While both OH and acetone absorb light in the same ultraviolet regions (OH has many narrow absorption lines between 280 and 320 nm, while acetone absorbs continuously from about 225 to 320 nm), the fluorescence from the two molecules is well separated in wavelength; OH emits primarily near 310 nm, while acetone emission occurs in the ~400-500 nm region. Thus simple optical filters can be used to discriminate between the two fluorescence signals.

The previous applications of combined OH and acetone imaging used a single XeCl excimer laser at 308 nm (~100-150 mJ pulse energy) to simultaneously excite the $S_1 \leftarrow S_0$ electronic transition in acetone and a rotational line in the $A \leftarrow X (0,0)$ vibrational band of OH [3-5]. In contrast, the current measurements use frequency-doubled, dye laser excitation near 285 nm to excite the OH (1,0) band along with acetone. The new approach allows for better rejection of laser scattering onto the OH camera and more flexibility in choosing the OH pump transition, e.g., the ability to choose a transition with less temperature dependence. In terms of signal strength, the lower laser energies available from the doubled-dye laser (~20-40 mJ) compared to the XeCl laser are partly compensated by: 1) the acetone absorption coefficient at 285 nm is approximately 3 times higher than at 308 nm; 2) the OH line pumped by the XeCl laser is poorly populated at high temperatures; and 3) the XeCl-excited fluorescence is partially saturated.

Again, the goal of the present diagnostic is to investigate the evolution of the instantaneous, large-scale spatial structures in a reacting mixing flow. In this light, highly accurate concentration measurements are not required. Still, the interpretation of the OH and acetone fluorescence deserves some attention. For the high-speed flow considered here, the Damköhler number for OH formation and destruction is on the order of unity; thus OH is not limited to chemical reaction zones but also marks regions of hot combustion products. Based on a simple mixing analysis between the two streams, the OH fluorescence signal is expected to track the OH concentration within $\pm 20\%$ across most OH-containing regions of the mixing layer. Similarly, the acetone fluorescence is expected to track the concentration of unburned fuel for high-speed hydrogen combustion. The fluorescence varies nearly linearly with acetone concentration [6]. In addition, the chemical removal of acetone is similar to that of hydrogen in the flow [5]. Therefore, acetone fluorescence performs as an adequate marker of unburned hydrogen concentration in the mixing layer.

Flow Facilities and Optical Layout

Double-pulse imaging experiments were performed in two flow facilities. Basic characterization measurements were carried out in a small-scale 10 cm × 4 cm flat flame burner. The burner was operated at atmospheric pressure in a premixed mode, burning a fuel-rich mixture of methane and air. The flow speeds in the resulting laminar, lifted flames did not exceed 1 m/s.

The mixing layer experiments were performed in a large-scale, blowdown facility, with a test section 8 cm × 10 cm in cross-section and 45 cm in length (Fig. 1). The facility is described in detail elsewhere [5]. In brief, a plane mixing layer is formed between a high-speed (540-960 m/s), high-temperature (1500 K static) oxidizing stream and a slower (150-185 m/s), low-temperature (270 K) fuel stream. The oxidizing stream exhausted from a vitiation heater, which burned oxygen-enriched air and hydrogen in a fuel-lean mixture, and then expanded through a supersonic nozzle. The oxidizing stream constituents were primarily oxygen (23%), water vapor (23%) and nitrogen. The fuel stream consisted of a 1:9 mixture of hydrogen diluted in nitrogen. A small amount of acetone (2500-3500 ppm) was seeded into the fuel stream by spraying liquid acetone through a fine atomizing nozzle located well upstream of the test section. For the measurements presented here, the imaged region was centered near the middle of the test section, approximately 22 cm downstream of the splitter plate.

The optical arrangement for the double-pulse imaging is also shown in Figure 1. Laser-induced fluorescence images of OH and acetone were produced by 8 ns pulses from a single Nd:YAG-pumped, frequency-doubled dye laser (Lumonics models YM-1200 and HD-500). The YAG laser was modified by the manufacturer to allow the Q-switch to gate twice during each (10 Hz) flashlamp pulse, with a user-variable pulse separation. A low energy, secondary reflection from the prism was directed to pulse energy and spectral lineshape monitors, similar to those used in an earlier study [7]. The sheet was formed with three cylindrical lenses: two lenses formed a telescope which spread the beam into a collimated, 83 mm tall sheet, and a third lens focused the laser to a narrow sheet.

Fig. 1

Each OH/acetone fluorescence imaging system consisted of two fiberoptically coupled, intensified CCD cameras (Princeton Instruments ICCD 576/RB, 578 × 384 pixels) mounted behind high quality photographic lenses. In order to increase the framing rate of the camera systems, and therefore the number of images acquired per run, on-chip binning of the pixels was employed, with each binned superpixel representing the sum of a 2×2 subarray. The OH fluorescence images were acquired through f/4.5 105 mm uv lenses, with glass filters to remove

the elastic laser scattering (Schott WG305) and the visible acetone fluorescence (Schott UG11). The acetone fluorescence was imaged through a 500 nm low-pass interference filter (Andover 500FL0750) and a glass $f/1.2$ 50 mm lens, neither of which transmitted the uv laser scattering or OH fluorescence. As shown in Fig. 1, the acetone and OH cameras viewed the planar region illuminated by the sheet from opposite sides. The intensifier gates were 400 ns for the OH camera and 200 ns for the acetone camera, with the shorter gate used to reduce the visible emission background.

For the double-pulse measurements, two nearly identical OH/acetone camera systems, i.e., four ICCD cameras, were employed. One OH/acetone camera pair viewed the illuminated plane at right angles; the other pair were placed slightly off-axis. Pixel-to-pixel spatial alignment between the cameras was ensured by simultaneously recording the image of a thin, transparent alignment target with each camera system. Careful attention was paid to the camera positioning during the measurements in order to minimize (or eliminate) post-experiment image processing intended to match the cameras' fields of view. All the images were corrected for background emission and scattering, spatially nonuniform response of the detection system, and variations in laser energy across the height of the sheet.

Double-Pulsed Laser Characterization

As with the combined acetone/OH approach, two complete laser systems could be used to produce the two laser pulses needed for a time-delayed measurement. However, the use of a single laser simplifies the setup and performance of the experiment. A potential tradeoff is a reduction in energy in each laser pulse. With the laser system described above, we have been able to produce two pulses near 285 nm, which were separated by 20-70 μ s and had energies of 2-6 mJ per pulse.

Since double-pulsing of a frequency-doubled dye laser with tens of microseconds between pulses is a novel mode of operation, a number of tests were performed to analyze the beam characteristics of the uv laser output in both single and double-pulse operation. These measurements included the energies, center wavelengths and spectral profiles of the beams. In addition, measurements of the spatial profiles of the sheets created by the laser beams were performed to ascertain any changes in the width and location of the sheet. The most significant variation between single- and double-pulse operation is the spectral detuning of the second pulse. For the pulse delays used in the results presented below (30 and 50 μ s), the first pulse has the same center wavelength and linewidth (~ 0.6 cm $^{-1}$) as in single-pulse operation, while the second

pulse is blue-shifted by approximately 0.005 nm, or 0.6 cm^{-1} , and has a 10-15% broader spectral profile.

Less change was seen in the spatial profile of the laser sheet, measured at the center of the imaged region. The fullwidth of the sheet, defined here as the distance between the points having 2% of the peak energy, was $630(\pm 50) \mu\text{m}$ for single-pulse operation. At both 30 μs and 50 μs delays, the first of the double pulses produced a sheet 560 μm wide. For the second pulses, the widths were 630 μm and 700 μm at 30 μs and 50 μs delays, respectively. The location of the image plane in the flow, as determined by the center of the sheet waist, did not move by more than 23 μm between the various test conditions.

The energy of the second pulse relative to the first was adjusted by varying the pulse timing relative to the YAG flashlamp; for these measurements, the second pulse had two-thirds of the total energy in order to partially offset the signal loss associated with its detuning. To further compensate for the detuning, the wavelength of the first pulse was slightly red-shifted with respect to the OH transition in the high-speed experiments. For the 30 μs delay, total pulse energies reached 7 mJ; in the 50 μs case, the maximum total energy was 9 mJ.

Results

As an example of the high quality images obtainable with the current approach for combined OH/acetone imaging, Fig. 2 shows a single-shot measurement in the supersonic (Mach 1.4 oxidizing stream) reacting mixing layer. The convective Mach number M_c [8] of the layer, commonly used to characterize the importance of compressibility is 0.70. The images shown in Fig. 2 were obtained with nearly 15 mJ of sheet energy (at the image plane) and with the laser tuned to the (1,0) $P_1(7)$ line of OH. Based on calibration measurements with the camera systems in a shock heated OH flow [7], the peak OH levels in the layer are found to be about 2000 ppm. The OH levels in the vitiated air stream are as high as 300 ppm, though closer to 100 ppm on average. For these data, the peak acetone levels are roughly 2500 ppm.

← Fig. 2.

Based on root-mean-squared variations in regions of nominally uniform signal in the corrected images, the signal-to-noise ratio (SNR) of the single-shot acetone images peaks at 12 in the undiluted freestream. For the OH data, the peak SNR in the mixing layer is between 10 and 12, and in the undiluted vitiated air stream, the SNR is 5. These SNR values compare well to the previous XeCl measurements in the same facility, which employed a $\sim 1 \text{ cm}^{-1}$ laser tuned to the more temperature dependent (0,0) $Q_1(3)$ line of OH. With approximately 50-60 mJ

reaching the flow in a sheet of nearly the same height, the peak SNR values in the previous measurements were about 15 for both molecules [3].

As mentioned previously, measurements were made of the double-pulse technique's capability to accurately record flow evolution by examining a flow which is nearly constant during the measurement. Figures 3a and 3b illustrate a pair of double-pulsed OH images from the laminar, low-speed methane-air flame, acquired with a 50 μ s pulse delay and a total sheet energy (at the image plane) of about 5.5 mJ. Again, the low-speed flame should be nearly frozen during the 50 μ s measurement period; convective motion of 1 pixel would require a local velocity greater than 4 m/s. Some change, however, in the chemical structure of the flame is possible. In order to create a distinct spatial structure to study, the burner exit velocity was increased until the flame lifted from the surface. Figure 3 shows the corrected results for one image pair from a set of 20 such pairs. A single scaling factor for an entire image was applied to force the average pixel value to be the same for both images. This scaling factor is nearly the same for each image pair; the variation (standard deviation) over the 20 pairs is 14% and reduces to 9% if the two extreme values are eliminated.

← Fig. 3

Figure 3c shows the difference between the second and first pulses (pulse 2 minus pulse 1), normalized by the average of the two. Thus, it represents the fractional difference, or error, between the two images, on a pixel by pixel basis. In order to reduce the shot-noise fluctuations and highlight any potential systematic errors, the images shown in Figs. 3a and 3b were convolved with a 3×3 low pass filter. Additionally, the error was set to zero at pixels with intensities considered to be in the background noise (~2-3% of the peak signals) for either image. While the overall structure of the original images is evident (since regions without OH signal have been zeroed), the error level is somewhat randomly distributed across the image. The errors, in general, tend to be larger near the edges of the flame, since the residual shot-noise is higher there.

A histogram of Fig. 3c, the fractional error image, is shown in Figure 4. For this particular image, there is a slight asymmetry of the distribution toward negative errors, i.e., a bias toward the first image in the pair. In most of the other image pairs, there is also some bias, either for the first or second pulse. For the example of Fig. 4, the averaged, absolute value of the errors is 12%; for the complete set of image pairs, it is nearly 15%. Again, much of the error is probably associated with shot-noise fluctuations between the images. Combined with the lack of significant spatial biasing, these relatively low errors should allow this technique to accurately record the evolution of the high-speed mixing layer.

← Fig. 4

For the double-pulsed measurements, both those reported above and the mixing layer data which follows, the laser was tuned to excite the overlapping $Q_1(9)$ and $Q_2(8)$ lines of OH. Combined, these lines have an absorption coefficient 2.5 times greater (at 1500-1600 K) than the $P_1(7)$ line used for the single-shot data and only a slightly greater temperature dependence. The higher absorption coefficient of the combined lines was used to partially compensate the OH signals for the lower energies available in the double-pulse measurements. For the mixing layer data, the acetone signals were further improved by increasing the acetone seeding in the mixing layer by about 40% (~3500 ppm).

Double-pulsed measurements were obtained for two mixing layer conditions: the $M_c=0.7$ case described in the previous single-pulse data; and a lower compressibility $M_c=0.32$ layer. In general, the freestream conditions are similar for the two cases. The higher compressibility case primarily differs in that the oxidizing stream has a higher stagnation temperature, 1800 K compared to 1590 K, and thus a higher speed, 960 m/s compared to 540 m/s. In addition, the low-speed fuel stream is slightly slower, 150 m/s compared to 185 m/s for the low compressibility case. Figure 5 shows an example result from the slower, lower compressibility layer, acquired with a total laser energy of ~6 mJ in the measurement plane and a 50 μ s delay between pulses. In the first pulse image, the peak SNR values are 7 for the acetone PLIF and 9 for the OH. For the second pulse, the peak acetone SNR increases to 9, while the OH value decreases to 7. Recall, the second pulse has twice the energy of the first, thus explaining the improved acetone signal, but the second pulse partially detunes from the OH line and therefore produces a weaker OH signal. Figure 6 depicts an image pair for the higher compressibility layer obtained with ~5 mJ of laser energy. For this higher speed layer, a 50 μ s pulse separation was not sufficient to keep much of the OH from leaving the imaged region. Thus, the images in Fig. 6 correspond to a shorter 30 μ s delay. The SNR values for these data are similar to those of Fig. 5.

← Fig 5-6

In the results for both layers, it is easy to see the correlation between the first and second pulse's acetone images. The lower portion of the mixing layer, i.e., the interface between the layer and the undiluted acetone, shows little distortion of the spatial structures. By measuring the movement of the interface features between the delayed image-pairs shown in Figs. 5 and 6, we can extract the convective velocity of the interface structures. For the low compressibility layer, the axial velocity is between 200 m/s and 230 m/s, which is 15-45 m/s faster than the fuel stream. For the higher speed $M_c=0.70$ case, the interface moves even faster, between 220 and 250 m/s, or 70 to 100 m/s above the fuel stream velocity. These velocities represent movements in the images of between 17 and 28 (super)pixels.

Moving on to the OH regions in the mixing layer, it becomes more difficult to visually correlate the data from the two pulses. As seen in the images of Figs. 5 and 6, the OH regions, which exists in the upper portion of the layer, move faster and farther than the acetone structures. Also, the OH structures appear to exhibit more distortion. This could be a result of in-plane deformation effects, e.g., stretching, or could be caused by out-of-plane motion or chemical changes. Still, some flow features can be identified and used to determine OH convective velocities. For the slower layer, the axial speed of the OH structures is around 480 m/s. For the higher compressibility conditions, the discernible OH features travel near 680 m/s. Thus as one might expect, we find that the combustion gases located higher in the layer move at higher speeds than the unburned fuel regions in the lower part of the layer. For the two particular image-pairs of Figs. 5 and 6, it is interesting to compute the mean speed between the acetone and OH structures, i.e., $U_{\text{structure}} = (U_{\text{acetone}} + U_{\text{OH}})/2$, and compare it to the mean speed between the two freestreams. The mean structure speed is just 4% less than the mean freestream speed for the lower compressibility layer and is 10% greater for the higher compressibility images. Thus in both cases, the mean speed between the parts of the layer marked by the OH and acetone is close to the mean freestream velocity.

Conclusions

We have demonstrated a combined acetone/OH PLIF imaging technique for recording the evolution of large-scale structures in high-speed nonpremixed combustion flows. In this approach, a single laser is used to simultaneously record the structure of regions with unburned fuel, marked by acetone, and of combustion gases containing OH, at two instants in time separated by tens of microseconds. We believe that this is the first time that a single laser system has been used to provide this level of pulse delay and energy sufficient to perform PLIF measurements of the evolution of combustion species.

The measurements were made with a double-pulsed, frequency-doubled dye laser. The spatial and spectral properties of the laser sheets produced by the two pulses were similar, except for a spectral shift of -0.005 nm by the second pulse, relative to the first. The accuracy of the technique was tested in a low-speed methane-air flame. Image-pairs obtained in this nominally frozen flow showed average pixel-to-pixel errors of 15%. The somewhat random distribution of these errors within an image suggests that much of the error is associated with signal shot-noise fluctuations.

The technique was also applied to a nominally two-dimensional, high-speed reacting mixing layer for two conditions: a slower, low compressibility layer and a supersonic, higher

compressibility condition. Reasonable quality images, having minimum noise levels of 11-14%, were obtained in both cases, with peak OH levels near 2000 ppm and acetone seeding levels of roughly 3500 ppm. The structures containing unburned fuel are relatively stable during the measurement periods used here (30-50 μ s), while the OH-marked hot combustion gases exhibit more changes, resulting from some combination of in-plane distortion, out-of-plane movement and chemical transformation. The measured convective speeds are reasonable; for the particular images presented here, the mean speed between the two parts of the layer, as marked by the OH and acetone, is close to the mean freestream velocity.

So far, the structural analysis of the mixing layer data has been limited to qualitative interpretation and visually determined, average convective velocities for the acetone and OH features. The reasonable signal-to-noise ratios obtained in the high-speed images and the low pixel-to-pixel differences measured in the low-speed flame data suggest that double-pulsed data could be successfully interrogated by more advanced local correlation and least-square fitting techniques [1]. Then, more complex questions regarding the evolution of the large-scale structures [9] could be addressed.

Acknowledgements

This work was supported by the U.S. Air Force Office of Scientific Research, Aerospace Sciences Directorate, with Dr. J. Tishkoff as the technical monitor.

References

1. Strickland, R. N., and Sweeney, D. W., *Appl. Opt.* 27: 5213-5220 (1988).
2. Hanson, R. K., Seitzman, J. M., and Paul, P. H., *Appl. Phys. B* 50: 441-454 (1990).
3. Yip, B., Miller, M. F., Lozano, A., and Hanson, R. K., *Exper. in Fluids*, submitted (1993).
4. Paul, P., and Clemens, T.: Planar Laser-Induced Fluorescence Imaging of Lifted H₂-Air Flames. Paper AIAA-93-0800 presented at the 31st AIAA Aerospace Sciences Meeting, Reno, Nev., Jan. 1993.
5. Miller, M. F., Island, T. C., Yip, B. Bowman, C. T., Mungal, M. G., and Hanson, R. K.: An Experimental Study of the Structure of a Compressible, Reacting Mixing Layer. Paper AIAA-93-0354 presented at the 31st AIAA Aerospace Sciences Meeting, Reno, Nev., Jan. 1993.
6. Lozano, A., Yip, B., and Hanson, R. K., *Exper. in Fluids* 13: 369-376 (1992).

7. Seitzman, J. M., Hanson, R. K., DeBarber, P. A., and Hess, C. F., *Appl. Opt.* in press (1994).
8. Papamoschou, D., and Roshko, A., *J. Fluid Mech.* 7:453-477 (1988).
9. Planché, O. H., *A Numerical Investigation of the Compressible Reacting Mixing Layer*, Stanford University, Ph.D. Thesis, 1992.

Figures

Figure 1. Schematic of mixing layer facility with laser sheet (top) and optical arrangement (bottom).

Figure 2. Single-pulse simultaneous images (211×152 pixels, 82×59 mm) of OH and acetone in a reacting mixing layer with $M_c=0.70$: (a) the OH distribution, (b) the acetone distribution, and (c) the overlay of the OH and acetone images. The sheet propagates upward in these sideview images of the mixing layer. As indicated black corresponds to minimum signal and white represents the peak signal in each image.

Figure 3. Double-pulsed images (281×143 pixels, 69×35 mm) of OH in the low-speed, lifted, premixed methane-air flame: (a) first pulse image; (b) second pulse ($50 \mu\text{s}$ delay) image; (c) fractional difference image, second pulse minus first pulse normalized by the average of the two. The sheet propagates right-to-left in these sideview images of the flame. The left color bar shows signal increasing linearly from black to white in (a) and (b). For (c) the color bar shows errors from -50% to +50%.

Figure 4. Histogram of fractional differences between pixels from the image of Fig. 3c. The spike at zero error results from forcing the error to be zero for pixels with signal levels within the background noise.

Figure 5. Overlayed (see Fig. 2), double-pulsed sideview images (82×59 mm) of acetone and OH in the mixing layer with $M_c=0.32$: (a) first pulse image and (b) second pulse image with a $50 \mu\text{s}$ delay. The color scaling is indicated in Fig. 2.

Figure 6. Overlayed (see Fig. 2), double-pulsed sideview images (82×59 mm) of acetone and OH in the mixing layer with $M_c=0.70$: (a) first pulse and (b) second pulse with $30 \mu\text{s}$ delay. The color scaling is indicated in Fig. 2.

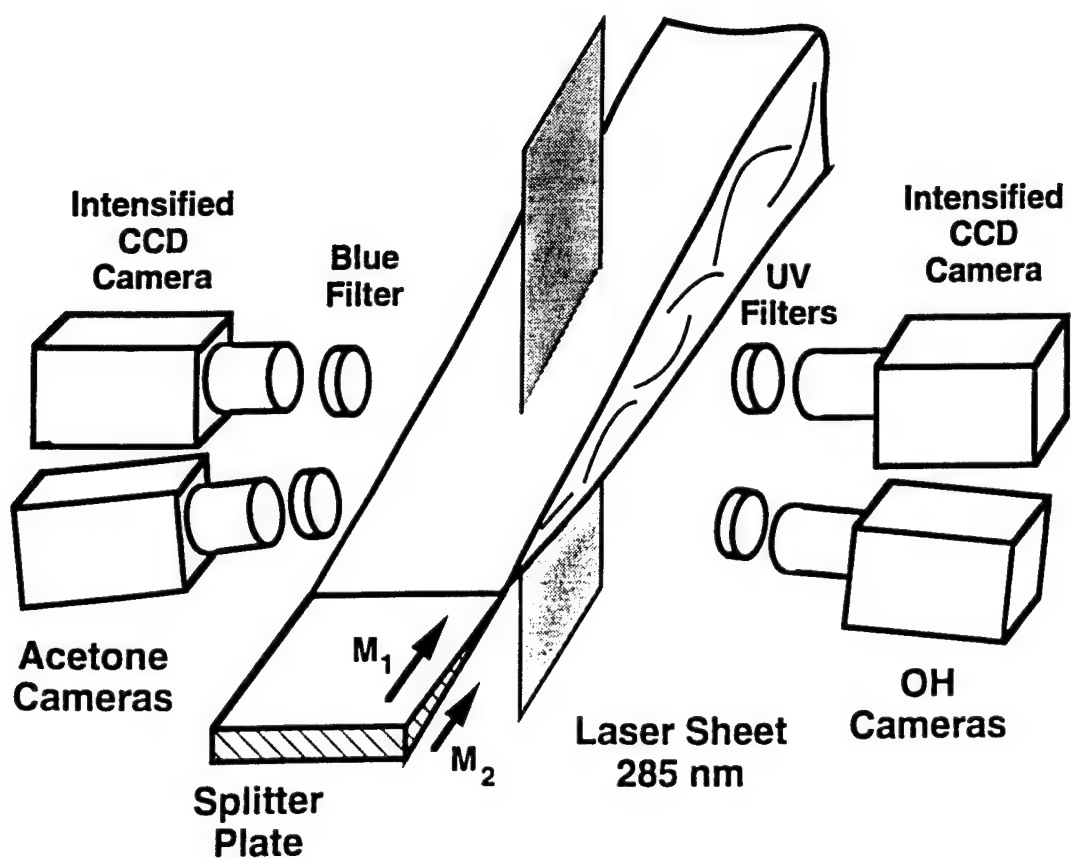
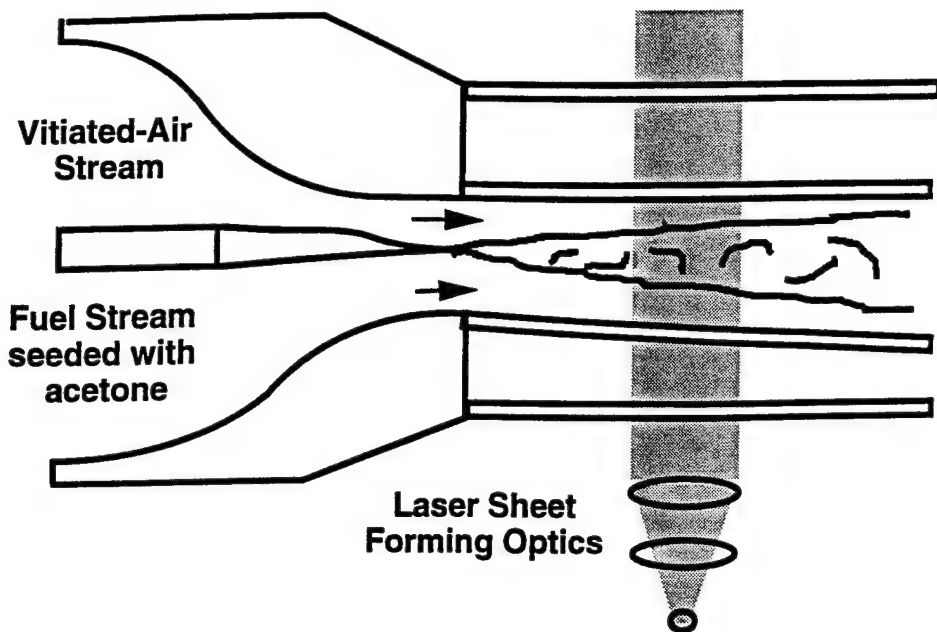


Figure 1.

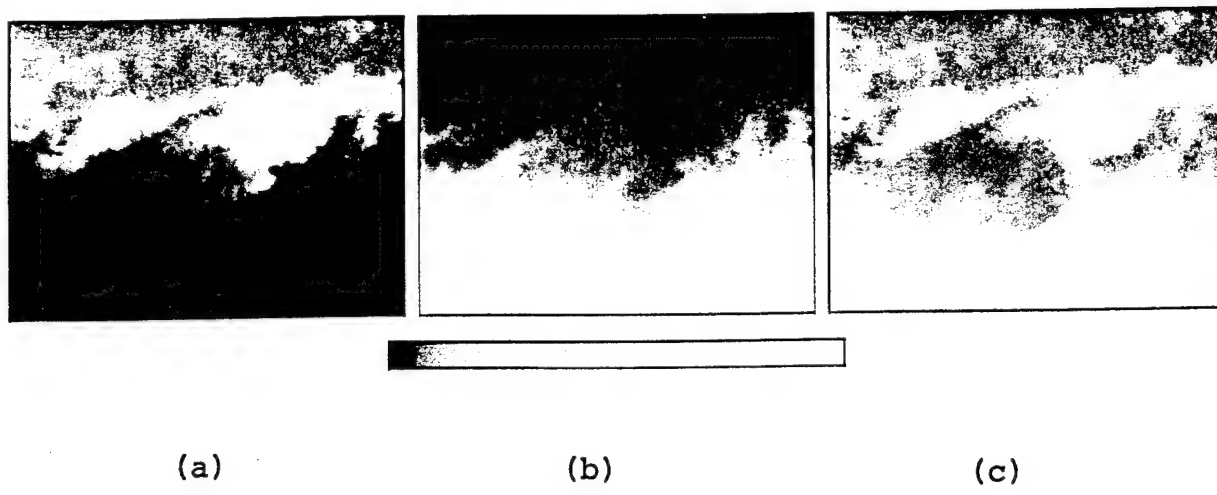


Figure 2.

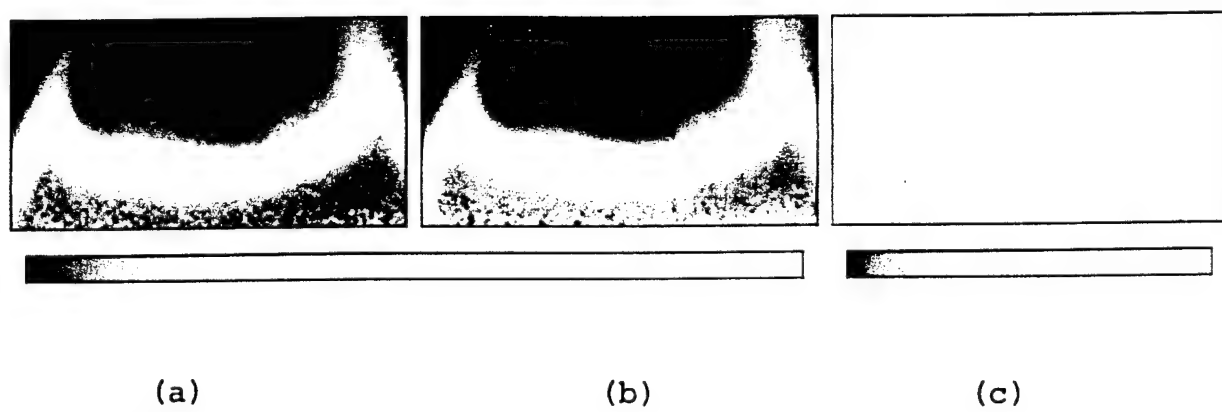


Figure 3.

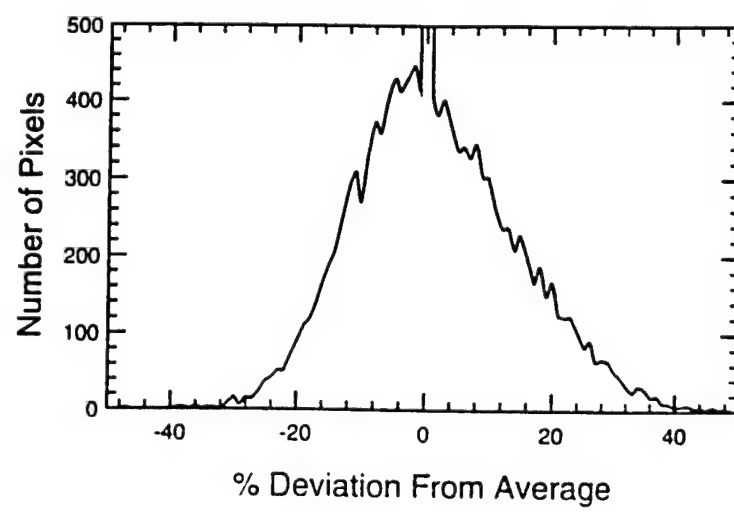
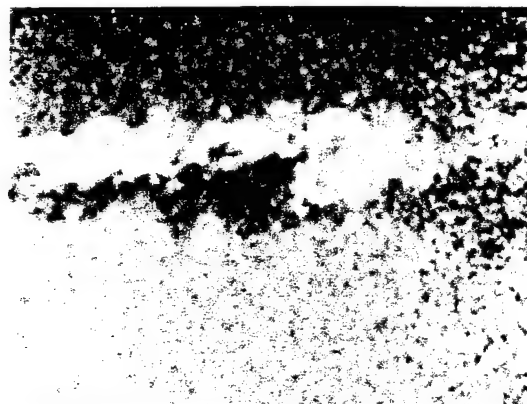
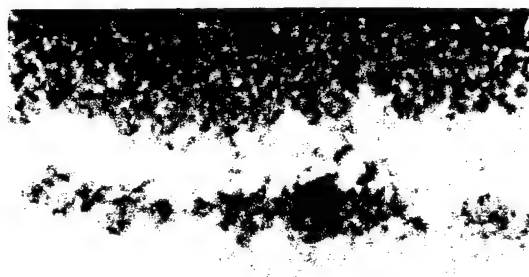


Figure 4.

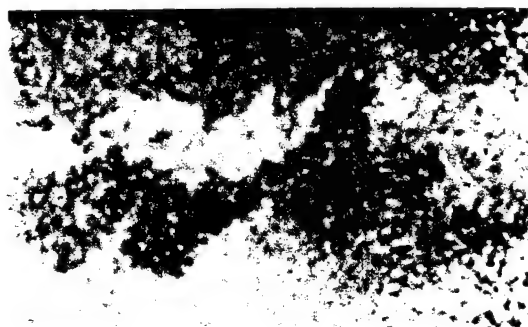


(a)

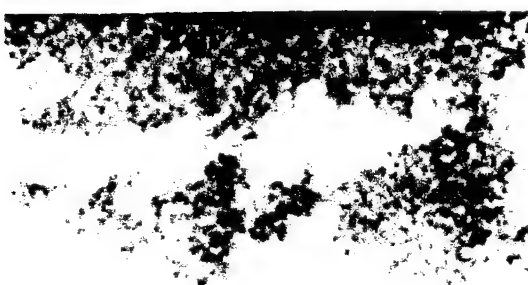


(b)

Figure 5.



(a)



(b)

Figure 6.



AIAA 94-0228

**Multiple Scalar Planar Fluorescence
Imaging for Reacting Flows**

J. M. Seitzman, M. F. Miller,
B. K. McMillin, R. K. Hanson
Stanford University
Stanford, CA

P. A. DeBarber and C. F. Hess,
MetroLaser
Irvine, CA

**32nd Aerospace Sciences
Meeting & Exhibit**

January 10-13, 1994 / Reno, NV

MULTIPLE SCALAR PLANAR FLUORESCENCE IMAGING FOR REACTING FLOWS

J. M. Seitzman*, M. F. Miller**, B. K. McMillin*, R. K. Hanson†

Stanford University

High Temperature Gasdynamics Laboratory

Department of Mechanical Engineering

Stanford, CA 94305

P. A. DeBarber* and C. F. Hess*

MetroLaser

18006 Skypark Circle, Suite 108

Irvine, CA 92714

Abstract

We describe recent advances for simultaneous imaging of multiple scalar fields in reacting flows. Fluorescence images of a gas seeded into the fuel and separate images of the OH radical were simultaneously acquired in two high-speed nonpremixed combustion flows. Combined NO and OH measurements, using two lasers and two detectors, are demonstrated in a SCRAMJET model flow. Simultaneous measurements of acetone and OH were acquired in a supersonic reacting mixing layer, utilizing a single laser. As fuel tracers in these flows, NO is relatively stable and acts as a conserved scalar, while acetone is a fuel and marks unburned fuel gases. Here, the NO fluorescence is only qualitatively representative of the NO mole fraction, while acetone fluorescence more accurately reflects its concentration. For both flows, OH marks the hot combustion gases, and OH fluorescence produced by exciting the (1,0) $P_1(7)$ line tracks the OH concentration with maximum errors between $\pm 6\text{--}25\%$. A new approach for combined acetone/OH imaging, excitation at 285 nm with a frequency-doubled dye laser is compared to previous measurements using a XeCl excimer laser at 308 nm. Finally, characterization measurements in a laminar flame show that multiple camera imaging can be performed in a manner which allows for quantitative results with respect to spatial alignment and signal level.

Introduction

Because of the strong reliance of humans on visual information, imaging techniques are powerful tools for studying complex flows.¹ One technique especially useful in reacting flows is planar laser-induced fluorescence (PLIF), since it combines excellent spatial resolution with high sensitivity, and species and quantum state specificity.² Most PLIF applications to date have

consisted of two-dimensional measurements of one scalar quantity, usually concentration of a single species. Unraveling the complex nature of reacting flows, however, often requires more information than that revealed by a single scalar variable. Here, we describe recent advances for *simultaneous* imaging of multiple scalar fields in reacting flows using PLIF. The approaches can be divided into two types: single and multiple laser techniques.

Some of the advantages of simultaneous planar imaging measurements have already been demonstrated. For example, planar images of elastic Lorenz-Mie scattering from particles combined with visible fluorescence (and phosphorescence) from biacetyl vapor have been obtained with a single ultraviolet laser and used to study differential diffusion in a nonreacting jet.³ A dual laser technique has been used to obtain (nearly) simultaneous images of OH and products of fuel pyrolysis, e.g., acetylene, in laminar flames.⁴ There, OH PLIF, with excitation near 283 nm and fluorescence detection near 310 nm, was combined with visible CH emission produced primarily by multiphoton photodissociation of acetylene at 193 nm. Finally, another dual laser approach was developed to image three species: a standard Nd:YAG-pumped, frequency-doubled dye laser produced OH PLIF according to the approach described above; and a custom high-power flashlamp-pumped dye laser at 431 nm was used to measure the combined signals at 489 nm produced by CH PLIF and spontaneous Raman scattering from CH_4 .⁵ The high power of the flashlamp laser was used to overcome the weak signals associated both with Raman scattering and with the weak, nonresonant CH detection scheme.

Here, we describe recent advances in two alternate approaches for combined species measurements using standard tunable laser systems. Both methods were developed for investigations of the role of large-scale structures in high-speed, nonpremixed reacting flows. In order to study these mixing and reacting flows, we acquire simultaneous PLIF images of two species, one

*Member AIAA

**Student Member AIAA

†Senior Member AIAA

marking the fuel gas stream and the other marking the combustion gases. In the first approach, two lasers are used to make combined NO and OH measurements, while the second method uses a single laser for combined acetone and OH imaging. The ability to acquire both quantities with a single laser system greatly reduces the complexity and cost of the measurement system. In this latter approach, a laser is tuned so as to simultaneously excite both species, while the fluorescence from the two is captured on separate cameras. Descriptive applications, as well as fundamental diagnostic issues and comparisons of the two techniques are presented.

Experimental Apparatus

Simultaneous imaging experiments were performed in three flow facilities. Simultaneous images of the same OH distribution in a small-scale 10 cm × 4 cm flat flame burner were acquired with a single laser and two detectors. The images were used to examine systematic errors associated with the experimental implementation of simultaneous species imaging. The burner was operated at atmospheric pressure in a premixed mode, burning a fuel-rich mixture of methane and air. A lifted flame was used to produce distinct spatial structures. The NO/OH and acetone/OH experiments were carried out in the high-speed flows described below.

The excitation and detection schemes for each case are also detailed below. For the laminar flame measurements, the laser excitation and detection systems are identical to those described in the acetone/OH experiment. In all cases, the simultaneous images were acquired by two cameras which viewed the illuminated plane from opposite sides of the flow. Pixel-to-pixel spatial alignment between the cameras was ensured by simultaneously recording the image of a thin, transparent alignment target with each camera system. Careful attention was paid to the camera positioning during the measurements in order to minimize (or eliminate) post-experiment image processing intended to match the cameras' fields of view. All the images were corrected for background emission and scattering, spatially nonuniform response of the detection system, and variations in laser energy across the height of the sheet.

NO/OH Experiment

The combined NO and OH measurements were carried out in a SCRAMJET model flowfield which has been described in detail elsewhere.⁶ Briefly, a transverse jet in a supersonic crossflow ($M=1.4$) was produced by injecting fuel through a pulsed solenoid valve, with a 2 mm diameter orifice, into the supersonic flow behind a shock wave that was generated in a pressure-driven 76 mm square shock tube. The valve was triggered so that the jet flow reached steady-state prior to the incident

shock arrival and the images were acquired nearly 200 μ s after passage of the incident shock. The jet contained 2% NO seeded into the hydrogen fuel at a stagnation temperature of 300 K, and the supersonic oxidizing flow consisted of 21% O₂ in Ar at 2160 K and 0.4 atm.

The laser and detection systems used in the PLIF imaging have also been described previously.⁷ Two frequency-doubled XeCl excimer-pumped dye lasers, with a pulse separation of 100 ns, were used to measure the OH and NO distributions. The first laser was tuned to the A←X (1,0) Q₁(7) transition of OH near 283 nm, while the second excited the A←X (0,0) Q₁+P₂₁(18) transition of NO around 226 nm. The lasers were combined and passed through the same cylindrical telescope and spherical focusing lenses in order to produce two nearly coplanar laser sheets 75 mm high and 300 μ m wide. For both lasers, approximately 0.5 mJ of sheet energy reached the test section. The PLIF images were acquired with a matched pair of thermoelectrically cooled, fiberoptically coupled, intensified CCD cameras (384 × 578 pixels) equipped with 105 mm, f/4.5 uv Nikkor lenses; one detection system was used for each species. UG-5 and WG-305 Schott glass filters were used to block the laser scattering for the NO and OH measurements, respectively. The intensifier gate widths were set to provide uniform gating times of 60 ns for the OH data and 200 ns for the longer lived NO.

Acetone/OH Experiment

The simultaneous acetone and OH experiments were performed in a large-scale, blowdown facility with mass flow rates above 1 kg/s and with roughly 7 s of test time.⁸ In brief, a plane mixing layer was formed between a high-speed high-temperature (~1500 K) oxidizing stream and a slower, low-temperature (~280 K) fuel stream. The oxidizing stream exhausted from a vitiation heater, which burned oxygen-enriched air and hydrogen in a fuel-lean mixture, and then the exhaust was expanded through a supersonic nozzle. The oxidizing stream constituents were primarily oxygen and water vapor, 23% each, in nitrogen. The fuel stream consisted of 10% hydrogen diluted in nitrogen. A small amount of acetone (2500 ppm) was seeded into the fuel stream by spraying liquid acetone through a fine atomizing nozzle located well upstream of the test section. The two flows were then brought together at the end of a thin splitter plate. For the measurements presented here, the imaged region was centered near the middle of the 8 cm × 10 cm test section, approximately 22 cm downstream of the splitter plate.

The PLIF images of OH and acetone were produced with a single Nd:YAG-pumped, frequency-doubled dye laser. A single uv laser system can be used to excite both OH and acetone since the OH A←X system has many strong absorption lines between 280 and 320 nm, while

the $S_1 \leftarrow S_0$ electronic transition of acetone exhibits continuous absorption from about 225 to 320 nm. The fluorescence from the two molecules is well separated in wavelength; OH emits primarily near 310 nm, while acetone emission occurs in the ~400-500 nm region. The current dye laser system was modified to allow the spectral bandwidth of the laser to be selectable between 0.05 and 1 cm⁻¹; a ~0.5 cm⁻¹ width was used here. A laser sheet, tuned to the OH (1,0) P₁(7) line near 285 nm, was formed with three cylindrical lenses. Two lenses: a -50 mm focal length lens and an 89 mm diameter, 500 mm lens, formed a cylindrical telescope which spread the beam into a collimated, 83 mm tall sheet. A third cylindrical lens, also 500 mm focal length, focused the sheet to a ~600 μm waist (fullwidth at 2% of peak). The sheet energy was roughly 15 mJ at the image plane and was not limited by the maximum energy available from the laser (~40 mJ).

The fluorescence from each species was simultaneously recorded on separate detectors, similar to those described above. In this case, however, the acetone fluorescence was imaged through a 500 nm low-pass filter and a glass, 50 mm f/1.2 photographic lens, neither of which transmitted the uv laser scattering or OH fluorescence. Also, a Schott UG11 filter was added to the OH detector to block the visible acetone fluorescence. The intensifier gates were 400 ns for the OH camera and 200 ns for the acetone camera.

Combined Species Imaging

As stated previously, the simultaneous scalar imaging techniques presented here were developed for a specific application, measurement of large-scale structures in high-speed nonpremixed combustion flows. Despite this narrow focus, a number of the issues addressed here are common to most simultaneous scalar imaging measurements. These issues include the choice of species, the interpretation of the individual images and the accuracy of correlations between simultaneous images. This last issue encompasses the systematic uncertainties associated with camera alignment and system repeatability when using separate detection systems (camera, optics, etc.) to record the fluorescing species, which is the most general approach for simultaneous imaging measurements.

Again, our method for measuring the large-scale structures responsible for mixing and entrainment requires images of regions containing fuel gas and simultaneous, but separate, images of combustion gas regions. OH was chosen as the combustion gas marker because it is one of the few products of both hydrogen and hydrocarbon combustion that has been well-characterized with PLIF.² Also for the high-speed flows considered here, the Damköhler number for OH

formation and destruction is on the order of unity; thus OH is not primarily limited to chemical reaction zones but also marks regions of (hot) combustion products.

Since most fuels of interest, e.g., hydrogen, are not readily amenable to high signal, single-shot planar imaging, a more appropriate fuel tracer must usually be added. Potential fuel tracers fall between two distinct regimes: 1) "stable" gases which permit conserved scalar-type measurements and 2) reacting species which mimic the fuel chemistry and thus allow measurements of unburned fuel gases. Especially in the latter case, the fuel dopant concentration should be low enough to prevent significant change in the reacting flowfield (specific heat, heat release, etc.). As discussed below, the NO technique falls primarily in the conserved scalar category, while the acetone images are more like unburned fuel measurements.

Even here where much of the emphasis is on the spatial character of the flow and where highly accurate concentration measurements are not required, the interpretation of the fluorescence images deserves some attention. Typically, the fluorescence signal is considered to scale linearly with the species concentration or mole fraction. For (nearly) isobaric flows, the principal systematic error concerns are the dependence of the signal on local temperature and gas composition (primarily related to collisional quenching).

Combined NO/OH Imaging

For many high-speed reacting flows like the SCRAMJET model flowfield presented here, NO seeded into the hydrogen fuel can be considered a conserved scalar. The chemical stability of NO was modelled for various gas compositions and temperatures representative of mixtures ranging from pure jet fluid to nearly pure freestream fluid. At worst, a roughly 6% loss of NO occurred during the first millisecond, which is 5 to 10 times longer than the approximate residence time of the NO in the measurement region.

There are, however, a number of potential drawbacks to the use of NO as a seed species. Even in cases where the NO is relatively stable, it can sensitize ignition in hydrogen combustion flows.⁹ This effect is not important here, since it is pronounced primarily at high pressures and at low to moderate mixture temperature, below 1000 K. Also, serious consideration must be given to the safety (and legal) issues surrounding the use of a toxic substance like NO, especially in large facilities which require sizable flow rates. Moreover, the NO excitation wavelengths are in the far uv and require high quality fused-silica optics. Finally, the large variation in NO quenching cross-sections for various gases, especially the large quenching rates for O₂ and combustion products like

H_2O and OH, limits the quantitative nature of NO fluorescence images.

In the SCRAMJET flow, with its large variations in gas composition and temperature, the NO fluorescence is only qualitatively representative of the NO mole fraction. Figure 1 shows the results of a simple mixing analysis of the fluorescence signal variation with jet mixture fraction. The mixing analysis represents a good first approximation to the variations in the flow, since the short residence times limit the degree of reaction and heat release.⁶ The results shown are for the $\text{Q}_1+\text{P}_{21}(18)$ line used in the current measurements; this line was chosen it provides good signal and tracks the NO mole fraction reasonably well. As seen in Fig. 1, the NO fluorescence does decrease with dilution but is not linearly proportional to jet mixture fraction (and thus NO mole fraction).

In contrast, a similar analysis for the OH fluorescence (Fig. 1) reveals that the accuracy of the OH PLIF in representing the OH concentration is good, with a maximum error of $\pm 25\%$ across all OH containing regions of the flow. This model of the accuracy includes variations in quenching, broadening, and Boltzmann fraction, i.e., temperature, as well as the experimental observation that measurable levels of OH are not observed for mixtures containing less than 25% freestream fluid.

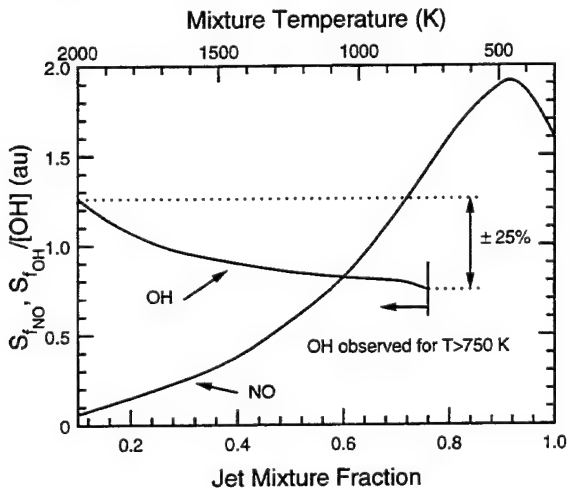


Figure 1. Modelled variation of the NO fluorescence signal ($S_{f\text{NO}}$) and the OH fluorescence normalized by the OH concentration ($S_{f\text{OH}}/[\text{OH}]$) with fuel jet mixture fraction. For fluorescence signals linearly proportional to species mole fraction alone, the NO curve would be a straight line and the OH curve would be a horizontal line.

Simultaneous Acetone/OH Imaging

Compared to a multiple laser approach like the NO/OH technique, the use of a single laser greatly simplifies the setup of a simultaneous multiscalar imaging

experiment. The combined acetone/OH method, only recently demonstrated,^{8,10,11} is an excellent example. The previous applications of combined OH and acetone imaging used a single XeCl excimer laser at 308 nm (~100-150 mJ pulse energy) to simultaneously excite acetone and a rotational line in the A \leftarrow X (0,0) vibrational band of OH.

In contrast, the current measurements use frequency-doubled, dye laser excitation near 285 nm to excite an OH line in the (1,0) band along with acetone. The new approach allows for better rejection of laser scattering onto the OH camera and more flexibility in choosing the OH pump transition, e.g., the ability to choose a transition with less temperature dependence. In terms of signal strength, the lower laser energies available from the doubled-dye laser (~20-40 mJ) compared to the XeCl laser are partly compensated by: 1) the acetone absorption coefficient at 285 nm is approximately 3 times higher than at 308 nm; and 2) the OH line pumped by the XeCl laser is poorly populated at high temperatures and its fluorescence is partially saturated.¹²

Unlike NO, acetone is expected to track the concentration of *unburned* fuel for high-speed hydrogen combustion at moderate temperatures (less than ~1600 K), since the chemical removal of acetone is similar to that of hydrogen in the flow.⁸ Compared to the short residence times in the mixing layer (< 1 ms), acetone pyrolysis is relatively slow and not a significant mechanism for acetone removal. In addition, the rates of acetone destruction by radical attack are similar to those of the hydrogen fuel itself. Because acetone fluorescence is insensitive to collisional effects and the importance of temperature variations appears to be small at the lower range of acetone excitation wavelengths, the acetone fluorescence, unlike NO, should vary nearly linearly with acetone concentration.¹³ Though acetone is a liquid under normal conditions, it is relatively easy to seed into gaseous flows through spray or bubbling techniques since its vapor pressure at 20 °C is about 180 Torr.¹³ While not a problem in the present facility, acetone condensation and droplet formation is a potential complication for flows that exhibit significant drops in temperature or pressure. Since acetone acts like a fuel, though, some properties of the mixing layer are changed. With the addition of acetone to the diluted hydrogen fuel, the heat of combustion of the fuel stream and the overall fuel-to-air ratio of the mixing layer both increase by about 15%.

In the mixing layer, the OH fluorescence again provides a relatively accurate measurement of the OH concentration. Figure 2 shows the results of a mixing analysis between the fuel and oxidizer streams that is intended to represent the range of compositions and temperatures present in the mixing layer. As seen in the figure, the OH fluorescence signal is expected to track the

OH concentration within $\pm 15\%$ across almost all OH containing regions of the mixing layer (fuel stream mixture fraction ξ_{fuel} less than one-half). Again, this accuracy includes variations in quenching, broadening, and temperature. For a smaller range of mixture fractions (ξ_{fuel} below one-third) which still represents most of the OH, the error in OH concentration is reduced to $\pm 6\%$.

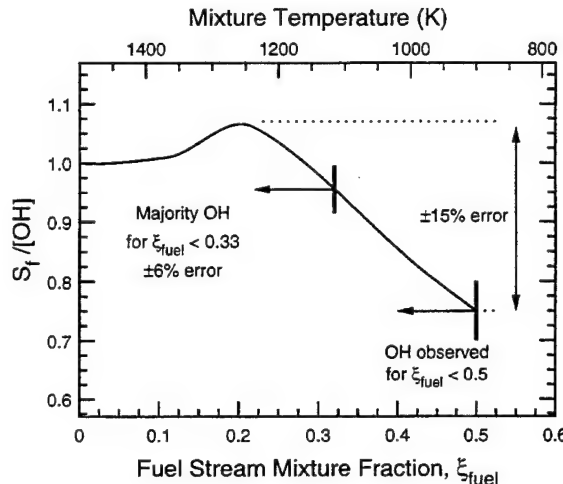


Figure 2. Variation of the OH fluorescence normalized by the OH concentration ($S_f/[OH]$) with fuel stream mixture fraction, modelled with a (nonreacting) mixing analysis.

Results

Laminar Flame Measurements

As mentioned previously, measurements were made of the experimental errors associated with simultaneous multiple camera imaging. Figure 3 illustrates a pair of OH images acquired in the laminar methane-air flame. The two images were acquired with two cameras from the same laser pulse, and should thus be identical in the absence of any random or systematic errors.

Figure 3 shows the background-corrected results for one image pair from a set of 20 such pairs; no spatial alignment corrections were applied. For the entire image, a single scaling factor was applied to force the conditionally averaged pixel value (omitting pixels with intensities in the background noise) to be the same for both images. This scaling factor is nearly the same for each image pair; the variation (standard deviation) over the 20 pairs is 1.7%. The greatest excursion in the scaling factor was 3.7%. These variations are small and may simply be within the uncertainty of the measurement procedure. Considering the number of pixels in the conditional averages (~1000-10,000), however, some of the variation is probably real, possibly a result of shot-to-shot changes in the cameras' sensitivities or differences in

the flowfield (e.g., different radiative trapping for the two optical paths).

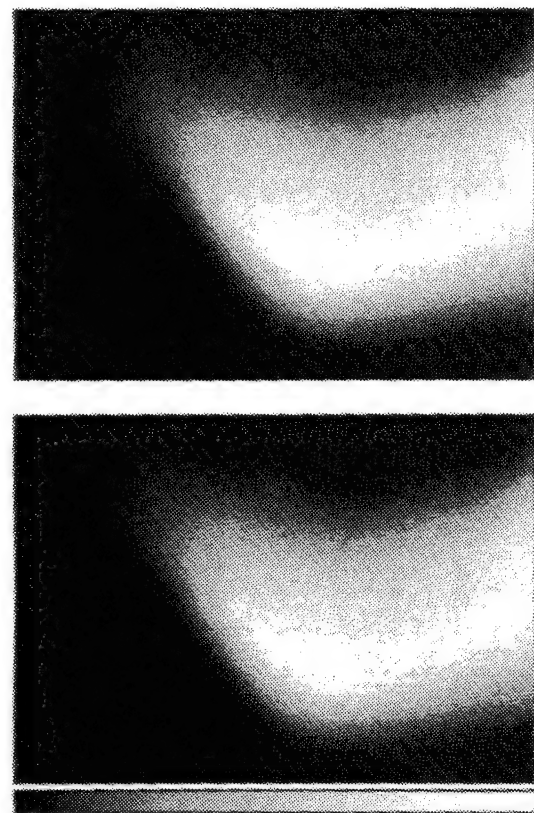


Figure 3. Simultaneous images (281×189 pixels, 69×47 mm) of OH in the lifted, premixed methane-air flame recorded with two detectors from the same laser pulse. The sheet propagates right-to-left in these sideview images of the flame. The color bar shows signal increasing linearly from black to white.

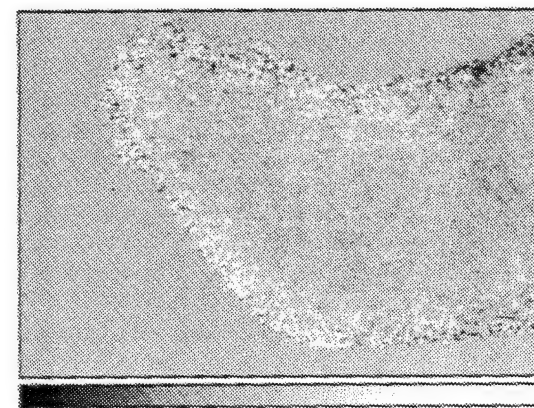


Figure 4. Difference between the two images of Fig. 3, normalized by the average of the two. The color bar shows errors from -50% to +50% (left to right).

Figure 4 shows the difference between the two images of Fig. 3, normalized by the average of the two. Thus, it represents the fractional difference, or error, between the two images, on a pixel by pixel basis. In order to highlight any potential spatial mismatch, the error was set to zero at pixels with intensities considered to be in the background noise ($\sim 2\%$ of the peak signals) for either image. While the overall structure of the original images remains, the error level is somewhat randomly distributed across the image. The errors, in general, tend to be larger near the edges of the flame, since the residual shot-noise is higher there.

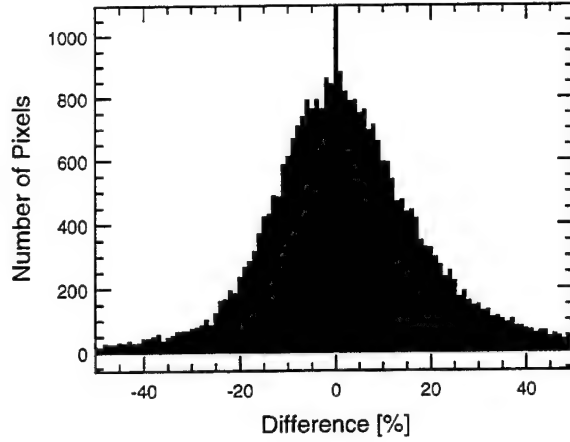


Figure 5. Histogram of the fractional differences between pixels from the image of Fig. 4. The spike at zero error results from forcing the error to be zero for pixels with signal levels within the background noise.

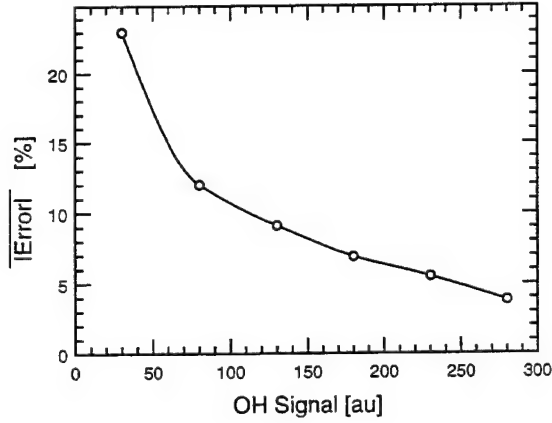


Figure 6. Signal level dependence of the error between two single-shot images of OH PLIF recorded simultaneously with two separate detection systems (see Fig. 4). The average absolute value of the fractional error is seen to decrease for higher signals.

The random distribution of the error is illustrated in Fig. 5, a histogram of the image shown in Fig. 4. While the mean of the distribution is nearly zero, the averaged, absolute value of the errors is 14.7%; for the complete set of image pairs, it is nearly 18%. Again, much of the error

is probably associated with shot-noise fluctuations between the images. This is seen in Fig. 6, which shows the error as a function of signal level. As would be expected for shot-noise, the fractional error declines for increasing signal. These results show that multiple camera imaging can be performed in a manner which allows for quantitative results with respect to spatial alignment and signal level.

Combined NO/OH Imaging

Simultaneous NO and OH visualizations were obtained from two overlapping 45×30 mm regions in the SCRAMJET model flow: an upstream region covering streamwise coordinates (x/D , D =jet diameter=2 mm) ranging from -5 to 17.5 and a downstream region from x/D of 10 to 32.5, with the jet located at x/D of zero. Figure 7 shows a composite of two sets of simultaneous image pairs, one set from a part of the upstream region ($-5 < x/D < 10$) and the other from the downstream location. Even for the low laser energies in the test section (~ 0.5 mJ), the signal-to-noise ratio (SNR) of the corrected images is quite good. The NO images have peak SNR values as high as 15 in the downstream image, where dilution has already decreased the signals (see Fig. 1). The peak NO levels are estimated to be a few thousand ppm in this region. The noise levels in the OH images are higher, with peak SNR values of 8 to 9.

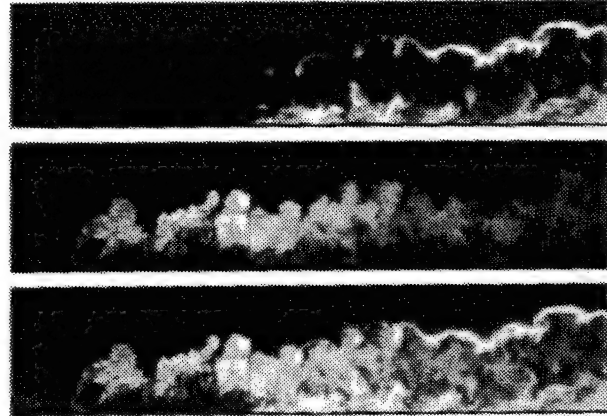


Figure 7. Simultaneous, single-shot composite images (75×15 mm) of NO and OH in the SCRAMJET model flowfield: (top) OH concentration, (middle) NO distribution, and (bottom) an overlay of the two. Each image represents a composite of separate realizations from two regions in the flow, $-5 < x/D < 10$ and $10 < x/D < 32.5$, with both clipped to show $0 < y/D < 7.5$, with the wall at $y/D = 0$. The sheet propagates downward in these sideview images of the jet, with the crossflow moving from left to right. As in Fig. 3, black corresponds to minimum signal and white represents the peak signal in each image.

The complementary nature of the regions marked by the two species is seen in the images and is even more evident in vertical cuts through the data (see Fig. 8). The NO marks the well-defined jet plume, while the OH is found primarily along the jet's boundaries. The presence of OH (combustion gases) within the jet is a rare occurrence until the downstream edge of the measured region. As the hydrogen jet begins to mix with the hot supersonic oxidizer in this self-igniting flow, OH is produced primarily in very high temperature (thus mostly fuel lean) regions. In fact the peak OH levels for regions near x/D of 18 occur for mixtures having roughly 8-10% jet fluid and temperatures of about 2000 K. These observations are consistent with calculated OH and ignition time scales.⁷

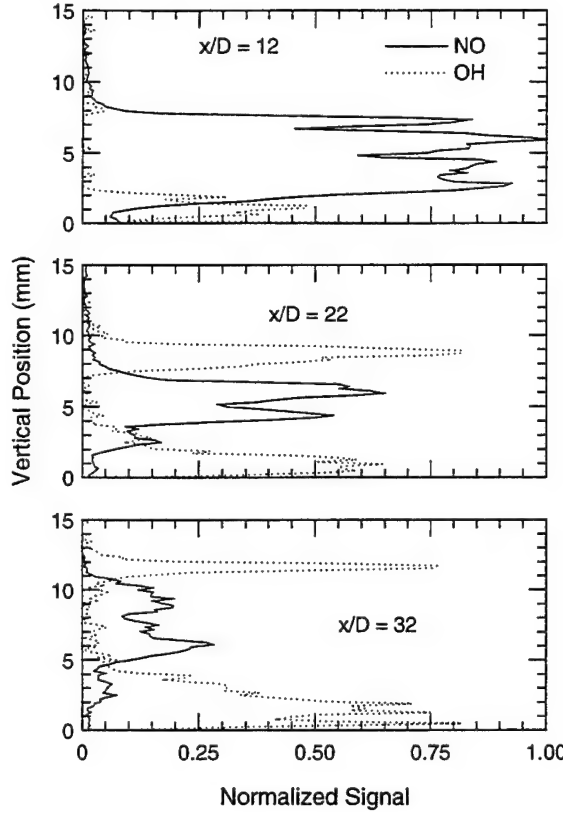


Figure 8. NO and OH signal profiles for vertical cuts through the images of Fig. 7 at three downstream locations. The drop in NO signal with downstream distance results from dilution, as the signals are scaled identically for each cut.

Simultaneous Acetone/OH Imaging

As an example of the images obtained with the doubled-dye laser approach for combined acetone/OH imaging, Fig. 9 shows a single-shot measurement (82×59 mm) in the mixing layer. The acetone concentration is maximum in the uniform region at the bottom of the images, which represents the undiluted fuel stream

(seeded roughly at 2500 ppm). The weaker acetone signals mark the boundary between the fuel stream and the bottom of the mixing layer. There, acetone has been either diluted or consumed by the hot oxidizing fluid. In general, the upper edge of the mixing layer coincides with the upper edge of the bright OH signals (maximum OH concentration). Above, residual OH from the vitiation heater is visible in the hot oxidizing stream. Based on calibration measurements with the camera systems in a shock heated OH flow,¹⁴ the peak OH levels in the layer were found to be about 2000 ppm. The OH levels in the vitiated air stream are as high as 300 ppm, though closer to 100 ppm on average.

As in the NO/OH experiment and for much the same reasons, the acetone and OH images provide complementary information. The mixture temperature, assuming low heat release, and the local stoichiometry are again related such that high temperatures are associated with lean mixtures. The sensitivity of the OH formation to temperature suggests that OH would primarily occur only in those regions with low acetone concentration.

The high quality of the images obtained with the current approach is clearly evident. Based on root-mean-squared variations in regions of nominally uniform signal in the corrected images, the SNR of the single-shot acetone images peaks at 12 in the undiluted freestream. For the OH data, the peak SNR in the mixing layer is between 10 and 12, and in the undiluted vitiated air stream, the SNR is 5. These SNR values compares well to the previous XeCl measurements in the same facility, which employed a $\sim 1 \text{ cm}^{-1}$ laser tuned to the more temperature dependent (0,0) $Q_1(3)$ line of OH.⁸ With approximately 50-60 mJ reaching the flow in a sheet of nearly the same height, the peak SNR values in the previous measurements were about 15 for both molecules. Thus, no significant loss in signal is associated with the new excitation approach, while some advantages in rejection of laser scattering and transition selection are realized.

In comparing the two approaches, the relative change in the acetone signal can be accurately predicted by a simple linear fluorescence model, with the only significant variations between the two cases being the different laser energies and absorption coefficients. The ratios of the laser energy and absorption coefficient for the XeCl experiment compared to the dye laser excitation were 4.0 and 0.36,¹³ respectively. Assuming a shot-noise relationship, $\text{SNR} \propto (\text{Signal})^{1/2}$, one would predict a 20% SNR advantage for XeCl excitation. The experimental comparison gives a value of 25%. For the OH measurements, a similar comparison of the two approaches with a linear fluorescence model which now includes laser energy, absorption coefficient, lineshape and fluorescence yield differences, predicts SNR values 3

to 4 times higher for XeCl excitation. The much lower measured ratio, 1.2 to 1.5, most likely results from saturation and bleaching caused by the high energy XeCl excitation of the strongly absorbing (0,0) $Q_1(3)$ line, and partially, perhaps, from poor locking of the narrowband XeCl laser used in the previous measurements.

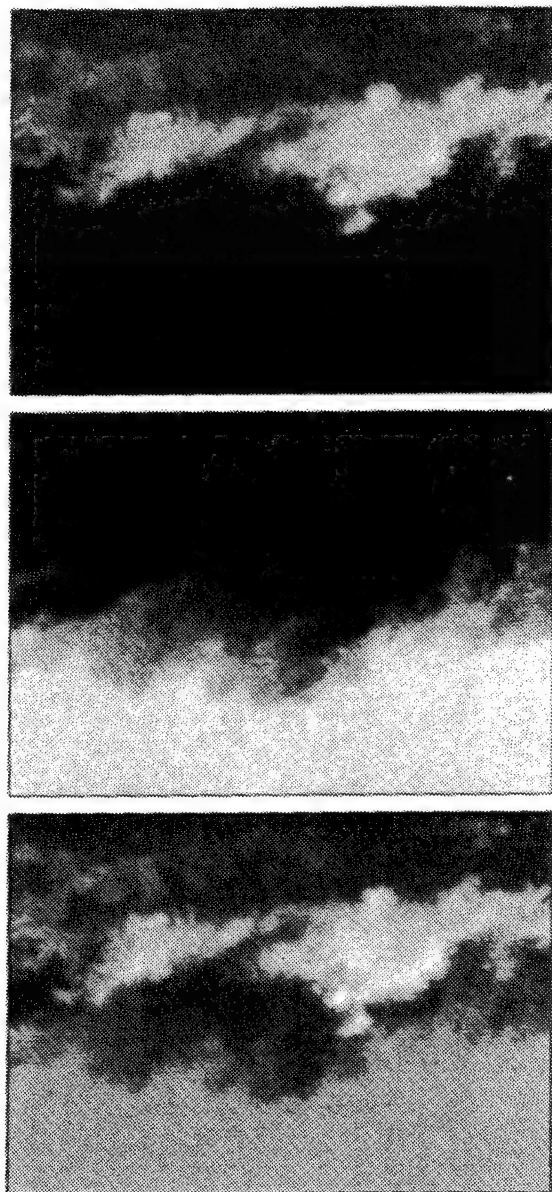


Figure 9. Single-pulse simultaneous images (211×152 pixels, 82×59 mm) of OH and acetone in a supersonic, reacting mixing layer: (top) the OH distribution, (middle) the acetone distribution, and (bottom) the overlay of the OH and acetone images. The sheet propagates upward in these sideview images of the mixing layer. The intensity encoding is similar to that shown in Fig. 3.

Conclusions

We have examined simultaneous PLIF imaging of two species for measurements of large-scale structures in high-speed nonpremixed combustion flows. Two methods were investigated and both are based on imaging a fuel gas marker seeded into the fuel stream and separately measuring a naturally occurring reaction product in order to mark the combustion gases. The first approach, using two lasers to make combined NO and OH measurements, was demonstrated in a SCRAMJET model flow. The second method, demonstrated in a supersonic reacting mixing layer, utilized a single laser for combined acetone and OH imaging. In all cases, good signal levels were achieved with best-case shot-noise errors between 6 and 12%.

The general experimental accuracy of simultaneous imaging measurements using multiple detection systems was also tested. A number of pairs of simultaneous OH images were acquired in a laminar methane-air flame, with each pair produced by the same laser pulse. Thus the two images in a pair should be identical in the absence of any random or systematic errors. No obvious pixel-to-pixel alignment errors were found. Average pixel-to-pixel differences of 18% were measured, though the deviation dropped to a few percent in the high signal regions, suggesting that most of the error is associated with signal shot-noise fluctuations. The shot-to-shot stability of the effective detection sensitivity was excellent; the ratio of the average signals recorded by the two detectors varied by less than 2% for a set of 20 image pairs. Thus, we find that multiple camera imaging can be performed in a manner which allows for quantitative results with respect to spatial alignment and signal level.

For both of the high-speed combustion flows studied, OH marks the hot combustion gases, not just the chemical reaction zones. In addition, modelling of the fluorescence signal's dependence on the temperature and composition variations expected in these nonpremixed flows indicated that the OH fluorescence is a relatively accurate monitor of the OH concentration, with maximum errors between $\pm 6\text{--}25\%$.

As applied here, the two fuel seeds represent two classes of fuel tracers: NO is a relatively stable gas and acts as a conserved scalar while acetone is a fuel and marks unburned hydrogen. While NO is easily seeded into most flows, its toxicity is a major concern. Also, the NO fluorescence is only qualitatively representative of the NO mole fraction in the current SCRAMJET flowfield, because of the large variations in gas composition and temperature in the flow and the significant species dependence of the NO quenching cross-sections. Since acetone fluorescence is less sensitive to collisional and temperature effects, the acetone fluorescence more closely reflects its

concentration. While not an issue in the mixing layer flow, acetone condensation and droplet formation is a potential complication for flows that exhibit significant drops in temperature or pressure. Finally the addition of acetone to some fuel streams can significantly change their overall combustion properties.

One major advantage of the combined acetone/OH approach is the ability to acquire both measurements with a single laser system, which greatly reduces the complexity and cost of the measurement system. As demonstrated here, frequency-doubled dye laser excitation of the 285 nm (1,0) OH band exhibits no significant loss in signal compared to the earlier XeCl excimer excitation at 308 nm, while advantages in rejection of laser scattering and transition selection are realized. Even for the relatively large image region (8×5 cm) and the moderate acetone and OH levels (less than ~0.2%) in the mixing layer experiment, the signal levels were high enough to permit measurements with a dynamic range better than fifty. Since the laser was operated with only half its maximum energy output, similar signal levels could be achieved in even larger facilities.

Acknowledgements

The authors acknowledge T. Island and W. Urban for their assistance in acquiring the mixing layer data, and Dr. G. B. Northam of NASA Langley Research Center for many helpful discussions. This work was supported in part by the U.S. Air Force of Scientific Research, Aerospace Sciences Directorate, with Dr. J. Tishkoff as the technical monitor.

References

- ¹Yang, W. G., ed., "Handbook of Flow Visualization," Hemisphere Publishing, New York, 1989.
- ²Hanson, R. K., Seitzman, J. M. and Paul, P. H., "Planar Laser-Fluorescence Imaging of Combustion Gases," Applied Physics B, Vol. 50, 1990, pp. 441-454.
- ³Long, M. B., Stärner, S. H. and Bilger R. W., "Differential Diffusion in Jets using Joint PLIF and Lorenz-Mie Scattering," Combust. Sci. and Tech., Vol. 92, 1993, pp. 209-224.
- ⁴Allen, M. G., "Digital Imaging Techniques for Single- and Multi-Phase Reacting Flowfields," Ph.D. Dissertation, Dept. of Mechanical Engineering, Stanford Univ., Stanford, CA, Apr. 1987.
- ⁵Schefer, R. W., Namazian, M. and Kelly, J., "Simultaneous Raman Scattering and Laser-Induced Fluorescence for Multispecies Imaging in Turbulent Flames," Opt. Lett., Vol. 16, 1991, pp. 858-860.
- ⁶McMillin, B. K., Palmer, J. L. and Hanson, R. K., "Two-Line Fluorescence Imaging of NO Temperature in a Transverse Jet in Supersonic Crossflow," Appl. Opt., 1994, in press.
- ⁷McMillin, B. K., Seitzman, J. M. and Hanson, R. K., "Comparison of NO and OH PLIF Temperature Measurements in a SCRAMJET Model Flowfield," AIAA 93-2035, AIAA/SAE/ASME/ASEE 29th Joint Propulsion Conference, Monterey (1993).
- ⁸Miller, M., Island, T., Yip, B., Bowman, C. T., Mungal, M. and Hanson, R. K., "An Experimental Study of the Structure of a Compressible, Reacting Mixing Layer," AIAA 93-0354, AIAA 31st Aerospace Sciences Meeting, Reno (1993).
- ⁹Slack, M. and Grillo, A. "Investigation of Hydrogen-Air Ignition Sensitized by Nitric Oxide and Nitrogen Dioxide," NASA CR-2896 (1977).
- ¹⁰Yip, B., Miller, M. F., Lozano, A. and Hanson, R. K., "A Combined OH/Acetone Planar Laser-Induced Fluorescence Imaging Technique for Visualizing Combusting Flows," Exper. in Fluids, 1993, submitted.
- ¹¹Paul, P. and Clemens, T., "Planar Laser-Induced Fluorescence Imaging of Lifted H₂-Air Flames," AIAA-93-0800 AIAA 31st Aerospace Sciences Meeting, Reno, (1993).
- ¹²Seitzman, J. M. and Hanson, R. K., "Comparison of Excitation Techniques for Quantitative Fluorescence Imaging of Reacting Flows," AIAA Journal, Vol. 31, 1993, pp. 513-519.
- ¹³Lozano, A., Yip, B. and Hanson, R. K., "Acetone: A Tracer for Concentration Measurements in Gaseous Flows by Planar Laser-Induced Fluorescence," Exper. in Fluids, Vol. 13, 1992, pp. 369-376.
- ¹⁴Seitzman, J. M., Hanson, R. K., DeBarber, P. A., and Hess, C. F., "Application of Quantitative Two-Line OH PLIF for Temporally Resolved Planar Thermometry in Reacting Flows," Appl. Opt., 1994, in press.

Shock tunnel flow visualization using planar laser-induced fluorescence imaging of NO and OH

J.L. Palmer and R.K. Hanson

High Temperature Gasdynamics Laboratory

Dept. of Mechanical Engineering, Stanford University

Stanford, CA 94305-3032 USA

Abstract. Temporal sequences of planar laser-induced fluorescence (PLIF) images of several high-speed, transient flowfields created in a reflection-type shock tunnel facility were acquired. In each case, the test gas contained either nitric oxide or the hydroxyl radical, the fluorescent species. The processes of shock reflection from an endwall with a converging nozzle and of underexpanded free jet formation were examined. A comparison was also made between PLIF imaging and shadow photography. The investigation demonstrated some of the capabilities of PLIF imaging diagnostics in complex, transient, hypersonic flowfields, including those with combustion.

Key words: Flow visualization, supersonic flow, transient flow, shock tunnel, planar laser-induced fluorescence, shadowgraphy

1. Introduction

Time-resolved flow visualization can yield insight into many aspects of transient supersonic phenomena. Classical techniques, such as shadow and Schlieren photography and interferometry, have long been applied in the study of high-speed flowfields. Recently, advanced, laser-based diagnostics have been utilized in a variety of supersonic and hypersonic flows, including several with combustion. Here, temporal sequences of planar laser-induced fluorescence (PLIF) images of several transient, supersonic flowfields created in a reflection-type shock tunnel facility have been acquired which demonstrate some of the capabilities of PLIF as a flow visualization tool. Shadow imaging has also been applied for comparison.

The tunnel utilizes the stagnant, high-enthalpy gas produced by the reflected wave in a shock tube as it exhausts through a small, axisymmetric, converging nozzle located in the endwall of the tube. An underexpanded free jet flowfield is created at the exit of the nozzle, as the gas expands into a test section. A large tank is connected past the test section to maintain a constant ambient pressure. A diaphragm may be placed at the nozzle exit, allowing an ambient gas with a different composition and pressure than the test gas to be used.

In PLIF imaging experiments, a thin sheet of laser light is directed through the flowfield in the desired plane of observation. The laser is tuned to resonantly excite a particular electronic transition of an atomic or molecular species present in the flow. A portion of the fluorescent radiation is collected perpendicular to the observation plane by an optical system and imaged onto a two-dimensional solid-state detector array. Use of a pulsed laser can provide images that are effectively instantaneous and acquired with precise timing. The resultant signal may then be analyzed computationally to extract a spatially resolved property field. The repeatability of the flow conditions and structures allowed a single pulsed dye laser and digital camera system to be used here in obtaining a series of PLIF images at different times in sequential firings of the facility.

Shadow photography is one of the simplest methods of flow visualization. Shadowgraphs with flow-stopping temporal resolution may be acquired with a short duration, high intensity source of visible light. Photons from a point source may be collimated with a lens or mirror and directed through the flowfield of interest, where rays are refracted due to density gradients normal to the direction of light propagation. The transmitted light may be focused onto a photographic plate or a digital camera array. In the application under discussion here, a single shadow image was acquired in each run of the facility and a temporal sequence was again obtained during separate firings.

Several fundamental questions about the evolution of the flow up- and downstream of the shock tunnel nozzle have been addressed in this investigation. PLIF imaging of nitric oxide (NO) in the tunnel's reservoir region was used to examine the shock reflection process in a test gas of argon (Ar) seeded with a small amount of NO. A series of NO PLIF images with high temporal and spatial resolution was acquired, providing midplane views of the flowfield at different delays with respect to the time at which the incident shock reached the endwall. The initial distortion of the reflected shock due to the nozzle entrance in the endwall and the resultant perturbations in the reservoir were observable. At long delay times, disturbances arriving from upstream altered the pressure and temperature of the gas, thereby terminating the period of stable reservoir conditions.

Downstream of the nozzle, the transient free jet flow was studied using NO PLIF imaging as well. The flow conditions were identical to those used in imaging the stagnation zone; and images were acquired with the same delays. The bursting of the diaphragm placed at the nozzle exit and its subsequent passage through the imaged region were observed. The diaphragm's effect on the flow and the time required for its flight out of the field of view were of concern. The process of jet startup to a quasi-steady flow condition is illustrated in detail in these images.

A comparison between NO PLIF and shadow imaging was made in observations of the underexpanded jet development transient. In both cases, the test gas was composed primarily of nitrogen (N_2); and no diaphragm was used at the nozzle exit. The flow was, therefore, initially quite orderly, providing a better environment in which to acquire short exposure shadow images of

the jet startup than in the case in which a diaphragm was employed. The two series of flow visualization images acquired under these conditions allowed a more detailed examination of the early wave interactions and vortex formation in the nascent free jet. Some of the advantages of planar flow measurements over classical, line-of-sight techniques are demonstrated in the results.

PLIF images of the starting process of the free jet were also obtained by exciting the hydroxyl radical (OH) in a test mixture of combustion gases. The flowfield was created by loading Ar with small amounts of hydrogen (H_2) and oxygen (O_2) into the driven section of the shock tunnel. Combustion in the reservoir yielded a gas mixture with ~2% OH. As the gas exhausted through the nozzle, partial chemical freezing occurred, leaving a concentration of OH in the free jet adequate for PLIF imaging of the flowfield. The resulting sequence demonstrates the use of PLIF imaging in a complex, transient combustion flowfield.

PLIF imaging has been used in several applications in this facility during its operation as a shock tube (McMillin et al. 1993; Seitzman et al. 1993) and as a shock tunnel (Palmer et al. 1991; Palmer and Hanson 1993a; 1993b; 1994). Temperature and velocity field measurements have been made in several flowfields, under a variety of flow conditions. The technique used here to construct a sequence of images from several runs of the facility was also used to examine the establishment of a bow shock over a circular cylinder downstream of a Mach 3, conical nozzle with PLIF and Schlieren photography (Palmer et al. 1994) and to study shock-induced ignition behind a reflected shock from an endwall with a V-shaped groove which created a combustion kernel (McMillin et al. 1990).

Historical reviews by Oertel (1983) and Reichenbach (1992) indicate the extensive use of classical flow visualization in the study of transient supersonic flow and shock phenomena. The process of shock reflection and nozzle starting or jet development in a planar nozzle with a rounded or sharp inlet, a transition nozzle, and an orifice plate was examined in detail by Amman and Reichenbach (1973), who obtained temporal sequences of shadowgraphs of these shock tunnel flows. Underexpanded free jet development has also been studied using several classical flow imaging techniques (Maslennikov and Dobrynin 1981; Golub et al. 1990; Emel'yanov and Eremin 1991). Recently, several investigators have computed the flowfield during the reflection process in a shock tunnel nozzle (Britan et al. 1987; Jacobs 1991; Prodromou and Hillier 1992; Yang 1992); and numerical simulations of jet transients have been carried out (Norman et al. 1982; Matsumura et al. 1990).

Other unsteady, supersonic flows with characteristics similar to those of the free jet expansion have been photographed using line-of-sight techniques. These examples include images showing the flow from a gun muzzle just prior to the exit of the projectile (Oswatitsch 1980) and shock formation upon diaphragm bursting in a shock tube (Liberman and Velikovich 1986). Flows induced by shock diffraction at the exit of a circular tube (Phan and Stollery 1983; Abe and

Takayama 1990; Bazarov et al. 1992; Da-Peng et al. 1993) and around a planar, convex corner (Maksimov 1988; Matsuo et al. 1990; Hillier 1991) have been studied experimentally and computationally. Photographs showing the blast wave and gas plume from an ablation target after pulsed laser irradiation also display many features in common with underexpanded free jet development (Kelly and Miotello 1993; Srinivasan 1994).

2. Imaging Techniques

2.1. PLIF

The spectrally and temporally integrated fluorescence signal per unit volume of gas for weak excitation of an isolated absorption line is given by:

$$S = \frac{E_p g B}{A_{las}} \left(\frac{\chi_a P}{kT} \right) f_{J''} \left(\frac{A}{A+Q} \right) C_{opt} \quad (1)$$

(Hanson et al. 1990). E_p is the laser pulse energy; g is the spectral convolution of the laser and absorption lineshapes; B is the rate of laser absorption; A_{las} is the cross sectional area of the laser sheet; χ_a is the mole fraction of the absorbing species; P is the pressure; T is the temperature; k is the Boltzmann constant; $f_{J''}$ is the Boltzmann fraction of the absorbing state; A is the effective rate of spontaneous emission from all directly and indirectly populated states; similarly, Q is the total electronic quenching rate of the excited state; and C_{opt} is a constant dependent on optical arrangement, collection efficiency, spectral filtering, temporal gating, etc.

The fluorescence signal is a function of temperature both explicitly, in an inverse manner, and implicitly, through the spectral convolution (Palmer and Hanson 1993b), lower state Boltzmann fraction (Vincenti and Kruger 1965), and photon yield ($A/A+Q$). The signal is proportional to the gas pressure, and other pressure dependencies enter through the spectral convolution and photon yield terms. These factors often make the interpretation of an individual PLIF image difficult; although analysis of two or more PLIF images of the flowfield can yield two-dimensional temperature and velocity fields (Palmer and Hanson 1993a; 1993b).

Selection of an absorption feature with an advantageous temperature sensitivity is important when imaging a flowfield with extreme property variations, such as a highly underexpanded free jet, as considered here. The absorption feature must also be sufficiently isolated spectrally to avoid laser interaction with neighboring transitions, so as not to introduce additional uncertainties into the analysis of the fluorescence signal. Overlapping transitions with degenerate frequencies may, however, be used to increase the lower state population fraction. In experiments with a test containing NO, the $R_1+Q_{21}(6)$ and $P_1(3)+P_1(14)$ transitions in the $A^2\Sigma^+ \leftarrow X^2\Pi(0,0)$ band of NO at 226.09 and 226.32 nm, respectively, were excited. The $A^2\Sigma^+ \leftarrow X^2\Pi(1,0)$ $P_1(1)$ transition of OH at 282.25 nm was used in imaging the reacting free jet. The temperature dependencies of the

lower state population fractions of these lines are shown in Fig. 1. The absorptions are strongest below 100 K, which is somewhat lower than the minimum temperature expected in the steady-state free jet flowfields. The curves in Fig. 1 suggest that as the temperature drops beyond the nozzle exit, an increasing fluorescence signal may be expected, since the signal is proportional to f_{J^*}/T , as shown in Eq. 1. However, since the flow is isentropic, the pressure decreases even more sharply than the temperature as the gas expands. These effects, combined with increases in the spectral convolution and fluorescence yield with decreasing temperature and pressure, minimize the dynamic range of the recorded PLIF signal. Images of the flow with adequate signal level and signal-to-noise ratio (S/N) throughout may thus be acquired. Overall, as will be seen below, the signal tends to decrease inside the core of the jet as the density ($\propto P/T$) falls, yielding a maximum dynamic range in the images of ~50-200 with S/N of ~10-50.

Across a normal shock, however, the signal typically has the opposite variation with density. The PLIF signal decreases behind the shock, where the temperature and pressure are elevated, primarily due to a decrease in Boltzmann fraction and an increase in electronic quenching. Examples of strong shocks observed in the images obtained here include the incident and reflected shocks in the reservoir region, the primary shock emerging from the nozzle during the jet starting process, and the Mach disk imbedded in the free jet. The line selection made here tends to maximize the change in PLIF signal across the shocks, while keeping it within the allowable dynamic range.

2.2. *Shadowgraphy*

The shadow signal recorded from a given point in the imaged region depends on the local second derivative of the flow density integrated across the width of the flowfield (Merzkirch 1987). Consequently, quantitative analysis of the flowfield properties is rarely possible. The difficulty is exacerbated when an axisymmetric, rather than planar, flowfield is examined. However, the technique is very useful in visualizing strong gradients, such as shock waves. The direction of propagation of a shock is easily identified in a shadowgraph, as each shock appears with a leading low signal edge followed by a bright "caustic" region. Turbulent areas of the flow yield a signal with a grainy appearance.

3. Experimental Facility

3.1. *Shock Tunnel*

The reflection-type shock tunnel facility in which these experiments were performed has been described in detail previously (Palmer et al. 1991; Palmer and Hanson 1993a). Figure 2 shows a schematic of the facility, along with the PLIF imaging system. The driver section of the

tube is 1.5 m in length; and the driven section is 4.5 m long, with a square interior cross section 7.6 cm on a side. Imaging experiments were performed in the reservoir and at the exit of a converging, axisymmetric nozzle with a 2.1 or 4.9 mm throat. Optical access was achieved through UV-grade fused silica windows mounted in the walls of the reservoir and jet test sections. The conditions for the flowfields imaged in this investigation are given in Table 1. The initial pressure, P_1 , at which the room temperature test gas was loaded into the facility is given, as is its composition. The conditions listed in the table for the reservoir region, P_s and T_s , are those calculated with one-dimensional shock theory from the measured shock speed or incident shock Mach number, M_s (Gaydon and Hurle 1963; Palmer et al. 1991). In the case of flow #4, additional chemical kinetics calculations were used to determine the properties (Palmer and Hanson 1994).

In the experiments with the larger converging nozzle (with throat diameter, $D = 4.9$ mm, flows #1 and 4), a diaphragm consisting of a 6 mm diameter circle of clear plastic tape was placed at the exit of the nozzle. The ambient gas composition and initial pressure were then allowed to differ from those of the test gas. With the smaller nozzle ($D = 2.1$ mm, flows #2 and 3), no diaphragm was used; and a single gas was loaded on both sides of the nozzle. The ambient gas composition, along with the ratio of the pressure of the reservoir gas to the ambient pressure, P_s/P_a , is given in Table 1 for each flow.

3.2. PLIF Imaging System

The technique used in imaging each of the flowfields considered here is listed in Table 1, along with the electronic transition that was pumped and the physical dimensions of the resulting images. Figure 3 shows the imaging geometry for each PLIF imaging experiment. In all the images, the primary flow is from left to right and the laser traverses the field of view from top to bottom.

Frequency-doubled photons from a tunable XeCl-pumped dye laser with Coumarin 450 or 540A dye were used to excite transitions in the $A^2\Sigma^+ \leftarrow X^2\Pi(0,0)$ band of NO and in the $A^2\Sigma^+ \leftarrow X^2\Pi(1,0)$ band of OH at 226 and 282 nm, respectively. In most regions of the flowfields, the laser was significantly broader than the absorption. The laser linewidth was $\sim 0.35\text{-}0.45\text{ cm}^{-1}$; while the absorption linewidth varied between 0.05 and 0.3 cm^{-1} . A thin, horizontal sheet of laser light was created using a series of lenses. Two cylindrical lenses telescopied the UV beam horizontally, expanding and then recollimating it to a width of 5-10 cm. A spherical lens focused the beam vertically to a thickness of $\sim 350\text{ }\mu\text{m}$ at the flow axis. The portion of the laser sheet that passed through the imaged region had 0.25-0.5 mJ in each 30 ns pulse.

Broadband fluorescence resulting from excitation of the test gas by a single laser pulse was collected normal to the direction of laser propagation, as shown in Fig. 2. The light was imaged onto an intensified CCD array and then transferred to computer. Spectral filtering eliminated elastic scattering and fluorescence from the excited ro-vibrational bands, while allowing detection of radiative relaxation in bands with longer wavelengths. Further details of the specific implementation of the PLIF diagnostic for each imaging experiment are given elsewhere (Palmer et al. 1991; Palmer and Hanson 1993a; 1994).

The timing of the laser shot, intensifier gating, and image acquisition was synchronized electronically using a series of delays. A trigger signal from the pressure transducer located in the driver section initiated charging of the excimer laser capacitor banks just before diaphragm rupture. The thin film gauge closest to the shock tube endwall initiated the sequence required to fire the laser/intensifier/camera system and to obtain a single PLIF image. A variable time delay that began the trigger sequence allowed observation of the flowfield at any desired time with respect to the moment at which the incident shock reached the shock tube endwall. The uncertainty in the delay for each image was $\pm 2 \mu\text{s}$, due to slight variations in the incident shock speed.

The procedures described by Seitzman (Seitzman et al. 1993) were used to correct the raw data images for laser sheet intensity variations, nonuniform collection efficiency, laser scattering, and background signal level on a pixel-by-pixel basis. Emission from the test gas, other than that induced by laser excitation, was neglected, since no signal above background was observed in images acquired in the usual way, except for the absence of the laser firing. Following correction, the image pixels were binned (2×2 or 3×3) and the results trimmed slightly. Table 1 lists the final dimensions of the images.

3.3. Shadow Photography System

In the shadow imaging experiments, light from a pulsed arc-discharge lamp, collimated with a 0.5 m focal length spherical mirror, was used to illuminate the flowfield for 25 ns. After passage through the test section, the light was imaged with a 35 mm lens onto an unintensified CCD array. Fig. 3c shows the imaging geometry. A timing system similar to that described above was used to fire the lamp and acquire the image. Passage of the incident shock over the last thin film gauge created the primary trigger signal; and a variable delay was used to obtain a shadow image at the desired moment during each shock tunnel run. Further details of the experimental arrangement are given by Palmer et al. (1991).

A correction for variations in illumination and transmittance through the test section not due to the flowfield was made to the shadowgraph images by subtracting an image obtained with the

test section evacuated. The images were trimmed slightly after correction; their final size is given in Table 1.

4. Results

4.1. Shock Tunnel Reservoir and Free Jet Transient Visualization

Figure 4 shows two series of NO PLIF images obtained in this investigation. The left image of each pair shows the shock tunnel reservoir region, bordering the endwall of the tube on the right, as shown in Fig. 3a; while that to the right shows the region downstream of the exit of the converging nozzle with $D = 4.9$ mm, as in Fig. 3b. The physical dimensions of the images and the conditions of the flowfield are given in table 1 as flow #1.

The scales to the far right of the image sequences indicate the signal levels corresponding to the colors in the images. Logarithmic scaling was used in both cases to increase the visibility of details in regions with low relative signal. The signal in the reservoir images was inverted before being displayed so that low signals (high densities) are represented by white and high signals (low densities) by black. In the jet images, high signals are shown in white and low signals in black. The density does not strictly increase with signal level in the jet images, although the trend is for the highest densities to be represented with white and the lowest ones with black, particularly inside the jet core beyond one diameter from the nozzle. The temperature sensitivity of the excited spectral feature of NO and the variations of the gas properties in the flowfields account for this apparent contradiction in signal dependence on density in the two imaged regions (see Sect. 2.1).

The first frame (a) of the reservoir image sequence shows the incident shock 15 μs prior to its reflection from the endwall, as it traveled into the stagnant test gas at 820 ± 5 m/s. The low density, stagnant gas before the shock appears black while the gas following the incident shock appears violet-blue in the image. In the next three frames (b-d), the nonplanar reflected shock, traveling from right to left, is visible. The shock separates the gas heated by the incident shock from the high pressure, high temperature gas that forms the reservoir for the free jet. The PLIF signal obtained from the reservoir gas translated to a red-orange shade in the images. Secondary shocks behind the primary wave are also observable, particularly in image c, where a curved, outwardly propagating conical shock extended from the primary wave back to the endwall. The circular intersection of these waves, which is a locus of triple points, quickly moved outward, as can be seen by comparing frames c and d, taken 30 ± 2 μs apart.

In frames e and f, disturbances in the reservoir caused by the flow of gas into the nozzle are visible. A compressive disturbance, seen as a bright, mushroom-shaped object in images g and beyond, then emerged from the nozzle entrance and propagated upstream. At the lip of the nozzle entrance, a vortex ring, appearing in the images as two dark circular spots, was generated behind

this wave. As the vortex ring traveled upstream and eventually exited the field of view (frames h-m), outflow through the nozzle continued and stable, though nonuniform, conditions persisted in the reservoir region for nearly 800 μs (frames n-r). The final images in the reservoir sequence (s and t) show an increase in signal level, caused by a decrease in temperature and pressure, as expansion waves from upstream arrived at the endwall, thereby ending the period of steady conditions in the nozzle reservoir.

In Fig. 4, the first images of the free jet region (a-e) show only the stagnant, NO-seeded ambient gas, as the primary shock wave had not yet traversed the nearly 10 cm long nozzle. In jet frame f, taken 150 μs after the incident shock reached the endwall, gas was observed emerging from the nozzle for the first time. A round blast wave-like shock emanated into the stagnant ambient region. Turbulence was introduced into the flow by the bursting of the circle of plastic tape used as a diaphragm at the nozzle exit. Pieces of the diaphragm can be seen as a bright (white) spot beyond which there is no PLIF signal because the tape lay in the laser sheet and as a dark (black) spot closer to the nozzle, caused by a fragment between the observation plane and the camera. The free jet grew rapidly in size, assuming a characteristic barrel shape, as seen in frames g and h. The diaphragm fragments are observable in these images for the last time, as they were pushed downstream, out of the field of view. Once out of the jet core (after $\sim 250 \mu\text{s}$), they no longer influenced its behavior; and the transient proceeded as though no diaphragm had initially been present (as will be seen in Sect. 4.2).

Following the expansion of the blast wave and jet gas in frames f-h, a recompression of the free jet took place as reflected waves traveled back to the flow axis from the sidewalls of the test section. This phenomenon is observed in the jet images shown in Figs. 4i-k. The process of jet formation and its expansion past the equilibrium size was repeated in frames l and m. In several runs of the experiment performed at each of these delays, the timing of this cyclical process was found to be highly repeatable. Beyond $\sim 600 \mu\text{s}$, the free jet was fairly stable, with variations in the barrel shock structure caused by weak interactions with the walls of the test section. Enlarging the test section would diminish these interactions and create a more steady shock shape. Jet images m-t, acquired up to and including the point of observable reservoir degradation (frames s and t), display a relatively constant signal variation with position inside the jet core, indicating stable gas properties there. Small deviations of the overall signal level or symmetry about the jet axis resulted from shot-to-shot changes in the laser spectral lineshape (Palmer et al. 1991; Palmer and Hanson 1993b), which affects the PLIF signal through the spectral overlap term, as shown in Eq. 1.

4.2. Comparison of PLIF and Shadow Imaging

Figure 5 shows a series of shadow images illustrating the free jet development process with a smaller converging nozzle ($D = 2.1$ mm). The conditions used are given in Table 1 and in Fig. 3c as flow #2. The scale at the bottom of the images gives the relative signal corresponding to a particular shade of gold in the images. High signals (shown in bright yellow) resulted when additional light rays were refracted into a given region in the image; while a low signal (shown in black) indicates that light was bent out of the path leading to that point in the image plane. The images were obtained under flow conditions which yielded an overall higher gas density in the flowfield than that used in acquiring the PLIF images described below, to enhance the shadow pattern.

As can be seen in Figs. 5a and b, after a portion of the incident shock passed through the nozzle, a nearly spherical, outwardly propagating shock wave formed, similar to that visible in Fig. 4f. The free jet rapidly grew in the test section, expanding beyond its equilibrium size. Up to this time, the flow of the jet gas was smooth and laminar (as seen in Figs. 5a and b), in contrast to that observed when a diaphragm was used (Figs. 4f and g). When the spherical front reached the walls of the test section, it reflected inward. The jet was greatly compressed by the incoming shock, its primary cell reaching a minimum size near the time displayed in frame c. An outwardly propagating wave, again, nearly spherical, except where disturbed by the outflow of gas along the axis, appears in the image shown in frame d. The cyclical wave pattern continued, but much less strongly, as the shocks continued to dissipate. The free jet flowfield began to equilibrate and to take on its characteristic shape soon after the second full cycle, as shown in Fig. 5e. The flowfield displayed in images e and f was the quasi-equilibrium free jet.

A similar series of NO PLIF images is shown in Fig. 6. The flow conditions used are given in Table 1 as flow #3; and, as before, the delay times are listed with the images. As shown in Fig. 3c, the images border the nozzle plate ($D = 2.1$ mm) on their left sides and are centered above the flow axis. The relationship between the signal level and the color displayed in the images is given on the scale at the bottom of the figure. Higher signals tend to indicate higher densities within the jet core and across shocks, with the exception of the Mach disk, behind which the signal generally decreases slightly. Attenuation of laser energy at the absorption wavelength in the ambient region caused the dip in signal near the centerline of the jet. Away from the jet axis, Doppler shifts of the absorption frequency due to the radial velocity of the gas resulted in an increase in the overlap integral as the absorption reached unattenuated portions of the laser lineshape (Palmer and Hanson 1993b). A decrease in the ambient region signal due to laser attenuation was visible in those areas of the raw PLIF images, although the procedure used to correct for spatial intensity variations in the laser sheet removed the effect in the processed images.

The same basic pattern of development took place for this jet as was seen in the shadow images of Fig. 5. The development time of the quasi-steady free jet was also similar, ~150-200 μ s. The two image sequences show the flow transients with roughly the same temporal progression, as may be seen by comparing Figs. 5a and 6a, Figs. 5b and 6b, etc. A notable exception occurs in the frames labeled c, where in the former an instant just after re-compression by inwardly propagating waves has taken place was captured and in the latter the greatly over-expanded jet existing before this event was observed. Otherwise, the structures visualized in the two sets of images are quite similar. A primary difference between the shadowgraphs and the PLIF images obtained here is that the fluorescence images more clearly reveal the three-dimensional flow structure. For example, the laminar rollers visible in the PLIF images shown in Figs. 6b and c are masked by turbulence and other structures in the corresponding shadowgraphs, because of their line-of-sight nature. Shocks and other wave structures apparent in the shadowgraphs are also sharper in the PLIF images.

4.3. Visualization of a Combustion Flowfield

A sequence of OH PLIF images illustrating the formation of a supersonic free jet of combustion gases is displayed in Fig. 7. Details of the flow conditions and the imaging technique used are given in Table 1 and in Fig. 3b. The scale to the right of the images indicates the relationship between the PLIF signal level and the colors in the images. Again, logarithmic scaling was used. The highest signal is represented with white, while the lowest signal is shown in black.

The test gas, containing approximately 2% OH by volume, emerged from the nozzle ~110 μ s after the incident shock wave reached the endwall of the tube. Figure 7a shows the jet region just after gas began to exhaust into the test section. In frame b, an event in the evolution of the flow similar to that observed in the jet image of Fig. 4f was captured. As seen previously in the NO PLIF images of the jet transient, diaphragm particles were initially imbedded in the jet. They were quickly propelled downstream by the gas plume, as seen in frames a-d. The establishment of the barrel shock structure took place promptly; and again, the jet was observed expanding into the test section (frames c and d) and then being compressed by inwardly propagating shocks reflected from the walls (frames e-g). In frame e, a structure closely resembling a laminar flame sheet is visible. The final frames, h and i, show the underexpanded free jet in an apparently quasi-steady state, with a slightly unsteady shock position and shape similar to that noted in discussion of the NO PLIF jet images in Sect. 4.1.

The ambient gas in this case yielded no fluorescence signal, since it contained only Ar. The test gas was diluted and OH radicals chemically quenched by mixing with the ambient, leading to low PLIF signals outside the jet core. The region downstream of the Mach disk, where elevated

temperatures led to enhanced chemical nonequilibrium and mixing had yet to take place, was an exception. The location of the highest PLIF signal was, however, inside the jet core, within a few diameters of the nozzle exit. Due to the combined effects of the changing flow conditions and the temperature dependence of the absorption line chosen, the region of highest density, at the nozzle exit, did not yield the highest PLIF signal in the images.

5. Conclusion

The flow characteristics up- and downstream of a small, axisymmetric, converging nozzle were observed in PLIF images of the shock reflection and free jet development processes with a test gas of Ar seeded with NO. A qualitative indication of the degree of disturbance of the reservoir caused by the nozzle was obtained. Stable reservoir conditions of 1600 K and 2.5 atm were found to exist for $\sim 800 \mu\text{s}$, for the flow considered here. In an image sequence acquired downstream of the nozzle, the unsteady process leading to the development of an underexpanded free jet was observed. The presence of a diaphragm at the nozzle exit was found to strongly affect the flow initially. However, $\sim 100 \mu\text{s}$ after bursting, its fragments were pushed out of the jet and had no further influence on the main flow. The quasi-steady free jet was established within $\sim 500 \mu\text{s}$ of the primary shock exiting the converging nozzle. After that time, images showed that the jet core was steady, although the size and shape of the surrounding barrel shock varied because of lateral wave reflections inside the test section.

A comparison was also made between NO PLIF imaging and shadow photography of free jet flowfields composed primarily of N₂. The reservoir conditions used in the shadow imaging (4.3 atm and 1300 K) yielded a higher gas density than those used in the PLIF experiments (2.8 atm and 2300 K). In contrast to the arrangement used in acquiring the other image sequences, no diaphragm was placed at the exit of the small diameter converging nozzle for these experiments. As a result, images acquired with small delay times displayed several features strikingly different from those seen in the other images. The flowfields were found to reach a quasi-steady state fairly rapidly, within $\sim 150\text{-}200 \mu\text{s}$ after the incident shock reached the endwall. The complementarity of the two visualization techniques was illustrated, although it was found that PLIF imaging provided information unobtainable with the line-of-sight technique.

Free jet formation was also observed in a series of OH PLIF images, using a reservoir with a mixture of combustion gases diluted in Ar with $\sim 2\%$ OH at 3400 K and 3.2 atm. As was the case previously, a great deal of detail was visible in the images. The high S/N of the signal, high spatial resolution, and flow-stopping temporal resolution allowed particularly fine visualization of the transient reacting flowfield. Many of the features seen in the other jet images were observed,

the most notable being the cyclical nature of the starting process. The flow was found to stabilize ~350 μ s after shock reflection.

Several aspects of PLIF imaging demonstrated in this investigation make it an excellent flow visualization tool. The spatial resolution inherent in a planar measurement allows a better understanding of complex, three-dimensional flowfields than is possible with traditional, line-of-sight techniques. PLIF imaging performed with a pulsed laser source provides the temporal resolution needed to capture the evolution of transient, hypersonic flows. Use of strongly fluorescent seeded or naturally occurring tracers, such as NO and OH, yields images with a high degree of in-plane spatial resolution and adequate S/N to allow observation of important details in the flow.

Acknowledgments. The authors gratefully acknowledge the assistance of Drs. B.K. McMillin and J.M. Seitzman in carrying out this work. The work was supported by the U.S. Air Force Office of Scientific Research, Aerospace Sciences Directorate.

6. Nomenclature

A	: spontaneous emission rate
A_{las}	: cross sectional area of laser sheet
B	: laser absorption rate
C_{opt}	: constant dependent on optical arrangement, collection efficiency, etc.
D	: nozzle throat diameter
E_p	: laser pulse energy
f_J	: Boltzmann fraction of absorbing state
g	: spectral convolution of laser and absorption lineshapes
k	: Boltzmann constant
M_s	: incident shock Mach number
N	: noise, root-mean-square signal fluctuation
P	: static pressure
P_1	: initial pressure of test gas in shock tube
P_a	: free jet ambient pressure
P_s	: stagnation pressure
Q	: electronic quenching rate of excited state
S	: PLIF signal
t	: time between shock reflection and image acquisition

T : static temperature
 T_s : stagnation temperature
 χ_a : mole fraction of absorbing species

References

Abe A, Takayama K (1990) Shock wave diffraction from the open end of a shock tube. In: Kim YW (ed) AIP Conf Proc 208: Current Topics in Shock Waves, 17th Int Symp on Shock Waves and Shock Tubes. American Institute of Physics, New York, NY, USA, pp 270-275

Amman HO, Reichenbach H (1973) Unsteady flow phenomena in shock-tube nozzles. In: Bershad D, Griffith WC (eds) Proc of the 9th Int Shock Tube Symp. Stanford University Press, Stanford, CA, USA, pp 96-112

Bazarov SB, Bazhenova TV, Bulat OV, Golub VV, Shul'meister AM (1992) Three-dimensional diffraction of shock wave. In: Takayama K (ed) Shock Waves, Proc of the 18th Int Symp on Shock Waves. Springer-Verlag, New York, NY, USA, pp 251-254

Britan AB, Rudnitskii AY, Starik AM (1987) Parameter formation behind the reflected wave in a shock tube with a nozzle. *Fluid Dyn* 22:622-628

Da-Peng Y, Peng-Cheng M, Hai-Lin W, An-Zhi H (1993) The methods of extracting and registering shock wave-fronts from series interferograms of transient flow field. In: Brown GM et al. (eds) Proc of the SPIE, Interferometry: Techniques and Analysis. SPIE, Bellingham, WA, USA, pp 184-189

Emel'yanov AV, Eremin AV (1991) Generalised empirical laws of starting discontinuity dynamics associated with the startup of underexpanded jets. *J Appl Mech Tech Phys* 32:665-669

Gaydon AG, Hurle IR (1963) The shock tube in high-temperature chemical physics. Reinhold, New York, NY, USA

Golub VV, Kharitonov AI, Sharov YL, Shul'meister AM (1990) Two-direction visualization of vortex rings emerging in the course of formation of the supersonic jet. In: Řezníček R (ed) Flow Visualization V, Proc of the 5th Int Symp on Flow Visualization. Hemisphere, New York, NY, USA, pp 556-561

Hanson RK, Seitzman JM, Paul PH (1990) Planar laser-fluorescence imaging of combustion gases. *Appl Phys B* 50:441-454

Hillier R (1991) Computation of shock wave diffraction at a ninety degrees convex edge. *Shock Waves* 1:89-98

Jacobs PA (1991) Simulation of transient flow in a shock tunnel and a high Mach number nozzle. NASA CR 187606, ICASE Rept No 91-60

Kelly R, Miotello A (1993) Pulsed-laser sputtering of atoms and molecules. Part I: Basic solutions for gas-dynamic effects. *Appl Phys B* 57:145-158

Liberman MA, Velikovich AL (1986) Physics of shock waves in gases and plasmas. Springer-Verlag, New York, NY, USA

Maksimov AI (1988) Diffraction of an oblique compression shock in the neighborhood of an external right angle. *J Appl Mech and Tech Phys* 28:608-617

Maslennikov VG, Dobrynin BM (1981) Onset of quasi-steady flow structure in the initial portion of two-dimensional nitrogen jets for different values of the environmental pressure. *Sov Phys Tech Phys* 26:698-702

Matsumura S, Sekine N, Takayama K, Onodera O (1990) Flow visualization study of shock waves in automobile exhaust systems. In: Řezníček R (ed) *Flow Visualization V*, Proc of the 5th Int Symp on Flow Visualization. Hemisphere, New York, NY, pp 779-784

Matsuo K, Aoki T, Kashimura H (1990) Diffraction of a shock wave around a convex corner. In: Kim YW (ed) *AIP Conf Proc 208: Current Topics in Shock Waves*, 17th Int Symp on Shock Waves and Shock Tubes. American Institute of Physics, New York, NY, USA, pp 252-257

McMillin BK, Lee MP, Paul PH, Hanson RK (1990) Planar laser-induced fluorescence imaging of shock-induced ignition. In: *23rd Symp (Int) on Combustion*. The Combustion Institute, Pittsburgh, PA, USA, pp 1901-1914

McMillin BK, Palmer JL, Hanson RK (1993) Temporally resolved, two-line fluorescence imaging of NO temperature in a transverse jet in a supersonic cross flow. *Appl Opt* 32:7532-7545

Merzkirch W (1987) *Flow visualization*, 2nd ed. Academic Press, Orlando, FL, USA

Norman ML, Smarr L, Winkler K-HA, Smith MD (1982) Structure and dynamics of supersonic jets. *Astron Astrophys* 113:285-302

Oertel H (1983) 33 years of research by means of shock tubes at the French-German Research Institute at Saint-Louis. In: Archer RD, Milton BE (eds) *Shock Tubes and Waves*, Proc of the 14th Int Symp on Shock Tubes and Shock Waves. New South Wales University Press, Sydney, Australia, pp 3-13

Oswatitsch K (1980) Intermediate ballistics. In: Schneider W, Platzer M (eds) *Contributions to the development of gasdynamics*. Vieweg, Braunschweig, Germany, p 343-372

Palmer JL, Hanson RK (1993a) Planar laser-induced fluorescence imaging in free jet flows with vibrational nonequilibrium. Paper No 93-0046. In: *Technical Digest of the 31st Aerospace Sciences Meeting and Exhibit*. American Institute of Aeronautics and Astronautics, Washington, DC, USA

Palmer JL, Hanson RK (1993b) Single-shot velocimetry using planar laser-induced fluorescence imaging of nitric oxide. Paper No 93-2020. In: *Technical Digest of the 29th Joint Propulsion Conf and Exhibit*. American Institute of Aeronautics and Astronautics, Washington, DC, USA

Palmer JL, Hanson RK (1994) PLIF measurements of temperature and velocity in a reacting supersonic free jet with OH. Paper No 94-0618. In: *Technical Digest of the 32nd*

Aerospace Sciences Meeting and Exhibit. American Institute of Aeronautics and Astronautics, Washington, DC, USA

Palmer JL, Houwing AFP, Thurber MC, Wehe SD, Hanson RK (1994) PLIF imaging of transient shock phenomena in hypersonic flows. Paper No 94-2642. In: Technical Digest of the 18th Aerospace Ground Testing Conf. American Institute of Aeronautics and Astronautics, Washington, DC, USA

Palmer JL, McMillin BK, Hanson RK (1991) Planar laser-induced fluorescence imaging of underexpanded free jet flow in a shock tunnel facility. Paper No 91-1687. In: Technical Digest of the 22nd Fluid Dynamics, Plasma Dynamics and Lasers Conf. American Institute of Aeronautics and Astronautics, Washington, DC, USA

Phan KC, Stollery JL (1983) The effect of suppressors and muzzle brakes on shock wave strength. In: Archer RD, Milton BE (eds) Shock Tubes and Waves, Proc of the 14th Int Symp on Shock Tubes and Shock Waves. New South Wales University Press, Sydney, Australia, pp 519-526

Prodromou P, Hillier R (1992) Computation of unsteady nozzle flows. In: 24th Symp (Int) on Combustion. The Combustion Institute, Pittsburgh, PA, USA, pp 1113-1118

Reichenbach H (1992) In the footsteps of Ernst Mach — A historical review of shock wave research at the Ernst-Mach-Institut. Shock Waves 2:65-79

Seitzman JM, Palmer JL, Antonio AL, Hanson RK, DeBarber PA, Hess CF (1993) Instantaneous planar thermometry of shock-heated flows using PLIF of OH. Paper No 93-0802. In: Technical Digest of the 31st Aerospace Sciences Meeting and Exhibit. American Institute of Aeronautics and Astronautics, Washington, DC, USA

Srinivasan R (1994) A comparative study of the ablation of polyimide (Kapton) films by pulsed (ns) ultraviolet and infrared (9.17 mm) lasers. In: Miller JC, Geohegan DB (eds) AIP Conf Proc. Laser Ablation: Mechanisms and Applications II. 2nd Int Conf. American Institute of Physics, New York, NY, USA, pp 439-443

Vincenti WG, Kruger CH (1965) Introduction to physical gas dynamics. Wiley, New York, NY, USA

Yang JY, Hsu CA, Jiang CT, Miller B (1992) Computation of shock diffraction in external and internal flows. In: 24th Symp (Int) on Combustion. The Combustion Institute, Pittsburgh, PA, USA, pp 1063-1068

Figure Captions

Fig. 1. Boltzmann fraction of absorbing state as a function of temperature for the NO and OH lines excited in the PLIF experiments.

Fig. 2. Schematic of the experimental facility with the associated optical and electronic components required for PLIF imaging.

Fig. 3. Imaging geometries used in the PLIF and shadow imaging experiments.

Fig. 4. NO PLIF images of the shock tunnel reservoir and free jet regions showing the transient flow process. The conditions used are listed in Table 1 as flow #1; the imaged areas are shown in Figs. 3a and b. Each image pair was acquired at the time shown with it.

Fig. 5. Shadowgraphs showing the jet starting process without a diaphragm. The flow conditions used are listed in Table 1 as flow #2; the imaged area is shown in Fig. 3c. Each image was acquired at the time given with it.

Fig. 6. NO PLIF images showing the jet starting process without use of a diaphragm at the nozzle exit. The flow conditions and imaging geometry are given in Table 1 and in Fig. 3c, respectively, as flow #3. The delay time at which each image was obtained is listed with it.

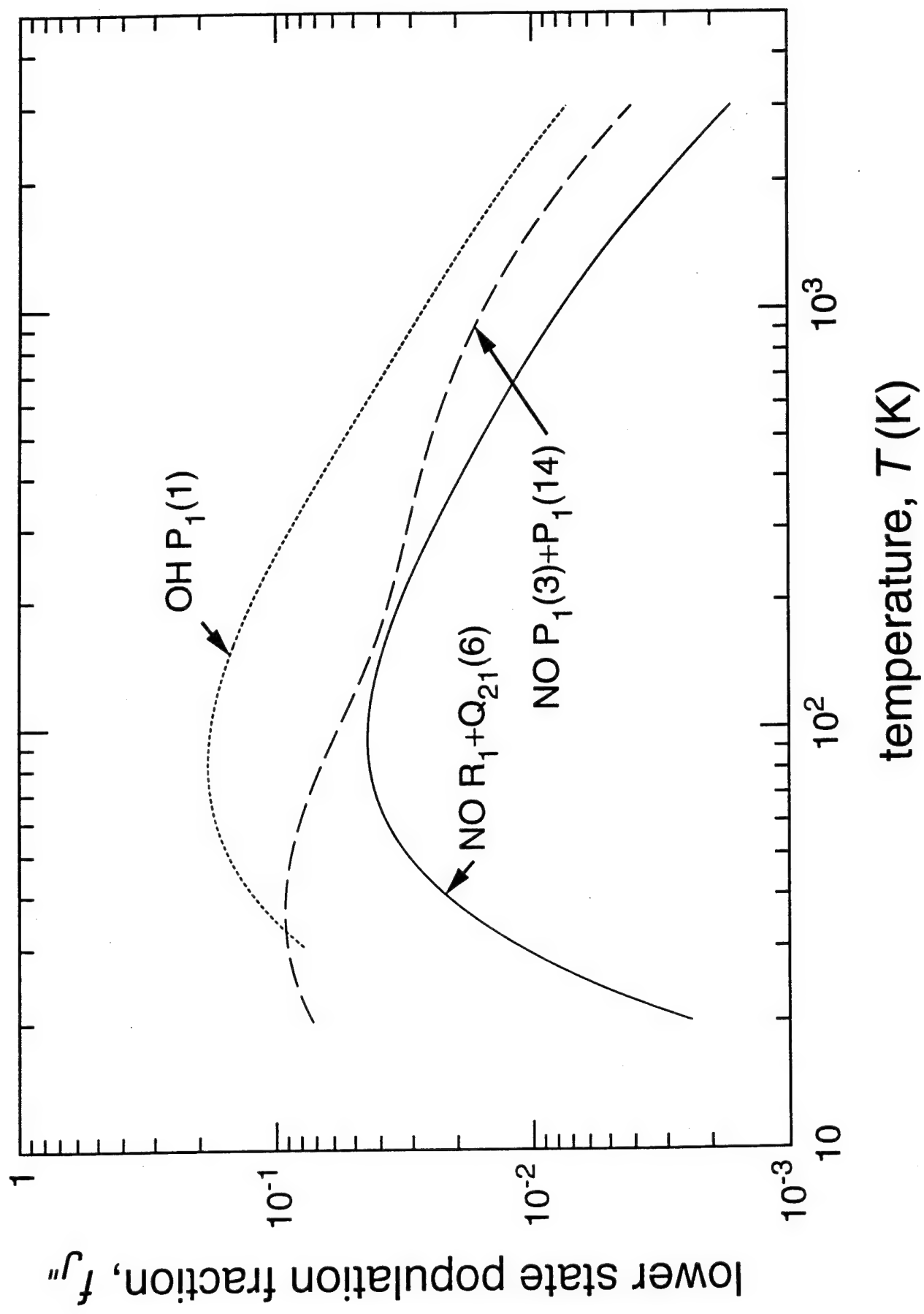
Fig. 7. OH PLIF images of the development of a free jet issuing from a sonic nozzle. The conditions used are listed in Table 1 as flow #4; the imaged area is shown in Fig. 3b. The delay time at which each image was obtained is listed with it.

flow #	test gas composition	P_1 (torr)	M_s	P_s (atm)	T_s (K)	ambient gas composition	D (mm)	P/P_a	imaging technique	line(s)	flowfield imaged	image size (mm)	image size (pixels)
1 ^a	0.5% NO/Ar	60	2.6	2.5	1600	0.5% NO/Ar	4.9	190	NO PLIF	$R_1+Q_{21}(6)$	reservoir	34.1 × 53.9	117 × 185
2 ^b	N ₂	60	3.1	4.3	1340	N ₂	2.1	55	shadow	N/A	jet	41.2 × 28.3	266 × 183
3 ^b	5% NO/N ₂	20	4.1	2.8	2300	5% NO/N ₂	2.1	110	NO PLIF	$P_1(3)+P_1(14)$	jet	17.0 × 12.6	485 × 240
4 ^c	5% H ₂ /5% O ₂ /Ar	22	4.3	3.2	3400	Ar	4.9	61	OH PLIF	$P_1(1)$	jet	27.8 × 20.1	239 × 113
												43.5 × 29.0	187 × 125

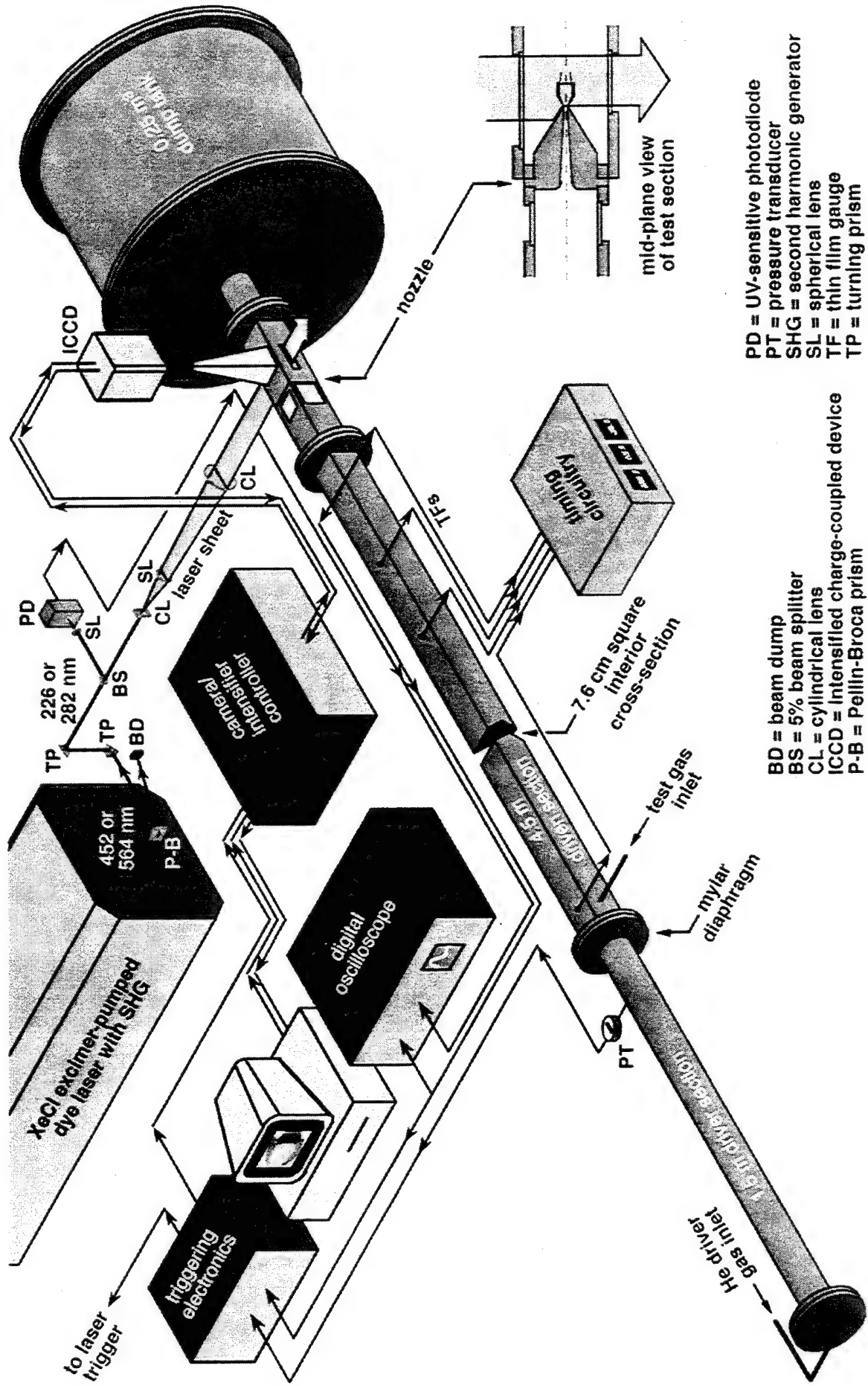
Table 1. Conditions used in shock tunnel imaging experiments.

- a. Palmer JL, Hanson RK (1993a) Planar laser-induced fluorescence imaging in free jet flows with vibrational nonequilibrium. Paper No 93-0046. In: Technical Digest of the 31st Aerospace Sciences Meeting and Exhibit. American Institute of Aeronautics and Astronautics, Washington, DC, USA
- b. Palmer JL, McMillin BK, Hanson RK (1991) Planar laser-induced fluorescence imaging of underexpanded free jet flow in a shock tunnel facility. Paper No 91-1687. In: Technical Digest of the 22nd Fluid Dynamics, Plasma Dynamics and Lasers Conf. American Institute of Aeronautics and Astronautics, Washington, DC, USA
- c. Palmer JL, Hanson RK (1994) PLIF measurements of temperature and velocity in a reacting supersonic free jet with OH. Paper No 94-0618. In: Technical Digest of the 32nd Aerospace Sciences Meeting and Exhibit. American Institute of Aeronautics and Astronautics, Washington, DC, USA

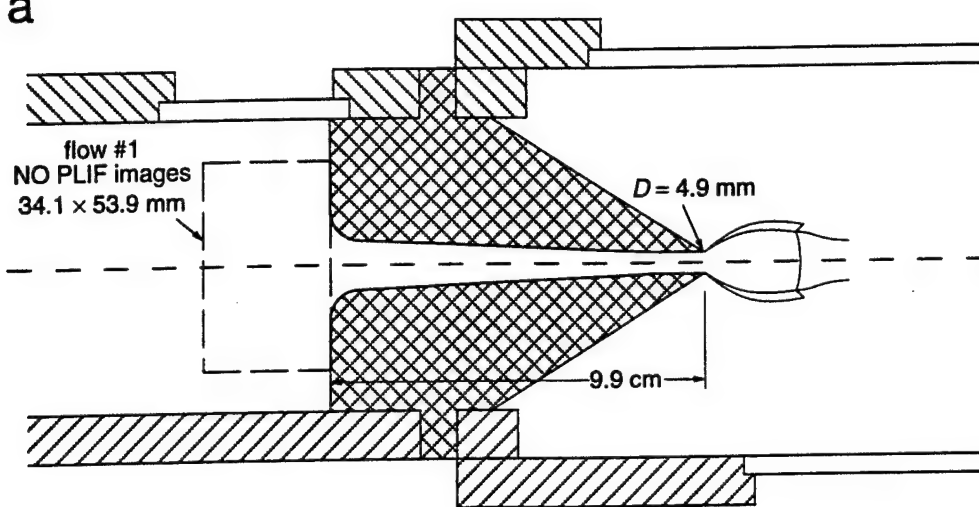
Fig. 1



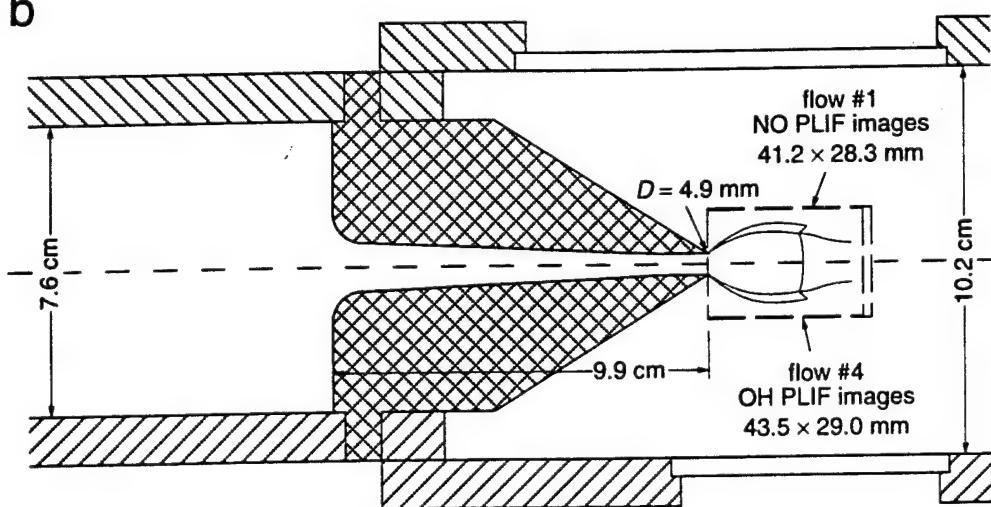
JL Palmer and RK Hanson Shock tunnel flow visualization using planar laser-induced fluorescence imaging of NO and OH
 Fig. 2.



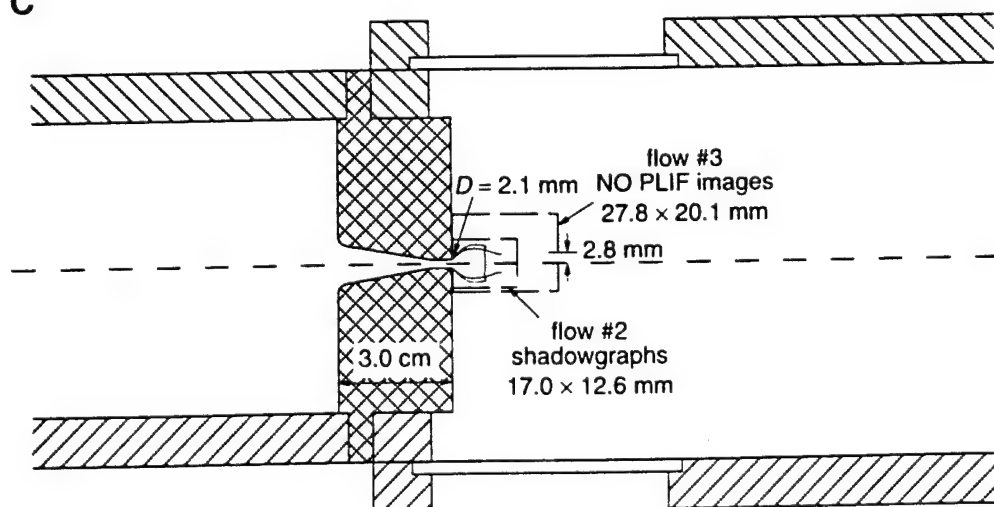
a



b



c



JL Palmer and RK Hanson, Shock tunnel flow visualization using planar laser-induced fluorescence imaging of NO and OH

Fig. 4.



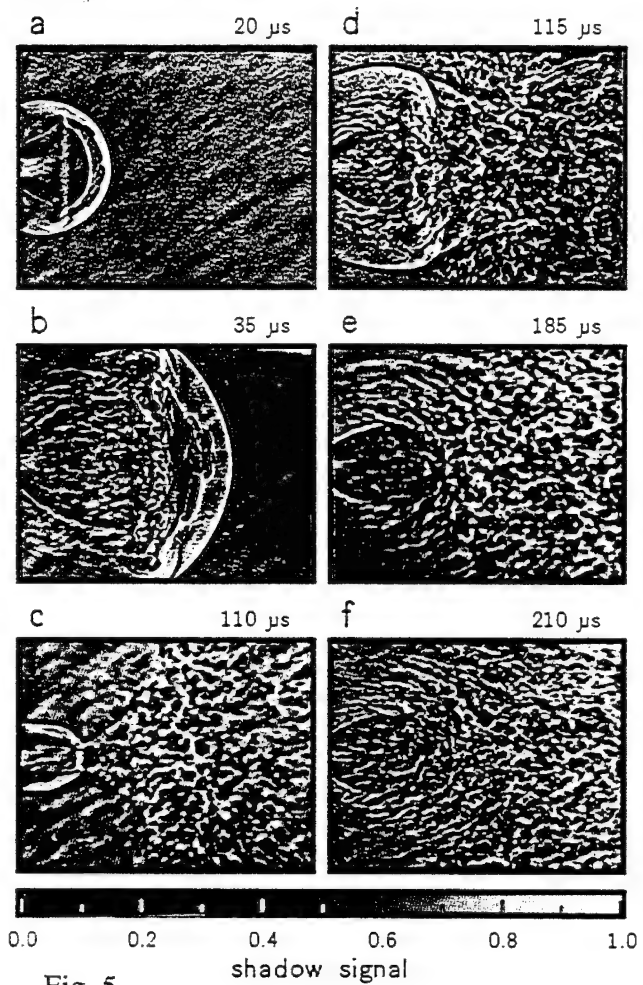


Fig. 5.

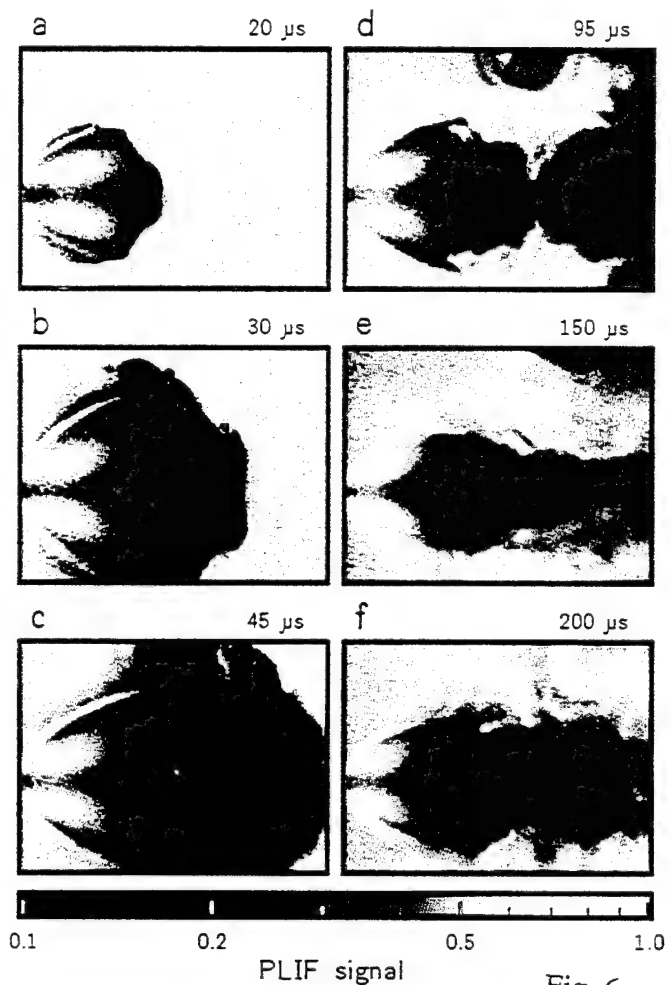


Fig. 6.

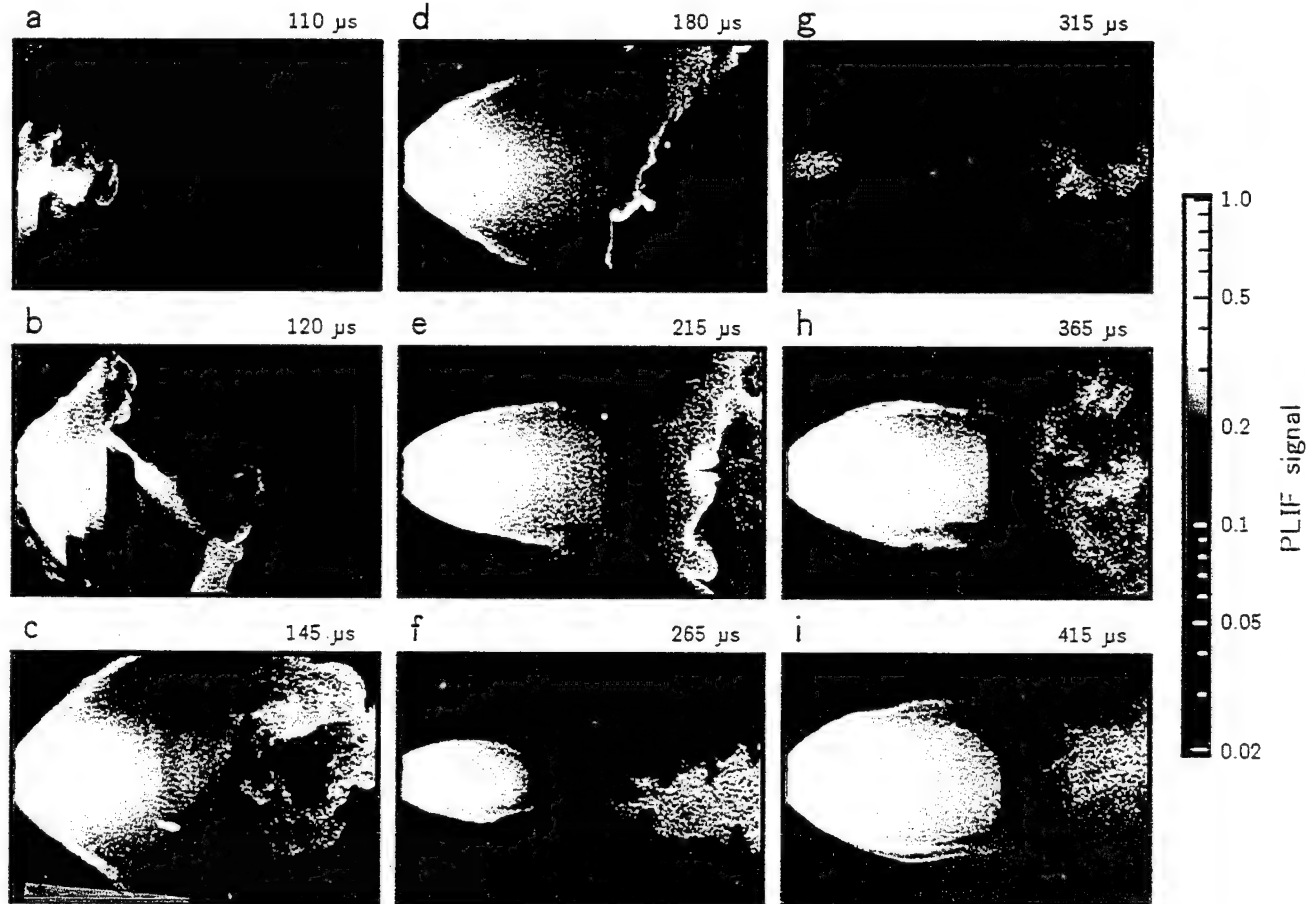


Fig. 7.



AIAA-94-0618

**PLIF MEASUREMENTS OF TEMPERATURE
AND VELOCITY IN A REACTING SUPERSONIC
FREE JET WITH OH**

J.L. Palmer and R.K. Hanson

High Temperature Gasdynamics Laboratory

Department of Mechanical Engineering

Stanford University, Stanford, CA 94305-3032

32nd Aerospace Sciences

Meeting & Exhibit

January 10-13, 1994 / Reno, NV

PLIF MEASUREMENTS OF TEMPERATURE AND VELOCITY IN A REACTING SUPERSONIC FREE JET WITH OH

J.L. Palmer[†] and R.K. Hanson[‡]
High Temperature Gasdynamics Laboratory
Department of Mechanical Engineering
Stanford University, Stanford, CA 94305-3032

Abstract

Single-shot rotational temperature and two-component velocity measurements were performed in a free jet of combustion gases diluted in argon using planar laser-induced fluorescence of the hydroxyl radical (OH). A shock tunnel facility provided a reservoir with 1.9% OH at 3350 K and 3.2 atm, which exhausted into a low pressure ambient of argon through a converging, axisymmetric nozzle. Counter-propagating laser sheets, formed from a single frequency-doubled dye laser pulse and separated temporally by 230 ns, allowed pairs of images with velocity sensitivity to be obtained under identical flow and excitation conditions. Broad-band excitation of the $A^2\Sigma^+ \leftarrow X^2\Pi(1,0)$ $P_1(1.5)$ and $Q_1(5.5)$ transitions of OH at 282.24 and 282.74 nm, respectively, and broad-band, integrated fluorescence detection were used. Analysis of the properties of the laser pulse used in creating an image pair yielded a relationship between PLIF signal level and flow velocity and allowed images created by pumping different transitions to be matched according to their excitation characteristics. The resulting single-shot and frame-averaged two-component velocity and rotational temperature fields were shown to be in good agreement with a simulation of the flowfield by the method of characteristics.

I. Introduction

Planar laser-induced fluorescence (PLIF) flow measurements are of growing value in high-speed aerodynamics and combustion research. Laser-based diagnostics are advantageous in severe flow environments, because they are nonintrusive; PLIF also has the potential to yield quantitative two-dimensional property fields on a nearly instantaneous basis. In high-enthalpy, short-duration flow facilities, an ability to obtain information on the flow at many points simultaneously is crucial, as a day or more may be required between facility firings.

The goal of the work presented here is the development and demonstration of compatible velocimetry and thermometry strategies applicable in reacting, supersonic flows. The hydroxyl radical (OH) is chosen as the fluorescent species, since its presence conveniently marks the reaction zone in many combusting flowfields. A reflection-type shock tunnel facility is used to generate a highly underexpanded, axisymmetric free jet of combustion gases diluted in argon (Ar) from a test gas initially containing 5% hydrogen (H_2) and 5% oxygen (O_2).

Several techniques previously demonstrated with PLIF of nitric oxide (NO)¹⁻³ here yield single-shot two-component velocity and rotational temperature images with OH. At present, the velocity fields are captured during a single laser pulse; while two separate runs of the tunnel are required to capture the temperature field, because only one excitation wavelength is used. However, the extension of the techniques described here to simultaneous, single-shot velocity and temperature measurements is straightforward.

In this experiment, sequential fluorescence bursts are induced by broad-band counter-propagating laser sheets directed at an angle through the axis of the jet. A single frequency-doubled dye laser pulse split into two parts forms the sheets, which therefore have identical spectral properties. A delay of ~230 ns in one of the beams temporally separates the PLIF signals, which are captured by gated, intensified charge couple device (CCD) arrays mounted above and below the test section. Opposite Doppler shifts of the absorption frequency with respect to the beams at each point in the flow cause a velocity dependence in the resultant image pair.

A difference-to-sum combination of the images, with an analysis of the single-shot laser spectrum and the assumption of flowfield symmetry, yields the instantaneous two-component velocity field of the free jet.³ The rotational temperature field is obtained by taking the ratio of images acquired by exciting two different ro-vibrational transitions with laser pulses having similar lineshapes and detuning from their

[†]Graduate Research Assistant, Student Member AIAA.

[‡]Professor, Senior Member AIAA.

Copyright 1994 by the authors. Published by the American Institute of Aeronautics and Astronautics with permission.

respective un-Doppler-shifted absorption line centers.⁴ Each image in the ratio is formed by summing images acquired simultaneously with a single laser shot. A method of characteristics (MOC) simulation of the flowfield^{1,2} is also used in assessing the velocity and temperature measurements.

Previously, PLIF imaging of OH has been implemented in several reacting, supersonic flows to examine flame structure and to measure rotational temperature and velocity fields. Several configurations for H₂ injection into a supersonic, oxidizing free stream have been investigated using single-shot imaging.⁵⁻⁷ Recently, extensive visualization and instantaneous rotational temperature results were reported in flowfields with jet injection from a flat wall and behind a rearward-facing step.^{8,9} The technique is similar to that initially demonstrated by another investigator, who used a two-laser/two-camera system to obtain nearly instantaneous PLIF images of OH rotational temperature fields in one-dimensional shock-heated flows.¹⁰ The approach has also been used with NO for instantaneous rotational temperature measurements in jet injection flows¹¹ and for instantaneous vibrational temperature measurements in a shock tunnel-generated free jet.¹² Frame-averaged OH PLIF velocity measurements in a high pressure free jet obtained by a technique similar to that used here have been reported as well.¹³

II. PLIF Measurement Strategies

A. PLIF Signal

The total fluorescence signal for weak excitation of an isolated absorption line is given by:

$$S = \frac{E_p g B}{A_{las}} \left(\frac{\chi_a P}{kT} \right) f_{J^*}(T) \left(\frac{A}{A+Q} \right) C_{opt}, \quad (\text{II.1})$$

where E_p is the laser pulse energy; g is the spectral convolution of the laser and absorption lineshapes; A and B are the rates of spontaneous emission and absorption, respectively; A_{las} is the cross sectional area of the laser sheet; χ_a is the mole fraction of the absorbing species; P is the pressure; T is the rotational temperature; k is the Boltzmann constant; $f_{J^*}(T)$ is the Boltzmann fraction of the absorbing state; Q is the total electronic quenching rate of the excited state; and C_{opt} is a constant dependent on optical arrangement, collection efficiency, etc.

The spectral convolution is given by:

$$g = \int_{-\infty}^{\infty} g_a(v - v_a + \Delta v_D, \Delta v_a) g_l(v - v_l, \Delta v_l) dv, \quad (\text{II.2})$$

where v_a and Δv_a are the absorption center frequency and full-width-at-half-maximum (FWHM); v_l and Δv_l are the same quantities for the laser. The Doppler shift of the transition, induced by the bulk motion of the flow, is given by:

$$\Delta v_D = \frac{\vec{V} \cdot \hat{k}}{2\pi} = v_a \frac{V \cos(\beta - \theta)}{c}, \quad (\text{II.3})$$

where \vec{V} is the vector velocity of the gas motion; V is the magnitude of the velocity vector; \hat{k} is the wave vector of the laser ($|k| = 2\pi v_l/c$); β is the angle between \hat{k} and the jet axis; θ is the angle between \vec{V} and the jet axis; and c is the speed of light. The orientations of \vec{V} and \hat{k} and the definitions of θ and β are illustrated in figure 1.

B. Velocity Imaging

In the present experiment, counter-propagating sheets pass through the mid-plane of the jet at an angle ($\beta \leq \pi/2$), as shown in figure 1. The Doppler shifts are proportional to a combination of the axial and radial components of the velocity, $V_x \cos\beta + V_r \sin\beta$ at $(x,+r)$ and $V_x \cos\beta - V_r \sin\beta$ at $(x,-r)$ with respect to laser sheet #1 and $-V_x \cos\beta - V_r \sin\beta$ at $(x,+r)$ and $-V_x \cos\beta + V_r \sin\beta$ at $(x,-r)$ with respect to sheet #2. Since the flowfield is symmetric, the signals S^+ (or, similarly, S^-) at $(x,+r)$ and $(x,-r)$ result from identical thermodynamic conditions, identical axial Doppler shifts, and equal-but-opposite radial Doppler shifts. The signals are related to the velocity in the direction of propagation of laser #1, $V_\beta = V \cos(\beta - \theta)$, by:³

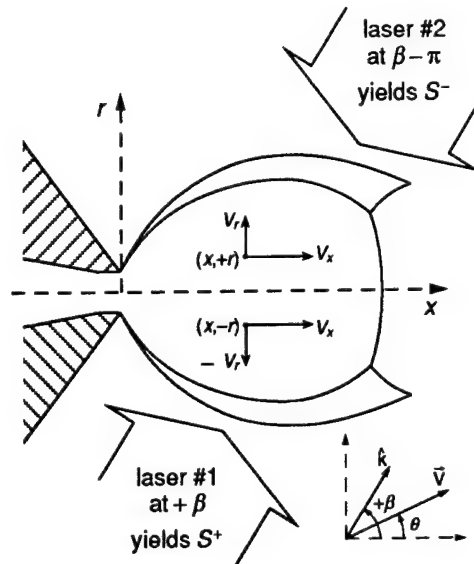


Figure 1: Counter-propagating laser sheets in a symmetric flowfield.

$$\frac{S^-(x,r) - S^+(x,r)}{S^-(x,r) + S^+(x,r)} = \frac{g^- - g^+}{g^- + g^+}. \quad (\text{II.4})$$

For given values of v_a , v_l , and V_β , the above ratio may be determined if the spectral convolution of the absorption and laser lineshapes is known as a function of frequency. Conversely, V_β may be inferred from the difference-to-sum signal ratio.³ After finding V_β , one may isolate the velocity components:

$$V_x(x, \pm r) = \frac{V_\beta(x, +r) + V_\beta(x, -r)}{2 \cos \beta},$$

$$V_r(x, \pm r) = \frac{V_\beta(x, +r) - V_\beta(x, -r)}{2 \sin \beta}. \quad (\text{II.5})$$

The assumption of flow symmetry necessary to obtain V_x and V_r simultaneously restricts the single-shot measurement to the jet core. Signals in the turbulent flow outside that region give only a qualitative indication of the velocity components. In a frame-averaged representation of the images, however, the average velocity components should be recovered.

C. Temperature Imaging

In the two-line thermometry technique used here, a ratio is taken of signals $S_1^\pm (= S_1^+ + S_1^-)$ and $S_2^\pm (= S_2^+ + S_2^-)$, obtained with the laser tuned first to excite one transition and then another from the same lower vibrational level, but a different rotational state. This gives the result:

$$R(T) = \frac{S_1^\pm}{S_2^\pm} = C_{12} \frac{E_{p1} g_1 2J''_1 + 1}{E_{p2} g_2 2J''_2 + 1} \frac{S_{J''_1 J_1}}{S_{J''_2 J_2}} \times \exp \left\{ - \frac{[F(J''_1) - F(J''_2)]}{kT} \right\} \frac{A+Q_2}{A+Q_1}, \quad (\text{II.6})$$

where subscripts 1 and 2 denote the terms of the respective equations describing the PLIF signals. $S_{J''J}$ is the normalized Hönl-London factor of the line used; and $F(J'')$ is the rotational term energy of its lower level. C_{12} is a normalization constant (ideally equal to unity) which allows the measured ratio to be scaled to that expected at a point in the flowfield where T is known. The rotational temperature field may thus be inferred from Eqn. II.6 if the values of the laser pulse energies, spectral convolutions, and total downward relaxation rates are known.

In the present approach, the pulse energy may be assumed to be unity after a correction for variations in the single-shot laser sheet energy profile has been applied to each of the raw images.^{4,11} The ratio of the spectral convolutions also cancels if the excitation characteristics (i.e., laser lineshape and frequency

detuning from the unshifted absorption line center) are matched for the image pairs used. Often $A+Q$ is identical for the two transitions and the last term in Eqn. II.6 may be assumed to be unity. However, for OH, particularly under low density conditions, the electronic quenching rate may depend on the upper rotational level.^{14,15} Since the flow conditions in the free jet vary greatly, a correction for the nonuniform fluorescence yield ratio would introduce additional uncertainties in the inferred temperature field. Therefore, the assumption will be made here that the total downward relaxation rates for the two lines are equal. The quality of this assumption may be estimated from the resulting temperature field. The equation describing the PLIF signal ratio then reduces to:

$$R(T) = C_{12} \frac{2J''_1 + 1}{2J''_2 + 1} \frac{S_{J''_1 J_1}}{S_{J''_2 J_2}} \times \exp \left\{ - \frac{[F(J''_1) - F(J''_2)]}{kT} \right\}. \quad (\text{II.7})$$

Because a single excitation system is used here, separate experiments must be performed to acquire the images needed for two-line thermometry. Fortunately, the flowfield is repeatable in the inviscid core of the free jet, except for slight shot-to-shot variations in the shock position. The instantaneous temperature in the turbulent portions of the flowfield is unobtainable with this method. It should also be noted that sum images are used here to improve the signal-to-noise ratio (S/N) in the inferred temperature field. Actually, only a ratio of S^+ or S^- images is required to measure the rotational temperature.

III. Experimental Facility and Procedure

A. Shock Tunnel System

The reflection-type shock tunnel facility in which these experiments were performed has been described in detail previously.^{1,2} Figure 2 shows a schematic of the facility, along with the PLIF imaging system. Here, a test gas mixture of 5% H₂ and 5% O₂ in Ar initially at 22 torr was used. Calculations indicate that the reservoir gas consisted of 1.9% OH, 2.6% H, 2.7% O, 1.0% H₂, 1.8% O₂, and 1.8% H₂O in Ar at stagnation conditions: $T_s = 3350 \pm 50$ K and $P_s = 3.2 \pm 0.1$ atm.⁴ Pure Ar at formed the ambient of the free jet, which had a pressure ratio $P_s/P_a = 61$.

B. PLIF Imaging System

Frequency-doubled photons from a broad-band, tunable XeCl-pumped dye laser with Coumarin 540A dye were used to excite the P₁(1.5) and Q₁(5.5)

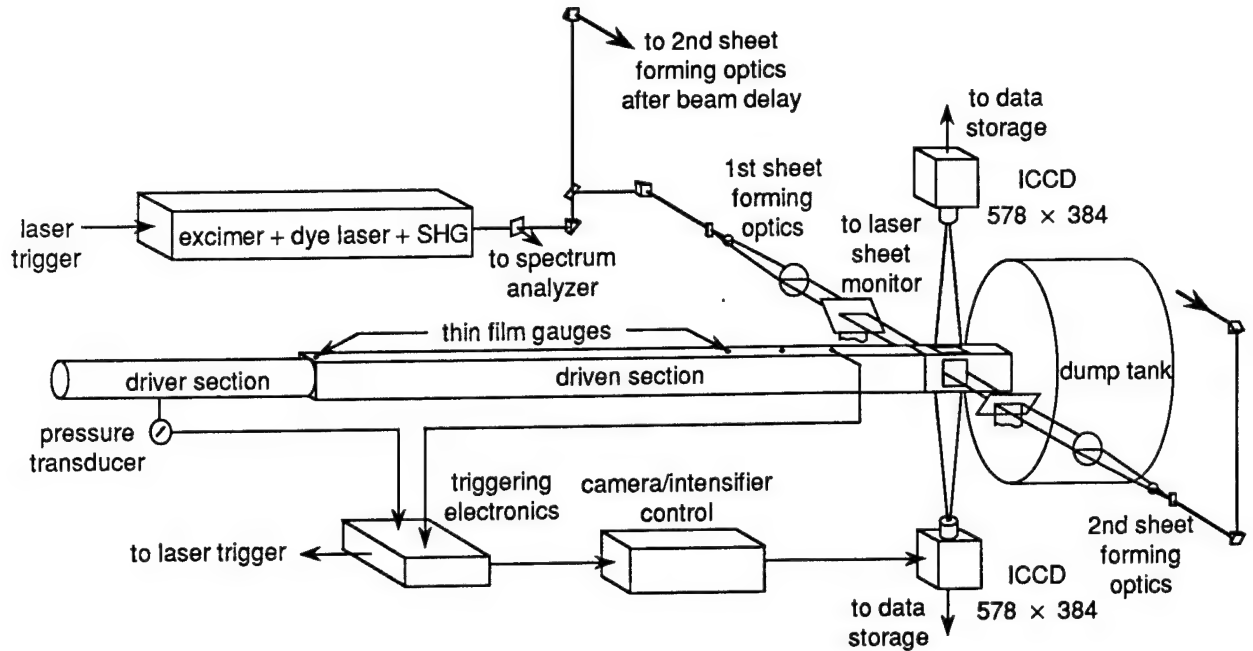


Figure 2: Schematic of experimental facility with associated optical and electronic components for instantaneous one-laser/ two-camera PLIF imaging.

transitions in the $A^2\Sigma^+ \leftarrow X^2\Pi(1,0)$ band of OH at 282.25 and 282.74 nm, respectively. The optical arrangement was very similar to that of a previously reported PLIF experiment with NO, where counter-propagating sheets were used in obtaining single-shot, two-component velocity images.³ The only significant difference between the current and previous optical setups was that a 2 mm WG-305 Schott glass filter was placed before each camera in addition to the UG-5 filters already in place for the NO measurements to block laser scattering and resonant fluorescence.

The laser sheets, each with ~ 0.25 mJ as it entered the test section, passed through the mid-plane of the flowfield at 59° and -121° with respect to the jet axis. One laser sheet was delayed by ~ 230 ns with respect to the other following 6 round trip passes through a 12-m long reflector cavity. Broad-band fluorescence resulting from excitation of the test gas by the individual laser sheets was collected normal to the direction of laser propagation, as shown in Fig. 2. The light was imaged onto two 578×384 pixel, cooled, intensified CCD array with ~ 230 ns gating by Nikkor UV lenses ($f/4.5$). The images were acquired ~ 300 μ s after the incident shock reached the endwall of the shock tube, at which time the flowfield was in a quasi-steady state.

The field of view in the PLIF experiments was $8.95 \times 5.95 D$ in size and approximately centered about the jet axis. Procedures described elsewhere were

used to correct the raw data images for single-shot laser sheet intensity variations, nonuniform collection efficiency, laser scattering, and background signal level on a pixel-by-pixel basis.^{4,11,12} After correction, the data images were binned 4×4 to improve their S/N and trimmed slightly. The resulting images were 139×95 pixels or $8.61 \times 5.89 D$ in size, each pixel representing $0.31 \times 0.31 \times 0.35$ mm in the flowfield.

C. Pulsed Spectrum Analyzer

The arrangement shown in figure 3 was used to monitor the lineshape and detuning of the individual laser pulse used in creating a pair of PLIF images. A small portion of the laser pulse energy was diverted from the main optical axis prior to sheet formation, as indicated in figure 2, for this purpose. The monitor beam was split into two parts, one of which repeatedly passed just above a flat flame methane-air burner, where an OH concentration sufficient to significantly absorb the beam existed. It was then re-directed to propagate nearly co-linearly with the unperturbed portion of the beam. The beams diverged following passage through a negative cylindrical lens (focal length, $f = -10$ mm) and were transmitted as distinct peaks or fringes by an air-spaced Fabry-Perot etalon with a free spectral range of 2 cm^{-1} and a finesse of 20. A spherical lens (nominal $f = 140$ mm) imaged the light onto a 512×240 pixel (8.8×6.6 mm) video CCD array.

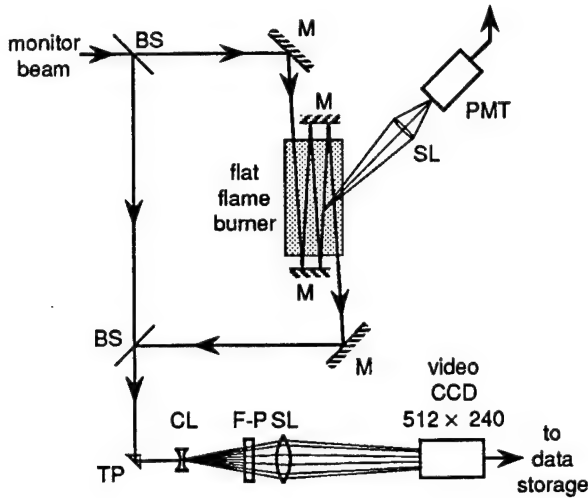


Figure 3: Schematic of equipment used for laser tuning and pulsed spectrum analysis. BS = beam splitter, M = mirror, TP = turning prism, CL = cylindrical lens, SL = spherical lens, F-P = Fabry-Perot etalon, PMT = photomultiplier tube.

Adjacent linear fringe patterns, spatially separated due to a small angle between the two incoming beams, were recorded. The fringe patterns were observed live on a video monitor or laboratory computer and/or stored for later analysis. Prior to a series of shock tunnel runs, several frame-averaged fringe patterns were collected with varying laser wavelength. From the total camera signal in the bleached fringe pattern and an analysis of the unbleached pattern to determine the laser peak wavelength,³ a measurement of the laser transmission through the flame as a function of frequency was obtained. Comparison of a single-shot unattenuated fringe pattern with the frame-averaged pattern acquired at the laser frequency where minimum transmission occurred then yielded the single-shot laser detuning from the un-Doppler-shifted absorption and the laser lineshape.³ Pressure shifts of the OH absorption¹⁶ in the flame were small with respect to the overall uncertainty in the peak wavelengths and were ignored when determining the laser detuning.

V. Results and Discussion

A. OH PLIF Images

Figure 4 shows two pairs of single-shot OH PLIF images obtained by exciting the $Q_1(5.5)$ (frames a and c) and $P_1(1.5)$ transitions (frames b and d). The scale located in the lower right corner of Fig. 4 shows the relationship between PLIF signal level and gray density in the images. Axial and radial distances are scaled by the nozzle throat diameter $D = 5$ mm. No OH PLIF signal was recorded in the upper left portion

of the images, as that region was beyond the edges of the laser sheets.

The frames displayed for each line were acquired nearly simultaneously with sequential counter-propagating laser sheets formed with a single frequency-doubled dye laser pulse. The laser was in each case tuned approximately to compensate for the Doppler shift due to the maximum axial velocity on the jet axis with respect to laser sheet #2. With $v_a - v_l \approx v_a V_{x,max} \cos\beta/c$, the resulting signal S^- (frames a and b) appears symmetric about the jet axis, since the velocity on the axis is greater than $0.9 V_{x,max}$ for $x/D \geq 1.5$; while S^+ (frames c and d) is asymmetric. The differences within each image pair illustrate the velocity sensitivity of the PLIF signal, as they were acquired with the same laser pulse (and, hence, spectral characteristics) and with high temporal resolution. Comparing the $Q_1(5.5)$ image pair with that created by $P_1(1.5)$ excitation illustrates the rotational temperature sensitivity. Inside the jet core, the S/N for the $P_1(1.5)$ images was fairly uniform at 10-15:1. The $Q_1(5.5)$ images had a maximum S/N of ~13:1 near the nozzle exit and a minimum of ~3:1 near the Mach disk. A thresholding operation was performed on the images before velocity or temperature processing to eliminate the small signal level in the ambient region of the flowfield.

B. Velocimetry

Frame-averaged and single-shot velocity component images obtained using the $P_1(1.5)$ transition of OH are displayed in Figs. 5a and b, respectively. Results from the MOC simulation of the flowfield are shown in Fig. 5c. The symmetry assumption necessary in the data analysis yields symmetric velocity component fields. Therefore, in each case, the radial velocity is shown only in the upper part of the image and the axial velocity in the lower part. The diagonal white lines in frame c indicate the edges of the laser sheets and their reflection about the jet axis. The scale located to the right of frame c shows the conversion between velocity and gray tone in the images.

The composite field displayed in Fig. 5a is the average of 10 single-shot velocity images, such as the one shown in Fig. 5b, which resulted from an analysis of the image pair shown in Figs. 4b and d. The S/N in the single-shot axial velocity image was ~17:1 near the Mach disk. A direct comparison of the frame-averaged and single-shot PLIF results with the simulation is given in Fig. 6, where the velocity components along the jet axis (a $r/D = 0$) and at several axial locations (b $x/D = 1$, c $x/D = 2$, and d $x/D = 3$) are graphed. In each case, the frame-averaged

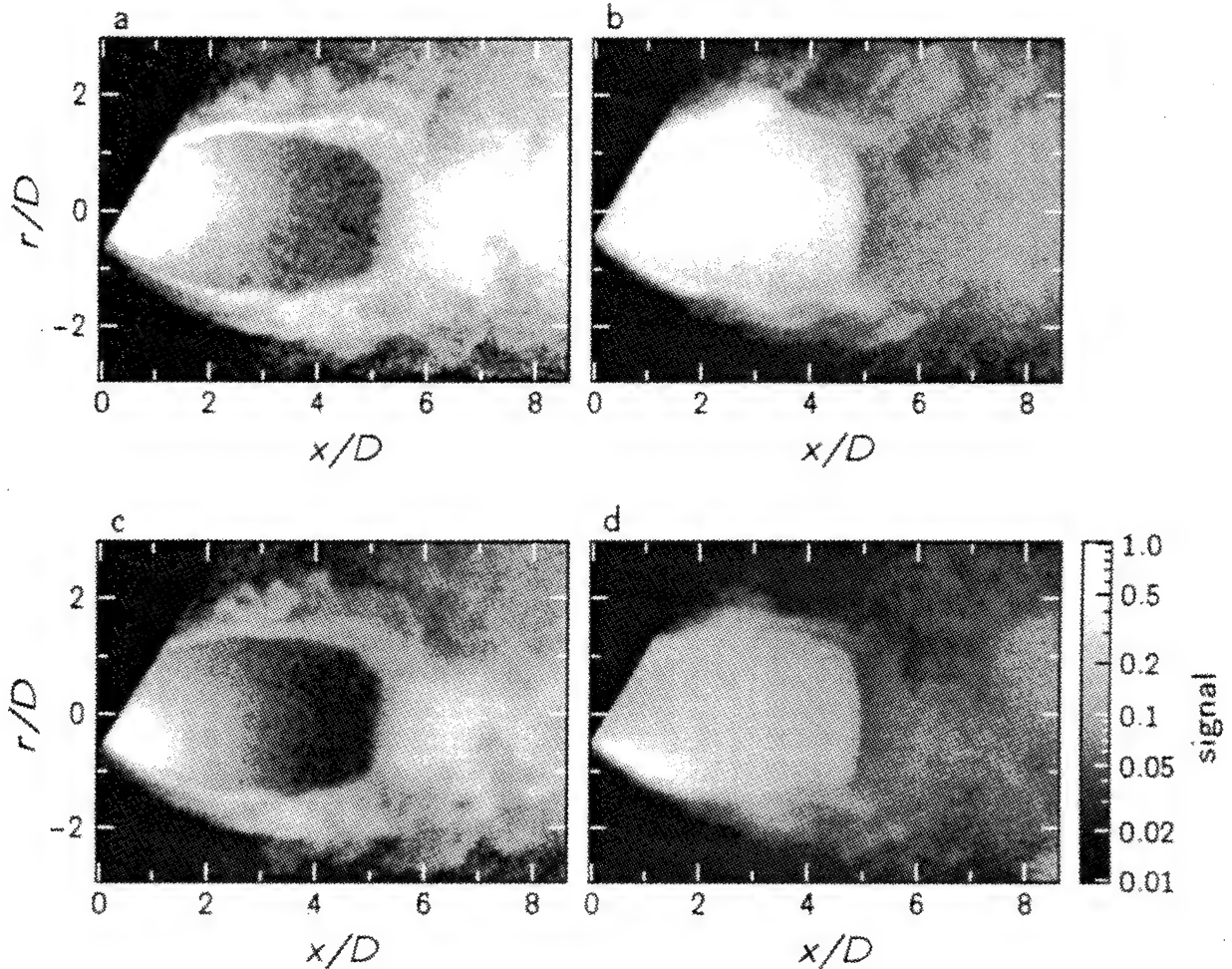


Figure 4: Single-shot OH PLIF images with laser detuning $v_a - v_l \approx v_a V_{x,max} \cos\beta/c$. Frames a and c, showing S^- and S^+ , respectively, were acquired simultaneously with the laser pumping the $A^2\Sigma^+ \leftarrow X^2\Pi(1,0)$ $Q_1(5.5)$ transition of OH. Similarly, frames b and d show images acquired with $P_1(1.5)$ excitation. The scale to the right of frame d indicates the relationship between the gray tones displayed in the images and the normalized PLIF signal. The images are $8.61 \times 5.89 D$ (139 \times 95 pixels) in size. The conditions of the free jet were: $T_s = 3350$ K, $P_s = 3.2$ atm, $P_s/P_a = 61$, with 1.9% OH in Ar and $D = 5$ mm.

result is shown with a solid line, the single-shot result with a dotted line, and the MOC prediction with a dashed line.

Along the jet axis, including the region beyond the Mach disk ($x/D \geq 5$), the agreement between the average measured and predicted velocity is good. The frame-averaged velocity is low near the nozzle exit due to absorption broadening effects.³ Differences in the single-shot and frame-averaged PLIF velocities probably result from uncertainties in the velocity conversion algorithm and from random error in the single-shot OH images. Some discrepancies exist between the average PLIF results and the MOC computation, particularly in the axial velocity in the regions of the jet away from the axis ($r/D \geq 1$).

Overall, however, the trends in the radial variation of the velocity components are captured in the frame-averaged and single-shot images.

C. Thermometry

Temperature fields inferred from a frame-average of 10 single-shot image ratios with excitation of the $Q_1(5.5)$ and $P_1(1.5)$ lines and from one single-shot ratio are displayed in Figs. 7a and b, respectively. The MOC prediction of the temperature field is shown in Fig. 7c, where the white line indicates the location of the edges of the laser sheets in the PLIF images. The scale to the right of frame c shows the relationship between the rotational temperature and gray density in the images.

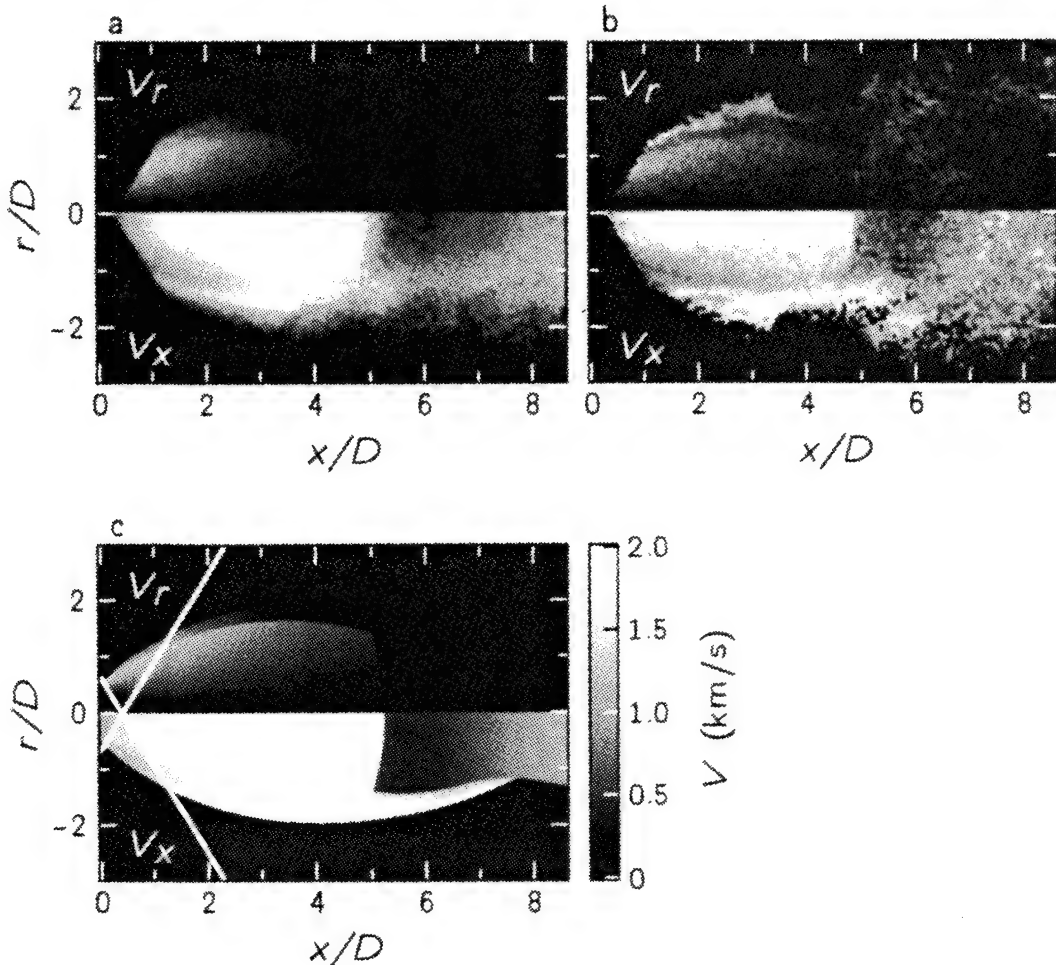


Figure 5: Velocity fields measured using OH PLIF (a and b) and predicted by the MOC (c). In each case, the radial velocity is shown in the upper part of the image and the axial velocity component in the lower. Frame a shows an average of 10 single-shot velocity images and b shows the velocity component fields inferred from the single-shot PLIF data shown in Figs. 4b and d. The white lines in c correspond to the edges of the laser sheets in the PLIF images and their reflection about the jet axis. The scale to the right of frame c indicates the relationship between the gray tones displayed in the images and the velocity.

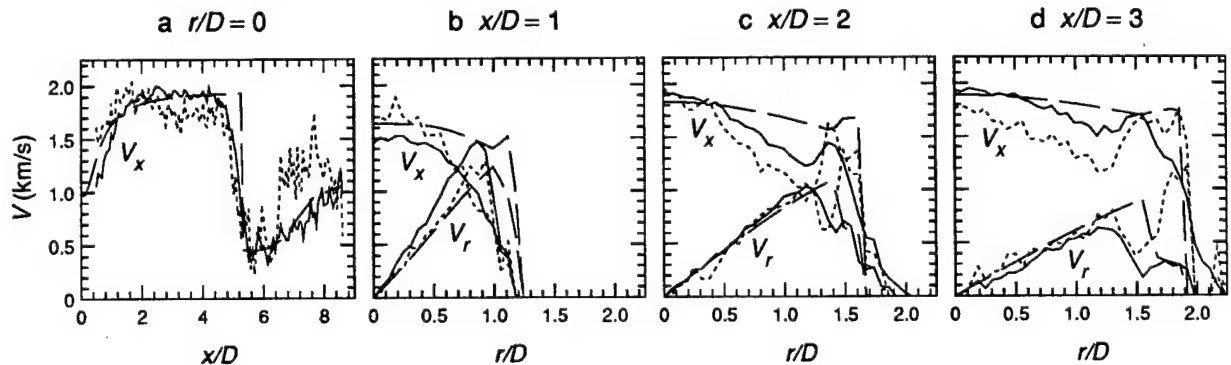


Figure 6: Measured and calculated velocity components as a function of normalized axial distance along the jet centerline (a) and as a function of normalized radial distance at several axial locations, $x/D = 1$ (b), $x/D = 2$ (c), and $x/D = 3$ (d), for the images shown in Fig. 5. Results from a single-shot velocity measurement and from an average of 10 single-shots are shown with dotted and solid lines, respectively. MOC results are shown with dashed lines.

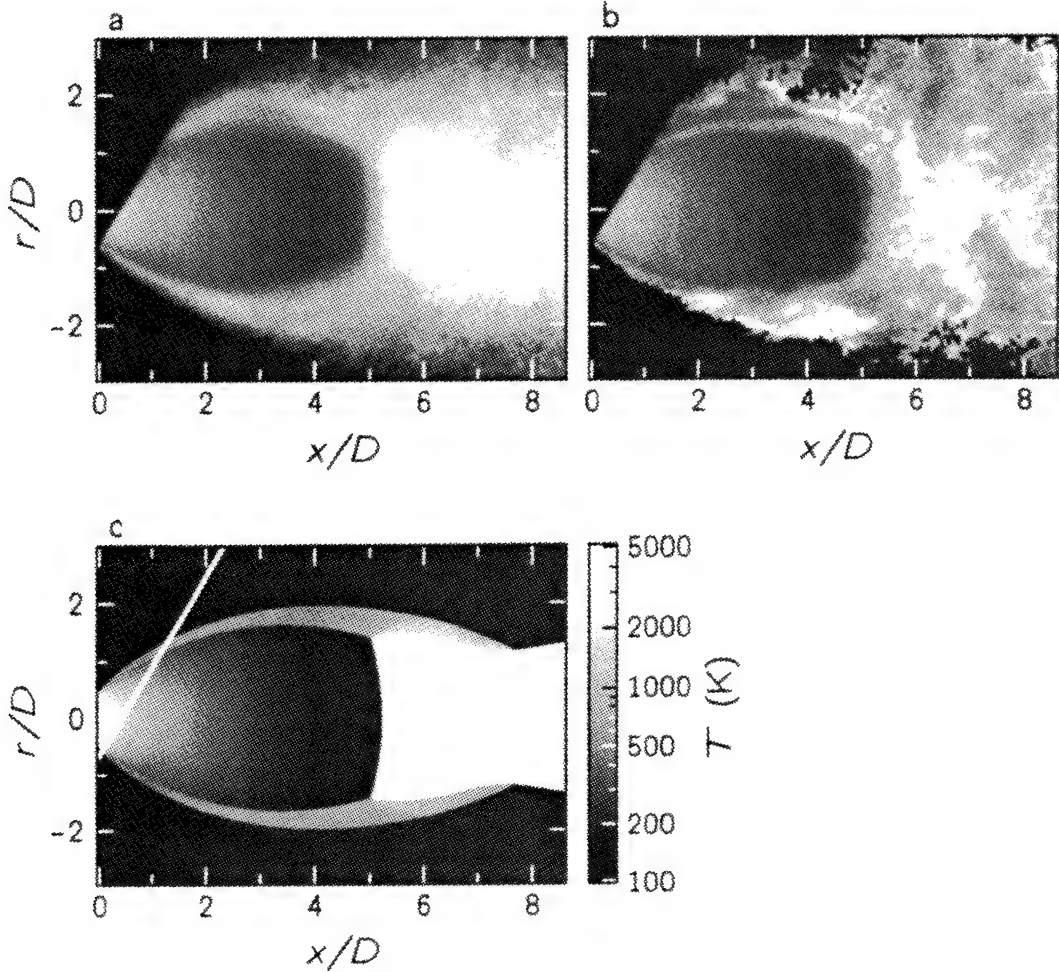


Figure 7: Rotational temperature fields measured using OH PLIF (a and b) and predicted by the MOC (c). Frame a shows an average of 10 single-shot temperature images inferred from ratios of individual $Q_1(5.5)$ and $P_1(1.5)$ image pair sums with similar laser excitation characteristics. Frame b shows the single-shot temperature field given by the ratio of Figs. 4a and c to Figs. 4b and d. The white line in c corresponds to the edges of the laser sheets in the PLIF images. The scale to the right of frame c indicates the relationship between the gray tones displayed in the images and the rotational temperature.

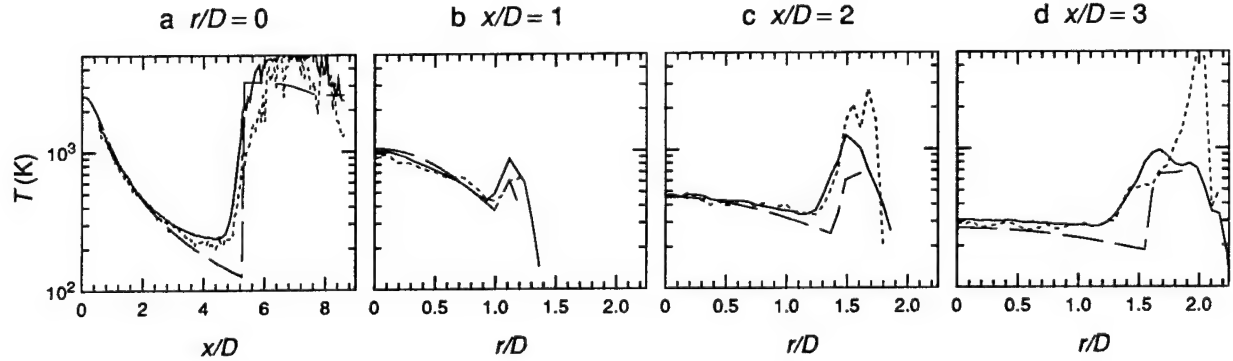


Figure 8: Measured and calculated rotational temperature as a function of normalized axial distance along the jet center line (a) and as a function of normalized radial distance at several axial locations, $x/D = 1$ (b), $x/D = 2$ (c), and $x/D = 3$ (d), for the images shown in Fig. 7. Results from a single-shot measurement and from an average of 10 single-shots are shown with dotted and solid lines, respectively. MOC results are shown with dashed lines.

Sums of the image pairs shown in Figs. 4a and c for $Q_1(5.5)$ and in Figs. 4b and d for $P_1(1.5)$ formed the numerator and denominator, respectively, of the ratio from which the image displayed in Fig. 7b was inferred. The symmetry of the temperature field, expected in an axisymmetric flowfield, demonstrates the similarity of the laser pulses used in acquiring each image pair used in the ratio. Likewise, ratios were formed from other image pairs having similar laser excitation characteristics ($v_a - v_l$ and lineshape) to create the frame-averaged temperature field in Fig. 7a. In each case, the measured temperature was scaled to that predicted by the MOC at $x/D = 1$ on the jet axis through the normalization constant C_{12} in Eqn. II.7. Values of C_{12} ranging from 0.94 to 1.12 were determined for the 10 individual ratios making up the average.

Figure 8 shows the rotational temperature variation along the jet axis (a $r/D = 0$) and at several axial locations (b $x/D = 1$, c $x/D = 2$, and d $x/D = 3$). In each case, the frame-averaged PLIF result is shown with a solid line, the single-shot result with a dotted line, and the MOC prediction with a dashed line. The agreement between the measured and calculated temperature is generally good for temperatures larger than ~ 300 K. Large fluctuations in the temperature field downstream of the Mach disk resulted from shot-to-shot changes in the flowfield and the relatively small lower level energy separation of the lines pumped (783.5 K) compared with the temperature (2500-3300 K).¹¹ Inside the jet core, the S/N of the inferred temperature varied between $\sim 7:1$ and $\sim 13:1$ for the single-shot field. The S/N for the frame-averaged temperature field was ~ 3 times higher. Discrepancies in the measured and simulated temperatures probably resulted from an unidentified background level in the images, rather than from rotational level-dependent quenching, rotational freezing, or chemical reaction.⁴

VI. Summary and Conclusions

In this investigation, PLIF thermometry and velocimetry techniques were demonstrated in a combusting, supersonic flowfield. A quasi-steady underexpanded free jet created in a shock tunnel facility was used as a model flowfield, representative of a variety of other flows in which the diagnostic techniques could be applied. The shock tunnel provided a reservoir of combustion gases diluted in Ar with 1.9% OH at 3350 ± 50 K and 3.2 ± 0.1 atm from a test gas with 5% H₂ and 5% O₂ in Ar, initially. The free jet flowfield was formed as this gas expanded into a low pressure test section following passage through a small, converging, axisymmetric nozzle.

An excimer-pumped, frequency-doubled dye laser system was tuned to excite isolated ro-vibrational transitions of OH. The lines pumped were $Q_1(5.5)$ at 282.74 nm and $P_1(1.5)$ at 282.25 nm in the $A^2\Sigma^+ \leftarrow X^2\Pi(1,0)$ band. A single UV laser pulse was used to form counter-propagating sheets which passed through the jet axis at 59° and -121° . A delay of ~ 230 ns in one beam separated the induced fluorescence signals temporally. A gated, intensified CCD array mounted above the test section collected the first fluorescence burst and an identical camera mounted below collected the second.

Simultaneously, a Fabry-Perot etalon/video camera system recorded data from which the characteristics of the laser pulse were obtained. Analysis of the fringe pattern resulting from transmission of a small portion of the UV pulse through the etalon yielded the laser lineshape and its center frequency relative to the unshifted absorption peak.

Data processing procedures applied to the PLIF images acquired with $P_1(1.5)$ excitation, along with the information on the spectral content of the laser yielded essentially instantaneous two-component velocity fields in the jet. Single-shot velocimetry results obtained in this manner were presented, as well as a frame-averaged result. The measured velocity in the axial and radial directions agreed fairly well with that predicted by the MOC. Some deviations of the single-shot result from the average were caused by uncertainties in the conversion from PLIF signal to velocity and by random error in the single-shot PLIF images.

Significant improvements in the S/N of the property fields could be obtained if more laser pulse energy were available. Only ~ 0.25 mJ across each 50 mm sheet was coupled into the experiment. The single-shot velocity measurement was particularly sensitive to random fluctuations in the raw PLIF image pairs. However, the overall agreement between the single-shot, frame-averaged, and predicted two-component velocity fields was encouraging.

Pairs of images obtained by exciting each of the transitions was necessary to measure the rotational temperature field. Because only one laser was used, separate shock tunnel runs were required to obtain the two image pairs. Thus, although the temperature measurement could not be made instantaneously, it was performed on a single-shot basis. Both frame-averaged and single-shot images of the rotational temperature showed good agreement with the MOC prediction, for temperatures above ~ 300 K. Below this temperature, the measured value was systematically higher than that predicted, probably as a

# laser wavelengths	# laser sheets/ # cameras	symmetric flow	# velocity components obtained	temperature obtained
1	1	y	1	n
1	2	n	1	n
1	2	y	2	n
1	4	n	2	n
2	3	y	2	y
2	4	n	2	y

Table 1: Instantaneous velocity and temperature imaging options. Listed are the number of laser wavelengths required, the number of laser sheets or cameras required, whether or not a symmetric flowfield is necessary, the number of velocity components that may be obtained, and whether or not the temperature may be obtained in a given experiment.

result of a background signal level in the PLIF images remaining after image correction.

Two pairs of single-shot OH images, one acquired with $P_1(1.5)$ excitation and the other with $Q_1(5.5)$ excitation, were presented. The laser was tuned in each case to compensate for the average Doppler shift in the absorption due to the centerline velocity in one of the images. These results clearly demonstrated both the velocity and temperature sensitivity of the PLIF technique. The single-shot images displayed were the ones processed to form the single-shot velocity and temperature images discussed above. Many other image pairs with varying laser detuning were acquired for each of the lines, and where appropriate, were used in the frame-averaged property fields.

Extension of the techniques described here to the simultaneous measurement of temperature and multi-component velocity fields on an instantaneous basis is conceptually simple, though experimentally complex. Table 1 shows in increasing order of complexity, the number of lasers and cameras needed to obtain an instantaneous velocity and/or temperature measurement, depending upon the symmetry properties of the flowfield. For example, the third line of the chart shows the requirements for the current experiment, in which two components of velocity in a symmetric flowfield are obtained instantaneously. A single excitation source is used to form two (counter-propagating) laser sheets, which induce fluorescence signals collected by two cameras. With the addition of another laser and camera (line 5), the measurement described here could be extended to obtain two velocity components and temperature instantaneously. Note that although four PLIF images were used here to improve the S/N in the single-shot rotational temperature measurement, only three images are strictly necessary. The last line in Table 1 shows the requirements for a measurement of the two-component

velocity and temperature in a flow without an axis of symmetry. The table could be continued to describe measurements of additional flow temperatures, corresponding to internal degrees of freedom in the molecules other than rotational (vibrational, for example).

Acknowledgment

The authors gratefully acknowledge the contributions of Drs. J.M. Seitzman and B.K. McMillin to the experimental effort. The work was supported by the U.S. Air Force Office of Scientific Research, Aerospace Sciences Directorate.

References

1. J.L. Palmer, B.K. McMillin, and R.K. Hanson, "Planar Laser-Induced Fluorescence Imaging of Underexpanded Free Jet Flow in a Shock Tunnel Facility," AIAA-91-1687, Jun., 1991.
2. J.L. Palmer, B.K. McMillin, and R.K. Hanson, "Planar Laser-Induced Fluorescence Imaging of Velocity and Temperature in Shock Tunnel Free Jet Flow," AIAA-92-0762, Jan., 1992.
3. J.L. Palmer and R.K. Hanson, "Single-Shot Velocimetry Using Planar Laser-Induced Fluorescence Imaging of Nitric Oxide," AIAA-93-2020, Jun., 1993.
4. J.L. Palmer and R.K. Hanson, "Single-Shot OH PLIF Thermometry in an Underexpanded Free Jet of Combustion Product Gases," submitted to the 25th Int'l. Symp. on Comb., Irvine, CA, Jul., 1994.
5. M.G. Allen, T.E. Parker, W.G. Reinecke, H.H. Legner, R.R. Fouter, W.T. Rawlins, and S.J. Davis, "Instantaneous Temperature and Concentration Imaging in Supersonic Air Flow Behind a Rear-Facing Step with Hydrogen Injection," AIAA-92-0137, Jan., 1992.

6. T.E. Parker, M.G. Allen, R.R. Foutter, D.M. Sonnenfroh, and W.T. Rawlins, "Exit Plane H₂O Concentration Measurements Correlated with OH PLIF Near-Injector Mixing Measurements for SCRAMJET Flows," NASA CP-3161, NASA Langley Meas. Tech. Conf., Apr., 1992, pp. 403-425.
7. T.M. Qualiarioli, G. Laufer, S.D. Hollo, R.H. Krauss, R.B. Whitehurst, and J.C. McDaniel, "KrF Laser-Induced OH Fluorescence Imaging in a Supersonic Combustion Tunnel," AIAA-92-3346, Jul., 1992.
8. B.K. McMillin, "Instantaneous Two-Line PLIF Temperature Imaging of Nitric Oxide in Supersonic Mixing and Combustion Flowfields," Ph.D. Thesis, Dept. of Mech. Eng., Stanford University, Stanford, CA, May, 1993.
9. B.K. McMillin, J.M. Seitzman, and R.K. Hanson, "Comparison of NO and OH PLIF Temperature Measurements in a SCRAMJET Model Flowfield," AIAA-93-2035, Jun., 1993.
10. J.M. Seitzman, J.L. Palmer, A.L. Antonio, R.K. Hanson, P.A. DeBarber, and C.F. Hess, "Instantaneous Planar Thermometry of Shock-Heated Flows Using PLIF of OH," AIAA-93-0802, Jan., 1993.
11. B.K. McMillin, J.L. Palmer, A.L. Antonio, and R.K. Hanson, "Instantaneous, Two-Line Temperature Imaging of a H₂/NO Jet in Supersonic Crossflow," AIAA-92-3347, Jul., 1992.
12. J.L. Palmer and R.K. Hanson, "Planar Laser-Induced Fluorescence Imaging in Free Jet Flows with Vibrational Nonequilibrium," AIAA-93-0046, Jan., 1993.
13. M. Allen, S. Davis, W. Kessler, H. Legner, K. McManus, P. Mulhall, T. Parker, and D. Sonnenfroh, "Nonintrusive, Multipoint Velocity Measurements in High-Pressure Combustion Flows," AIAA-93-2032, Jun., 1993.
14. C.B. Cleveland, J.R. Wiesenfeld, "Electronic Quenching of Highly Rotationally Excited OH (A² Σ^+ , v'=0,1) by H₂O," *Chem. Phys. Lett.*, Vol. 144, 1988, pp. 479-485.
15. S.I. McDermid and J.B. Laudenslager, "Radiative Lifetimes and Quenching Rate Coefficients for Directly Excited Rotational Levels of OH (A² Σ^+ , v'=0)," *J. Chem. Phys.*, Vol. 76, 1982, pp. 1824-1831.
16. A.Y. Chang, "Rapid-Tuning Continuous-Wave Laser Technique Applied to Nitric Oxide Spectroscopy and Flow Measurements," Ph.D. Thesis, Dept. of Mech. Eng., Stanford University, Stanford, CA, Aug., 1991.

A combined OH/acetone planar laser-induced fluorescence imaging technique for visualizing combusting flows

B. Yip, M. F. Miller, A. Lozano, R. K. Hanson

330

Abstract A combined OH/acetone planar laser-induced fluorescence (PLIF) imaging technique that provides simultaneous visualizations of regions of unburned fuel and of combustion in a reacting flow is described. OH marks the location of chemical reaction and of combustion products, and acetone vapor, which is seeded into the fuel stream, marks unburned fuel. A single pulse from an ultraviolet laser is used to simultaneously excite both the OH and acetone, and the fluorescence from each is detected on separate cameras. Acetone spectroscopy and chemistry are reviewed to provide a basis for interpreting acetone fluorescence signals in high-temperature combusting environments. The imaging technique is applied to two nonpremixed turbulent reacting flows to assess the utility of the technique for visualizing the instantaneous flow structure and to illustrate the dependence of the interpretation of the acetone PLIF images on the flow conditions.

1

Introduction

Insights into the manner in which fuel and oxidizer mix and burn in nonpremixed turbulent reacting flows can be gained by studying their instantaneous structure. Planar laser imaging techniques (Hanson 1988) are well suited for investigating flow structure because they provide a time-resolved, two-dimensional map of a chosen flow variable (e.g., species number density). In particular, planar laser-induced fluorescence (PLIF) imaging of OH has been used widely because high signals are easily attainable and because OH is naturally present in many of the combusting flows of interest. However, OH measurements only provide information about regions of the flow where combustion has occurred.

A better understanding of the mechanisms of mixing and combustion in a reacting flow can be obtained if information

about both reacting and nonreacting regions can be obtained simultaneously. Experiments where two detectors were employed to simultaneously visualize different flowfield properties in flames have been reported previously (Long et al. 1985, Dibble et al. 1986, Namazian et al. 1988, Schefer et al. 1990). While these visualization techniques yielded good results, they may not be easily applicable in larger flames or enclosed combustors. In such facilities, where the signals from Rayleigh scattering, Raman scattering or C₂ fluorescence may be too weak relative to background scattering or fluorescence, a more practical diagnostic which produces larger signals is needed.

Recently, acetone and acetaldehyde have been demonstrated as fluorescent tracer molecules in nonreacting flows and flames, and strong signals were obtained (Lozano et al. 1992, Arnold et al. 1990, Tait and Greenhalgh 1992). These large molecules exhibit a broadband UV absorption feature which overlaps the (0, 0), (1, 0) and (3, 0) vibrational bands of the A ← X system of OH, all of which have been used for OH laser-induced fluorescence (LIF) measurements. Thus, a single UV laser can be used to simultaneously excite fluorescence from the fuel stream tracer molecule and from OH. Since OH fluoresces in the UV and acetone and acetaldehyde fluoresce in the visible, optical filtering can be used to separate the signals.

This paper presents a combined OH/acetone PLIF imaging technique which provides simultaneous, time-resolved visualizations of regions of combustion and of unburned fuel. OH marks regions of combustion, and acetone, which is seeded into the fuel stream, marks regions of unburned fuel. The technique offers the significant practical advantages that only one laser is required to excite both the OH and the acetone, and the signal levels are high. Additionally, acetone is an attractive fuel stream tracer since it is relatively inexpensive and nontoxic and high seeding levels are possible. These qualities make the application of this technique to large facilities possible. The spectroscopy of acetone and its chemical behavior in high-temperature environments is discussed in order to establish a basis for interpreting acetone PLIF images. Since OH imaging is a well-established combustion diagnostic and extensive documentation exists in the literature, it will not be discussed in detail here. The combined OH/acetone technique is demonstrated in a low-speed methane flame and in a supersonic, hydrogen-air mixing layer.

Received: 13 October 1993/Accepted: 10 May 1994

B. Yip, M. F. Miller, A. Lozano, R. K. Hanson
High Temperature Gasdynamics Laboratory,
Mechanical Engineering Department, Stanford University,
Stanford, CA 94305, U.S.A.

Correspondence to: M. F. Miller

Support was provided for this work by the Air Force Office of Scientific Research, Aerospace Sciences Directorate, with Julian Tishkoff as Technical Monitor, and is gratefully acknowledged. The contributions of Mr. T. C. Island in operating the supersonic flow facility are also greatly appreciated.

2

Acetone spectroscopy and chemistry

The acetone molecule (CH₃COCH₃) displays an electronic structure characteristic of the carbonyl group, with a singlet

ground electronic state S_0 , a first excited singlet state S_1 and a corresponding excited triplet state T_1 at slightly lower energy. Acetone, which has a broadband absorption feature extending from 225 to 320 nm, can be promoted from S_0 to S_1 by ultraviolet excitation, and the excited singlet emits a blue broadband fluorescence between 350–550 nm (Lozano et al. 1992). The fluorescence yield ($\sim 0.2\%$) is limited by an internal molecular process – rapid, nonradiative intersystem crossing from S_1 to T_1 , which determines the excited singlet lifetime. Phosphorescence from the triplet state is strongly quenched by molecular collisions (Borge et al. 1990), particularly by molecular oxygen, and is negligible compared to the fluorescence measured with a gated detector using microsecond or less gate times under atmosphere pressure conditions.

A number of properties make LIF of acetone attractive for flow visualization, including: strong signals, short lifetime (~ 3 ns) and good linearity with number density and laser pump intensity (Lozano et al. 1992). Practical advantages of acetone include its low cost and low toxicity in comparison to other fluorescent tracers currently available (e.g., nitric oxide and acetaldehyde). Acetone has a molecular weight of 58.08 g/mol and a heat of combustion of 428 kcal/mol. The strong fluorescence signals of acetone allow low seeding levels to be used (e.g., an acetone seeding level of 0.2% by volume was used in the experiment to be presented in Sect. 5); thus, the perturbations to the fuel stream's density and heat of combustion are minimized. The acetone seeding level is limited by its saturation vapor pressure at the gas temperature.

For the application of acetone to nonisothermal flows, such as flames, a consideration is the dependence of acetone fluorescence yield on temperature. Ideally there should be no temperature dependence at all so that acetone fluorescence signal can be interpreted directly as acetone concentration. Indeed, some researchers have observed negligible influence of both temperature and pressure on acetone LIF (Andresen 1993). Using an excitation wavelength of 308 nm, Tait and Greenhalgh (1992) report a significant increase (70%) in the laser-induced emission from acetone with increasing temperature ($300 \text{ K} < T < 700 \text{ K}$) and attribute this behavior to a contribution of emission from non-thermalized, vibrationally-excited triplets which suffer temperature-dependent quenching. The contribution of this emission may vary significantly with the carrier gas composition (Borge et al. 1990). Paul and Clemens (1993) argue that at atmospheric pressure, the quenching of the non-thermalized triplets should be rapid enough that the temperature dependence of the fluorescence yield will be weak. In the present work, this issue was not investigated directly; however, no anomalies were found in the acetone images of the flows studied here that suggest a strong temperature dependency of acetone fluorescence yield.

In combusting flows, the interpretation of acetone as a marker of unburned fuel requires that several additional issues be addressed. Differences in the chemical behavior of acetone and the fuel of interest must be considered. At elevated temperatures acetone pyrolyzes and reacts with combustion radicals such as H, O, OH and CH_3 . The extent to which acetone marks the major fuel species is determined by the relative rates of acetone pyrolysis and radical destruction compared to those of the fuel gas. Additionally, differences in the diffusion

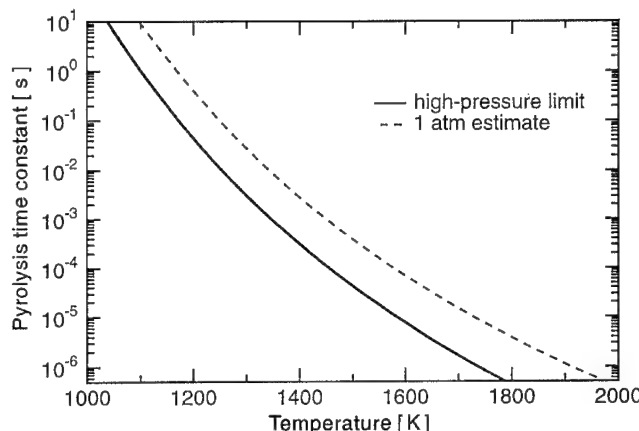


Fig. 1. Acetone pyrolysis time constants as a function of temperature

velocities between acetone and the fuel gas may be important. Each of these issues will be discussed below.

Acetone pyrolyzes by the reaction $\text{CH}_3\text{COCH}_3 \rightarrow \text{CH}_3\text{CO} + \text{CH}_3$, which is a unimolecular reaction and therefore is a function of pressure as well as temperature. Measurements of this rate, which have been reported for temperatures between 1350 K and 1650 K and for number densities less than 10^{-3} mol/cm^3 (Ernst et al. 1976), indicate that for number densities less than 10^{-5} mol/cm^3 (corresponding to typical combustion temperatures at 1 atm) the pyrolysis rate is in the fall-off region. Listed in Table 1 are two reaction rate expressions for acetone pyrolysis: the high-pressure limit rate from Ernst et al. and an estimate for the rate at 1 atm based on their data. The time constants associated with each of these pyrolysis rates are shown as a function of temperature in Fig. 1. The pyrolysis rates for hydrogen and methane are negligible compared to that of acetone; thus, application of acetone as a marker of methane and hydrogen is best suited to reacting flows with lower combustion temperatures and short residence times where the effects of pyrolysis will be minimized. The pyrolysis rates of more complicated hydrocarbon fuels, such as ethane and propane, are comparable to that of acetone; thus, pyrolysis may present less of a complication in these flows. In the present work, only the application of acetone to methane and hydrogen flames will be considered.

Radical attack on acetone is characterized by the general hydrogen atom abstraction reaction $\text{R} + \text{CH}_3\text{COCH}_3 \rightarrow \text{RH} + \text{CH}_2\text{COCH}_3$, where R represents a radical species. Measured reaction rate coefficients for attack by H (Ambridge et al. 1976), O (Herron 1988), OH (Atkinson et al. 1989) and CH_3 (Shapiro and Weston 1972) are listed in Table 1. Although these radical attack rate coefficients are fits to measurements made at temperatures below 1000 K, extrapolation of these fits to higher temperatures typical of combusting flows is adequate to assess the significance of radical attack on acetone. The rate coefficients for the reactions with H, O and OH are plotted as a function of temperature in Fig. 2. Also plotted in Fig. 2 and listed in Table 1 are the rate coefficients for O and OH attack on hydrogen (Miller and Bowman 1989). Comparison of the H atom removal rates of hydrogen and acetone indicates that all of these rates are within an order of magnitude over the full range of combustion temperatures; thus, the overall rates of

Table 1. Reaction rate coefficients: $k = AT^b \exp(-E_a/RT)$

Reaction	<i>A</i>	<i>b</i>	<i>E_a</i> (kcal/mole)	units
$\text{CH}_3\text{COCH}_3 \rightarrow \text{CH}_3\text{CO} + \text{CH}_3$				
a) high-pressure limit	2.7×10^{16}	0	81.6	s^{-1}
b) 1 atm estimate	3.0×10^{15}	0	81.6	
$\text{R} + \text{CH}_3\text{COCH}_3 \rightarrow \text{RH} + \text{CH}_2\text{COCH}_3$				
a) $\text{R} = \text{H}$	1.86×10^{13}	0	6.36	$\text{cm}^3/\text{mole/s}$
b) $\text{R} = \text{O}$	1.0×10^{13}	0	5.96	
c) $\text{R} = \text{OH}$	1.0×10^{12}	0	1.19	
d) $\text{R} = \text{CH}_3$	3.24×10^{11}	0	9.63	
$\text{O} + \text{H}_2 \rightarrow \text{OH} + \text{H}$	5.06×10^4	2.67	6.29	$\text{cm}^3/\text{mole/s}$
$\text{OH} + \text{H}_2 \rightarrow \text{H}_2\text{O} + \text{H}$	1.17×10^9	1.3	3.63	

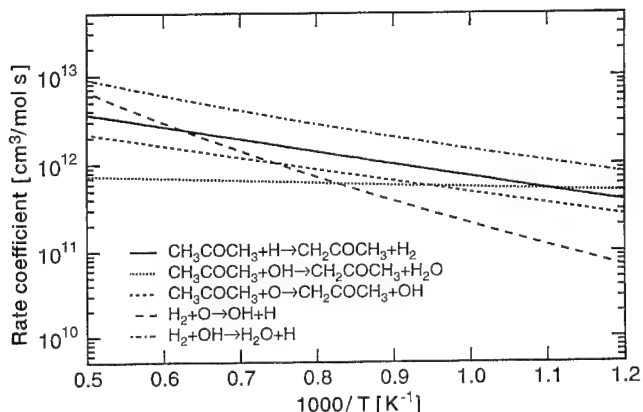


Fig. 2. Reaction rate coefficients for radical attack on acetone and molecular hydrogen as a function of temperature

destruction of acetone and hydrogen by radical attack will be similar. Although not shown, the H atom removal rates of methane and other hydrocarbons by radical attack are similar to that of acetone as well.

Another issue relevant to the discussion of acetone as a marker of fuel gas is the preferential diffusion of the fuel relative to acetone, particularly for light fuels such as methane or hydrogen. In imaging experiments where the goal is to visualize the large-scale structure of the flow, it is usually not possible to resolve the zones of diffusive mixing – the size of which is usually below the resolution of the imaging system. Thus, it is only necessary to consider the effect of preferential diffusion on the composition of the products of combustion. In a turbulent reacting flow, the significance of the effects of preferential diffusion on the rates of consumption of reactants will scale with Damköhler number. For high Damköhler numbers, reactants are consumed predominantly in strained laminar flames; hence, the rates of consumption of reactants and therefore the composition of the combustion products will be sensitive to the effects of preferential diffusion. However, for small Damköhler numbers most of the chemical reaction occurs after the reactants have been molecularly mixed; thus, the composition of the combustion products will be insensitive to the effects of preferential diffusion. Hence, the degree to which the interpretation of acetone signal as a marker of unburned fuel will be complicated by the effects of preferential diffusion will

scale with Damköhler number. For heavier hydrocarbon fuels, which have molecular weights closer to that of acetone, the effects of preferential diffusion may not be significant; however, the extent to which differences in the transport properties are important will have to be assessed on a case-by-case basis.

In summary, the interpretation of acetone as a marker of unburned fuel concentration is complicated primarily by two factors: pyrolysis and preferential diffusion. Both of these effects are exacerbated in combusting flows with long residence times and high temperatures (i.e., high Damköhler flows).

3

Experimental apparatus

Acetone's broadband absorption in the UV allows it to be excited by the same laser used to excite OH. Several different pumping schemes, each with its own advantages and disadvantages, have been employed for OH LIF imaging (Seitzman and Hanson 1993); all of these schemes can be used for simultaneous excitation of acetone fluorescence. Figure 3 shows a schematic diagram of the experimental apparatus. For the low-speed experiments (Sect. 4), a Lambda Physik Model 203MSC (Göttingen, Germany) broadband (~ 0.5 nm) XeCl excimer laser producing up to 300 mJ of energy per pulse at 308 nm was used. A narrow linewidth (~ 0.01 nm), Lambda Physik Model 150T (Göttingen, Germany) XeCl excimer laser tuned to the $Q_1(3)$ line of the $(0, 0)$ band of the $A^2\Pi^+ \leftarrow X^2\Sigma$ system of OH and producing 100 mJ per pulse was used for the high-speed experiments (Sect. 5).

The large spectral separation between the OH fluorescence, at ultraviolet wavelengths, and the acetone fluorescence, which occurs in the visible spectrum (380–540 nm), allows the use of optical filtering to discriminate between these signals. The fluorescence signals are recorded simultaneously on separate intensified CCD video cameras. The OH camera is equipped with a Schott UG 11 (Duryea, Pennsylvania) color-glass filter to block visible emission, and a 105 mm, f/4.5 UV photographic lens (quartz optics). The acetone camera is equipped with a UV-blocking, 50 mm, f/1.2 standard glass lens. A 2 μ s intensifier gate duration (overlapping the laser pulse) allows LIF signal collection while rejecting natural luminous emission from the flame.

The simultaneous image pairs are acquired with a frame grabber in a PC/AT computer at 8 bits/pixel digital resolution and an effective framing rate of 8 Hz. They are later corrected for

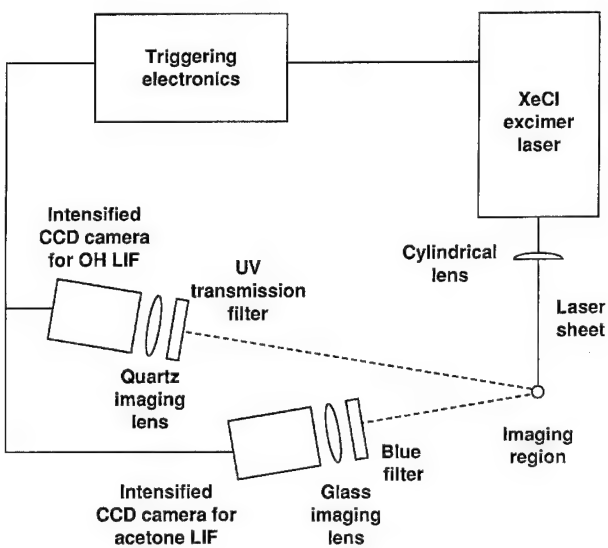


Fig. 3. Experimental setup for OH/acetone planar laser-induced fluorescence imaging

background scattering, nonuniform laser sheet intensity and camera response, as well as for the slightly differing fields of view of the two cameras. Due to the short OH and acetone fluorescence lifetimes, the temporal resolution is determined by the 20 ns laser pulse duration which is sufficient to eliminate any motion blur in the images. The spatial resolution, which is limited by the laser sheet thickness, is roughly 0.3 mm.

4

Low-speed jet flames

Initial development of this imaging technique was carried out in low Reynolds number methane and hydrogen jet diffusion flames using a broadband XeCl excimer laser with maximum pulse energies of 300 mJ. Excellent signals were obtained, but the image interpretation was complicated by a number of factors, most of which are similar to those encountered by Tait and Greenhalgh (1992) who used acetaldehyde as a fuel stream marker under similar conditions. Results from the methane flame experiments are presented to illustrate these effects.

The flame consists of a methane jet diffusion flame in ambient air. The Reynolds number of the fuel jet at the nozzle exit ($d = 2.2$ mm) is 3100. The methane is bubbled through a bath of liquid acetone to produce an acetone seeding level of 10% by volume; the seeding level is determined from Rayleigh scattering measurements. Although this seeding level perturbs the fuel stream density and heat of combustion, which are increased by 26% and 10%, respectively, these effects are tolerable for the purpose of demonstrating the technique.

Figure 4 shows simultaneous acetone and OH LIF images of the acetone-seeded flame. The imaged area is 6.8 cm high and 4.2 cm wide, and the bottom of the images is 3.7 cm (17 nozzle diameters) above the end of the fuel nozzle. The region of the flowfield imaged was chosen because the flame is mostly free of visible soot emission over this range of positions. Based on mean velocity of the fuel jet, the convective time from the fuel nozzle to the bottom of the imaged region is 4.7 ms, and the time to convect across the imaged area is 8.5 ms.

These residence times greatly exceed the acetone pyrolysis time constant for the range of combustion temperatures in this flow; thus, significant destruction of acetone by pyrolysis will occur in the hotter regions of the flow. Since methane pyrolysis is much slower than acetone pyrolysis, the acetone fluorescence is not expected to be a good indicator of the methane concentration. Additionally, the Damköhler number for this flow is high due to the high combustion temperatures and low flow velocities; thus, the effects of preferential diffusion on the reactant consumption rates will be significant as well.

As discussed by Tait and Greenhalgh (1992), interferences present in hydrocarbon flames include laser-induced incandescence from soot and LIF from polycyclic aromatic hydrocarbons (PAH's) formed from the products of fuel pyrolysis. These spurious signals can to a large degree be reduced by spectral filtering (a blue glass filter that rejected wavelengths greater than 480 nm was used here), but residual interference can introduce ambiguities in interpreting acetone LIF images. The left image in Fig. 4 shows the visible laser-induced fluorescence. In addition to the strong acetone LIF from the center of the fuel jet, weak emission (~3% of the maximum acetone fluorescence) due to these sources exists at the limit of detection between the central fuel jet and the regions of OH. This interference probably scales with the acetone seeding here, but in flames burning heavier hydrocarbons, which pyrolyze similarly to acetone, such emission will set a lower limit on the level of acetone seeding required for monitoring the parent fuel concentration.

The centre image of Fig. 4 is the ultraviolet laser-induced emission. The two long, thin regions of OH fluorescence mark the flame reaction zones. Between the two braids of OH fluorescence, a ghost image of the jet is produced by Rayleigh scattering from the methane-acetone fuel mixture. Surrounding the jet, laser scattering from particulates in the unfiltered laboratory air is seen. Without wishing to overemphasize the point (because interpretation is complicated by the unknown response of the particulates to the high-temperature environment), we remark that large regions of low UV emission are evident between the ambient air and the regions of OH fluorescence. A looped structure corresponding to Mie scattering from soot appears at the top of the image, on the fuel-rich side of the right-hand OH braid. A tunable narrowband laser (as used in the experiments of Sect. 5) could be employed to significantly increase the OH LIF signal relative to these interferences.

When the acetone and OH images are overlaid as in the right-hand image of Fig. 4, little correlation between the acetone and OH LIF is seen. A sizable region of almost zero acetone signal appears between the center of the fuel stream and the OH regions, corresponding to the destruction of acetone by pyrolysis. The same effect is seen in low-speed acetone-seeded hydrogen jet flames (e.g., Paul and Clemens 1993). Although the acetone fluorescence does not represent the methane concentration, which will extend closer to the flame zone than the acetone, it does indicate that a significant degree of mixing between the central fuel jet and hot combustion gases is occurring. Additionally, the images show the reaction zones are laminar-like, indicating the flow has locally relaminarized, an effect which has been observed previously in flames at similar Reynolds numbers (e.g., Takagi et al. 1980).

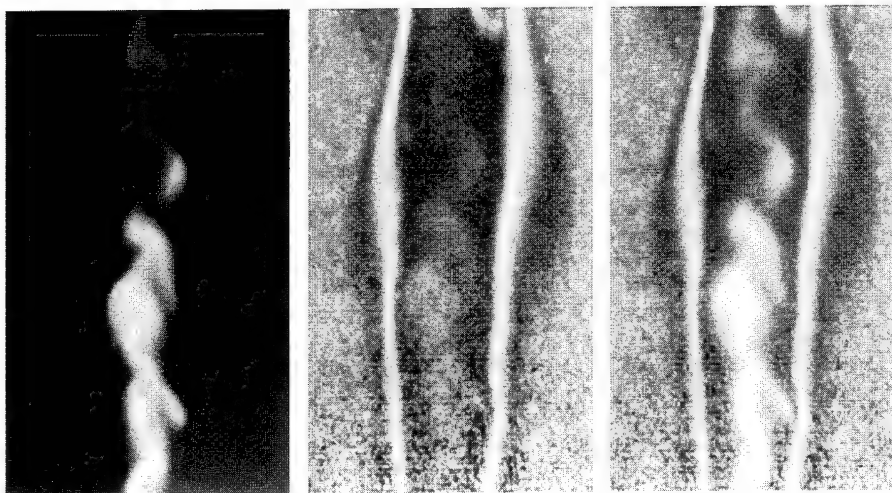


Fig. 4. Simultaneous OH/acetone PLIF images of a methane jet diffusion flame. The fuel jet nozzle is 17 diameters below the bottom of the image; the images are 6.8 cm high and 4.2 cm wide. From left to right, the images show the acetone, OH and overlaid OH and acetone

Table 2. Mixing layer free stream conditions

	Stream 1: oxidizer	Stream 2: fuel
Total temperature (K)	1600	270
Mach number	1.4	0.3
Static temperature (K)	1250	26.5
Velocity (m/s)	970	110
Molar composition	$X_{O_2} = 0.23$ $X_{H_2O} = 0.25$ $X_{N_2} = 0.52$	$X_{H_2} = 0.10$ $X_{N_2} = 0.90$ $X_{CH_3COCH_3} = 0.002$ 0.45
Mass flowrate (kg/s)	0.60	
Static pressure = 0.88 atm		

In summary, the OH/acetone imaging technique is not well-suited for studying low-speed flames where the fuel has a very different pyrolysis rate and diffusion velocity than that of acetone (e.g., methane and hydrogen). This technique may find application in flames burning heavier hydrocarbon fuels which pyrolyze and diffuse similarly to acetone; however, in these flames, interferences from laser-induced incandescence of soot and fluorescence of polycyclic aromatic hydrocarbons may present significant difficulties for this technique as they do for other laser-based visualization methods.

5

Supersonic reacting mixing layer

Experiments were also performed in a large-scale, blowdown flow facility which produces a plane mixing layer between a supersonic, high-temperature, oxidizing stream and a subsonic, ambient-temperature, fuel stream (Miller et al. 1993). The high-temperature, oxidizing stream is produced by burning oxygen-enriched air and hydrogen in a vitiation heater and expanding the combustion products through a supersonic nozzle. The vitiation heater is operated fuel-lean; thus, the major products of combustion are oxygen, water vapor and nitrogen. The fuel stream consists of hydrogen diluted with nitrogen. For imaging purposes, acetone is seeded into the fuel stream by spraying liquid acetone through a fine atomizing spray nozzle which produces droplet diameters below 100 microns.

Subsequently, the acetone droplets evaporate in the flow system prior to entering the test section. The test section measures 8 cm by 10 cm in cross-section and 45 cm in length, with uncooled quartz windows providing full optical access for most of its length.

Table 2 lists the mixing layer free stream conditions for the results presented here. The mixing layer Reynolds number, defined as $Re = (U_1 - U_2) \delta / v$, where U_1 and U_2 are the high- and low-speed free stream velocities, respectively, δ is the width of the mixing layer and v is the average kinematic viscosity, is approximately 370,000 at the imaging position. The fuel stream acetone seeding level is 2000 ppm, which represents a compromise between the desire to minimize the perturbation to the flow and to maximize the signal-to-noise ratio in the acetone images. This seeding level (~ 1 Torr) is well below the saturation vapor pressure of acetone at the fuel stream static temperature (40 Torr at 265 K). Addition of acetone to the fuel stream has a negligible effect (<1%) on its density; however, the heat of combustion of the fuel stream mixture and the overall fuel-to-air ratio of the mixing layer both increase by about 15%. While these effects are not negligible, they do not interfere with the goals of the experiment.

A representative selection of simultaneous OH/acetone PLIF images of the mixing layer in side-view are shown in Fig. 5. The digital images (300 \times 233 pixels) correspond to a region 7 cm wide by 5 cm tall, centered 22 cm downstream of the splitter tip.

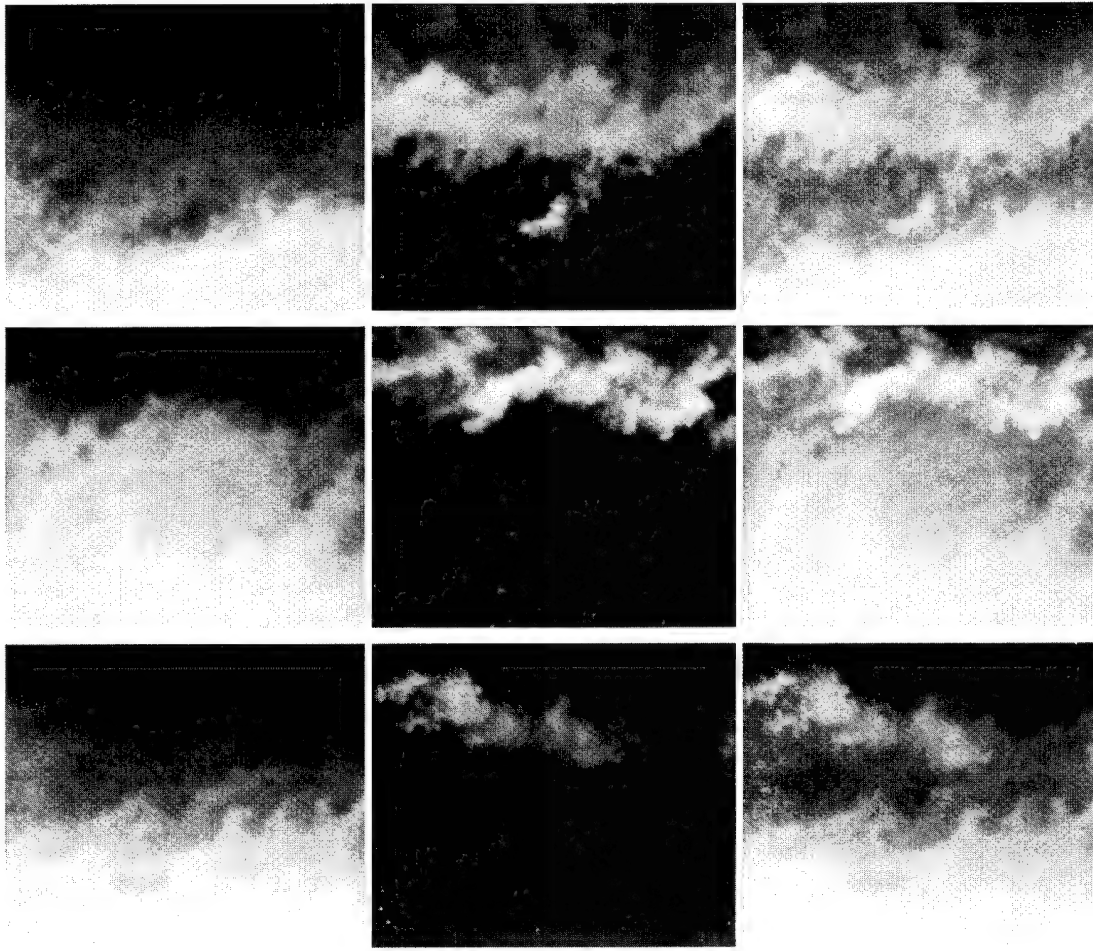


Fig. 5. Three simultaneous OH/acetone PLIF images of the mixing layer in side-view. The flow is left to right; the supersonic vitiated-air stream is on the top, and the subsonic fuel stream is on the bottom. The image

size is 7 cm wide by 5 cm high, and the center of the image is 22 cm downstream of the splitter tip. From left to right, the images show the acetone, OH and overlaid OH and acetone

The average convective time from the splitter tip to the imaging station is about 0.5 ms, and the convective time across the imaged area is 140 μ s. The pyrolysis time constant at 1 atm and 1250 K, which is the maximum temperature in the mixing layer (Miller et al. 1993), is about 50 ms. Comparing this time with the residence times indicates the pyrolysis is not a significant mechanism for acetone destruction in the mixing layer. Additionally, estimates of the chemical times for product formation in the mixing layer indicate that the overall Damköhler number of the mixing layer is about unity (Miller et al. 1993). The discussion of the scaling of preferential diffusion effects with Damköhler number presented previously suggests that the effects of preferential diffusion will not be significant in this flow. These results indicate that acetone is a reasonable marker of unburned hydrogen in the mixing layer.

The peak signal-to-noise ratio, based on root-mean-squared noise levels, is about fifteen for both OH and acetone images. Attenuation of the laser beam was not observed, which is consistent with the estimated optical depth of the OH and acetone regions of the flow. Some radiative trapping of the emitted OH fluorescence may occur due to the depth of the reacting layer between the detector and the laser-illuminated

plane. A small number of unvaporized acetone droplets, which elastically scattered the laser light, are seen as small, bright points in the OH images. This problem arose because in the present configuration, the acetone seeding station could not be placed sufficiently far upstream of the test section for complete vaporization of all droplets. The droplets cannot be discerned in the acetone images, implying that their size and number density are small. Since they are confined to the low speed stream and rarely appear in the mixing layer, the acetone droplets do not affect the results of this experiment.

In the acetone images, the region of maximum signal level at the bottom of the frame corresponds to the fuel stream, where the acetone was initially seeded. Regions of lower signal correspond to fluid from the fuel stream which has been entrained into the mixing layer; the lower acetone signal levels result from dilution by and chemical reaction with existing fluid in the mixing layer. The boundary between the region of maximum acetone signal (fuel stream) and the region of lower acetone signals (mixing layer) represents the instantaneous position of the lower edge of the mixing layer. Based on the previous discussion of acetone behavior in high temperature environments, the amount of unburned hydrogen at a given

point scales with the acetone signal at that point. Although acetone is not a conserved scalar, different signal levels necessarily indicate different mixture compositions; thus, higher acetone signals mark the cooler regions of the mixing layer rich in fuel-stream fluid, and lower acetone signals indicate hotter regions of the mixing layer rich in oxidizing-stream fluid and combustion products.

In the OH images, the signal is limited primarily to a region adjacent to the high-temperature stream; the upper edge of the mixing layer coincides with the upper edge of the OH signal. Residual OH from the vitiation heater is visible in the high-temperature stream in some of the images. Based on the measured detection sensitivity of the imaging system, the peak OH levels in the images are estimated to be between one and two orders of magnitude greater than equilibrium, indicating significant OH production in the mixing layer.

Although the instantaneous appearance of the images varies, all of the images show that high acetone signals and OH signals are mutually exclusive, indicating that regions of OH and regions of high acetone concentration have distinctly different mixture fractions. This observation suggests that the mixing layer is comprised primarily of two zones: a hot, combusting zone containing OH and a cooler, nonreacting zone containing unburned fuel. The structural features of the reacting mixing layer seen in these images are similar to those of nonreacting mixing layers at similar compressibilities (Clemens and Mungal 1992), supporting the present interpretation of the acetone and OH signals. The relatively low combustion temperatures and short residence times in this flow allow the interpretation of acetone as a marker of unburned hydrogen.

6

Conclusion

A simple two-camera PLIF imaging technique for simultaneous visualization of OH radicals and unburned fuel in turbulent reacting flows has been developed. In this technique, OH and acetone laser-induced fluorescence are excited simultaneously by a single pulse from an ultraviolet laser and are imaged separately on two intensified cameras. For combusting flows in which the primary fuel is hydrogen or methane, analysis of the chemical behaviour of acetone indicates that the interpretation of acetone as a marker of unburned fuel is complicated primarily by two factors: pyrolysis and preferential diffusion. Both of these effects are exacerbated in flows with long residence times and high temperatures. The imaging technique was applied to a low Reynolds number methane-air diffusion flame and a supersonic, hydrogen-air mixing layer to illustrate the dependence of the signal interpretation on the flow properties. It is concluded that the technique is best suited to high-speed flows with low combustion temperatures ($<1600\text{ K}$) or flames burning heavier hydrocarbon fuels whose chemical behavior and transport properties are similar to that of acetone.

One significant improvement to this technique would be to use nonresonant excitation of OH so that elastic laser scattering can be rejected by optical filtering. In fact, subsequent work in the supersonic combustion tunnel has used a frequency-doubled dye laser (20 mJ at 285 nm) to excite the (1, 0) band of OH with collection of fluorescence from the (0, 0) and (1, 1) bands.

The resulting OH and acetone fluorescence signals have been found to be comparable to those obtained in the present work (Miller et al., 1993b).

References

- Ambridge PF; Bradley JN; Whitlock DA (1976) Kinetic study of the reactions of hydrogen and oxygen atoms with acetone. *J Chem Soc Faraday Trans I*, Vol. 72: 1870–1876
- Andresen P (1993) Private communication
- Arnold A; Becker H; Suntz R; Monkhouse P; Wolfrum J; Maly R; Pfister W (1990) Flame front imaging in an internal-combustion engine simulator by laser-induced fluorescence of acetaldehyde. *Opt Lett* 15: 831–833
- Atkinson R; Baulch DL; Cox RA; Hampson RF Jr.; Kerr JA; Troe J (1989) Evaluated kinetic and photochemical data for atmospheric chemistry: Supplement III. *J Phys Chem Ref Data* 18, 881
- Borge MJG; Figuera JM; Luque J (1990) Study of the emission of the excited acetone vapor at intermediate pressures. *Spectrochim. Acta* 46A (4): 617–621.
- Clemens NT; Mungal MG (1992) Two- and three-dimensional effects in the supersonic mixing layer. *AIAA J* 30(4): 973–981
- Dibble RW; Long MB; Masri A (1986) Two-dimensional imaging of C_2 in turbulent nonpremixed jet flames. *Prog Astronaut Aeronaut* 105: 99–109.
- Ernst J; Spindler K; Wagner HGg (1976) Untersuchungen zum thermischen Zerfall von Acetaldehyd und Aceton. *Berichte der Bunsen-Gesellschaft für Physikalische Chemie* 80(7): 645–650.
- Hanson RK (1988) Combustion diagnostics: planar imaging techniques. Twenty-first Symposium (International) on Combustion/The Combustion Institute, 1677–1691.
- Herron JT (1988) Evaluated chemical kinetic data for the reactions of atomic oxygen O(3P) with saturated organic compounds in the gas phase. *J Phys Chem Ref Data* 17: 967
- Long MB; Levin PS; Fourquette DC (1985) Simultaneous two-dimensional mapping of species concentration and temperature in turbulent flames. *Opt Lett* 10: 267–269
- Lozano A; Yip B; Hanson RK (1992) Acetone: a tracer for planar concentration measurements in gaseous flows by planar laser-induced fluorescence. *Exps in Fluids* 13: 369–376.
- Miller JA; Bowman CT (1989) Mechanism and modeling of nitrogen chemistry in combustion. *Prog Energy Combust Science* 15 (4): 287–338.
- Miller MF; Island TC; Yip B; Bowman CT; Mungal MG; Hanson RK (1993a) An experimental study of the structure of a compressible, reacting mixing layer. *AIAA paper 93-0345*, 31st Aerospace Sciences Meeting, Reno, NV
- Miller MF; Island TC; Seitzman JM; Mungal MG; Bowman CT; Hanson RK (1993b) “Compressibility Effects in a Reacting Mixing Layer,” AIAA-93-1771, presented at 29th AIAA/SAE/ASME/ASEE Joint Propulsion Conference, Monterey, CA.
- Namazian M; Schmitt RL; Long MB (1988) Two-wavelength single laser CH and CH_4 imaging in a lifted turbulent diffusion flame. *Appl Opt* 27: 3597–3600.
- Paul P; Clemens NT (1993) Planar laser-induced fluorescence imaging of lifted H_2 -air flames. *AIAA paper 93-0800*, 31st Aerospace Sciences Meeting, Reno, NV.
- Schefer RW; Namazian M; Kelly J (1990) CH, OH and CH_4 concentration measurements in a lifted turbulent-jet flame. Twenty-third Symposium (International) on Combustion/The Combustion Institute, 669–676
- Seitzman JM; Hanson RK (1993) Comparison of excitation techniques for quantitative fluorescence imaging of reacting flows. *AIAA J* 31 (3): 513–519
- Shapiro JS; Weston RE Jr. (1972) Kinetic isotope effects in the reaction of methyl radicals with molecular hydrogen. *J Phys Chem* 76: 1669–1679
- Tait NP; Greenhalgh DA (1992) 2D laser-induced fluorescence imaging of parent fuel fraction in nonpremixed combustion. Twenty-fourth Symposium (International) on Combustion/The Combustion Institute, 1621–1628.
- Takagi T; Shin H; Ishio A (1980) Local laminarization in turbulent diffusion flames. *Comb. and Flame* 37: 163–170

Large-scale structure and entrainment in the supersonic mixing layer

By N. T. CLEMENS† AND M. G. MUNGAL

High Temperature Gasdynamics Laboratory, Mechanical Engineering Department, Stanford University, Stanford, CA 94305, USA

(Received 10 August 1992 and in revised form 2 August 1994)

Experiments were conducted in a two-stream planar mixing layer at convective Mach numbers, M_c , of 0.28, 0.42, 0.50, 0.62 and 0.79. Planar laser Mie scattering (PLMS) from a condensed alcohol fog and planar laser-induced fluorescence (PLIF) of nitric oxide were used for flow visualization in the side, plan and end views. The PLIF signals were also used to characterize the turbulent mixture fraction fluctuations.

Visualizations using PLMS indicate a transition in the turbulent structure from quasi-two-dimensionality at low convective Mach number, to more random three-dimensionality for $M_c \geq 0.62$. A transition is also observed in the core and braid regions of the spanwise rollers as the convective Mach number increases from 0.28 to 0.62. A change in the entrainment mechanism with increasing compressibility is also indicated by signal intensity profiles and perspective views of the PLMS and PLIF images. These show that at $M_c = 0.28$ the instantaneous mixture fraction field typically exhibits a gradient in the streamwise direction, but is more uniform in the cross-stream direction. At $M_c = 0.62$ and 0.79, however, the mixture fraction field is more streamwise uniform and with a gradient in the cross-stream direction. This change in the composition of the structures is indicative of different entrainment motions at the different compressibility conditions. The statistical results are consistent with the qualitative observations and suggest that compressibility acts to reduce the magnitude of the mixture fraction fluctuations, particularly on the high-speed edge of the layer.

1. Introduction

The role of compressibility in turbulent mixing remains an important issue in the design of high-speed propulsion devices. Of particular interest are the free-shear flows such as mixing layers, jets and wakes, where the stabilizing effect of compressibility may reduce the efficiency of engines which utilize these flows to mix the fuel and oxidizer. The mixing layer is a particularly important flow for the study of compressibility because the free-stream conditions (and hence overall compressibility) remain constant with downstream distance. This is in contrast to the jet and the wake which evolve to incompressible flow behaviour with downstream distance.

Although not as well studied as its incompressible counterpart, the compressible mixing layer (figure 1) has been studied for several decades. Until recently, however, studies of supersonic mixing layers involved mainly time-averaged growth rate measurements, with fewer studies providing velocity or scalar fluctuation data. Birch & Eggers (1972) summarized the current growth rate data and showed a clear trend of reduced mixing layer growth rates with increasing Mach number. Bogdanoff (1983)

† Present address: Department of Aerospace Engineering and Engineering Mechanics, The University of Texas at Austin, Austin, TX 78712, USA.

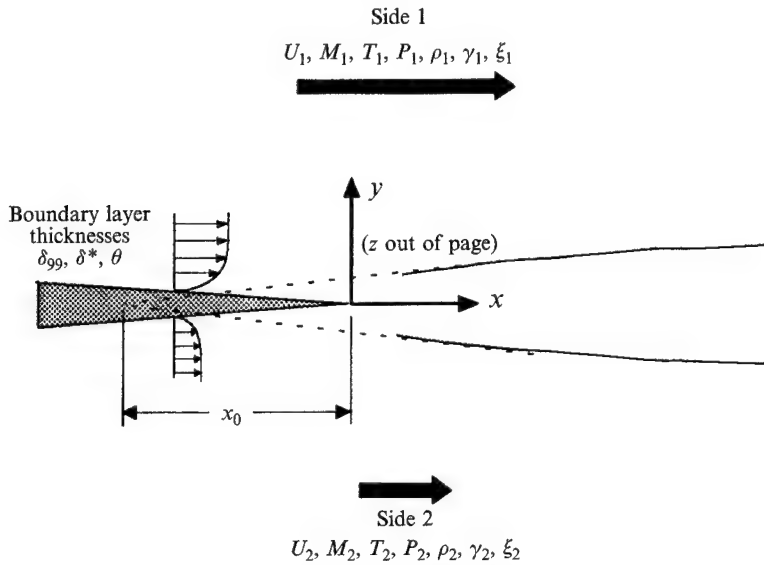


FIGURE 1. Schematic diagram of the mixing layer flow field.

and Papamoschou & Roshko (1988) generalized this result for both single- and two-stream mixing layers with the concept of the convective Mach number. In this paper, we will refer to the convective Mach number, $M_c = (U_1 - U_2)/(a_1 + a_2)$, which is the same as the Papamoschou & Roshko (1988) formulation for equal ratio of specific heats (U_1 and U_2 , and a_1 and a_2 , are the high- and low-speed free-stream velocities and speeds of sound, respectively).

Studies have shown that in addition to decreasing mixing layer growth rates, compressibility acts to suppress turbulence intensities and Reynolds stresses (Ikawa & Kubota 1975; Elliott & Samimy 1990; Goebel & Dutton 1991). Numerical studies using both linear stability theory and direct simulations have shown that at low compressibility ($M_c < 0.6$) the structure is dominated by the two-dimensional Kelvin–Helmholtz instability, while at higher levels of compressibility, the dominant instability waves are oblique (Ragab & Wu 1989; Jackson & Grosch 1989; Zhuang, Dimotakis & Kubota 1990), resulting in highly three-dimensional structure in the non-linear regime (Sandham & Reynolds 1991).

Several experiments using both flow visualization and fast response pressure measurements have shown that low convective Mach number supersonic mixing layers exhibit an organized quasi-two-dimensional structure similar to that found in incompressible mixing layers (Clemens & Mungal 1992a; Messersmith, Dutton & Krier 1991; Shau & Dolling 1992; Elliott, Samimy & Arnette 1993; Petullo & Dolling 1993). The trend of decreasing organization or increased three-dimensionality with increasing convective Mach number has also been observed by a number of investigators (Fourguette, Mungal & Dibble 1990; Clemens & Mungal 1992a; Messersmith *et al.* 1991; Samimy, Reeder & Elliott 1992; Elliott *et al.* 1993; Bonnet, Debisschop & Chambres 1993). Possibly related to the increased three-dimensionality of the compressible layer is the observation that the large-scale structures do not travel at the speed predicted by the convective Mach number formulation of Papamoschou & Roshko (1988) (Papamoschou 1991; Fourguette *et al.* 1990; McIntyre & Settles 1991; Hall, Dimotakis & Rosemann 1991a).

A few passive scalar mixing measurements have also been reported. Passive scalar

Study	Fluid	Re_δ	L/λ_B	PDFs	Mean inflection point
Sunyach & Mathieu (1969)	Gas	50000	600	—	Single
Fiedler (1974)	Gas	100000	100	—	Triple
Batt (1977)	Gas	70000	100	Marching	Single
Konrad (1977)	Gas	40000	11	Non-marching	Triple
Rajagopalan & Antonia (1981)	Gas	35000	70	—	Triple
Koochesfahani & Dimotakis (1986)	Water	23000	700	Non-marching	Triple
Masutani & Bowman (1986)	Gas	3200	250	Non-marching	Triple

TABLE 1. Comparison of scalar measurement data

mixing measurements can in general be problematic, however, because the spatial and temporal resolution must be sufficient to resolve the smallest scalar fluctuations, otherwise the amount of mixed fluid will be overestimated. The smallest mixing scale is the Batchelor scale, $\lambda_B = \beta \delta Re_\delta^{3/4} Sc^{-1/2}$, where β is a constant, δ is the local layer width, Re_δ is the local Reynolds number based on the velocity difference of the shear flow and δ , and $Sc = \nu/D$ is the Schmidt number, or the ratio of the kinematic viscosity to the mass diffusion coefficient. Dowling & Dimotakis (1990) made high-resolution measurements in jets and suggest $\beta \approx 25$. As a means of quantifying the resolution of an experiment, we will refer to the relative resolution, L/λ_B , where L is the largest dimension of the probe volume and λ_B is defined above with $\beta = 1$. The relative resolutions of several incompressible mixing layer experiments are shown in table 1 and will be discussed further in §5.

Passive scalar mixing measurements in supersonic mixing layers were made by Dutton *et al.* (1990) using Mie scattering from seeded particles, and Clemens *et al.* (1991), Messersmith & Dutton (1992) and Clemens & Paul (1993) using nitric oxide laser-induced fluorescence. These studies report probability density functions (PDFs) of mixture fraction whose peak value ‘marches’ with cross-stream direction across the layer. This result is in agreement with the incompressible mixing layer measurements of Batt (1977) and Karasso & Mungal (1992), but not with the results of Konrad (1977) and Koochesfahani & Dimotakis (1986), where the peak mixture fraction was found to be constant with cross-stream location. Dutton *et al.* (1990) and Clemens *et al.* (1991) also found that the fraction of mixed fluid within the layer increased from low to moderate convective Mach numbers. The measurements of Messersmith & Dutton (1992), which were made at similar convective Mach numbers, did not show a clear trend for the fraction of mixed fluid. The results of these studies should be interpreted with caution as the measurements were highly under-resolved ($L/\lambda_B > 500$).

As a means of avoiding the problem of poor resolution in making mixing measurements, Hall, Dimotakis & Rosemann (1991b) made quantitative measurements of product formation using H_2 - F_2 -NO chemistry in planar supersonic shear layers. They studied two convective Mach number cases ($M_c = 0.51$ and 0.96) and determined that the fraction of mixed fluid was lower at the high convective Mach number condition, which is opposite to the trend observed by Dutton *et al.* (1990) and Clemens *et al.* (1991). Clemens & Paul (1993) used a fluorescence quenching technique that mimics a fast chemical reaction, and thus is highly insensitive to finite resolution. They found in axisymmetric mixing layers that the fraction of mixed fluid was virtually the same at convective Mach numbers of 0.35 and 0.82.

In the present study, the structure of low to moderately compressible mixing layers was investigated using extensive flow visualizations with planar laser Mie scattering

(PLMS) from a seeded alcohol fog. These visualizations are compared to those made using planar laser-induced fluorescence (PLIF) imaging of seeded nitric oxide. The PLIF images are also used to generate statistical quantities, such as mean profiles, root-mean-square (RMS) fluctuations and probability density functions of mixture fraction.

Section 2 provides a description of the experimental apparatus, run conditions and diagnostic techniques used. Section 3 provides some background and theoretical justification for the optical diagnostic techniques, and the experimental results are discussed in §§4 and 5. Section 6 provides an overall discussion of the results, with conclusions offered in §7. Limited PLMS visualizations of the turbulent structure at three convective Mach numbers can be found in Clemens & Mungal (1992a). Complete details on all aspects of this work are detailed in Clemens (1991).

2. Experimental apparatus and run conditions

In this section the experimental facility, diagnostics set-up and experimental run conditions are discussed.

2.1. Wind tunnel

A schematic diagram of the flow system is shown in figure 2. The high-speed stream was supplied by a 6.9 MPa, 5 m³ vessel, while the low-speed side was supplied by a 3.4 MPa, 2.5 m³ vessel. A compressor delivered filtered and dried air to both tanks, and the two main flows were controlled using globe valves combined with microprocessor-based controllers. Maximum run times were 30–60 s, depending on the condition, with typical run times being 10–20 s.

The wind tunnel consisted of the plenum sections, nozzles, test section and diffuser. The tunnel was rectangular in cross-section with a width of 10 cm that remained constant over its entire length of about 180 cm. The high- and low-speed plenum sections (figure 3) were each 12 cm high, 10 cm wide and 55 cm and 85 cm long, respectively. The high-speed-side plenum had one station of honeycomb with a 0.8 mm cell size and 5 cm in length. The low-speed plenum contained two perforated plates of 55% porosity followed by two stations of honeycomb identical to that on the high-speed side. Stagnation pressures were measured using static pressure taps located on the sidewalls of each plenum. The high- and low-speed flows then passed through contractions of 9:1 and 4:1, respectively. The nozzle design was similar to that of Papamoschou & Roshko (1988) where a centre-body contained both the supersonic and subsonic contours. The supersonic contours were designed using a closed form solution to the method of characteristics (Foelsch 1946) and the subsonic contour of the centre-body followed a fifth-order polynomial. Three aluminium nozzles were used with design exit Mach numbers of 1.5, 2.0 and 2.2.

The high-speed nozzle exit height (*y* dimension) was 2.5 cm for all three nozzles. The low-speed nozzle exit height was either 3 cm or 4.5 cm depending on the particular convective Mach number condition: the 3 cm height for the lowest convective Mach number case and the 4.5 cm height for the higher Mach number cases. The differing heights were used to accommodate the differing rates of mixing layer growth. The test section length (*x* dimension) was 48 cm and 10 cm in width (*z* dimension). For variation of the streamwise pressure gradient, the top and bottom walls were adjustable using a thin flexible member design similar to that of Papamoschou & Roshko (1988). Optical access was provided through the sides from −0.5 cm to 45 cm from the splitter tip, and through the top and bottom from 15 cm to 45 cm. The windows were constructed of acrylic for all runs except for the PLIF experiments where smaller fused silica windows were used. The windows were carefully mounted so as to minimize the

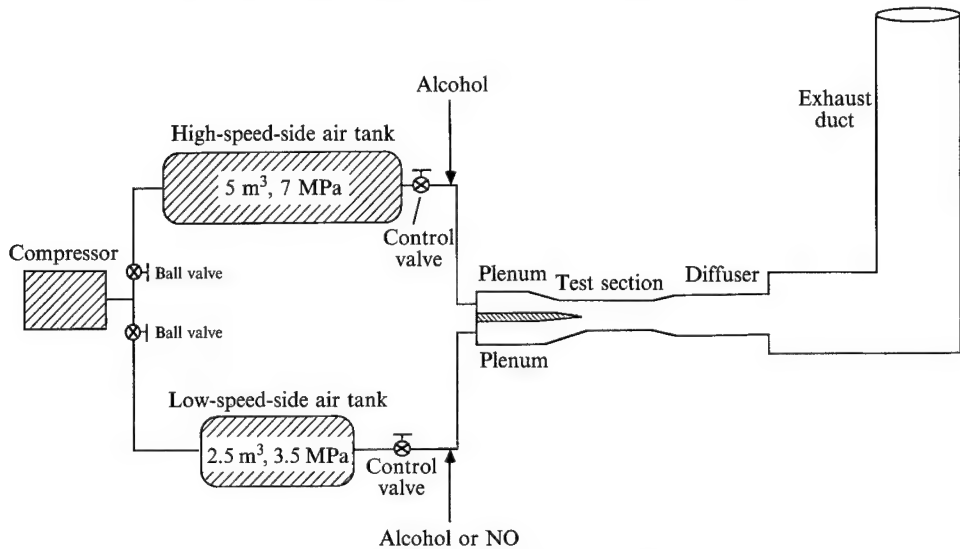


FIGURE 2. Simplified diagram of the gas supply system.

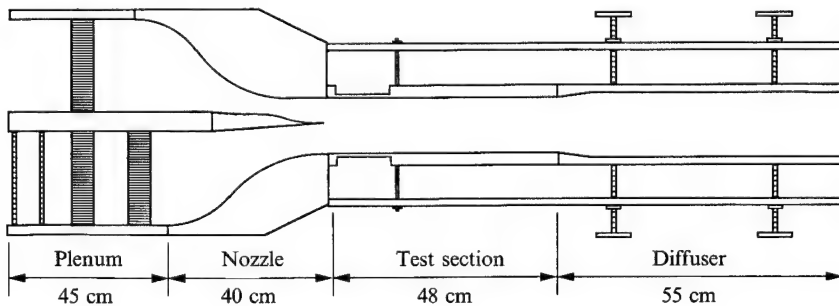


FIGURE 3. Diagram of the wind tunnel showing the plenum sections, nozzles, and the test and diffuser sections. The figure is not to scale.

Case	$M_c = 0.28$	$M_c = 0.42$	$M_c = 0.50$	$M_c = 0.62$	$M_c = 0.79$
Gas ₁ , Gas ₂	Air, air	Air, air	Air, air	Air, air	Air, argon
M_1, M_2	1.64, 0.91	1.52, 0.51	1.50, 0.38	2.0, 0.40	2.2, 0.39
U_1, U_2 (m s^{-1})	430, 275	416, 165	413, 118	480, 130	508, 110
T_{01}, T_{02} (K)	265, 260	270, 271	271, 259	265, 260	265, 260
T_1, T_2 (K)	172, 223	187, 260	188, 252	150, 252	140, 253
P_{01}, P_{02} (kPa)	302, 115	310, 100	265, 80	495, 75	600, 67
\dot{m}_1, \dot{m}_2 (kg s^{-1})	1.6, 0.77	1.5, 0.53	1.3, 0.51	1.8, 0.37	1.84, 0.39
$U_1/\nu_1, U_2/\nu_2$ ($\text{cm}^{-1} \times 10^{-5}$)	4.8, 1.9	5.0, 1.1	4.3, 0.75	6.5, 0.74	7.0, 0.55
Density ratio, s	0.77	0.72	0.75	0.59	0.77
Velocity ratio, r	0.63	0.40	0.29	0.27	0.22
$(\omega_{alc})_1, (\omega_{alc})_2$	0.002, 0.004	—, 7.6	2.1, 6.6	0.002, 0.008	0.0016, 0.008
$(\chi_{NO})_2$ (p.p.m.)	1700	—	—	3500	—

TABLE 2. Run conditions

mismatch between the window and the frame. The importance of removing such discontinuities was demonstrated by Clemens & Mungal (1992b), who showed that through the generation of shock waves, sidewall discontinuities can significantly perturb supersonic mixing layers. Eight 0.8 mm diameter static pressure taps, with a separation of about 5 cm, were located on the top and bottom walls of the test section. After exiting the test section, the flow entered a straight duct supersonic diffuser and then exited to the atmosphere through an exhaust duct 50 cm diameter by 10 m long.

2.2. Diagnostics

The principal diagnostics used for this study were Pitot pressures, schlieren photography, PLMS visualization and PLIF. The Pitot probes were used to obtain the overall growth rate of the mixing layer while the schlieren and PLMS images were used for identification of the turbulent structure. The PLIF allowed further visualizations as well as the ability to make quantitative determinations of scalar transport. In addition to the imaging measurement, stagnation temperatures and static pressures were recorded as facility diagnostics. A 16 channel pressure scanner (Pressure Systems Inc.) was used to monitor the pressures throughout the test and diffuser sections.

The Pitot probes were constructed of 18 gauge (1.3 mm outer diameter) hypodermic needles of varying lengths, soldered to a stainless steel strut 1.6 mm thick by 2.54 cm wide (in the streamwise direction). The probe was moved vertically through the flow using a computer-controlled stepping motor with each trace consisting of about 30 points acquired in about 10 s.

The schlieren system was composed of a Xenon Nanolamp with a 20 ns pulse width, 30 cm diameter F/6 parabolic mirrors, 30 cm by 10 cm flat mirrors, a razor blade knife edge, and a CCD video camera (Pulnix TM540) with a telephoto lens as the imaging device.

The condensation fog methods involved the seeding of ethanol liquid into the low- or high-speed streams using an atomizing spray nozzle. The injection points were located approximately 5 m upstream of the test section providing enough time for the droplets to fully evaporate and become uniformly mixed before reaching the test section. The mass fractions of seeded ethanol vapour, ω_{alc} , were from 0.002 to 0.008, with the actual values given in table 2.

For the PLMS visualizations, the laser used was a frequency-doubled Nd:YAG laser (Quantel 660B), with a 6 ns pulse width, pulse energy of 150 mJ and a 10 Hz repetition rate. The laser was formed into a sheet that was typically 15 cm wide and 300 μm thick at the waist. The detector was a standard CCD video camera (Pulnix TM540) whose output was acquired using a Data Translation 2851 frame grabber installed in an IBM AT compatible computer equipped with 10 Mbytes of extended memory. The images were stored using the extended memory where a maximum of 80 images of 512×240 resolution could be acquired at a rate of about 3 Hz.

For the PLIF studies, the $A \leftarrow X (0, 0) Q_1(J = 10.5)$ transition of nitric oxide (NO) was excited with laser light of wavelength 226.159 nm. The laser source was a XeCl (Lambda Physik EMG 160) pumped dye laser (Lambda Physik FL 3002) frequency doubled in BBO. The UV laser pulse width was about 20 ns with a spectral width of about 0.45 cm^{-1} . The sheet was typically 6–7 cm wide and about 250–350 μm thick at the waist. The camera system was an image-intensified CCD video camera (Amperex), of 512×240 resolution, coupled to an $F/1.2, f = 95 \text{ mm}$ Casagrainian reflective lens. The imaged region was about 5 cm, thus the nominal resolution was about $125 \times 200 \times 300 \mu\text{m}$, for the streamwise (x), cross-stream (y) and spanwise (z) directions (figure 1), where the spanwise resolution is given by the sheet thickness. The actual

spatial resolution was worse than this, however, owing to filtering by the frame grabber, and the lens and image intensifier response characteristics. Paul (1991) discusses the resolution of the camera system used in the present study and concludes the resolution is further degraded by a factor of about 1.7, resulting in an actual resolution of about $400 \times 400 \times 300 \mu\text{m}$. We note, however, that owing to the low signal-to-noise ratios of the measurements, the resolution is actually approximately a factor of two worse than this (see § 5).

The nitric oxide delivery system consisted of a bottle of pure NO which was located outside the building and brought into the laboratory through a 1.3 cm stainless steel line pressurized to 340 kPa and metered using a precision needle valve. The NO was seeded into the low-speed stream far enough upstream of the test section for it to become uniformly mixed.

2.3. Run conditions

Results will be presented for five convective Mach numbers: 0.28, 0.42, 0.50, 0.62 and 0.79. The different convective Mach number cases were achieved by varying the supersonic and subsonic Mach numbers and the low-speed gas molecular weight, with the specific conditions given in table 2. For all but the lowest convective Mach number case, the test section upper wall was kept level while the lower wall was converged about 0.5° in order to obtain a constant streamwise pressure distribution. For the $M_c = 0.28$ case, however, both the upper and lower walls were diverged about 0.5° . This had the effect of accelerating both free streams to higher Mach numbers, such that the resulting convective Mach number was reduced significantly from its non-accelerated value.

Splitter plate boundary layer thicknesses were calculated using STAN7, a turbulent boundary layer code (Crawford & Kays 1976). The high-speed nozzle exit momentum thickness Reynolds numbers, $Re_\theta = U_1 \theta_1 / \nu_1$, were calculated to be 7.2×10^3 , 10^4 , and 1.1×10^4 for the $M_1 = 1.5$, 2.0 and 2.2 nozzles, respectively. For Reynolds numbers of this magnitude, the boundary layers are expected to be turbulent. The calculated high-speed boundary layer thicknesses, δ_{99} , at the nozzle exit, are 1.6, 1.5 and 1.6 mm, while the momentum thicknesses are, $\theta_1 = 0.15$, 0.14 and 0.12 mm, for the $M_1 = 1.5$, 2.0 and 2.2 nozzles, respectively. For the low-speed side, δ_{99} boundary layer thicknesses were typically 1.0–1.5 mm. The calculations of the high-speed-side boundary layer thicknesses, δ_{99} , agree well with the thicknesses of about 1.5 mm scaled from close-up schlieren photographs.

3. Diagnostic techniques

This section provides background information and theory for the PLMS and PLIF diagnostics.

3.1. Planar laser Mie scattering

The primary flow visualization method used in this study was planar laser Mie scattering from droplets that were formed from the condensation of seeded alcohol vapour. The condensation occurred in one of two modes, depending on whether the high- or low-speed stream was seeded. When the vapour was seeded into the low-speed stream, condensation would occur from the mixing of the low-speed fluid with the cold (140–180 K) high-speed fluid. Condensation, therefore, occurred only upon the molecular mixing of high- and low-speed fluid, and in this way, mimics product formation of a finite-rate chemical reaction (Masutani & Bowman 1986; Mungal & Frieler 1988). For this reason, we call this the ‘product formation’ method, in analogy to combustion systems. Alternatively, when the alcohol vapour was seeded into the

high-speed stream, the vapour condensed within the supersonic nozzle forming a fairly uniform marker of high-speed fluid (McGregor 1961). This method is analogous to passive scalar visualizations that have been used in incompressible mixing layers (Batt 1977; Breidenthal 1981; Masutani & Bowman 1986), thus we call it the ‘passive scalar’ method. Owing to droplet growth and evaporation, the scattering signals for the product formation and passive scalar methods are not strictly proportional to either the concentration of product or of high-speed fluid, respectively, as will be discussed below.

The condensation fog methods are discussed in detail in Clemens & Mungal (1991), and some of their most relevant results will be summarized here. The alcohol droplets were measured to have a mean diameter of less than $0.2 \mu\text{m}$, which is small enough to satisfy the Samimy & Lele (1991) criterion for correct visualizations of the large-scale turbulent structure. The number densities are large enough ($> 10^9 \text{ cm}^{-3}$) that the droplets are expected to coagulate as they travel downstream, thus potentially affecting the scattering signal. Such coagulation, however, will cause a relatively gradual signal change and is not expected to affect the visualization of the turbulent motions. For certain mixture fractions, droplet re-evaporation is also expected to occur. This is particularly a problem with the passive scalar method when the high-speed fluid (which carries the droplets) becomes sufficiently diluted with the relatively warm low-speed fluid. This effect is expected to be largest for the low convective Mach number case, but even for this case, most of the mixed fluid should be visualized.

The time for complete condensation of ethanol vapour in a supersonic nozzle was measured by Wegener, Clumpner & Wu (1972) to be approximately $50 \mu\text{s}$, which we will use as an order of magnitude estimate for the ‘chemical time’ with the product formation method. This time is slow enough that finite rate effects should be evident, since this is of the same order as the local large-scale time, $\delta/\Delta U$ ($x = 30 \text{ cm}$), for all of the cases. It is believed, however, that conclusions concerning the large-scale structure of the flow are not compromised by finite rate effects for any of the convective Mach number cases. This is because no change in the turbulent structure is observed for a factor of three change in fluid timescales, or from $x = 15 \text{ cm}$ until the end of the test section at $x = 45 \text{ cm}$.

3.2. Planar laser-induced fluorescence

Laser-induced fluorescence measurements can in general be difficult to interpret because the signal depends on the temperature, pressure, and the mole fractions of all species which collide with the fluorescent species. A simple fluorescence model can be used to obtain a relation between the fluorescence signal, S_f , and the flow field variables (Hanson, Seitzman & Paul 1990),

$$S_f \propto \chi_{NO} N(P, T) f_B(T) E_L \frac{1}{1 + Q_{el}/A}, \quad (1)$$

where χ_{NO} is the mole fraction of NO, N is the total number density, f_B is the Boltzmann fraction, E_L is the laser energy, A is the spontaneous emission rate (which is constant), and Q_{el} is the electronic quenching rate, or the rate at which excited state molecules are de-excited through collisions. In the present experiments, where the NO is seeded into air and mixes only with air, we find that $Q_{el} \propto NT^{1/2}$ and $Q_{el} \gg A$. Equation (1) then reduces to

$$S_f \propto \chi_{NO} \frac{f_B(T)}{T^{1/2}} E_L. \quad (2)$$

The Boltzmann fraction is determined by the ground-state energy level that is pumped, and a level can be chosen such that $f_B \propto T^{1/2}$ over the temperature range of interest. Equation (2) then reduces to the relation $S_f \propto \chi_{NO}$, showing that the fluorescence signal is proportional to the NO mole fraction and is independent of pressure and temperature. The NO mole fraction is a conserved scalar, and upon normalization of the signal by its free-stream value we can define the mixture fraction, ξ , as

$$\xi = 1 - \chi_{NO}/(\chi_{NO})_2, \quad (3)$$

where the subscript 2 is used since, for all cases, the NO was seeded into the low-speed stream. The mixture fraction, ξ , represents the mass (or mole) fraction of high-speed fluid present within the probe volume. Clemens (1991) shows that the fluorescence signal is a linear function of mixture fraction to within 2–3 %. It should be noted that the laser beam was noticeably absorbed (20–30 %) on traversing the low-speed side of the layer, and all of the images were corrected for this using Beer's law.

4. Experimental results: conventional measurements and PLMS imaging

This section describes the experimental results, first the conventional diagnostics and then PLMS visualizations. Note that not all of the diagnostics available were applied to each of the compressibility cases.

4.1. Static and Pitot pressures

The test section static pressure distributions for all cases are shown in figure 4. As discussed previously, for the $M_c = 0.28$ case, the flow was accelerated in order to obtain a lower convective Mach number. This is seen where the pressures on the high- and low-speed side are matched at the exits of both nozzles at about 80 kPa (corresponding to $M_1 = 1.5$ and $M_2 = 0.7$); the two flows then accelerate, reaching a uniform pressure of about 65 kPa from about 15–45 cm, where the pressures vary by less than 5 % from the mean, with new free-stream Mach numbers of 1.64 and 0.91. The Pitot thickness growth rates were determined in this constant-pressure region. The pressures for the other cases remained constant to within about 20 % throughout the test section.

Pitot traces for the three convective Mach number cases, 0.28, 0.62 and 0.79, are shown in figure 5 where the positions of each profile on the page are approximately to scale. The profiles for the $M_c = 0.28$ case show that both free streams were relatively uniform throughout the entire test section. The bumps in the profiles are due to weak shocks and expansion waves which are also seen in the schlieren visualizations. Near the end of the test section the boundary layers on the top and bottom walls can be seen, and in all cases are less than about 7 mm thick. As with the static pressure distributions, stronger free-stream non-uniformity is seen at the higher convective Mach numbers. This non-uniformity is due to shock and expansion waves which diminish in strength with downstream distance.

In figure 6 the $0.05\Delta P_{pit}$ and $0.95\Delta P_{pit}$ points are plotted versus downstream distance for $M_c = 0.28$, 0.62 and 0.79, in order to show the growth and spatial location of the layers. The layers for all cases exhibit approximately linear growth in the downstream 2/3 of the test section where the effects of the initial shocks have largely dissipated.

The Pitot thickness, δ_{pit} , was determined from the distance between the $0.05\Delta P_{pit}$ and $0.95\Delta P_{pit}$ points and when plotted versus downstream distance, the slope gives the growth rate, while the x -intercept gives the virtual origin, x_0 . The slope was obtained

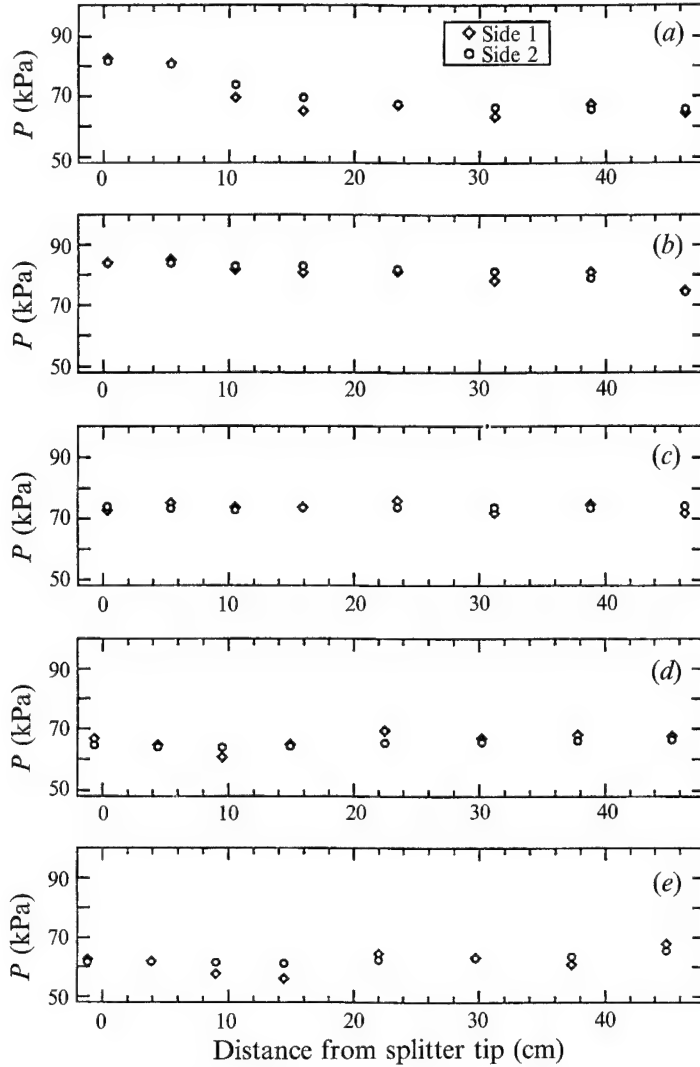


FIGURE 4. Test section static pressure distributions: (a) $M_c = 0.28$, (b) $M_c = 0.42$, (c) $M_c = 0.50$, (d) $M_c = 0.62$, (e) $M_c = 0.79$.

using a linear least squares fit to the last three points for the $M_c = 0.28$ case, and the last four points for the higher Mach number cases. Only the last three points were used for the $M_c = 0.28$ case in order to omit points taken in the accelerating flow region. In addition to Pitot thickness growth rates, for all of the cases normalized visual thickness, δ_{vis} , growth rates are also shown. The visual thickness growth rates were obtained by fitting lines ‘by eye’ to the edges of time-averaged schlieren and PLMS images. The growth rate data are shown in table 3.

The growth rates were normalized by the incompressible growth rates at the same velocity and density ratios using the incompressible growth rate formula of Papamoschou & Roshko (1988):

$$\frac{d\delta}{dx} = C_\delta \frac{(1-r)(1+s^{1/2})}{1+rs^{1/2}}, \quad (4)$$

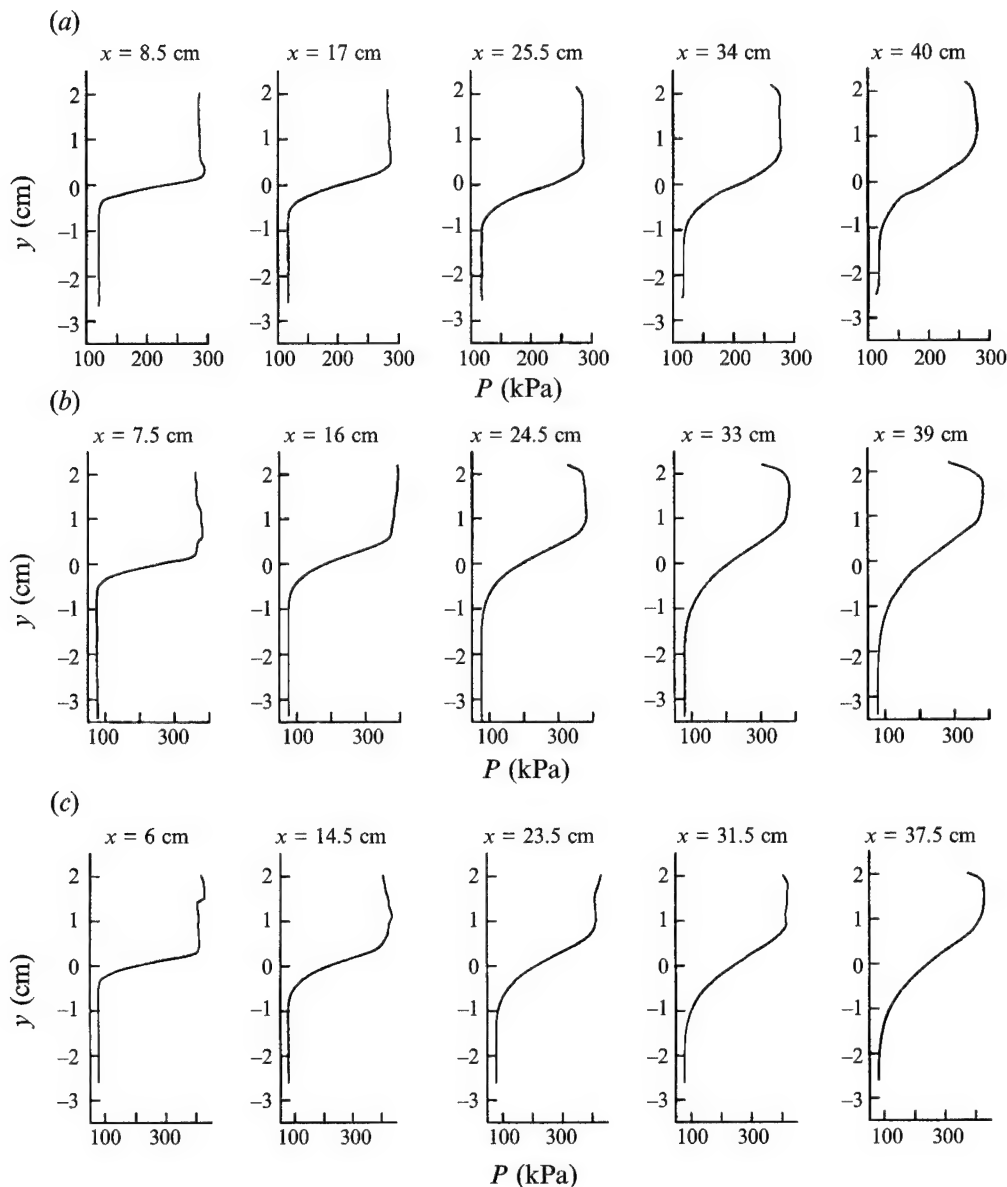


FIGURE 5. Transverse Pitot pressure profiles for several streamwise locations. Each profile is located approximately to scale with its x -location: (a) $M_c = 0.28$, (b) $M_c = 0.62$, (c) $M_c = 0.79$.

where r is the velocity ratio U_2/U_1 , s is the density ratio ρ_2/ρ_1 , and C_δ is a constant that depends on the particular definition of layer thickness ($C_\delta = 0.14$ for the Pitot thickness and $C_\delta = 0.17$ for the visual thickness). The normalized growth rates are shown in figure 7, in addition to data from other studies. The uncertainties in the present measurements are due mainly to the small sample of points used in the fit, the high-speed-side Pitot pressure non-uniformity of about 10%, and run-to-run total pressure variations of about $\pm 2\%$. Visual growth rates obtained using the schlieren and PLMS images gave similar results, although the procedure in general is somewhat subjective, and this is reflected in the relatively large error bars shown in the figure. Figure 7 shows

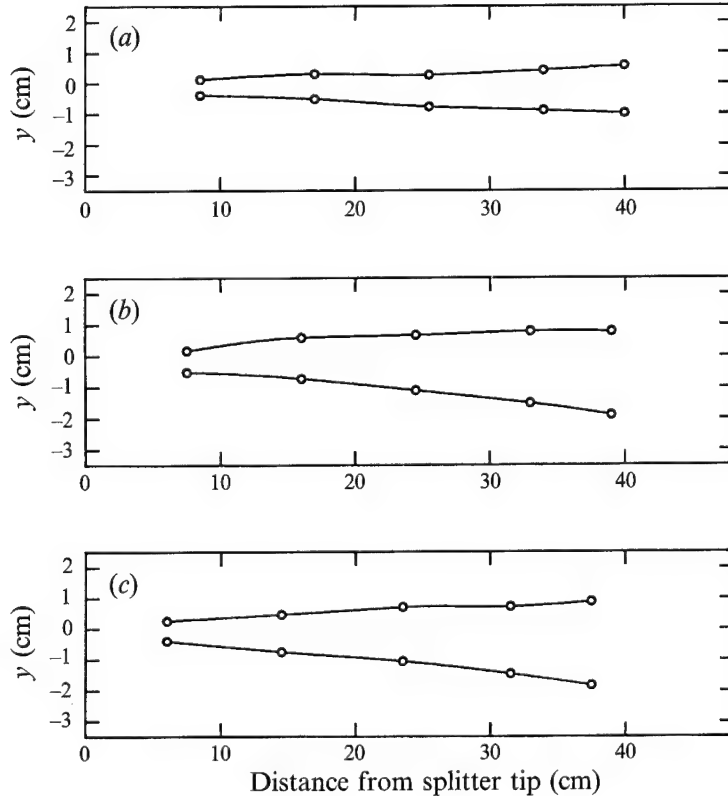


FIGURE 6. $0.05 \Delta P_{pit}$ and $0.95 \Delta P_{pit}$ points versus streamwise location: (a) $M_c = 0.28$,
(b) $M_c = 0.62$, (c) $M_c = 0.79$.

Case	$M_c = 0.28$	$M_c = 0.42$	$M_c = 0.50$	$M_c = 0.62$	$M_c = 0.79$
$\delta'_{pit} = d\delta_{pit}/dx$	0.036	—	—	0.061	0.063
$(x_0)_{pit}$ (cm)	-3.0	—	—	-4.0	-4.3
$\delta'_{pit}/(\delta'_{pit})_{inc}$	0.59	—	—	0.41	0.36
δ'_{vis}	0.055	0.090	0.10	0.073	0.09
$(x_0)_{vis}$ (cm)	-4.1	-1.0	-4.0	-5.3	-6.5
$\delta'_{vis}/(\delta'_{vis})_{inc}$	0.72	0.63	0.56	0.39	0.42

TABLE 3. Mixing layer growth rate data

that the present data are in general agreement with the trend of reduced normalized growth rate with increasing convective Mach number.

It should be noted in figure 7 that although the data for all of the studies shown exhibit a large amount of scatter, the results for a given study show considerably less scatter, suggesting that most of the scatter may result from systematic errors in the various experiments. For example, at the incompressible limit ($M_c \approx 0$), the growth rates range from 60% to 125% of the incompressible rates. The reason for this discrepancy may be related to initial condition effects (e.g. laminar *vs.* turbulent splitter plate boundary layers), which are important if the flows had not achieved their fully developed state (Browand & Latigo 1979). In addition, the large acoustic fluctuations which are present in supersonic wind tunnels can increase the ‘flapping’ of the layer,

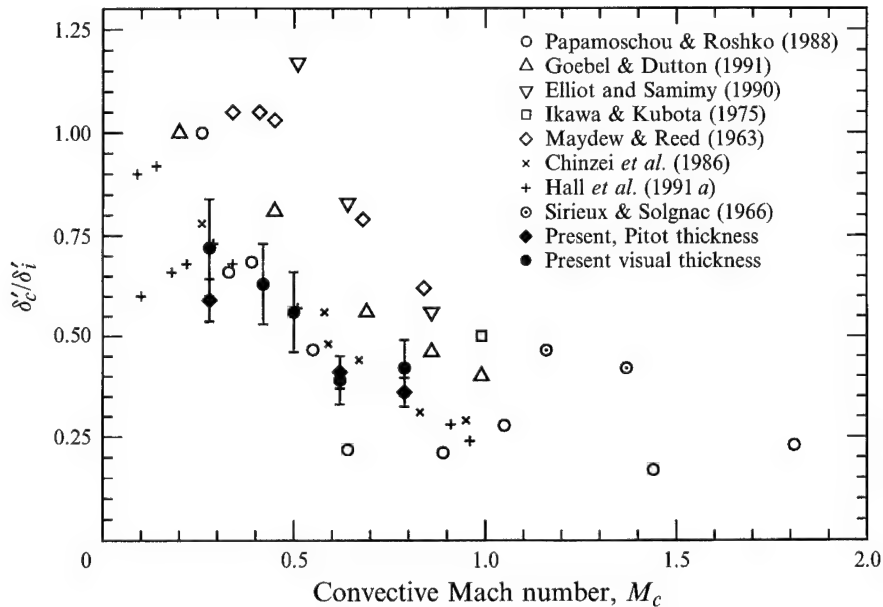


FIGURE 7. Comparison of normalized growth rate data as a function of convective Mach number.

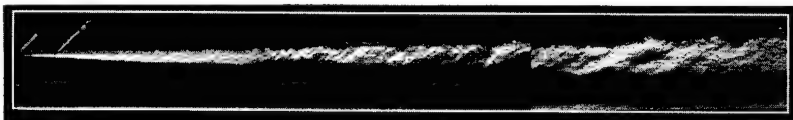


FIGURE 8. Instantaneous composite schlieren image, $M_c = 0.28$ and $x = 0\text{--}45$ cm. The panel is composed of three uncorrelated images 15 cm in length.

leading to higher mean growth rates. Also, as suggested by Papamoschou & Roshko (1988), compressibility may act differently on different measures of the mixing layer thickness.

4.2. Schlieren and PLMS

4.2.1. $M_c = 0.28$

A side view schlieren image of the entire test section, where $x = 0\text{--}45$ cm, is shown in figure 8. The figure is a composite of three independent images of 15 cm in length. The knife edge position is horizontal and it is pushed far enough into the focused beam to block the light intensity maximum, thus rendering the background as dark, with the gradients appearing as light. Evident in figure 8 is a relatively weak shock wave from the splitter tip, and a Mach wave which originates from the supersonic nozzle/test section wall junction. The schlieren images show that coherent large-scale structures, or Brown-Roshko structures (Brown & Roshko 1974), persist to several thousand x/θ_1 downstream and to very high local Reynolds numbers ($Re_{\delta_{vis}} \approx 380\,000$). These results are in agreement with the low convective Mach number schlieren photographs of Chinzei *et al.* (1986), but not with those of Goebel & Dutton (1991) and Hall *et al.* (1991a) where Brown-Roshko structures were found to be less dominant. The differing results may be due to the schlieren visualization technique which emphasizes different types of structures depending on the position of the knife edge.

The PLMS results will be presented in the order of side (x, y), plane (x, z) and end

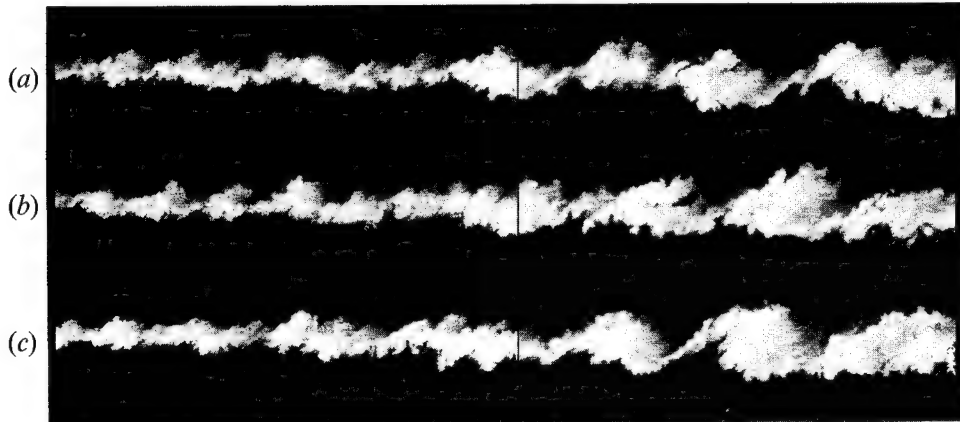


FIGURE 9. Product formation side views, $M_e = 0.28$ and $x = 15-45$ cm. Each panel is a composite composed of two uncorrelated images.

(y, z) views. As noted in §2, the end view was taken at an oblique angle, which results in a small amount of distortion. In all cases several realizations are shown to allow the reader to form a better impression of the layer structure.

Figure 9 shows three composite side view cuts using the product formation method where the total region imaged was $x = 15-45$ cm. The images are composed of two 15 cm images which will be called a ‘panel’, and all of the images are uncorrelated in time. The signal-to-noise ratios (SNRs) for the product formation images are 20–25. Although all of the cuts presented here were made through the centreline of the test section ($z = 0$ cm), no noticeable differences were seen for cuts made at $z = 2$ cm.

The PLMS images of figure 9 reveal much more detail of the turbulent structures than the schlieren visualizations. The vortex cores, which are elliptical in shape, are composed of large amounts of mixed fluid separated by thinner braid regions which can also contain significant amounts of mixed fluid. It is of note that, in general, the structures appear more roller-like towards the downstream portion of the test section. This is also the case in the schlieren images of figure 8, and may contradict the view that the structures should degenerate into three-dimensionality with downstream distance (Chandrsuda *et al.* 1978).

Owing to the large Schmidt number of the droplets ($Sc = 10^5-10^6$), it may seem unexpected that the highly strained braid regions often contain significant amounts of product (Broadwell & Breidenthal 1982). The high product levels are not surprising, however, as although the product has a large Schmidt number, the reactants (air and ethanol vapour) have Schmidt numbers of order unity.

Figure 9 also reveals details such as pairing events (last structure of *a*), and what may be a tertiary instability appearing as a sequence of bumps on the braid structures and vortex cores (second to last structure of *c*). Figure 9 also shows that the cores are not completely uniform, but can exhibit a large variation in signal.

Figure 10 shows composite side views using the passive scalar method where $x = 15-45$ cm and $z = 0$ cm. The SNR for the passive scalar images was about 15–18, somewhat lower than for the product formation images. The figure shows that the passive scalar method also reveals the domination of the layer by coherent structures. This is particularly evidenced by the large intrusions of free-stream fluid into the layer. The low-speed fluid intrusions, which are black, appear to be deeper than is actually the case (see, for example, *b*), owing to the limited dynamic range of the reproduction, and also to the possible evaporation of the droplets. This is seen by comparing to

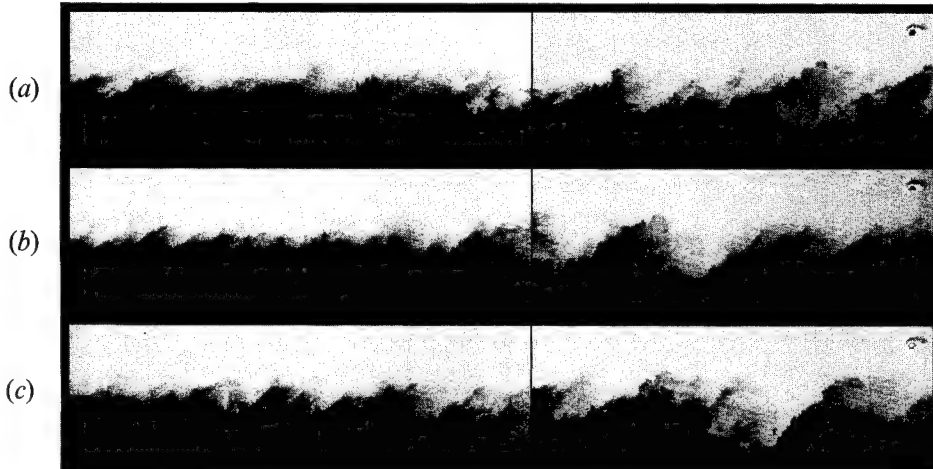


FIGURE 10. Passive scalar side views, $M_c = 0.28$ and $x = 15-43$ cm. Each panel is a composite composed of two uncorrelated images.

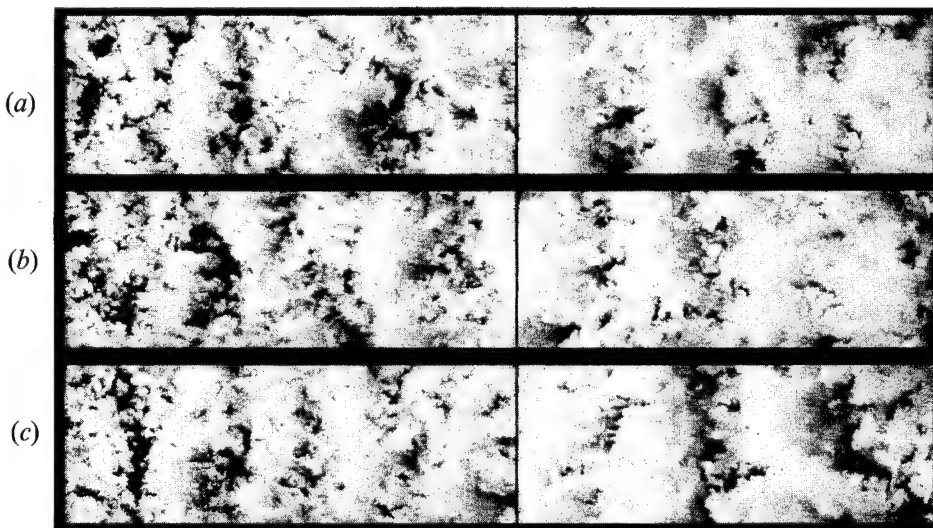


FIGURE 11. Product formation plan views through the middle of the layer, $M_c = 0.28$, $x = 15-45$ cm, $z = -2.5-2.5$ cm and $y = 0$ cm. Each panel is a composite composed of two uncorrelated images.

figure 9 where regions of pure low-speed fluid are rarely seen to cross the centreline of the layer. The bumps from the above-mentioned tertiary instability are also seen in figure 10 in the last structure of (a).

Owing to the contrast in the scattering signals, the product formation method emphasizes turbulent motions which bring mixed fluid next to unmixed fluid, whereas the passive scalar method emphasizes motions which bring pure high-speed fluid next to pure low-speed fluid. Therefore, the product formation method emphasizes the structure cores, while the passive scalar method emphasizes the braids, which are thin regions bordering high- and low-speed fluid.

Plan view product formation images are shown in figure 11, where $x = 15-45$ cm, $z = -2.5-2.5$ cm, and the laser sheet is at the splitter tip level ($y = 0$ cm) which roughly corresponds to the middle of the mixing layer. The test section sidewalls are at $z = -5$

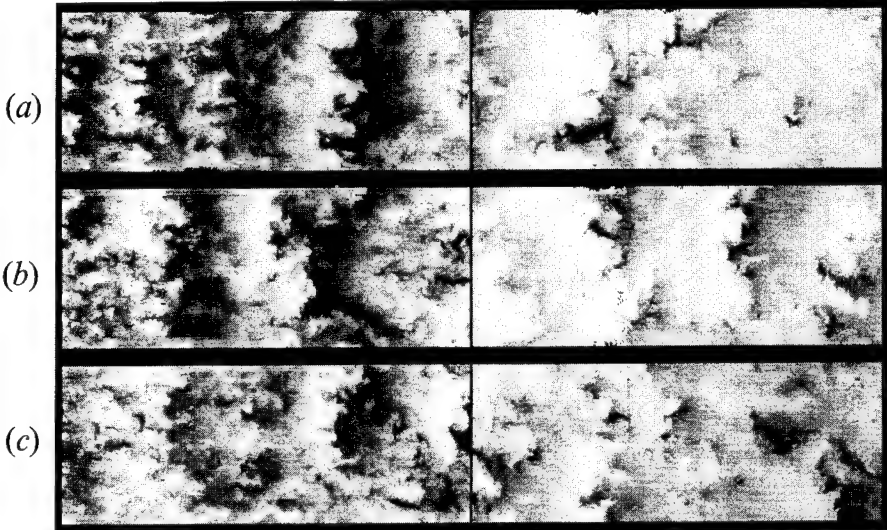


FIGURE 12. Passive scalar plan views through the middle of the layer, $M_e = 0.28$, $x = 15\text{--}42 \text{ cm}$, $z = -2.5\text{--}2.5 \text{ cm}$ and $y = 0 \text{ cm}$. Each panel is composed of two uncorrelated images.

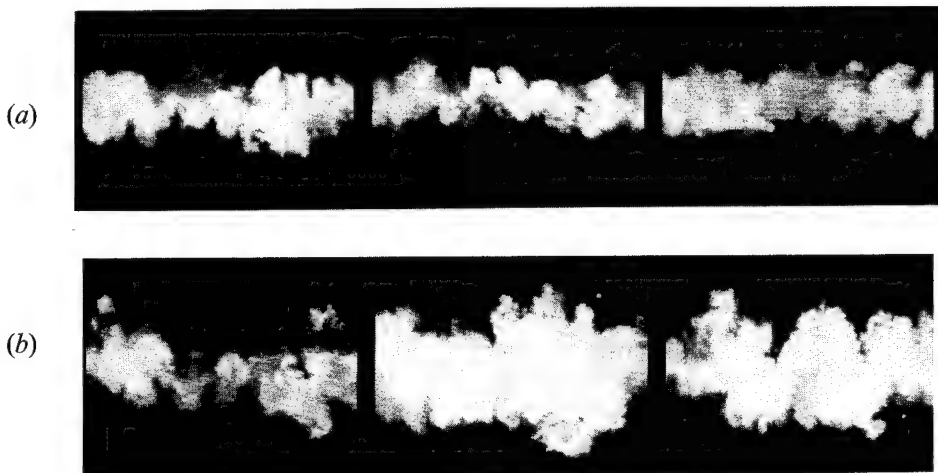


FIGURE 13. Product formation end views, $M_e = 0.28$ and $z = -2.5\text{--}2.5 \text{ cm}$
(a) $x = 19 \text{ cm}$, (b) $x = 34 \text{ cm}$.

and 5 cm, thus the boundary layers are not in the field of view. In many of these images the structures span the width of the field of view in agreement with previous studies in incompressible flow (Brown & Roshko 1974; Wygnanski *et al.* 1979; Browand & Troutt 1985; Bernal & Roshko 1986). Unlike the lower Reynolds number results of Brown & Roshko and Bernal & Roshko, however, the structures often appear skewed and bent, in agreement with the results of Browand & Troutt (1985). Furthermore, the structures are connected by smaller oblique structures which may be related to the helical pairings found by Chandrsuda *et al.* (1978). As with the side views, the mixing layer sometimes appears highly irregular with no apparent organization.

Passive scalar plan view images through the middle of the layer are shown in figure 12, where the sheet and camera locations are the same as in figure 11. In agreement with the product formation images, the passive scalar images also reveal the quasi-two-

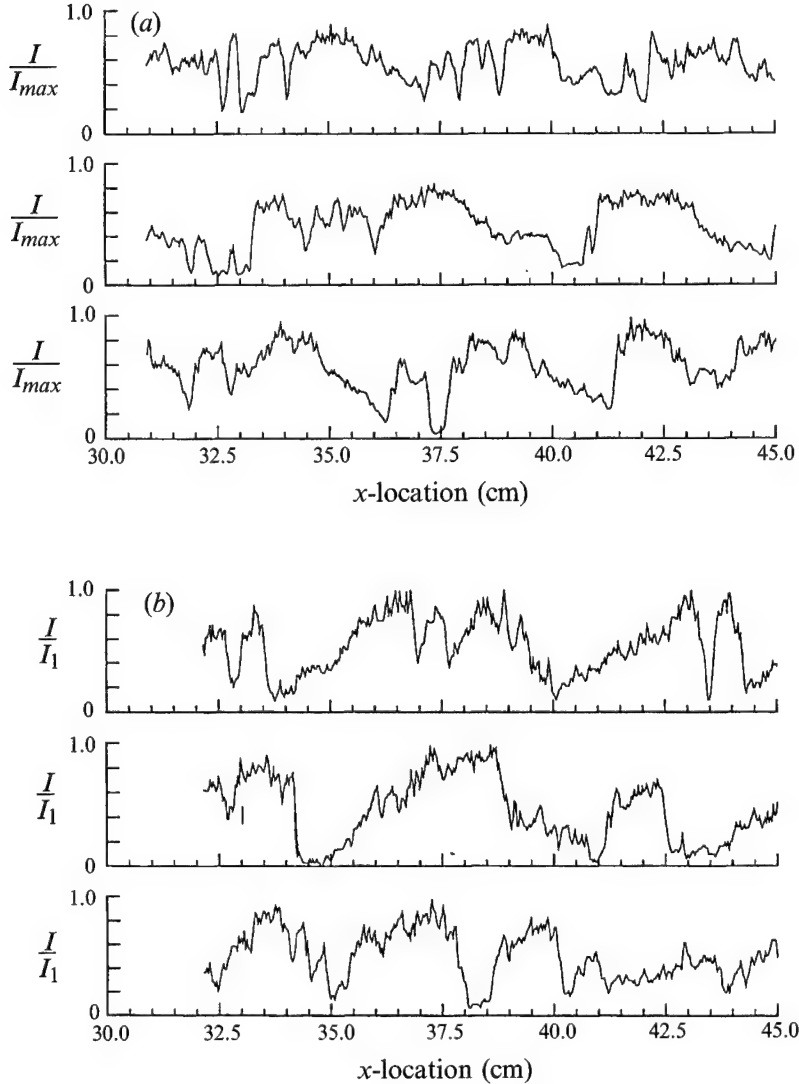


FIGURE 14. Streamwise signal intensity profiles through $M_e = 0.28$ side view images for (a) the production formation method and (b) the passive scalar method.

dimensionality of the structures. The structures seen in figures 11 and 12 are not the same, however, since with the product formation method, the cores appear as white bands, whereas with the passive scalar method the white bands result from intrusions of pure high-speed fluid between the structures. The vortex cores, in figure 12, appear as the grey regions to the left of these white bands. Also very apparent in figure 12, are the streamwise braid vortices (bright-dark intersections) observed in low-speed incompressible mixing layers (Bernal & Roshko 1986). These vortices are seen to be quite prominent at this very large Reynolds number.

Typical end view cuts using the product formation method are shown in figure 13 for $x = 19$ and 34 cm and $z = -2.5$ – 2.5 cm. The trends are best seen in the $x = 34$ cm cuts where the images often appear as thick regions of mixed fluid which may correspond to cuts through the cores of the Brown-Roshko structures. Sometimes thinner highly

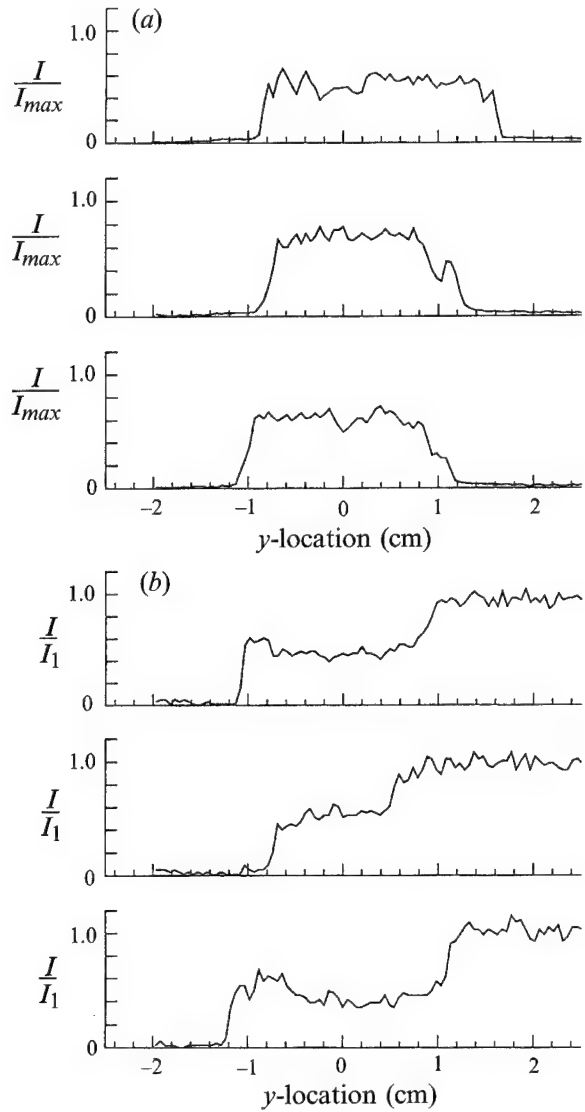


FIGURE 15. Cross-stream signal intensity profiles through $M_e = 0.28$ side view images for (a) the product formation method and (b) the passive scalar method.

convoluted structures are observed and probably correspond to cuts through the braid regions between the structures. It is also of note that the signal intensity is seen to be relatively uniform across the cores whereas it is highly variable across the braids. End view passive scalar images were made for some of the cases but owing to poor quality are not shown.

Information concerning the state of mixing in the layer can be obtained by considering the actual signal levels of the fog images. This is shown in figure 14 where three intensity profiles through the product formation and passive scalar side views are compared. The product formation profiles were normalized by the maximum signal of the three profiles, while the passive scalar profiles were normalized by the high-speed free-stream intensity. These profiles were taken at the y -location corresponding to the peak in the mean product formation profile. Figure 14 shows that the signals often

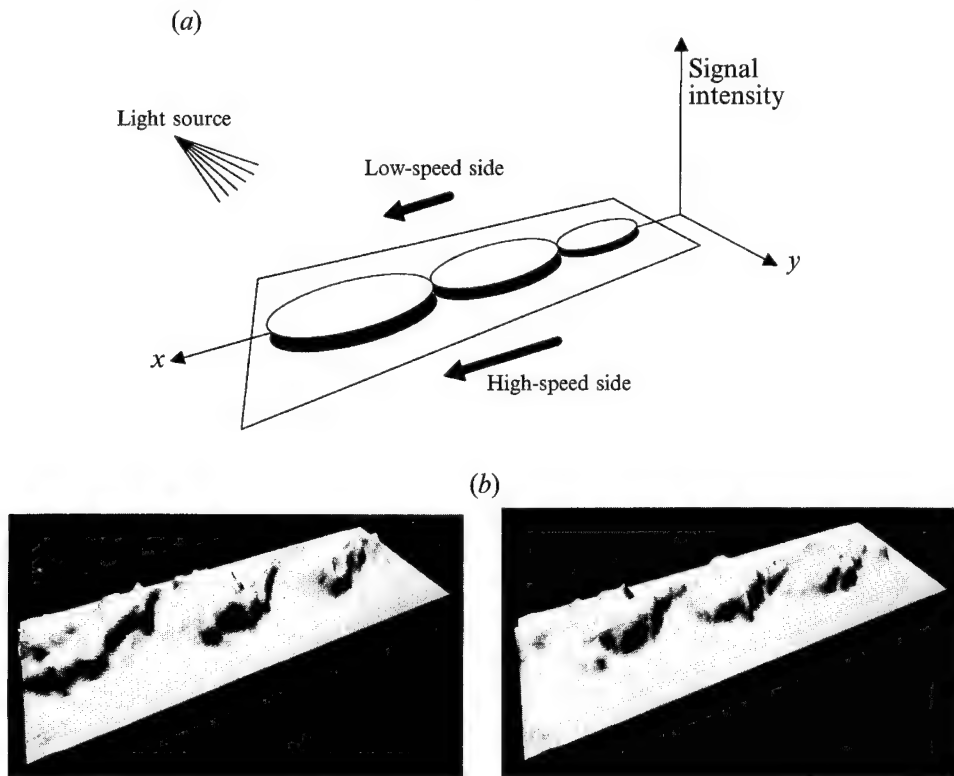


FIGURE 16. (a) Schematic diagram showing the axes orientation and light source location for the perspective views. (b) Perspective views of $M_e = 0.28$ product formation side view images, $x = 15-30$ cm.

exhibit negatively and positively sloped regions for the product formation and passive scalar methods, respectively. These sloped regions are similar to the ‘sawtooth’ or sloped temperature traces observed by Fiedler (1974) in an incompressible planar mixing layer where one stream was slightly heated. Fiedler argued that the sloped traces are due to the vortex core concentration being biased to the side from which it entrains free-stream fluid. This causes the sign of the slope to depend on whether the high- or low-speed free stream was heated. The product formation profiles also show remarkable resemblance to the incompressible reacting mixing layer product time traces of Mungal & Dimotakis (1984) where the signals are sloped and reveal that pure fluid only rarely reaches the middle of the layer.

Cross-stream (*y*-direction) profiles through select structures are shown in figure 15. The figure shows that the cross-stream scattering profiles for the product formation method can be ‘top hat’ shaped, suggesting that the structures are relatively uniform in this direction, in agreement with Fielder. The passive scalar profiles also show this uniformity as seen by the stepped profiles of figure 15.

Additional details of the mixing can be seen by considering the four product formation side views shown in perspective in figure 16, where $x = 30-45$ cm. The perspective views were generated by mapping the signal intensities into elevation and rendering it as a volume consisting of a solid surface. A point source of light is then used to illuminate the surface. Elevation, therefore, represents the signal intensity while the light and dark regions are shadows which aid the eye in determining the elevation.

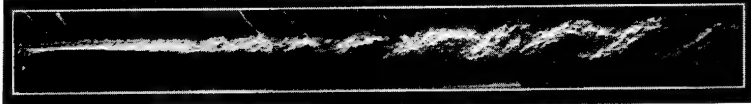


FIGURE 17. Composite schlieren image, $M_c = 0.42$ and $x = 0\text{--}45$ cm.

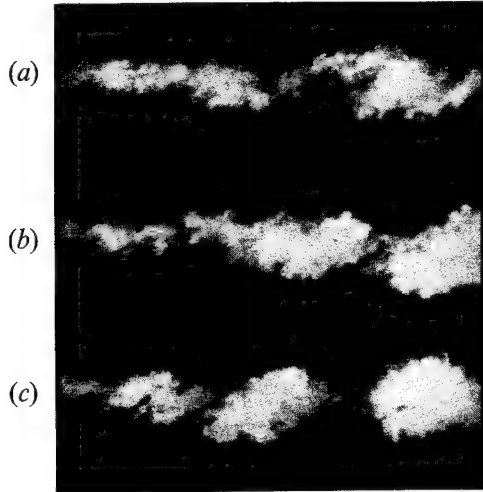


FIGURE 18. Side view product formation images, $M_c = 0.42$ and $x = 15\text{--}30$ cm.

As shown in figure 16(a), the point of view is from the high-speed side looking toward the low-speed side; thus the flow is from right to left with the low-speed side on top. The images in figure 16(b) show that the layer consists of relatively distinct vortex cores separated by the braid regions which often exhibit large gradients. In agreement with the profiles, the core concentrations are sloped in the streamwise direction but more uniform in the cross-stream direction.

4.2.2. $M_c = 0.42$

A composite schlieren image for the $M_c = 0.42$ case, extending from $x = 0$ to 45 cm, is shown in figure 17. As with the lower convective Mach number case, Brown-Roshko structures dominate the layer. For this case the local Reynolds number, $Re_{\delta vis} > 700000$ at the exit of the test section.

Side view product formation images are shown in figure 18 where the imaged region is $x = 15\text{--}30$ cm. The structures seen in figure 18 are similar to those for the $M_c = 0.28$ case, but are also subtly different. The main difference is that the structures appear less elliptical and typically have a more disorganized appearance. This is not believed to be a Reynolds number effect because the difference is apparent even at streamwise locations where the Reynolds numbers are equal (e.g. at $x = 45$ cm for $M_c = 0.28$ and at $x = 15$ cm for $M_c = 0.42$). Plan views through the middle of the layer ($y = 0$ cm) are shown in figure 19 and show that the structures remain quasi-two-dimensional. Nevertheless, they appear even more skewed than found for $M_c = 0.28$. The end views of figure 20, located at $x = 18.5$ cm and $z = -2.5\text{--}2.5$ cm, appear qualitatively similar to the $M_c = 0.28$ case where either thick cores or thin convoluted braids are observed. Again, the cores tend to exhibit a relatively uniform concentration.

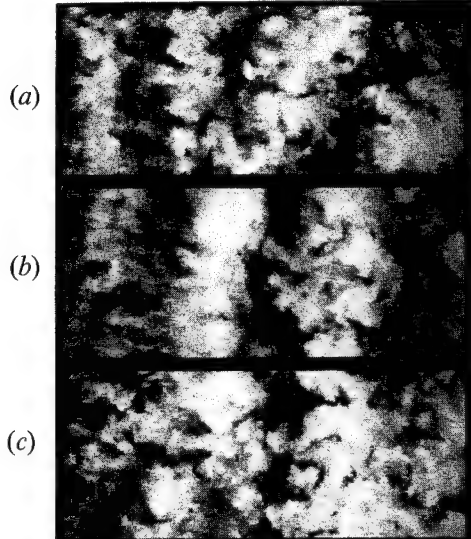


FIGURE 19. Plan view product formation images, $M_c = 0.42$, $x = 15\text{--}30 \text{ cm}$ and $y = 0 \text{ cm}$.



FIGURE 20. End view product formation images, $M_c = 0.42$, $x = 18.5 \text{ cm}$ and $z = -2.5\text{--}2.5 \text{ cm}$.

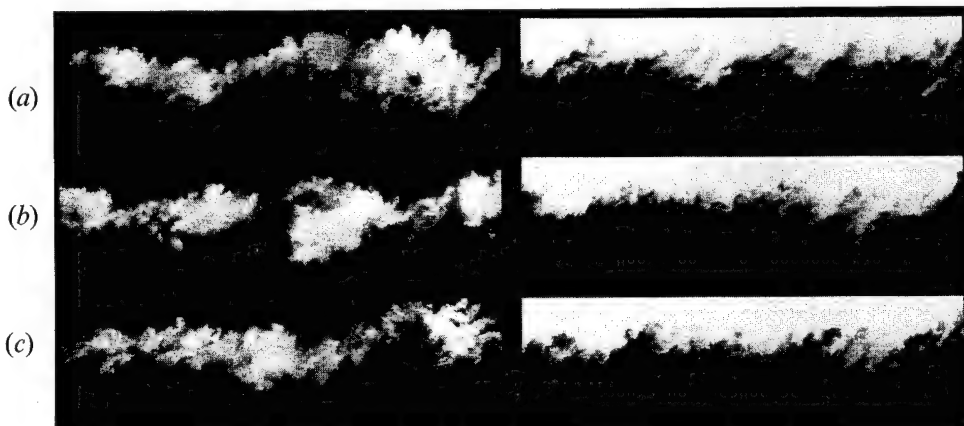


FIGURE 21. Side view images, $M_c = 0.50$ and $x = 15\text{--}30 \text{ cm}$. Product formation and passive scalar images are at the left and right, respectively.

4.2.3. $M_c = 0.50$

Product formation and passive scalar fog images at $M_c = 0.50$ are shown in figure 21. Only fog side views were obtained for this case, thus schlieren images and fog plan and end views are not shown. The imaged region is $x = 15\text{--}30 \text{ cm}$ and $Re_{\delta vis} = 700000$



FIGURE 22. Composite schlieren image, $M_c = 0.62$ and $x = 0\text{--}45$ cm.

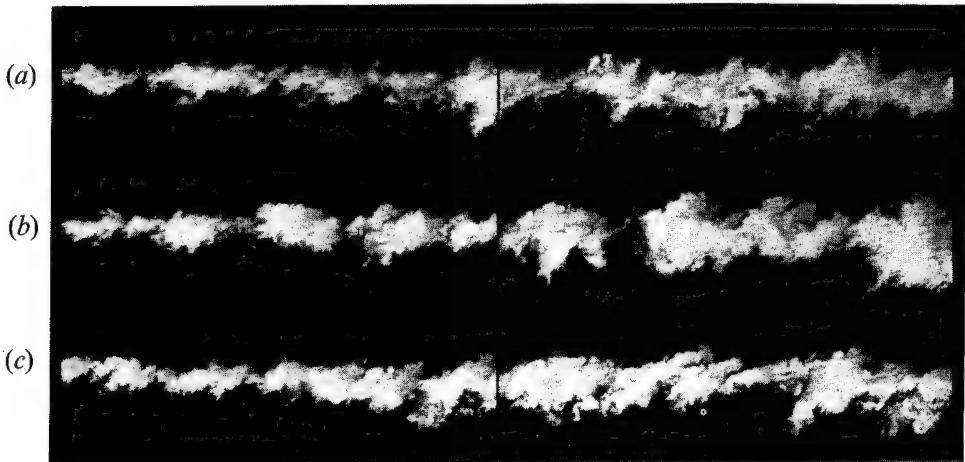


FIGURE 23. Product formation side views, $M_c = 0.62$ and $x = 15\text{--}45$ cm.

at $x = 30$ cm. This figure shows that rollers are also apparent at this convective Mach number, although we can generalize that the layer appears to be less organized than the lower convective Mach number cases. Although large-scale rollers are often present, as with the $M_c = 0.42$ case, they are not elliptical, but instead appear more irregular and are almost polygonal (e.g. b). This change in shape will be discussed further in §4.3.

4.2.4. $M_c = 0.62$

A composite schlieren image covering the entire test section for the $M_c = 0.62$ case is shown in figure 22. At this higher convective Mach number, the Brown–Roshko rollers are not readily identifiable, although large-scale structures are observed near the end of the test section. The structures appear as irregularly spaced bands that are oriented at a dominant angle of about 30° from the horizontal. Similar indistinct structures can be found in the schlieren photographs of Papamoschou & Roshko (1988) and Goebel & Dutton (1991).

Figure 23 shows product formation side view cuts where $x = 15\text{--}45$ cm, $z = 0$ cm and $Re_{\delta_{vis}} = 10^6$ and $x = 45$ cm. This figure shows that the layer is composed of large-scale structures, but they rarely appear as the coherent Brown–Roshko type. Although Brown–Roshko structures are rare, possible examples are seen in (b) (left). As shown by Clemens & Mungal (1992a), the structures of figure 23 appear more irregular, with the high- and low-speed side interfaces often appearing more jagged than at $M_c = 0.28$. The jagged interfaces may be due to an increase in the number of small-scale structures which cause sharp intrusions into the layer. Passive scalar side view images are shown in figure 24 and similarly show these irregular structures. Taken as a whole, figures 23 and 24 show that there is considerable variation in structure among the different realizations.

Figure 25 shows product formation plan view cuts through approximately the

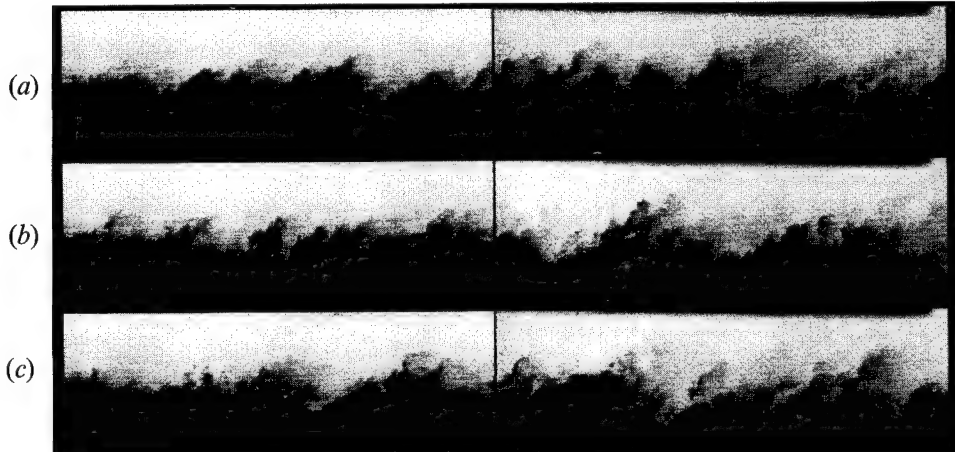


FIGURE 24. Passive scalar side views, $M_e = 0.62$ and $x = 15-45$ cm.

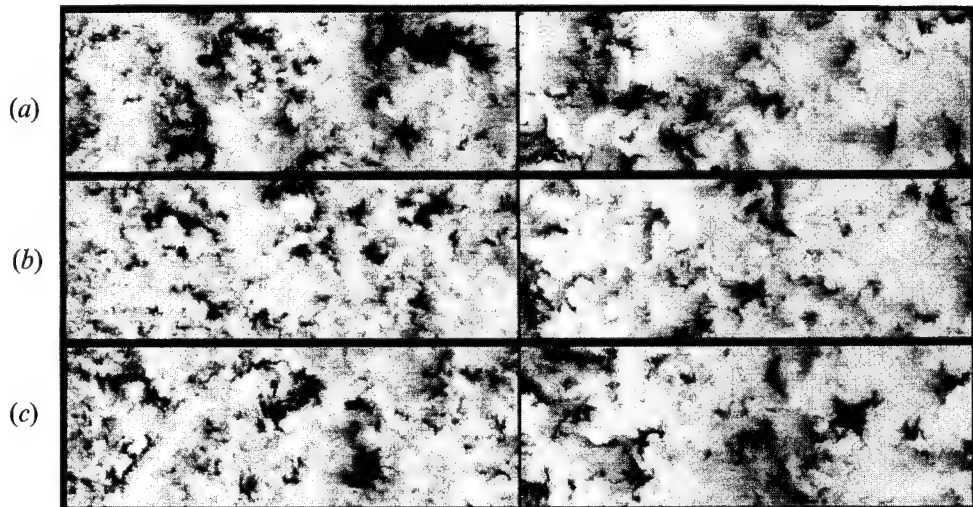


FIGURE 25. Product formation plan views through the middle of the layer, $M_e = 0.62$, $x = 15-45$ cm, $z = -2.5-2.5$ cm and $y = 0$ cm.

middle of the layer ($y = 0$ cm) where $x = 15-45$ cm and $z = -2.5-2.5$ cm. These plan view images show that the structures are not nearly as two-dimensional as at the lower convective Mach number. Sometimes skewed spanwise bands occur although they are not usually followed, nor preceded, by other spanwise bands (a, left). This is consistent with the side views where only occasional rollers are seen. In some of the images (a, left) oblique structures can be seen, but they do not appear to be a dominant feature of the flow. In general, these plan view cuts appear highly three-dimensional and apparently lack any obvious spatial regularity or organization.

Passive scalar plan views are shown in figure 26 where the imaged region and sheet location are the same as in figure 25. These images are consistent with the highly three-dimensional character seen with the product formation method. Since these passive scalar images will emphasize turbulent motions which bring pure non-seeded low-speed fluid into the layer, it is seen from randomly oriented dark patches that these motions are neither primarily spanwise nor streamwise.

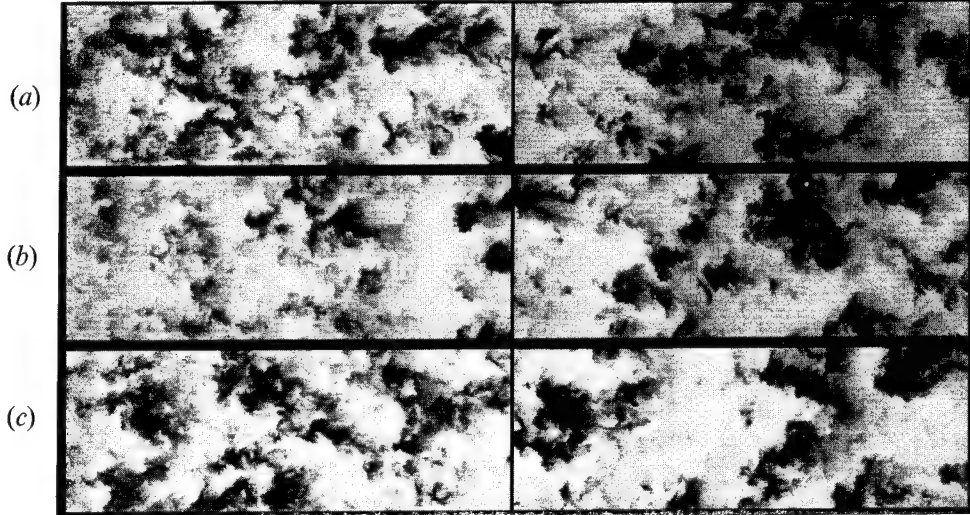


FIGURE 26. Passive scalar plan views through the middle of the layer, $M_e = 0.62$, $x = 15\text{--}45\text{ cm}$, $z = -2.5\text{--}2.5\text{ cm}$ and $y = 0\text{ cm}$.

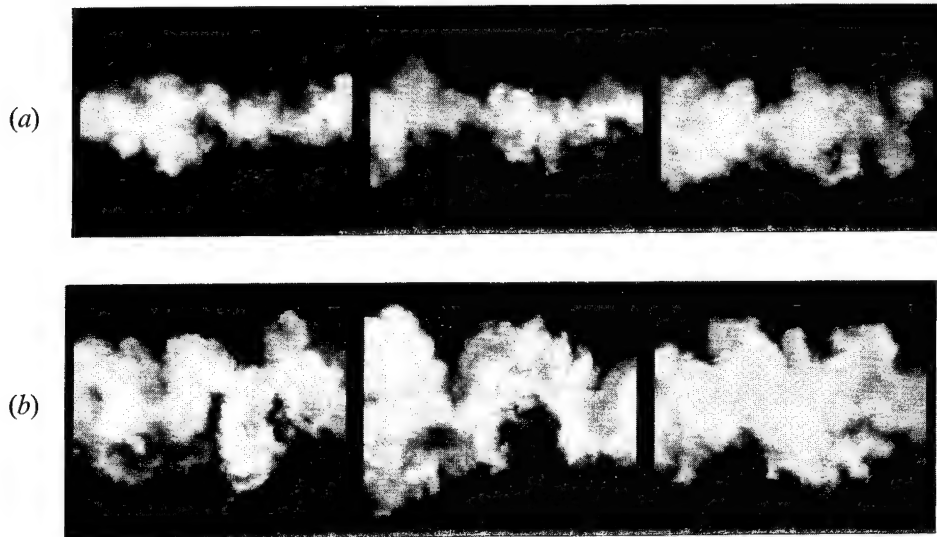


FIGURE 27. Product formation end views, $M_e = 0.62$ and $z = -2.5\text{--}2.5\text{ cm}$: (a) $x = 22\text{ cm}$, (b) $x = 36.5\text{ cm}$.

Figure 27 shows product formation end view cuts at the $x = 22$ and 36.5 cm locations, where the imaged region is $z = -2.5\text{--}2.5\text{ cm}$. While these images appear similar to the $M_e = 0.28$ case, there are some differences. The first difference is that the images cannot be easily characterized as cuts through the vortex core or braid regions as was possible at $M_e = 0.28$ and 0.42 . In contrast to the lowest convective Mach numbers most of the end views are highly convoluted suggesting that the layer is more dominated by streamwise vorticity. Also seen are what appear to be mushroom structures caused by counter-rotating vortices (left image of figure 27b). Another difference from the lower compressibility cases is that the structure signal levels are less uniform.

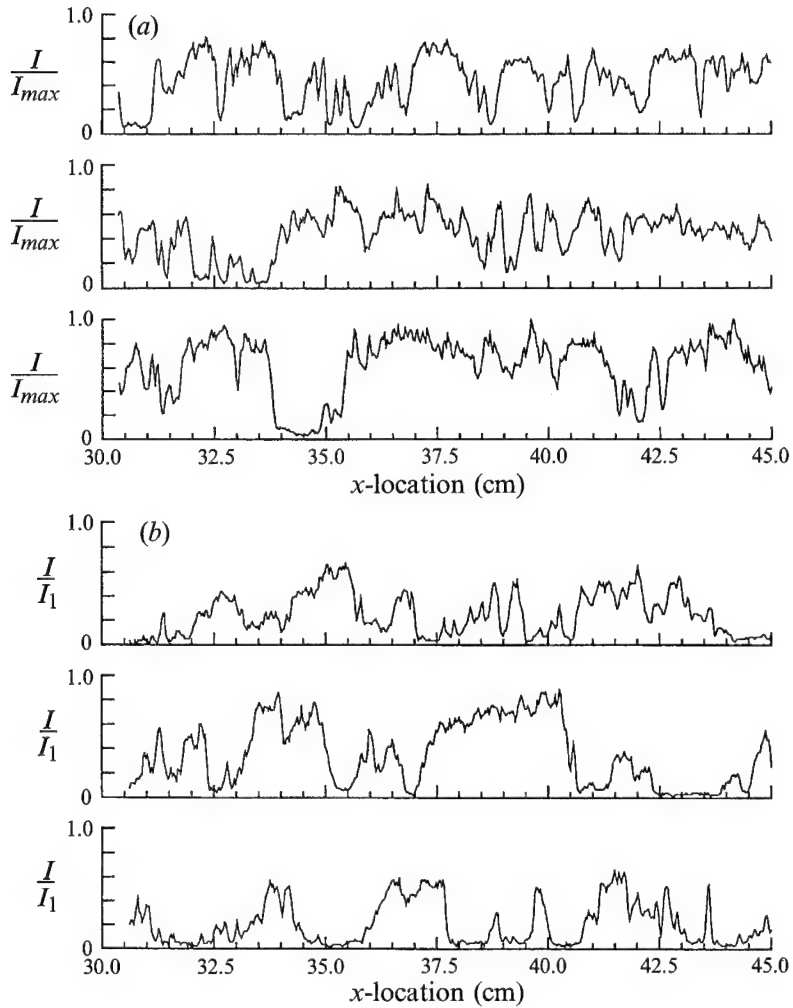


FIGURE 28. Streamwise signal intensity profiles through $M_e = 0.62$ side view images for (a) the product formation method and (b) the passive scalar method.

In order to see how these structural differences are reflected in the mixing, signal intensity profiles are shown in figure 28. These profiles show that although streamwise sloped signals are found, they are not as dominant as at $M_e = 0.28$. This provides evidence that the entrainment of fluid does not occur through predominantly spanwise motions, in agreement with the plan view visualizations. Sloped structures do sometimes appear, however, thus some spanwise motions are undoubtedly present. Cross-stream profiles are shown in figure 29 and show that the structures can be uniform in the cross-stream direction, but can also exhibit considerable variation. This is seen especially in the passive scalar profiles, where the signals appear both stepped and linearly sloped from the lowest to the highest signal levels.

Perspective views of selected product formation images for the $x = 30\text{--}45$ cm station are shown in figure 30. The orientation of the axes is as shown in figure 16(a), thus the flow moves from right to left with the low-speed fluid on top. The perspective views show the irregular nature of the structures, especially the jagged high- and low-speed interfaces discussed above. This figure also shows that the structures exhibit

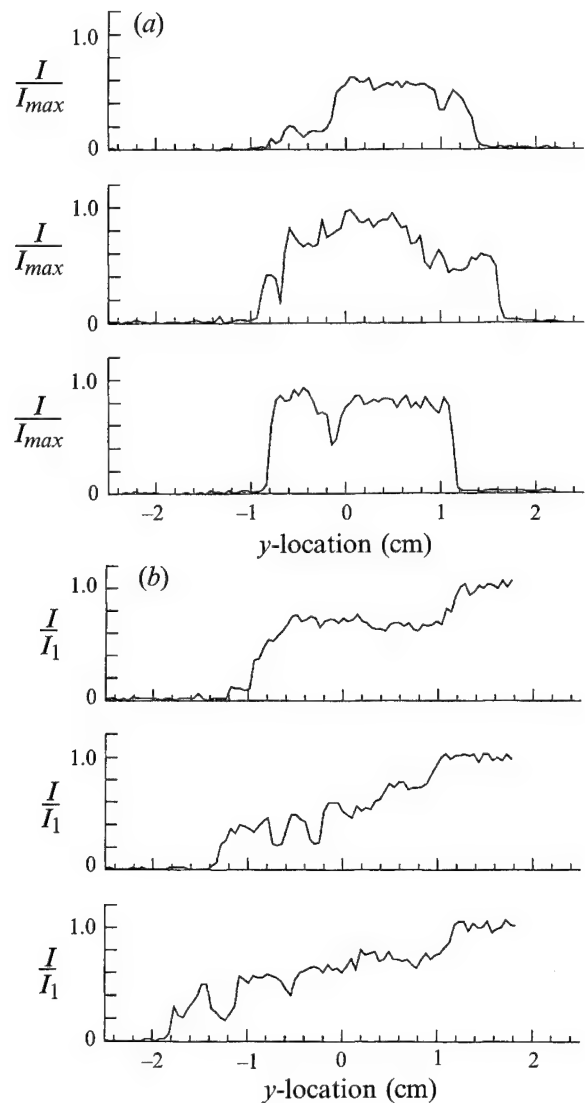


FIGURE 29. Cross-stream signal intensity profiles through $M_e = 0.62$ side view images for (a) the product formation method and (b) the passive scalar method.

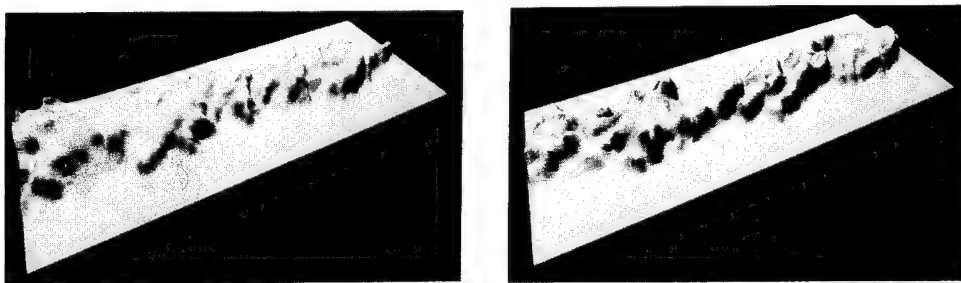


FIGURE 30. Perspective views of $M_e = 0.62$ product formation side view images, $x = 15-30$ cm.

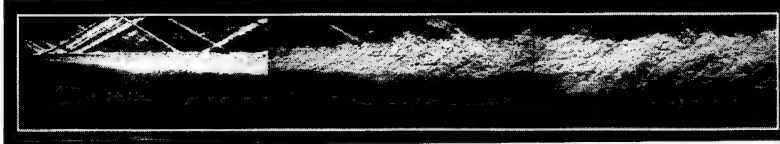


FIGURE 31. Composite schlieren image, $M_c = 0.79$ and $x = 0-45$ cm.

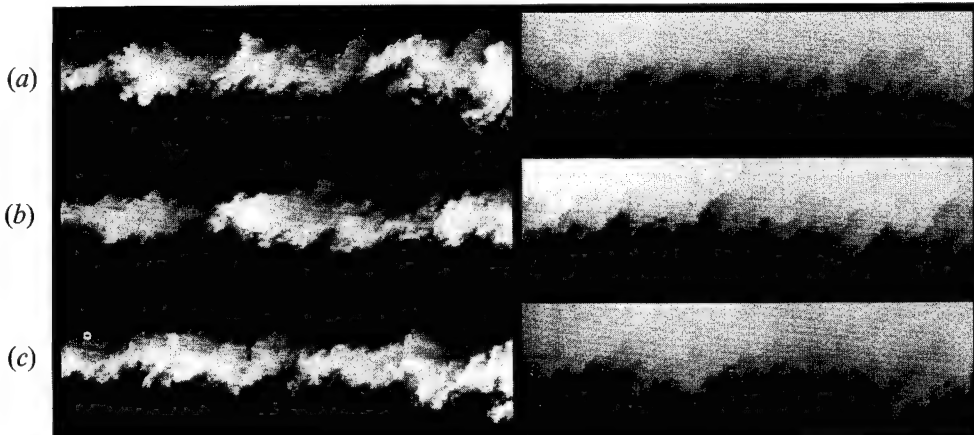


FIGURE 32. Side view images, $M_c = 0.79$ and $x = 18-33$ cm. Product formation and passive scalar images are at the left and right, respectively.

significantly more variation in the cross-stream direction than the $M_c = 0.28$ case. It is interesting that many of the structures appear to be aligned with a dominant angle in agreement with McIntyre & Settles (1991) and the schlieren images of figure 22.

4.2.5. $M_c = 0.79$

Figure 31 shows a side view schlieren composite image of the entire test section for the $M_c = 0.79$ case. As with the $M_c = 0.62$ case, the only evidence for large-scale structures is the inclined bands near the end of the test section.

Side view planar visualizations are shown in figure 32, where the product formation and passive scalar images are shown on the left and right, respectively, for $x = 18-33$ cm. This figure shows that the structure is similar to the $M_c = 0.62$ case, where rollers are rare and both high-and low-speed interfaces appear jagged.

Plan view cuts through the middle of the layer for $x = 18-33$ cm, $z = -2.5-2.5$ cm and $y = 0$ cm are shown in figure 33, where the product formation and passive scalar methods are shown on the left and right, respectively. The product formation images (left) show the highly three-dimensional structure that is characteristic of the $M_c = 0.62$ case, with no obvious spanwise, streamwise or oblique organization. The passive scalar images (right) are also three-dimensional, but additionally show some evidence of streamwise structure.

End views using the product formation method are shown in figure 34, where $x = 18$ and 32 cm. Again the layer is seen to be highly convoluted suggesting that streamwise (or oblique) motions are present. Similar streamwise motions were observed in the axisymmetric mixing layer measurements of Fourguette *et al.* (1990). Also of note in these end views is that some of the images appear to be composed of two distinct regions of mixed fluid. This is seen in figure 34(b), where distinct low- and high-signal regions appear on the top and bottom of the layer, respectively. These

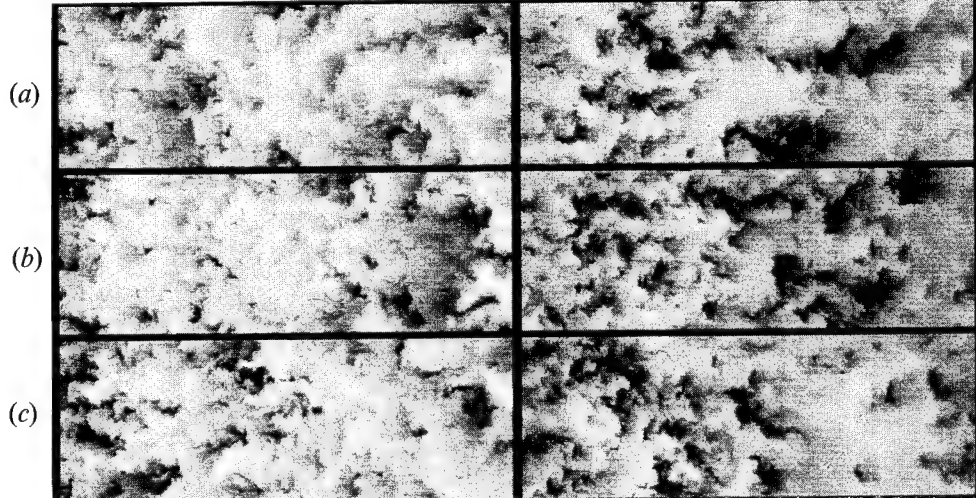


FIGURE 33. Plan view images through the middle of the layer, $M_e = 0.79$, $x = 18\text{--}33\text{ cm}$, $z = -2.5\text{--}2.5\text{ cm}$ and $y = 0\text{ cm}$. Product formation and passive scalar images are at left and right, respectively.

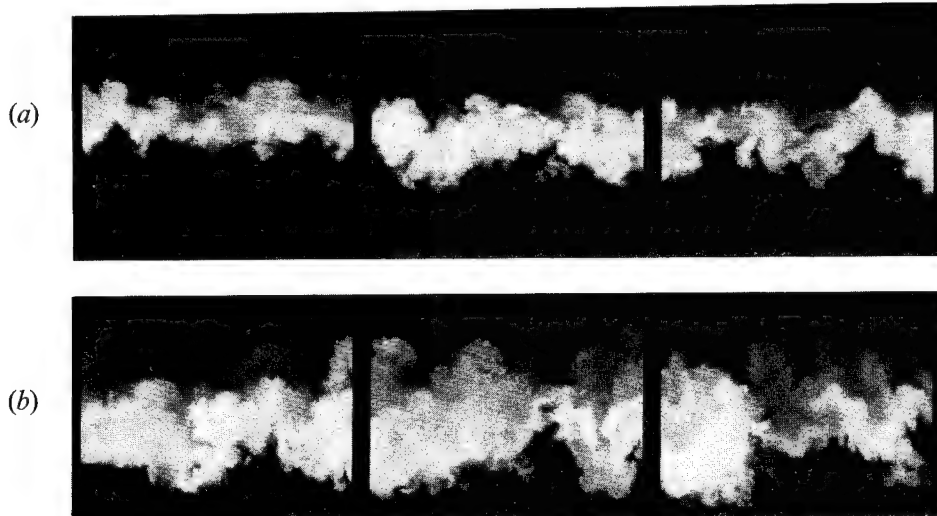


FIGURE 34. Product formation end views, $M_e = 0.79$ and $z = -2.5\text{--}2.5\text{ cm}$:
(a) $x = 18\text{ cm}$, (b) $x = 32\text{ cm}$.

images should be contrasted with the more uniform end view structures of figure 13(b). This double-level characteristic is sometimes apparent in the side view images of figure 32, where regions of low signal are present along the high-speed side interface (b, left).

Streamwise signal intensity profiles are shown in figure 35 where the signals are sometimes sloped, but not predominantly so. Cross-stream profiles through select structures are shown in figure 36 and reveal a subtle difference from the profiles of the $M_e = 0.28$ case. The primary difference is that the structure scattering signals are not uniform but are biased toward the side to which they are closest. This is seen in the product formation profiles as the negative slopes and less clearly in the passive scalar profiles as the positive slopes. Some of these profiles also appear to be composed of two regions of relatively uniform fluid, as seen in the third product formation profile and

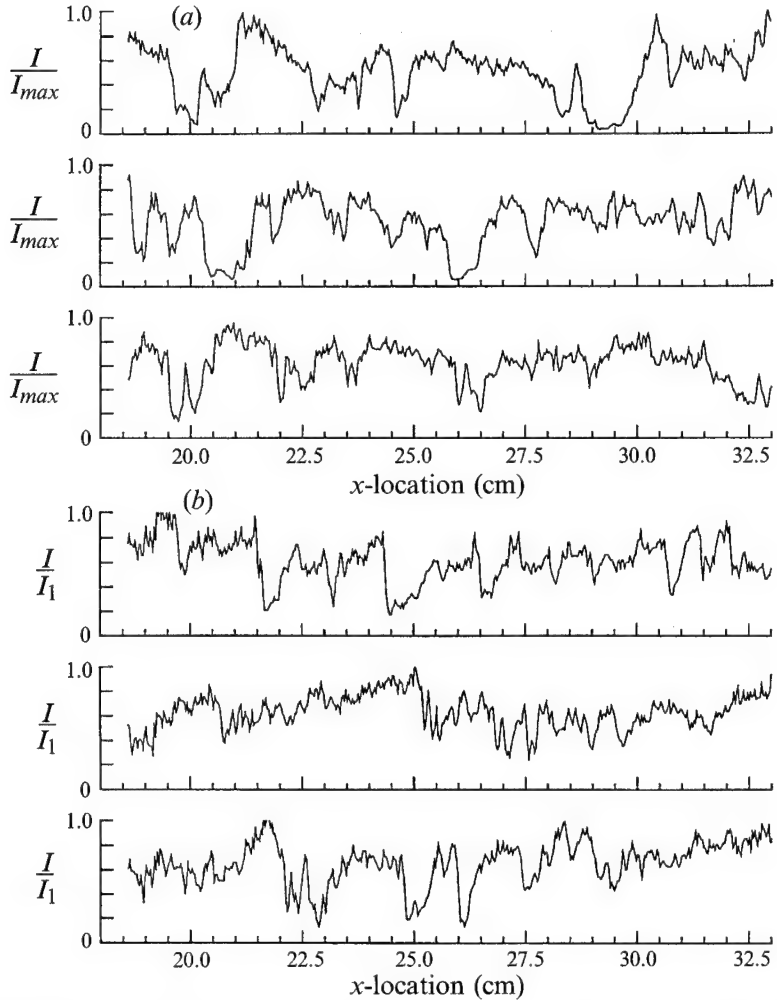


FIGURE 35. Streamwise signal intensity profiles through $M_c = 0.79$ side view images for (a) the product formation method and (b) the passive scalar method.

the second passive scalar profile. These separate regions of mixing are easier to see in the side views of figure 32 (b, left), and in the end view of figure 34(b), where light and dark regions are observed on the low- and high-speed sides, respectively.

Some of these features are further seen in the perspective views of select product formation side views shown in figure 37, where the axes are defined as in figure 16(a). Many of the structures are irregular, with jagged high- and low-speed side interfaces.

4.3. Discussion of the PLMS results

It has been shown that the mixing layer makes a clear transition from quasi-two-dimensionality at low convective Mach number, to three-dimensionality at moderate convective Mach number. Perhaps related to this transition is what appears to be a change in the nature of the spanwise rollers with increasing convective Mach number. This is shown in figure 38(a) where several (presumed) rollers are shown at convective Mach numbers of 0.28, 0.42, 0.50 and 0.62 using the PLMS product formation technique. At $M_c = 0.28$, the roller cores appear relatively ‘round’ or ‘elliptical’, but become progressively more ‘square’ or ‘polygonal’ at higher M_c . This change is shown

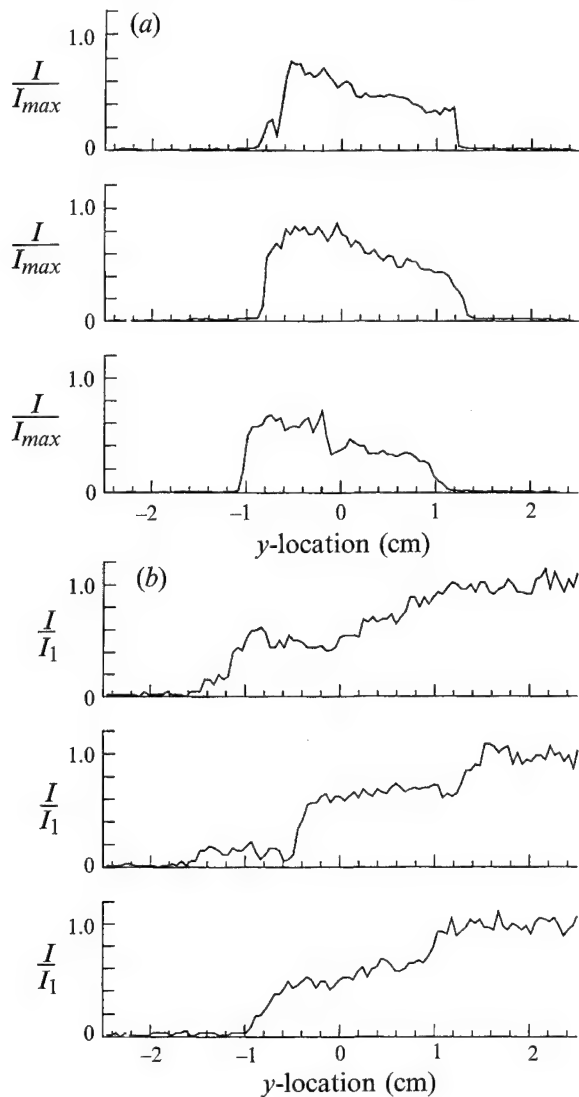


FIGURE 36. Cross-stream signal intensity profiles through $M_e = 0.79$ side view images for (a) the product formation method and (b) the passive scalar method.

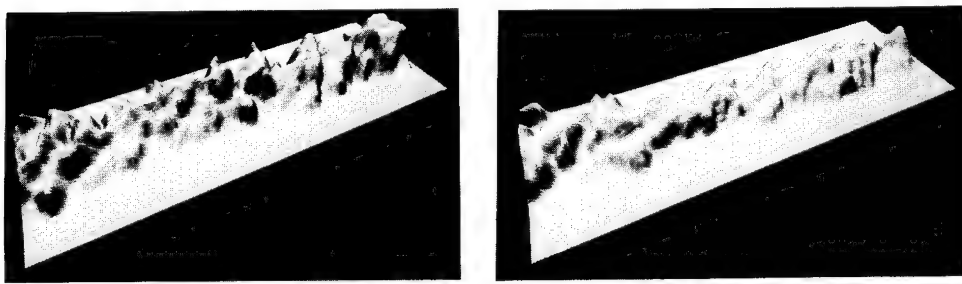


FIGURE 37. Perspective views of $M_e = 0.79$ product formation side view images ($x = 18-33$ cm).

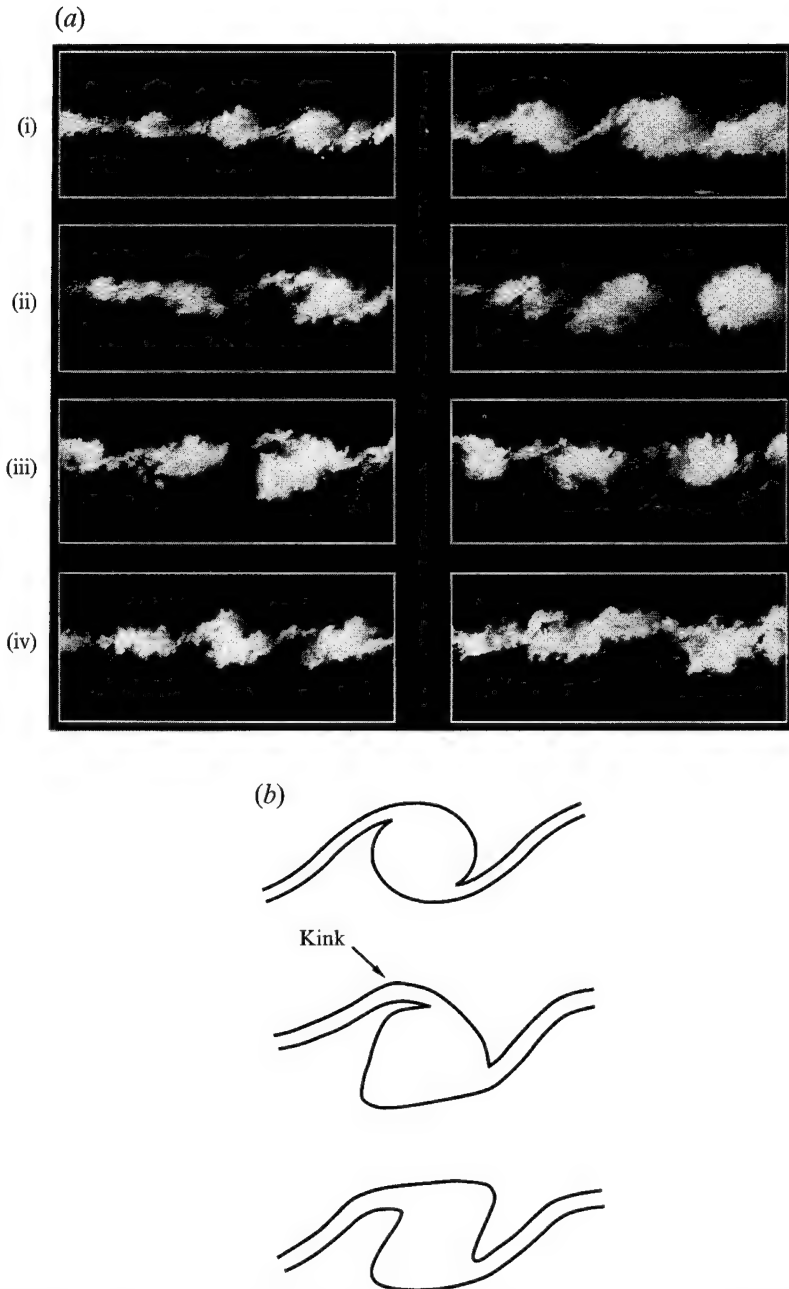


FIGURE 38. (a) Select images comparing roller structure at different convective Mach numbers: (i) $M_c = 0.28$, (ii) $M_c = 0.42$, (iii) $M_c = 0.50$, (iv) $M_c = 0.62$. (b) Schematic diagram showing roller structure: (top) low compressibility (middle, bottom) higher compressibility structures that exhibit polygonal appearance and a kink in the braid region.

schematically in figure 38(b). In addition to the change in the shape of the structure cores, the braid regions develop a 'kink' which is particularly noticeable at $M_c = 0.5$ and 0.62, but is not observed at $M_c = 0.28$. The reason for this change in the rollers is not known, and does not appear to have been predicted by linear stability theory or direct numerical simulations.

The changes from two- to three-dimensionality are in general agreement with the imaging results of Messersmith *et al.* (1991) and Elliott *et al.* (1993), where a decrease in organization of the layer was found with increasing convective Mach number. The present results also show general agreement with the static pressure space-time correlation results of Samimy *et al.* (1992) where the higher convective Mach number case was characterized by smaller spanwise correlation lengths. Furthermore, the $M_c = 0.7$ visualizations of Fourguette *et al.* (1990), who used the condensation of water vapour in the product formation mode, also exhibit strong similarities with the side view images of the $M_c = 0.62$ case.

This trend of increasing three-dimensionality was predicted using linear stability theory, and in the numerical simulations of Sandham & Reynolds (1991). The hairpin-type vortical structures found by Sandham & Reynolds, however, are not readily apparent from the present visualizations. The reason for this may be: (i) that the structures do not exist in real flows, (ii) that we are not visualizing them with the proper technique, or (iii) that the structures exist but so do many other modes which render any individual mode indistinguishable. It is not known which of the above explanations is correct but the simulations of Chen (1991) show that while the vortical structures are organized, the passive scalar field can appear disorganized. This is because the passive scalar field is affected by both recent and past vortical motions. The third reason also has merit however, as linear stability theory predicts that at the highest convective Mach numbers of this study, many oblique waves, of differing angles, are approximately equally amplified. Given that supersonic wind tunnels experience significant acoustic perturbations, this may result in a complex set of interacting instability modes. We should note that there is some disagreement on this issue since both the studies of Samimy *et al.* (1992) and Elliott *et al.* (1993) report evidence of structures that are similar to those simulated by Sandham & Reynolds (1991).

It should be emphasized that we do not believe that the observed changes from two- to three-dimensionality result from a Reynolds number effect. One reason for this is that since the Reynolds number varies by a factor of three from $x = 15$ to 45 cm, Reynolds number effects would appear as a change in structure from the beginning to the end of the test section. This is not observed in any of the visualizations, however, since the character of the layer appears the same in all regions of the flow at a given Mach number. Furthermore, the Reynolds numbers are nearly the same for the $M_c = 0.28$ case at $x = 45$ cm and the $M_c = 0.62$ case at $x = 15$ cm, but the turbulent structure at those locations is completely different.

In addition to the observed transition from two- to three-dimensionality, several generalizations can be made regarding mixing and entrainment in the compressible layer. It was previously mentioned that at $M_c = 0.28$ the structure core concentration is streamwise sloped and cross-stream uniform, which is consistent with a layer that is dominated by two-dimensional rollers. At $M_c = 0.62$ and 0.79 , however, streamwise profiles suggest that the structures are less often streamwise sloped, and the cross-stream profiles indicate that the structures are less uniform in the cross-stream direction than the lower convective Mach number cases. In particular it was noted that many of the structures exhibited profiles which were cross-stream sloped and even two-levelled, suggesting that the mixing occurs in steps across the layer. The perspective views show, however, that there are particular structures where a profile would appear to be two-levelled, but this is due to the overlap of two closely spaced structures. These closely spaced structures are possibly streamwise (or oblique) vortices, that are inclined from the x -axis. If this is so, then in the regions where the vortices are overlapping, the entrainment would occur in steps, with each vortex preferentially entraining fluid from

the side to which it is closest. The end views of figures 27 and 34 provide some evidence for this, because they can appear both highly convoluted, and seem to contain two separate regions of mixed fluid (these characteristics are particularly apparent at $M_c = 0.79$, for example, figure 34*b* (right)). Although speculative, this view is in general agreement with the direct numerical simulations of Sandham & Reynolds (1991) and Chen (1991), where in some regions two streamwise vortices of opposite sign are located such that one resides on top of the other.

Observation of the full ensemble of images suggests that the cross-stream sloped structures are a more dominant feature of the compressible layer than are the overlapping structures. It is also apparent that the cross-stream slopes are consistent with the observation that the original side view images (such as figure 32) appear to have a ‘fuzzy’ (small gradient) top interface, and a ‘sharp’ (large gradient) bottom interface. Although not as apparent as at $M_c = 0.79$, this same characteristic is also found at $M_c = 0.62$, but not at $M_c = 0.28$ where both the top and bottom sides exhibit a sharp interface. The fuzzy high-speed side interface is consistent with the hot-wire measurements of Bonnet *et al.* (1993) who found that the mass flux fluctuations on the high-speed side of the layer were lower than at the low-speed side interface. It is also of note that the suppression of the fluctuations on the high-speed interface might be a direct result of the eddy convection velocity which is biased towards the velocity of the high-speed stream (Papamoschou 1991; Fourguette *et al.* 1990; McIntyre & Settles 1991; Hall *et al.* 1991*a*). Such a velocity bias results in structures which feel less shear on the high-speed interface, with a resulting decrease in the fluctuations on the high-speed side.

5. Experimental results: PLIF

This section presents PLIF visualizations and statistical results extracted from the images. A detailed discussion of the results follows in §6.

5.1. PLIF imaging: $M_c = 0.28$

Two single-shot corrected and smoothed images for the $M_c = 0.28$ case are shown in figure 39. The images have been corrected for laser sheet non-uniformity and laser beam absorption, and were low pass filtered to improve the SNR (see §5.3.1). The NO was seeded into the low-speed stream, the flow is from left to right and $x = 28\text{--}33$ cm. It should be emphasized that these images are quantitative representations of the instantaneous mixture fraction field. The images reveal a similar structure to that found using the PLMS methods, where large rollers dominate the flow field. As with the PLMS, however, not all of the images appear as rollers. Of particular note in these images are the ‘tongues’ of pure high- or low-speed fluid which sometimes penetrate well into the layer.

In figure 40, perspective views of the side view images are shown. The orientation of the axes is the same as in figure 16(*a*), where the point of view is from the high-speed side looking towards the low-speed side. The flow is therefore from right to left and the low-speed side, whose signal intensities have been mapped into height, is at the top. In this figure, the slopes discussed previously are shown very dramatically to extend from the lowest to the highest signal levels. Furthermore, the large gradients of the braid regions between the structures are rendered as very steep cliffs. The slopes are further seen to be fairly uniform in the cross-stream direction as was also found with the PLMS signals. As shown in figure 40(*a*), this cross-stream uniformity results in the mixed fluid being separated from each free stream by a relatively steep gradient.

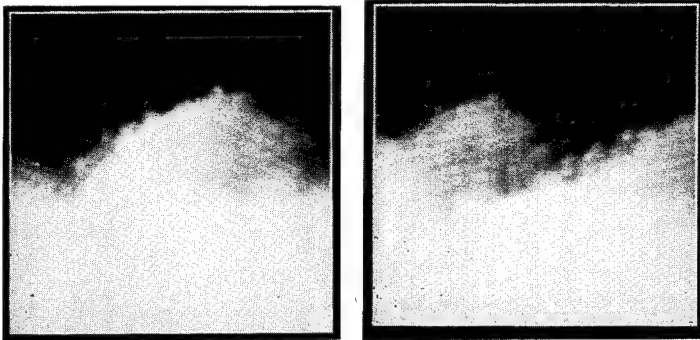


FIGURE 39. Side view PLIF images, $M_c = 0.28$, $x = 28\text{--}33$ cm and $z = 0$ cm. The flow direction is from left to right.

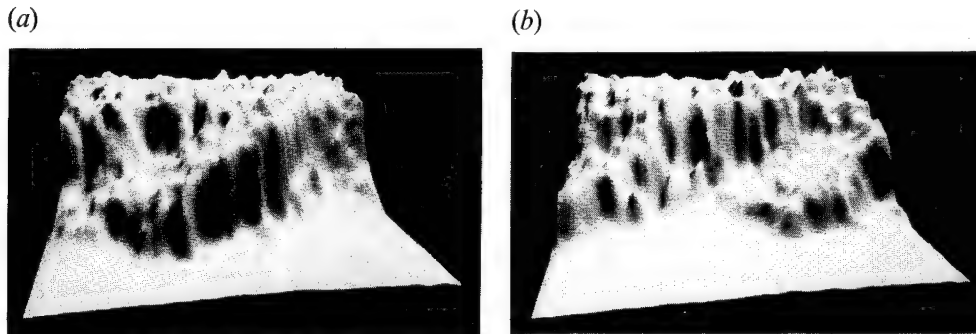


FIGURE 40. Perspective views of the side view PLIF images at $M_c = 0.28$.

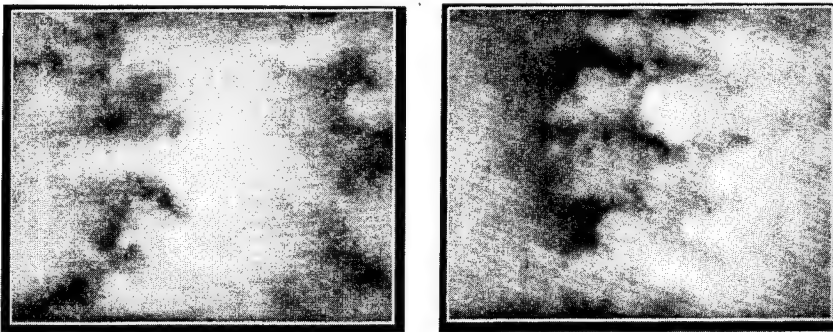


FIGURE 41. Plan view PLIF images, $M_c = 0.28$, $x = 28\text{--}33$ cm, $z = -2.5\text{--}2.5$ cm and $y = 0$ cm. The flow is from left to right.

Figure 40 also shows that the structure cores exhibit a large variation in mixture fraction. Figure 40(b) also shows that the slopes are not restricted to the streamwise direction only, as the core is both streamwise and cross-stream sloped.

In addition to side views, plan view images were taken at $M_c = 0.28$. These images cover the region from $x = 28\text{--}33$ cm (about 1/3 that of the PLMS methods) with a width of 5 cm. The width of the image is the same as with the PLMS methods and the sheet was located at $y = 0$ cm. Two independent images are shown in figure 41 which show the spanwise bands connected by streamwise braid structures as found with the passive scalar PLMS images of figure 12. A comparison of figures 41 and 12 shows that the streamwise structures appear to be oriented in opposite directions, resulting from

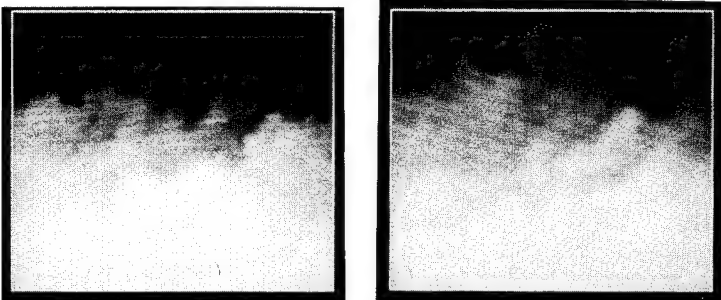


FIGURE 42. Side view PLIF images, $M_c = 0.62$, $x = 26\text{--}31$ cm and $z = 0$ cm.

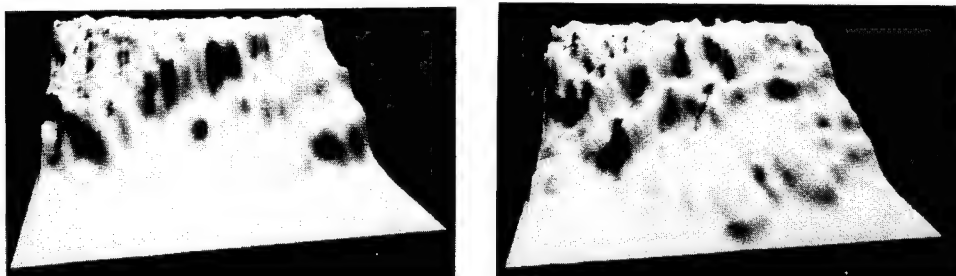


FIGURE 43. Perspective views of the side view PLIF images at $M_c = 0.62$.

the seeding of opposite free streams in the two cases. In general, it is seen that these quantitative PLIF images provide clear confirmation of the trends observed using the PLMS technique.

5.2. PLIF imaging: $M_c = 0.62$

In figure 42, two single-shot corrected and smoothed images for the $M_c = 0.62$ case are shown. The field of view is also 5 cm and extends from $x = 26$ to 31 cm, and the same amount of smoothing was performed on these images as with the $M_c = 0.28$ case. The SNR for this case was about 40 % higher than at $M_c = 0.28$, owing to the higher seeding levels used. These images reveal a structure which appears quite different from the lower convective Mach number case. For example, although large-scale structures are still present (as was seen with the PLMS images), they do not appear as roller-like. This is evidenced by the absence of large tongues of pure fluid penetrating deep into the layer.

Perspective views of these images are shown in figure 43. The viewing direction is the same as for figure 40, where the point of view is on the high-speed side looking towards the low-speed side. These perspective views provide a much clearer picture of the mixture fraction field than the images of figure 42, and reveal clear differences from the lower Mach number case. In agreement with the fog images, this case is dominated by structures that have mixture fraction fields which are sloped in the cross-stream rather than streamwise direction.

As was suggested by the profiles through the fog side views, the images of figure 43 show the two-levels of mixed fluid which are separated from each other by relatively steep gradients. In the first image, these two regions exist as parallel streamwise sloped structures, which are much thinner than the sloped structures at the lower convective Mach number. For the other image, the two regions are not as sloped but are separated by an even steeper gradient. This image also shows that most of the mixed fluid of this structure exists in the large diffuse region which is dominated by high-speed fluid. As

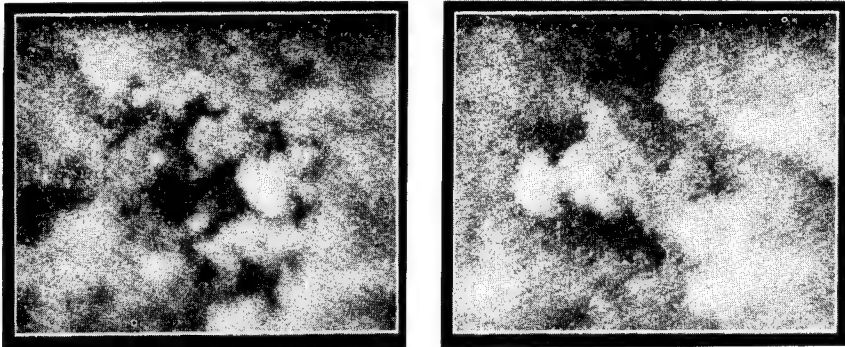


FIGURE 44. Plan view PLIF images, $M_c = 0.62$, $x = 26\text{--}31 \text{ cm}$, $z = -2.5\text{--}2.5 \text{ cm}$ and $y = 0 \text{ cm}$.

was discussed previously, the two-levelled structures appear to be caused by slanted and overlapping structures which may entrain fluid preferentially from the free stream to which they are closest. Furthermore, the large diffuse regions that are dominated by high-speed fluid are consistent with the fog visualizations that indicated a ‘fuzzy’ (i.e. weak gradient) high-speed interface.

Plan views for the $M_c = 0.62$ case are shown in figure 44, where $x = 26\text{--}31 \text{ cm}$, $z = -2.5\text{--}2.5 \text{ cm}$, $y = 0 \text{ cm}$, and the flow is from left to right. These images reveal the same highly three-dimensional structure observed in the PLMS plan views.

5.3. PLIF statistical results

5.3.1. Defining equations

Various statistical quantities for both convective Mach number cases were computed using the full sets of 120 images. The statistics were computed by treating each row of an image as a record of time series data. To take advantage of the higher SNR near the centre of the images (near the peak of the sheet profile) only about 40% (about 2 cm) of the image area was used. At this location, the layer grows by less than 5% over the width of the processing region, which was considered small enough so as not to influence the results when treating the data as a time series. The total amount of data considered corresponded to the passage of about 80 large-scale structures and about 24000 data points per y -location, and is consistent with previous studies where approximately 100 structures were averaged (Mungal & Dimotakis 1984; Koochesfahani & Dimotakis 1986). The images were low pass filtered to approximately double the SNR to a value of about 20. The filtering resulted in a significant loss in resolution, such that $L/\lambda_B = 500\text{--}800$. This is worse than all of the measurements of table 1, except that of Koochesfahani & Dimotakis (1986). We caution that although the signal grey scales are interpreted here as ‘mixed’ fluid, the actual extent of molecular mixing cannot be determined at the sub-resolution scale. For the relative resolution of the present measurements, the true amount of mixed fluid may be overestimated by as much as a factor of two (Koochesfahani & Dimotakis 1986).

For the statistical computations, the intensity data were converted to high-speed fluid mixture fraction using equation (3). The mixture fraction, ξ , is defined such that pure high-speed fluid is unity and pure low-speed fluid is zero.

The normalized cross-stream direction, η , is designated

$$\eta = (y - y_{0.5})/\delta_1, \quad (5)$$

where $y_{0.5}$ is the cross-stream location where the mean mixture fraction equals 0.5, and δ_1 is the thickness corresponding to the 1% and 99% mean mixture fraction points.

The statistical quantities presented below are profiles of the mean mixture fraction and the root-mean-square (RMS) fluctuations, which are calculated from the PDFs of mixture fraction. The PDF of mixture fraction, $P(\xi, \eta)$, at a given η -location, is calculated for each row of an image by compiling a histogram of the range of mixture fractions. Each PDF is normalized such that

$$\int_{-\infty}^{\infty} P(\xi, \eta) d\xi = 1. \quad (6)$$

The integration is between plus and minus infinity rather than zero and unity because noise creates a distribution of values around the pure state. The mean mixture fraction, $\bar{\xi}$, and RMS fluctuations, $(\bar{\xi}'^2)^{1/2}$ are calculated from the relations for the mean and the variance:

$$\bar{\xi} = \int_{-\infty}^{\infty} \xi P(\xi, \eta) d\xi, \quad (7)$$

$$\bar{\xi}'^2 = \int_{-\infty}^{\infty} (\xi - \bar{\xi})^2 P(\xi, \eta) d\xi. \quad (8)$$

5.3.2. $M_c = 0.28$

Figure 45(a) shows the mean and RMS fluctuation profiles of mixture fraction for the $M_c = 0.28$ case. The mean profiles are largely insensitive to resolution (Koochesfahani & Dimotakis 1986) and also to SNR as long as the statistics have converged. Figure 45(a) shows that the mean profile exhibits a single inflection point, in agreement with the results of Batt (1977) and Sunyach & Mathieu (1969). Several investigators, however, have measured mean profiles with a characteristic ‘S’ shape or triple inflection point (table 1), as will be discussed further in §6.

The RMS fluctuations do not go to zero at either free stream owing to the shot noise of the measurement. Since shot noise is proportional to the square root of the signal, the noise is highest in the low-speed free stream. If this noise offset were removed, the profile would appear more top-hat shaped in agreement with the results Fiedler (1974), Batt (1977), and Konrad (1977), where either double-peaked or top-hat profiles were measured. Furthermore, the peak fluctuations are about 17% (about 2% of which is noise) whereas Konrad (1977), Fiedler (1974) and Batt (1977) found fluctuations levels of 40%, 30% and 20%, respectively.

The PDFs of mixture fraction are shown in figure 45(b), and show that the most probable mixture fraction marches across the layer. This marching behaviour is in agreement with the incompressible results of Batt (1977) and Karasso & Mungal (1992) and the supersonic mixing layer measurements of Dutton *et al.* (1990) and Clemens & Paul (1993). The marching PDFs do not agree, however, with the results of Konrad (1977) and Koochesfahani & Dimotakis (1986) and the pre-mixing transition measurements of Masutani & Bowman (1986). Mungal & Dimotakis (1984) suggest that marching PDFs, such as that of Batt (1977), are an artifact resulting from insufficient resolution. It is seen in table 1, however, that there does not appear to be an obvious relationship between relative resolution and the shape of the PDFs. In fact, both the best and worst resolution experiments exhibit non-marching PDFs.

5.3.3. $M_c = 0.62$

Figure 46(a) shows the mean and RMS fluctuation profiles for the $M_c = 0.62$ case. As was found at $M_c = 0.28$, the mean profile exhibits a single inflection point. The RMS fluctuations profile exhibits a shape similar to that at $M_c = 0.28$, but only attains a maximum value of 13% (about 2% of which is noise).

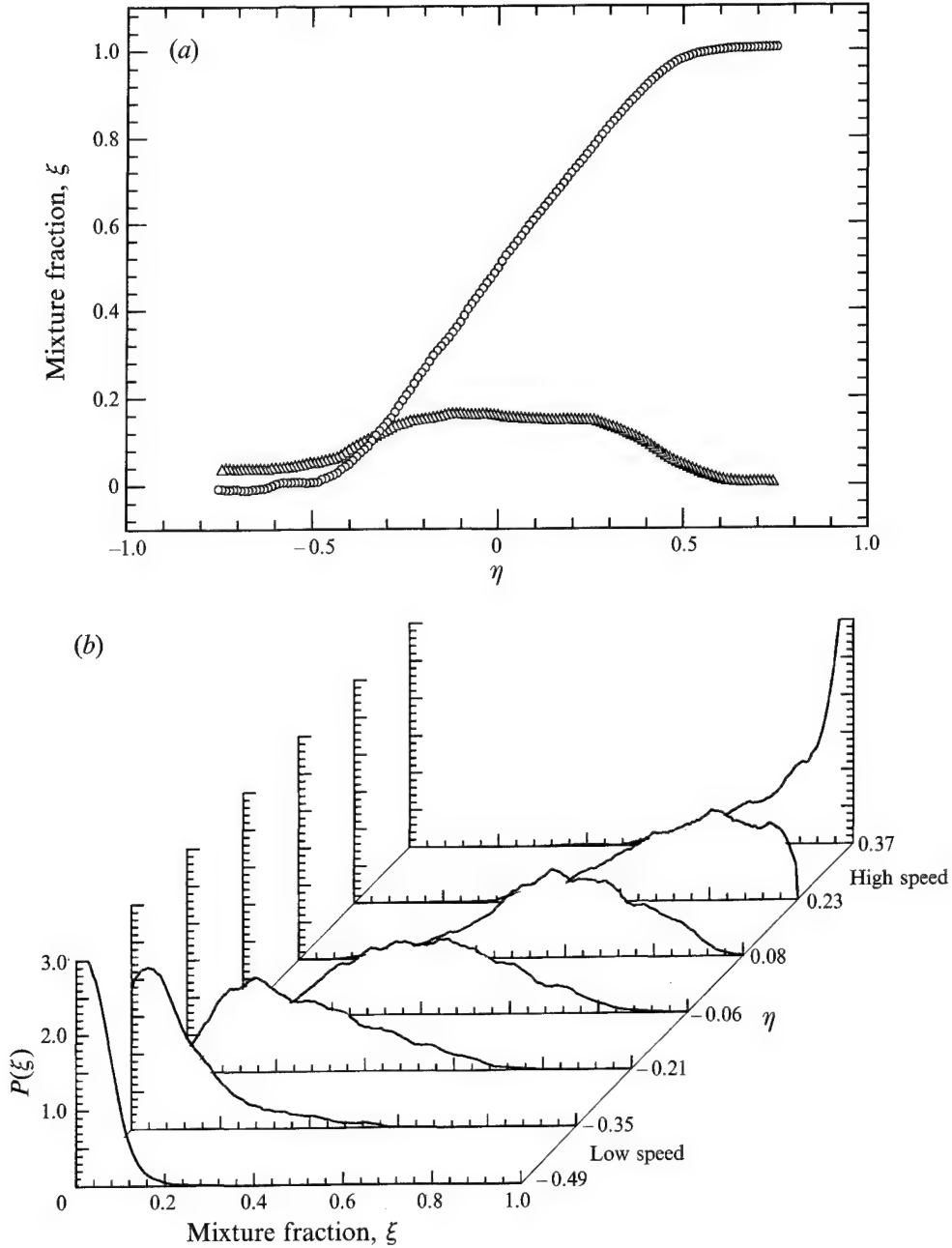


FIGURE 45. Mixture fraction statistics for $M_c = 0.28$: (a) mean (\circ) and RMS (\triangle) fluctuations, (b) PDFs for several cross-stream locations.

Figure 46(b) shows that the PDFs of mixture fraction also exhibit marching behaviour. Compared to figure 45(b), however, the PDF at each location has a higher peak and a smaller width, suggesting that for the $M_c = 0.62$ case a smaller range of mixture fractions are present at a given location. Several of the PDFs in figure 46(b) also appear to be flat topped (or even double-humped), which may be related to the multi-levelled structures of figure 43.

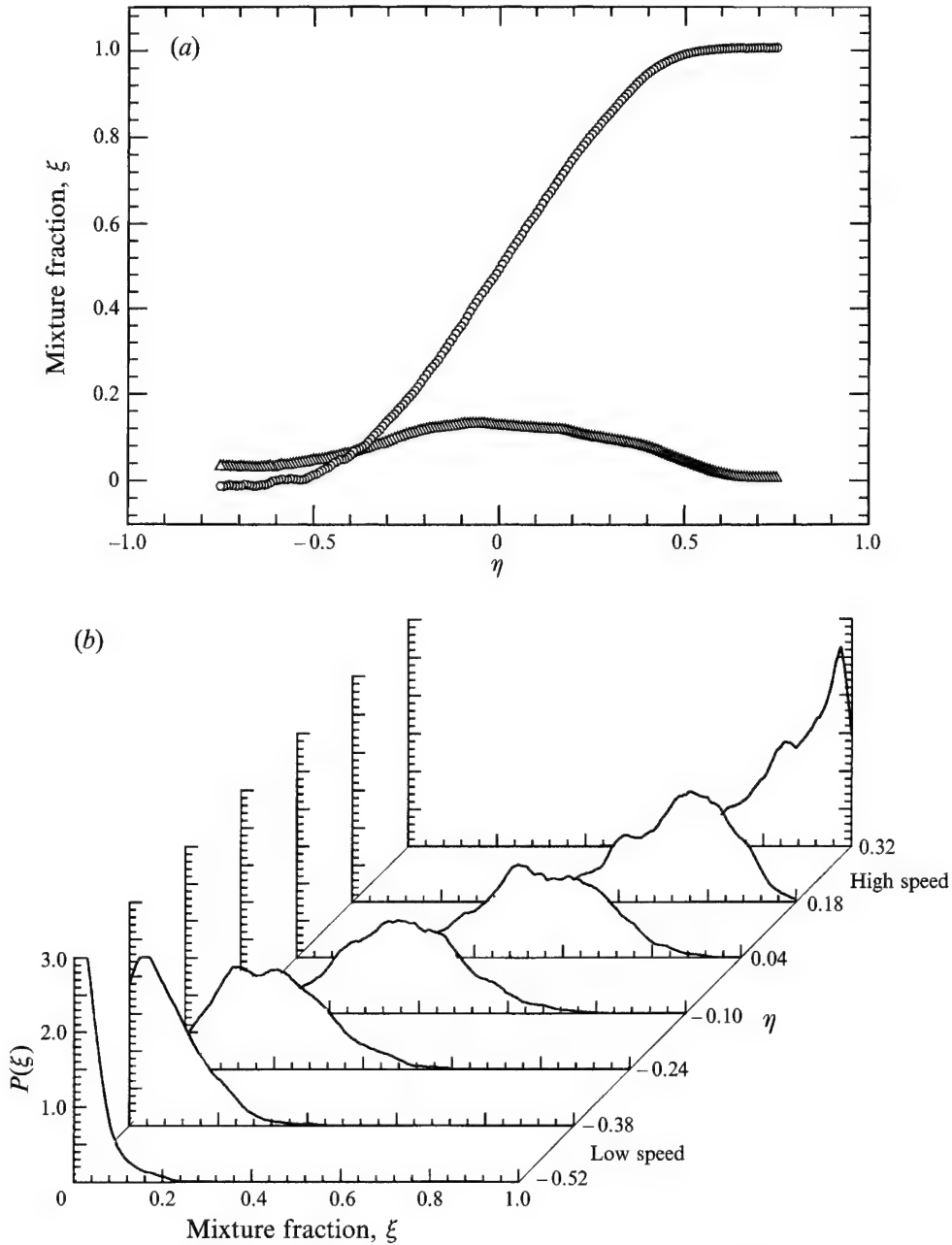


FIGURE 46. Mixture fraction statistics for $M_c = 0.62$: (a) mean (\circ) and RMS (\triangle) fluctuations, (b) PDFs for several cross-stream locations.

6. Discussion

In figure 47(a), the mean profiles at $M_c = 0.28$ and 0.62 are shown plotted together. The profiles are now seen to be nearly identical. This is not surprising, however, when one considers that the mean is the first moment of the PDF, thus a single inflection point is a consequence of PDFs that are both marching and symmetric about the η -axis. A similar argument can be made for the triple inflection point, which is a natural consequence of non-marching PDFs. This is seen in table 1, where there is a good

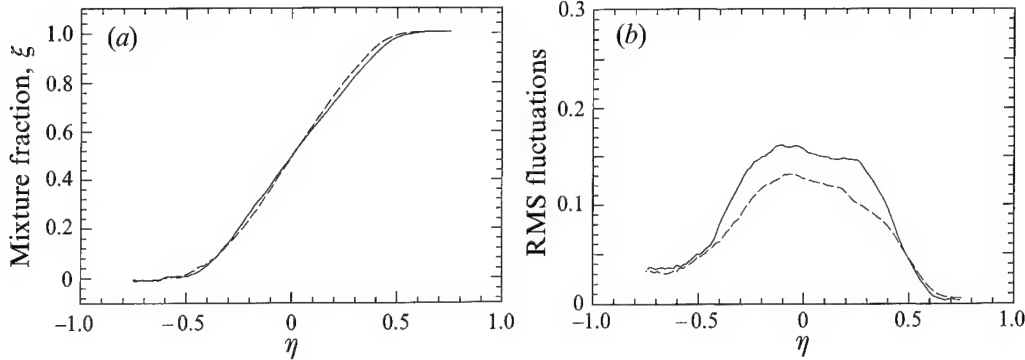


FIGURE 47. Comparison of profiles at $M_c = 0.28$ (—) and $M_c = 0.62$ (---): (a) mean, (b) RMS fluctuations.

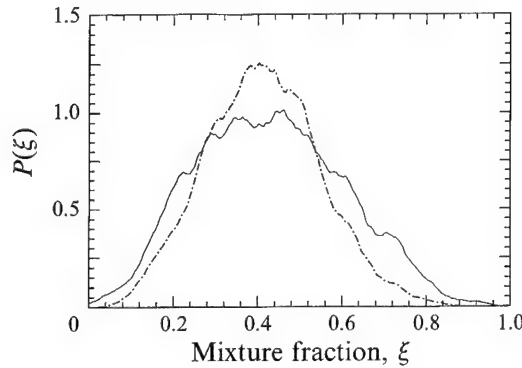


FIGURE 48. Comparison of PDFs of mixture fraction for $M_c = 0.28$ (—) and $M_c = 0.62$ (---) for $\eta \approx 0$.

correlation between the triple inflection point and non-marching PDFs. From the clear triple inflection point in the mean profiles of Fiedler (1974), we would expect his PDFs (if presented) to be non-marching.

Fiedler (1974) argued that triple inflection point profiles result from layers that are dominated by coherent structures with compositions that are cross-stream uniform and streamwise sloped. Although, in this study at $M_c = 0.28$, the trend of cross-stream uniform and streamwise sloped structures was observed, there was sufficient variation in the composition of the structures to remove any indication of a triple inflection point.

The RMS fluctuations for the two cases are compared in figure 47(b), and show the fluctuations at $M_c = 0.28$ are about 15% greater than those at $M_c = 0.62$. This is in agreement with the results of Dutton *et al.* (1990) and Clemens & Paul (1993) for a similar convective Mach number range. The hot-wire measurements of Bonnet *et al.* (1993) indicate that at moderate compressibility mass flux fluctuations are suppressed to a larger extent on the high-speed edge of the layer. This also appears to be the case for the mixture fraction fluctuations of figure 47(b) at $M_c = 0.62$.

The narrower PDFs for the higher convective Mach number case were mentioned above and this is more clearly seen in figure 48 which shows PDFs at $\eta \approx 0$ for the two cases. This figure shows that at $M_c = 0.62$, the PDF is somewhat narrower than at $M_c = 0.28$. A Gaussian profile was fit to each curve and showed that the e^{-1} width is about

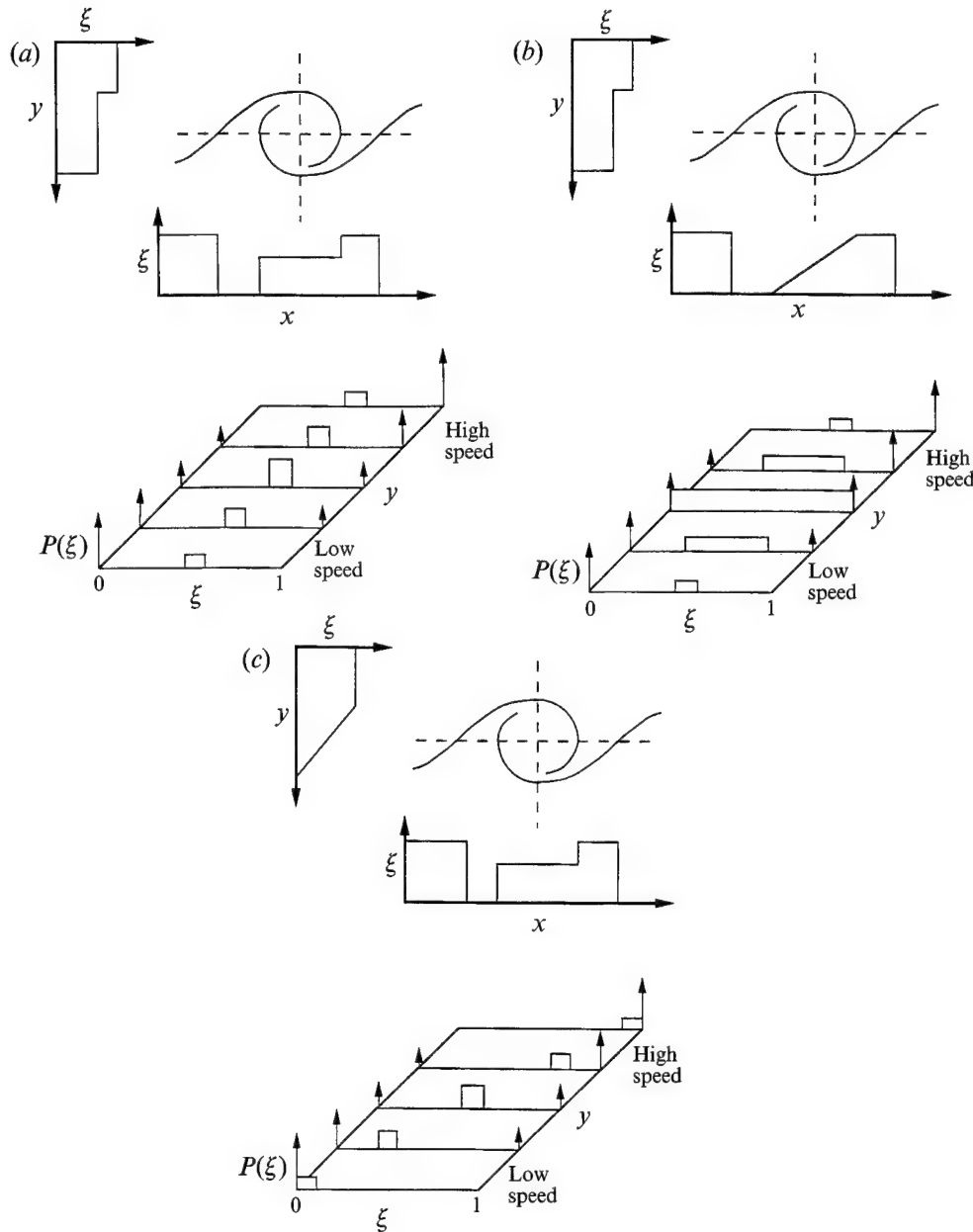


FIGURE 49. Model PDFs: streamwise and cross-stream profiles are shown at the top, and the model PDFs are shown at the bottom: (a) uniform core, (b) streamwise sloped and cross-stream uniform, (c) streamwise uniform and cross-stream sloped.

20 % larger at $M_c = 0.28$. Broader PDFs imply that a larger range of mixture fraction values is present at a given location. These broad PDFs are responsible for the larger RMS fluctuations found at the lower convective Mach number.

The obvious issue that arises is what types of turbulent structures are responsible for the resulting PDFs. As a means of understanding this, we consider three model turbulent structures. The first, figure 49(a), is similar to that modelled by Broadwell & Breidenthal (1982) and is uniform in both the streamwise and the cross-stream

directions. For this type of structure the PDFs would exhibit a preferred mixture fraction at all transverse locations across the layer. If the typical structure is sloped in the streamwise direction, yet uniform in the cross-stream direction (figure 49*b*), as was suggested by Fiedler (1974), then the PDFs also exhibit a preferred mixture fraction which is invariant with the transverse location. The PDFs are different from figure 49(*a*), however, because the slope results in a much broader range of mixture fractions populating a given location. The final model, figure 49(*c*), is that of a structure which resembles the mean because it is uniform in the streamwise direction and sloped in the cross-stream direction. In this case, the PDFs appear as a series of marching delta functions which reflect the small range of mixture fractions that are present at each cross-stream location.

The model PDFs suggest that the mixing layer at $M_c = 0.28$ may exhibit characteristics of both the streamwise and cross-stream sloped models, because the PDFs are both broadly distributed and marching. Some evidence of this is provided by the perspective views of figure 40 which exhibit both types of sloped structure. For the $M_c = 0.62$ case, the narrower PDFs are consistent with the cross-stream sloped model, as are the perspective views of figure 43. This suggests that the compressible layer, unlike its incompressible counterpart, is composed of turbulent structures whose instantaneous mixture fraction profiles more closely resemble the mean profile. This view is consistent with the 'sonic eddy' model developed by Breidenthal (1992), which predicts that compressibility acts to reduce the eddy lengthscales which are responsible for entrainment. The entrainment by smaller-scale eddies results in instantaneous cross-stream profiles which are similar to the mean profile.

Unfortunately, owing to the limited resolution of the measurement, we cannot make a definitive statement as to the extent of molecular mixing. This was shown by Koochesfahani & Dimotakis (1986) in incompressible mixing layers and by Clemens & Paul (1993) in compressible axisymmetric mixing layers, where under-resolved passive scalar measurements were shown to significantly overestimate the amount of mixed fluid in the layer. Since under-resolved passive scalar measurements cannot be trusted to provide information on molecular mixing, it is necessary to rely on measurements which are insensitive to limited resolution. Hall *et al.* (1991*b*) used fast chemical reactions and found that the fraction of mixed fluid in the layer is about 30% greater at $M_c = 0.51$ than at $M_c = 0.91$. In axisymmetric mixing layers, Clemens & Paul (1993) found little difference in the fraction of mixed fluid at convective Mach numbers of 0.35 and 0.82. The reason for the difference in the two measurements is not known, but it should be safe to conclude that compressibility does not greatly increase the fraction of mixed fluid.

For the present results, the observed changes in the entrainment with compressibility such as increased three-dimensionality, closely spaced and cross-stream sloped structures and smaller scalar fluctuations, are probably more consistent with a compressible mixing layer which has a larger fraction of mixed fluid. If we assume that these effects increase the amount of stirring at the large scales, then we might expect this to facilitate the mixing process (i.e. inter-diffusion). The mixing measurements mentioned above, however, indicate that this is not the case, or is at most a very small effect. This leads to the possibility that compressibility increases the amount of stirred fluid at the larger scales, while somehow reducing stirring and/or diffusion at the smaller scales. This, of course, is largely conjecture, but it does suggest the need for continued research into this very complex problem.

Even though the exact nature of the mixing process at the small scales is not well understood, the changes in the structure and entrainment process that we have

documented have strong implications for the understanding of reacting mixing layers. In particular, we have seen that the breakdown of the two-dimensional structure results in a mixture fraction field which differs significantly from what is found under incompressible conditions. Since in a reacting situation the mixture fraction field will determine the local stoichiometry and temperature, the mode of burning can be expected to be significantly modified. This indeed appears to be the case as suggested by the reacting mixing layer results of Miller *et al.* (1993) who studied H₂/vitiated air supersonic mixing layers at moderate levels of heat release, and cite similarities in the structure of the fuel and OH fields to that found in the present cold flow studies.

7. Conclusions

Studies of the large-scale structure, entrainment motions, and mixture fraction fluctuations were made at a range of convective Mach numbers. Flow visualizations using planar laser Mie scattering from condensed alcohol droplets reveal a mixing layer that is dominated by spanwise rollers at $M_c = 0.28$ and 0.42 , but much more three-dimensional and apparently unorganized structures at $M_c = 0.62$ and 0.79 . There is also some evidence for increased streamwise structure at the highest convective Mach numbers. The convective Mach number of 0.50 appears to be transitional as both rollers and the more unorganized structures seen at higher M_c are observed. A change was also seen in the character of the structure core and braid regions of the rollers with increasing compressibility. The shape of the structure cores transition from elliptical to polygonal, and the braids developed a characteristic 'kink'. Observations of entrainment of fluid into the mixing layer suggest that at low M_c the mixture fraction field is sloped in the streamwise direction, but more uniform in the cross-stream direction. At $M_c = 0.62$ and 0.79 , the mixture fraction field was often found to be sloped in the cross-stream direction and sometimes showed two distinct regions of mixing due to closely spaced overlapping structures. The exact vertical structure which causes these overlapping structures could not readily be identified, but the likely cause is closely spaced streamwise vortices.

Quantitative images of the mixture fraction field were obtained using planar laser-induced fluorescence of seeded nitric oxide at convective Mach numbers of 0.28 and 0.62 . These images provided validation of the trends seen in the Mie scattering visualizations and provided an opportunity to quantitatively investigate the mixture fraction field. Mixture fraction statistical quantities were computed, such as the mean, RMS fluctuations and PDFs. The mean profiles are similar for both cases but the RMS fluctuations are about 15% smaller at $M_c = 0.62$. The fluctuations are particularly suppressed on the high-speed edge of the layer. The PDFs for both cases exhibit a peak in mixture fraction which marches across the layer, but individual PDFs are typically broader at $M_c = 0.28$. These results are consistent with the qualitative observations at $M_c = 0.62$ of fewer pure fluid intrusions into the layer and of weaker scalar gradients on the high-speed edge of the layer. The present results also suggest that compressibility increases the amount of stirring at the large scales which might help the layer to become better mixed. Previous mixing measurements, however, suggest that this is not the case, as compressibility appears to reduce or have little effect on the efficiency of molecular mixing.

This work was sponsored by the US AFOSR, Aerospace Sciences Directorate, J. Tishkoff technical monitor, and the NASA Ames/Stanford University Center for Turbulence Research. We gratefully acknowledge the help of Mr M. F. Miller in

construction of the facility. The PLIF diagnostics were also developed under the sponsorship of the AFOSR by Professor R. K. Hanson. The expert help of Dr P. H. Paul and R. K. Hanson in conducting these measurements is gratefully acknowledged.

REFERENCES

BATT, R. G. 1977 Turbulent mixing of passive and chemically reacting species in a low-speed shear layer. *J. Fluid Mech.* **82**, 53–95.

BERNAL, L. P. & ROSHKO, A. 1986 Streamwise vortex structure in plane mixing layers. *J. Fluid Mech.* **170**, 499–525.

BIRCH, S. F. & EGGLERS, J. M. 1972 A critical review of the experimental data for developed free turbulent shear layers. *NASA SP-321*, pp. 11–40.

BOGDANOFF, D. W. 1983 Compressibility effects in turbulent shear layers. *AIAA J.* **21**, 926–927.

BONNET, J. P., DEBISSCHOP, J. R. & CHAMBRES, O. 1993 Experimental studies of the turbulent structure of supersonic mixing layers. *AIAA Paper 93-0217*.

BREIDENTHAL, R. 1981 Structure in turbulent mixing layers and wakes using a chemical reaction. *J. Fluid Mech.* **109**, 1–24.

BREIDENTHAL, R. 1992 Sonic eddy – A model for compressible turbulence. *AIAA J.* **30**, 101–104.

BROADWELL, J. E. & BREIDENTHAL, R. E. 1982 A simple model of mixing and chemical reaction in a turbulent shear layer. *J. Fluid Mech.* **125**, 397–410.

BROWAND, F. K. & LATIGO, B. O. 1979 Growth of the two-dimensional mixing layer from a turbulent and nonturbulent boundary layer. *Phys. Fluids* **22**, 1011–1019.

BROWAND, F. K. & TROUTT, T. R. 1985 The turbulent mixing layer: Geometry of the large vortices. *J. Fluid Mech.* **158**, 489–509.

BROWN, G. L. & ROSHKO, A. 1974 On density effects and large structure in turbulent mixing layers. *J. Fluid Mech.* **64**, 775–816.

CHANDRSUDA, C., MEHTA, R. D., WEIR, A. D. & BRADSHAW, P. 1978 Effect of free-stream turbulence on large structure in turbulent mixing layers. *J. Fluid Mech.* **85**, 693–704.

CHEN, J. H. 1991 The effect of compressibility on conserved scalar entrainment in a plane free shear. *Eighth Symp. on Turbulent Shear Flows, Munich, Germany*.

CHINZEI, N., MASUYA, G., KOMURO, T., MURAKAMI, A. & KUDOU, K. 1986 Spreading of two-stream supersonic mixing layers. *Phys. Fluids* **29**, 1345–1347.

CLEMENS, N. T. 1991 An experimental investigation of scalar mixing in supersonic turbulent shear layers. PhD thesis, High Temperature Gas Dynamics Laboratory, Mechanical Engineering Department, Stanford University.

CLEMENS, N. T. & MUNGAL, M. G. 1991 A planar Mie scattering technique for visualizing supersonic mixing flows. *Expts Fluids* **11**, 175–185.

CLEMENS, N. T. & MUNGAL, M. G. 1992a Two- and three-dimensional effects in the supersonic mixing layer. *AIAA J.* **30**, 973–981.

CLEMENS, N. T. & MUNGAL, M. G. 1992b Effects of sidewall disturbances on the supersonic mixing layer. *J. Propulsion Power* **8**, 249–251.

CLEMENS, N. T. & PAUL, P. H. 1993 Scalar measurements in compressible axisymmetric mixing layers. *AIAA Paper 93-0220*.

CLEMENS, N. T., PAUL, P. H., MUNGAL, M. G. & HANSON, R. K. 1991 Scalar mixing in the supersonic shear layer. *AIAA Paper 91-1720*.

CRAWFORD, M. E. & KAYS, W. M. 1976 STANS-A program for numerical computation of two-dimensional internal and external boundary layer flows. *NASA CR-2742*.

DOWLING, D. R. & DIMOTAKIS, P. E. 1900 Similarity of the concentration field of gas-phase turbulent jets. *J. Fluid Mech.* **218**, 109–142.

DUTTON, J. C., BURR, R. F., GOEBEL, S. G. & MESSERSMITH, N. L. 1990 Compressibility and mixing in turbulent free shear layers. *Presented at the 12th Symposium on Turbulence, Sept. 24–26, Rolla, MO*, p. A21-1.

ELLIOTT, G. S. & SAMIMY, M. 1990 Compressibility effects in free shear layers. *Phys. Fluids A* **2**, 1231–1240.

ELLIOTT, G. S., SAMIMY, M. & ARNETTE, S. A. 1993 Study of compressible mixing layers with filtered Rayleigh scattering based visualizations. *AIAA J.* **30**, 2567–2569.

FIEDLER, H. E. 1974 Transport of heat across a plane turbulent mixing layer. *Adv. Geophys.* **18**, 93–109.

FOELSCH, K. 1946 A new method of designing two-dimensional laval nozzles for a parallel and uniform jet. *Rep. NA-46-235-2*. North American Aviation, Inc.

FOURGUETTE, D. C., MUNGAL, M. G. & DIBBLE, R. W. 1990 Time evolution of the shear layer of a supersonic axisymmetric jet at matched conditions. *AIAA J.* **29**, 1123–1130.

GOEBEL, S. G. & DUTTON, J. C. 1991 Experimental study of compressible turbulent mixing layers. *AIAA J.* **29**, 538–546.

HALL, J. L., DIMOTAKIS, P. E. & ROSEMANN, H. 1991a Experiments in non-reacting compressible shear layers. *AIAA Paper* 91-0629.

HALL, J. L., DIMOTAKIS, P. E. & ROSEMANN, H. 1991b Some measurements of molecular mixing in compressible turbulent shear layers. *AIAA Paper* 91-1719.

HANSON, R. K., SEITZMAN, J. M. & PAUL, P. H. 1990 Planar laser-induced fluorescence imaging of combustion gases. *Appl. Phys. B* **50**, 441–454.

IKAWA, H. & KUBOTA, T. 1975 Investigation of supersonic turbulent mixing layer with zero pressure gradient. *AIAA J.* **13**, 566–572.

JACKSON, T. L. & GROSCH, C. E. 1989 Inviscid spatial stability of a compressible mixing layer. *J. Fluid Mech.* **208**, 609–637.

KARASSO, P. S. & MUNGAL, M. G. 1992 LIF measurements of mixing in turbulent shear layers. *Sixth Intl Symp. on Applications of Laser Techniques to Fluid Mechanics, Lisbon, Portugal*.

KONRAD, J. H. 1977 An experimental investigation of mixing in two-dimensional turbulent shear flows with applications to diffusion-limited chemical reactions. PhD thesis, California Institute of Technology.

KOOCHESFAHANI, M. M. & DIMOTAKIS, P. E. 1986 Mixing and chemical reactions in a turbulent liquid mixing layer. *J. Fluid Mech.* **170**, 83–112.

MASUTANI, S. M. & BOWMAN, C. T. 1986 The structure of a chemically reacting plane mixing layer. *J. Fluid Mech.* **172**, 93–126.

MAYDEW, R. C. & REED, J. F. 1963 Turbulent mixing of compressible free jets. *AIAA J.* **1**, 1443–1444.

MCGREGOR, I. 1961 The vapor screen method of flow visualization. *J. Fluid Mech.* **11**, 481–511.

MCINTYRE, S. S. & SETTLES, G. S. 1991 Optical experiments on axisymmetric compressible turbulent mixing layer. *AIAA Paper* 91-0623.

MESSERSMITH, N. L. & DUTTON, J. C. 1992 An experimental investigation of organized structure and mixing in compressible turbulent free shear layers. *Rep. UILU-ENG* 92-4002. University of Illinois, Dept. of Mechanical and Industrial Engineering.

MESSERSMITH, N. L., DUTTON, J. C. & KRIER, H. 1991 Experimental investigation of large scale structures in compressible mixing layers. *AIAA Paper* 91-0244.

MILLER, M. F., ISLAND, T. C., SEITZMAN, J. M., BOWMAN, C. T., MUNGAL, M. G. & HANSON, R. K. 1993 Compressibility effects in a reacting mixing layer. *AIAA Paper* 93-1771.

MUNGAL, M. G. & DIMOTAKIS, P. E. 1984 Mixing and combustion with low heat release in a turbulent shear layer. *J. Fluid Mech.* **148**, 349–382.

MUNGAL, M. G. & FRIELE, C. E. 1988 The effects of Damköhler number in a turbulent shear layer. *Combust. Flame* **71**, 23–34.

PAPAMOSCHOU, D. 1991 Structure of the compressible turbulent shear layer. *AIAA J.* **29**, 680–681.

PAPAMOSCHOU, D. & ROSHKO, A. 1988 The compressible turbulent shear layer: an experimental study. *J. Fluid Mech.* **197**, 453–477.

PAUL, P. H. 1991 The application of intensified array detectors to quantitative planar laser-induced fluorescence imaging. *AIAA Paper* 91-2315.

PETULLO, S. P. & DOLLING, D. S. 1993 Large-scale structure orientation in a compressible turbulent shear layer. *AIAA Paper* 93-0545.

RAGAB, S. A. & WU, J. L. 1989 Linear instabilities in two-dimensional compressible mixing layers. *Phys. Fluids A* **1**, 957–966.

RAJAGOPALAN, S. & ANTONIA, R. A. 1981 Properties of the large structure in a slightly heated turbulent mixing layer of a plane jet. *J. Fluid Mech.* **105**, 261–281.

SAMIMY, M. & LELE, S. K. 1991 Motion of particles with inertia in a compressible free shear layer. *Phys. Fluids A* **3**, 1915–1923.

SAMIMY, M., REEDER, M. F. & ELLIOTT, G. S. 1992 Compressibility effects on large structures in free shear flows. *Phys. Fluids A* **4**, 1251–1258.

SANDHAM, N. D. & REYNOLDS, W. C. 1991 Three-dimensional simulations of large-eddies in the compressible mixing layer. *J. Fluid Mech.* **224**, 133–158.

SHAU, Y. R. & DOLLING, D. S. 1992 Exploratory study of turbulent structure of a compressible shear layer using fluctuating Pitot pressure measurements. *Exps Fluids* **12**, 293–306.

SIRIEIX, M. & SOLIGNAC, J. L. 1966 Contribution a l'étude expérimentale de la coche de mélange turbulent isobare d'un écoulement supersonique. *AGARD CP* **4**, 242–270.

SUNYACH, M. & MATHIEU, J. 1969 Mixing zone of a two-dimensional jet. *Intl J. Heat Mass Transfer* **12**, 1679–1697.

WEGENER, P. P., CLUMPNER, J. A. & WU, B. J. C. 1972 Homogeneous nucleation and growth of ethanol drops in supersonic flow. *Phys. Fluids* **15**, 1869–1876.

WYGNANSKI, I., OSTER, D., FIEDLER, H. & DZIOMBA, B. 1979 On the perseverance of a quasi-two-dimensional eddy-structure in a turbulent mixing layer. *J. Fluid Mech.* **93**, 325–335.

ZHUANG, M., DIMOTAKIS, P. E. & KUBOTA, T. 1900 The effect of walls on a spatially growing supersonic shear layer. *Phys. Fluids A* **2**, 599–608.



AIAA-95-0517
SINGLE-SHOT OH PLIF THERMOMETRY IN A
REACTING, SUPERSONIC FREE JET

J.L. Palmer and R.K. Hanson
High Temperature Gasdynamics Laboratory
Department of Mechanical Engineering
Stanford University, Stanford, CA 94305-3032

**33rd AIAA Aerospace Sciences Meeting
and Exhibit**

January 9-12, 1995 / Reno, NV

SINGLE-SHOT OH PLIF THERMOMETRY IN A REACTING, SUPERSONIC FREE JET

J.L. Palmer[†] and R.K. Hanson[‡]

High Temperature Gasdynamics Laboratory

Department of Mechanical Engineering

Stanford University, Stanford, CA 94305-3032

Abstract

Temperature measurements were performed in a shock tunnel-generated reacting free jet of hydrogen and oxygen diluted in argon using a two excitation line planar laser-induced fluorescence technique with the hydroxyl radical (OH) as a tracer. The shock tunnel provided a reservoir for the flow with 1.9% OH at 3350 ± 50 K and 3.2 ± 0.1 atm, which exhausted into a pure argon ambient at 40 torr. Single-shot images were obtained using broad-band excitation of isolated transitions in the $A^2\Sigma^+ \leftarrow X^2\Pi(1,0)$ band of OH near 282 nm, with broad-band, temporally-integrated detection of the resulting nonresonant emission. Care was taken to quantify the signals through the use of single-shot laser monitoring and image processing procedures. The rotational temperature field was derived by taking the ratio of single-shot images obtained with laser excitation of two different ro-vibrational lines. A measurement of the fluorescence lifetime in the free jet showed no variation with excited rotational level, allowing a relatively simple conversion between signal ratio and rotational temperature. The measured temperature throughout the free jet flowfield was shown to be in good agreement with that predicted using a method of characteristics simulation.

I. Introduction

Development of optical combustion diagnostics is an ongoing research topic in many laboratories.¹ Planar laser-induced fluorescence (PLIF) is an attractive technique for studies in many reacting environments.² It can provide species and quantum state specific data with high temporal and spatial resolution. This allows radical concentration,^{3,4} temperature,⁵⁻⁸ and velocity⁹⁻¹¹ measurements, as well as the visualization of transient combustion phenomena.¹²⁻¹⁸ The hydroxyl radical (OH) has frequently been used as a tracer in PLIF imaging. It is a naturally occurring

species which marks the reaction zone of many combusting flows, has been well characterized spectroscopically, and exhibits strong UV absorption and high nonresonant fluorescence yield. In some applications, OH fluorescence signal interpretation is plagued by the possible rotational state dependence of the electronic quenching. This difficulty is not insurmountable, however.¹⁹⁻²¹

The objective of the work presented here is the development of OH PLIF imaging for temperature measurements in a transient hypersonic flowfield. This effort is part of an overall project aimed at developing and demonstrating PLIF thermometry and velocimetry diagnostics compatible with use in pulsed flow facilities.^{8,22-24} The technique described here is an extension of a two-line PLIF imaging method used previously in making instantaneous temperature measurements in shock tube flows with nitric oxide (NO)^{7,24} and OH.⁶⁻⁸ Application in a supersonic free jet of combustion gases requires several modifications of the experimental technique because of the extreme variations of pressure and temperature and high speed encountered. These include the selection of transitions with sufficient lower state population to ensure reasonable signal level throughout the flowfield; active laser pulse spectral monitoring to eliminate systematic errors associated with large, variable Doppler shifts of the absorption frequency; the careful verification of the linearity of the fluorescence signal with input laser energy; and data collection and processing procedures which take into account the long lifetime of the fluorescence signal in the low density portions of the jet.

A pressure driven, reflection-type shock tunnel has been used to generate a highly underexpanded, axisymmetric free jet of combustion gases diluted in argon (Ar) from a test gas initially containing 5% hydrogen (H_2) and 5% oxygen (O_2). Sequential fluorescence bursts are induced by broad-band counter-propagating laser sheets directed at an angle through the axis of the jet and tuned to excite isolated $A^2\Sigma^+ \leftarrow X^2\Pi(1,0)$ transitions of OH. A single frequency-doubled dye laser pulse split into two parts

[†]Graduate Research Assistant, Student Member AIAA.

[‡]Professor, Associate Fellow AIAA.

Copyright 1995 by the authors. Published by the American Institute of Aeronautics and Astronautics with permission.

forms the sheets, which therefore have identical spectral properties. A brief delay in one of the beams temporally separates the PLIF signals, the nonresonant components of which are captured by gated, intensified charge coupled device (ICCD) arrays mounted above and below the test section.

Opposite Doppler shifts of the absorption frequency at each point in the flow result in a velocity dependence in the resultant image pair. A difference-to-sum combination of the signals induced by the sheets, with an analysis of the single-shot laser spectrum and the assumption of flowfield symmetry may be used to infer the instantaneous two-component velocity field of the free jet.¹¹ The rotational temperature field is obtained by taking the ratio of images acquired by exciting two different ro-vibrational transitions with laser pulses having similar lineshapes and relative detuning from their unshifted absorption linecenters. Each image in the ratio is formed by summing images acquired simultaneously with a single laser sheet. Although the thermometry technique was demonstrated here using a single excitation system, making the acquisition of images during sequential facility firings necessary, it is extendible to instantaneous measurements in a straight-forward manner. A method of characteristics (MOC) simulation of the flowfield²⁵ was used in assessing the temperature measurements.

II. OH PLIF Thermometry

The total fluorescence signal from a volume V_c in the flow, under weak (linear) excitation of an isolated absorption line is given by:²

$$S_f = \frac{E_p g B}{A_{las}} \left(\frac{\chi_a P}{kT} \right) f_{J''} V_c \left(\frac{A}{A+Q} \right) \eta_c, \quad (1)$$

where E_p is the laser pulse energy; g is the spectral convolution of the laser and absorption lineshapes; B is the Einstein coefficient for absorption; A_{las} is the cross sectional area of the laser sheet; χ_a is the mole fraction of the absorbing species; P is the pressure; T is the translational/rotational temperature; k is Boltzmann's constant; $f_{J''}$ is the Boltzmann fraction of the absorbing state, which has rotational quantum number J'' ; A is the effective rate of spontaneous emission for all directly and indirectly populated states; similarly, Q is the total electronic quenching rate of the excited state; and η_c is the efficiency with which photons emitted from the gas are converted to photoelectrons, which depends on the collection optical arrangement, spectral filtering, temporal gating, photocathode quantum efficiency, and intensifier gain. The term $A/A+Q$ is also known as the fluorescence efficiency Φ .

The spectral convolution is given by:

$$g = \int_{-\infty}^{\infty} g_a(v - v_a - \Delta v_D, \Delta v_a) g_l(v - v_l, \Delta v_l) dv, \quad (2)$$

where v is the frequency; g_a and g_l are the absorption and laser lineshapes, respectively; v_a and Δv_a are the absorption center frequency and full-width-at-half-maximum (FWHM); and v_l and Δv_l are the same quantities for the laser. The Doppler shift of the transition, induced by the bulk motion of the flow, is given by:

$$\Delta v_D = \frac{\vec{V} \cdot \hat{k}}{2\pi} = v_a \frac{V \cos(\beta - \theta)}{c}, \quad (3)$$

where \vec{V} is the vector velocity of the gas motion; V is the magnitude of the velocity; \hat{k} is the wave vector of the laser ($|\hat{k}| = 2\pi v_l/c$, with $v_l \approx v_a$ because the laser is tuned to the absorption); β is the angle between \hat{k} and the jet axis; θ is the angle between \vec{V} and the jet axis; and c is the speed of light. The orientations of \vec{V} and \hat{k} are illustrated in Fig. 1.

In these experiments, counter-propagating laser sheets passed through the mid-plane of the jet at an angle ($\beta \leq \pi/2$), as shown in Fig. 1. The laser pulses were identical spectrally, as they were created from a single laser shot, but they were separated temporally to allow the capture of two images, S_f^+ and S_f^- , during each experiment. The time interval between their acquisition was sufficiently small so that no significant flow motion took place. Differences in the signal levels at a given point resulted from the Doppler shifts of the absorption, relative to each laser sheet. Since the flowfield was symmetric, the axial and radial components of the velocity, V_x and V_r ,

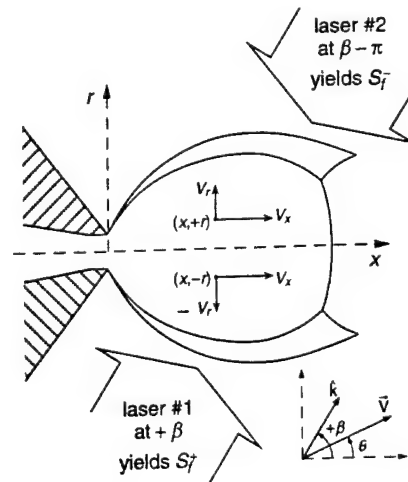


Figure 1: Counter-propagating laser sheets in a symmetric flowfield.

respectively, could be inferred from a comparison of the two signals.^{11,23}

In the two-line rotational thermometry technique, a ratio is taken of signals S_{f1} and S_{f2} , obtained with laser photons first exciting one transition and then another from the same lower vibrational level, but a different rotational state. Each of these signals is the sum of the two PLIF signals captured during an experiment ($S_f = S_f^+ + S_f^-$). Because a single excitation system is used here, separate experiments were performed to acquire the necessary images. Fortunately, the inviscid core of the free jet flowfield was repeatable, except for slight shot-to-shot variations in the shock position. Only information about the mean temperature in the turbulent portions of the flowfield was obtainable with this method. Taking the ratio of the signals gives:

$$R(T) = \frac{S_1}{S_2} = \frac{E_{p1} g_1 2J''_1+1 S_{J''J1}}{E_{p2} g_2 2J''_2+1 S_{J''J2}} \times \exp \left\{ - \frac{[F(J''_1) - F(J''_2)]}{kT} \right\} \frac{\Phi_1 \eta_{c1}}{\Phi_2 \eta_{c2}}, \quad (4)$$

where subscripts 1 and 2 denote the terms of the respective equations describing the PLIF signals. $S_{J''J}$ is the normalized Hönl-London factor of the line used, where J'' is the lower rotational level and J' the upper; and $F(J'')$ is the rotational term energy of the lower level. The rotational temperature field may thus be inferred from Eqn. 4 if the ratios of the laser pulse energies, spectral convolutions, fluorescence yields, and collection efficiencies are known.

The pulse energy ratio may be assumed to be unity after a correction for variations in the laser sheet energy profile has been applied to each of the raw signals. The images may also be normalized to remove the effect of variations in η_c , reducing η_{c1}/η_{c2} to a constant. The ratio of the spectral convolutions cancels if the excitation characteristics (i.e., laser lineshape and frequency detuning) are matched for the images used. An analysis of the single-shot laser spectral properties is, thus, necessary here. Details of the laser pulse monitoring systems implemented in the experiments are given in the next section. Use of the procedures described there allows the elimination of the laser pulse energy, spectral convolution, and collection efficiency ratios from Eqn. 4.

Often the fluorescence yield is identical for the two excited transitions and Φ_1/Φ_2 in Eqn. 4 may be assumed to be unity. Caution must be exercised, though, because for OH, the electronic quenching rate may depend on the upper rotational level J' , particularly at low temperature.^{26,27} Since the flow conditions in the free jet vary greatly, J' -dependent

effects could introduce significant uncertainties into the temperature results. However, as discussed in the following sections, measurements performed during the course of this work showed that for the conditions existing in the free jet and with the transitions used, Φ is independent of J' , allowing the cancellation of the ratio of fluorescence yields from Eqn. 4.

Under the above conditions, the equation describing the PLIF signal ratio reduces to:

$$R(T) = C_{12} \frac{2J''_1+1}{2J''_2+1} \frac{S_{J''J1}}{S_{J''J2}} \times \exp \left\{ - \frac{[F(J''_1) - F(J''_2)]}{kT} \right\}. \quad (5)$$

where C_{12} is a normalization constant (ideally equal to unity) which allows the measured ratio to be scaled to that expected at a point in the flowfield where T is known.

Specific transitions within the $A^2\Sigma^+ \leftarrow X^2\Pi(1,0)$ band of OH were selected for the thermometry experiments on the basis of several criteria: their isolation from neighboring lines, the temperature sensitivity associated with their use in two-line measurements, and the expected PLIF signal based on their lower level population fractions at rotational temperatures present in the free jet. The minimum separation between spectral features necessary to fulfill the first of these criteria is $\sim 1 \text{ cm}^{-1}$, a requirement satisfied by many lines in the (1,0) band of OH.⁸

The two remaining criteria dictate the selection of an absorption originating from a very low-lying rotational state and one from a higher energy level that yields a detectable signal in the low temperature, low density portions of the jet flowfield. The chosen transitions are listed in Table 1, along with their wavelengths λ , Hönl-London factors, and lower state rotational energies. Images were obtained with two transitions from high-lying rotational states, $R_1(4)$ and $Q_1(5)$, and with one low- J'' transition, $P_1(1)$. The Boltzmann fractions of the rotational states from which these lines originate are shown as a function of gas temperature in Fig. 2. The rotational temperature in the jet flowfield ranges from $\sim 100 \text{ K}$ before the Mach disk to $\sim 3400 \text{ K}$ downstream of it. The temperature dependence of the signal ratio $R_1(4):P_1(1)$ or $Q_1(5):P_1(1)$ is strong at low temperatures, where changes in the rotational temperature result in large variations in $f_{J''}$ for $J'' = 4.5$ or 5.5 . Diminished sensitivity of the signal ratio and, hence, amplified random error in the inferred temperature are anticipated where the temperature is greater than the energy separation of the two lower states (512 K for $R_1(4):P_1(1)$ and 783 K for $Q_1(5):P_1(1)$).

transition	λ (nm)	$S_{J''J'}$	$F(J'')$ (cm $^{-1}$)
P ₁ (1.5)	282.249	0.588	-38.5
R ₁ (4.5)	281.243	0.355	317.0
Q ₁ (5.5)	282.743	0.878	505.6

Table 1. Data for $A^2\Sigma^+ \leftarrow X^2\Pi(1,0)$ transitions of OH used in PLIF experiments.

III. Experimental Facility and Procedure

A. Shock Tunnel System

Figure 3 shows a schematic of the cold helium-driven, reflection-type shock tunnel facility in which these experiments were conducted. Its performance characteristics are well known.^{25,28} The flowfield presently under discussion was created by shock-heating a test gas of 5% H₂, 5% O₂, and 90% Ar initially at 22.0 torr. Calculations based on measurements of the incident shock speed (1.4 mm/ μ s) indicate that the conditions behind the reflected shock were 3800 ± 50 K and 3.4 ± 0.1 atm, assuming that the gas was vibrationally-equilibrated and chemically inert. A chemical kinetics calculation²⁹ shows that the gas rapidly combusted and, after ~ 100 μ s, reached an equilibrium composition of 1.9% OH, 2.6% H, 2.7% O, 1.0% H₂, 1.8% O₂, 1.8% H₂O, and 88.2% Ar at a stagnation temperature T_s of 3350 ± 50 K and a stagnation pressure P_s of 3.2 ± 0.1 atm. This gas formed the reservoir for the underexpanded free jet flowfield created in the test section, downstream of a converging nozzle with throat diameter $D = 5$ mm. The reacting flow in the nozzle has also been modeled;³⁰ the results indicate that the gas exited the throat at 2700 ± 40 K and 1.65 ± 0.05 atm, with near chemical equilibrium and 1.5% OH.

A diaphragm was placed at the nozzle throat; and the test section and dump tank were initially loaded with pure Ar at 300 K and an ambient pressure P_a of 40.0 torr. The pressure ratio of the free jet was, therefore, $P_s/P_a = 61$. The conditions in the free jet were modeled using the MOC, with the assumption that the gas was vibrationally- and chemically-frozen.²⁵ Neglecting vibrational energy transfer and chemical reactions in the flowfield should have little effect on the bulk properties calculated by the MOC, because of the relatively small initial mole fractions of H₂ and O₂ used. Changes in OH mole fraction (χ_a in Eqn. 1) have no effect on the rotational temperature measured by the two-line technique as they cancel in the signal ratio (Eqn. 4).

B. PLIF Imaging System

The optical arrangement used in acquiring PLIF images is shown in Fig. 3. Frequency-doubled

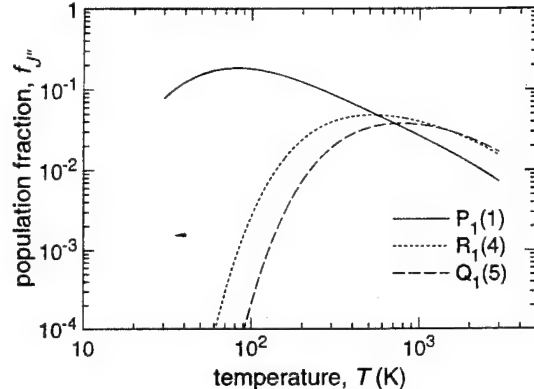


Figure 2: Lower level rotational Boltzmann population fraction as a function of gas temperature for the transitions excited in the experiments.

photons from a tunable, XeCl-pumped dye laser with Coumarin 540 dye were used to excite transitions in the $A^2\Sigma^+ \leftarrow X^2\Pi(1,0)$ band of OH. The laser sheets, each with ~ 0.25 mJ before entering the test section, passed through the mid-plane of the flowfield at 59° and -121° with respect to the jet axis. One sheet was delayed by ~ 230 ns with respect to the other following 6 round trip passes through a 12-m long reflector cavity. The resulting broad-band, integrated fluorescence was imaged onto two 578×384 pixel, cooled, intensified charge-couple device (ICCD) arrays with ~ 230 ns gating by Nikkor UV lenses (f/4.5).

Resonant fluorescence and laser scattering were blocked by 2 mm WG-305 Schott glass filters placed in front of the cameras, along with 2 mm UG-5 filters used to block visible radiation. The transmission curves for the filters,³¹ as well as the transition probabilities of the OH bands of interest,³² are shown in Fig. 4, as a function of wavelength. The excitation and detection scheme utilized here allowed a strong, nonresonant fluorescence signal to be obtained from the $A^2\Sigma^+ \leftarrow X^2\Pi(1,1)$ and (0,0) bands of OH at 312 and 308 nm, respectively. This technique largely avoided the problem of radiative trapping, as most of the fluorescence collected terminated in the unpopulated first excited vibrational level.

Acquisition of PLIF images at the desired moment during the shock tunnel transient required the use of an elaborate electronic triggering system.³³ As indicated in Fig. 3, the signal from the thin film gauge located closest to the shock tunnel nozzle served as the primary trigger for the PLIF experiment. When the incident shock reached that position, a sequence of electronic triggers were initiated which fired a single laser shot 700 μ s later, allowing time for the shock to reach the endwall of the tube and for the free jet

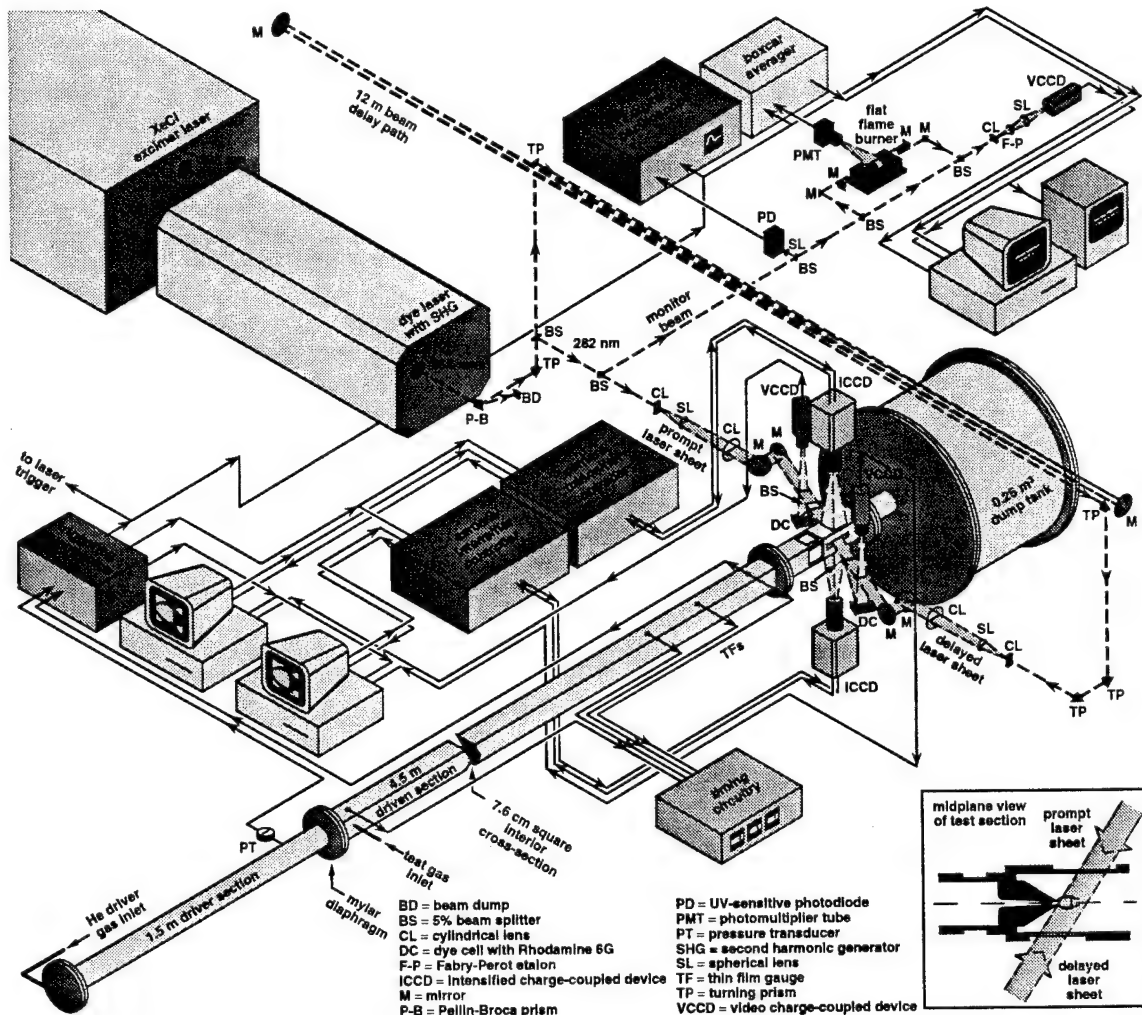


Figure 3: Schematic of experimental facility with associated optical and electronic components for instantaneous one-laser/two-camera PLIF imaging.

flowfield to become established.¹⁸ The intensifier for the camera mounted above the test section was fired just prior to the laser, to capture part of the fluorescence burst due to the prompt laser sheet; while the same fraction of the fluorescence induced by the delayed sheet, beginning 230 ns later, was captured on the camera mounted below the test section, in addition to the portion of the fluorescence induced by the first sheet occurring during the time its intensifier was active. Each laser sheet thus arrived at the test section at the same time relative to its respective intensifier gate. Figure 5 shows the timing of the intensifier gates, input laser pulses, and resulting fluorescence decays, calculated using a five level fluorescence model³⁴ for conditions corresponding to a point on the jet axis $3D$ from the nozzle exit.

In addition to individual image pairs, S_f^+ and S_f^- , which were used in the temperature measurements, images were acquired with the second laser sheet

blocked. This allowed a measurement of the fraction of the first fluorescence burst appearing in the second image. As indicated in Fig. 5, a significant portion of

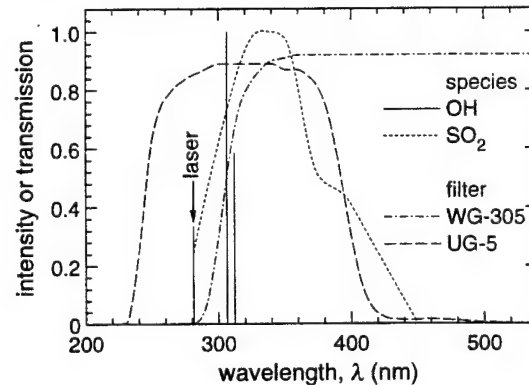


Figure 4: Emission features of OH and SO₂ and transmission of Schott glass filters used in the PLIF experiments.

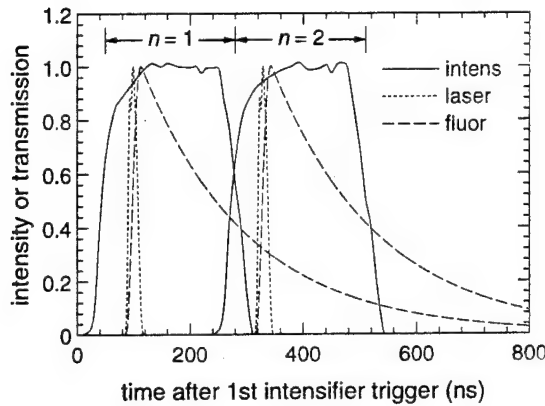


Figure 5: Timing characteristics of the intensifier gates (intens), laser pulses, and fluorescence bursts (fluor) in imaging experiments.

the fluorescence occurred during the time that the second intensifier was active; the actual fraction depended on the electronic quenching rate, and thus on the local thermodynamic conditions. The measured relative signal served as an indication of the lifetime of the fluorescence burst and allowed the signals induced by each sheet to be isolated during the data analysis.

A series of PLIF images were also recorded with filters of various strength placed in front of the test section entrance window for the delayed laser sheet to vary its energy. The prompt sheet was blocked during these measurements. The OH PLIF signal in the jet was found to be linear with incident laser energy for the relatively low amounts of pulse energy available in the sheets. In a separate set of experiments, the results of which are not reported here, the delayed sheet and the second camera were eliminated and the full laser pulse energy (~ 3 mJ) was channeled into a single laser sheet. PLIF images recorded with varying input laser energy indicated that the fluorescence became nonlinear in the low density portion of the jet (i.e., far from the nozzle exit) as E_p/A_{las} increased to 3-4 times that used in the present experiment.

C. Data Correction Procedures and Laser Sheet Monitoring

Procedures similar to those described elsewhere^{8,33} were used to correct the raw data images for single-shot laser sheet intensity variations, nonuniform collection efficiency, laser scattering, and background signal level on a pixel-by-pixel basis. As mentioned previously, the signal due to each sheet was isolated prior to correcting for sheet intensity variations by subtracting the signal due to the first laser sheet from the total signal recorded by the second camera. The contribution was found by multiplying the raw PLIF

image from the first camera, after background correction and alignment,³³ by the appropriate fraction at each point in the image.

The system used to record the single-shot energy profile across the laser sheet during the PLIF imaging experiments is displayed in Fig. 6, which gives in greater detail part of the overall experimental arrangement shown in Fig. 3. A UV-grade quartz plate diverted a small fraction of the laser energy onto a quartz cell filled with Rhodamine 6G dye at high concentration in methanol. The distance between the beam splitter and the dye cell was approximately equal to that between the splitter and the test section centerline. A video camera (VCCD) located above the plane of the laser sheet collected the broad-band, visible fluorescence, centered near 580 nm,³⁵ from the dye. Identical recording systems were erected on either side of the test section to capture images from which the energy profile of each sheet could later be extracted.

Images showing the profile of the laser sheets as they passed through a static gas in the test section were required for use in correcting the images for nonuniformities in the collection efficiency over the field of view of each camera. Because OH does not normally exist at room temperature, another species had to be used in acquiring this signal. In previous OH PLIF experiments, acetone was used,⁸ although it has the disadvantage of fluorescing in the visible region of the spectrum. Removal of the UG-5 filters would thus have been necessary. Sulfur dioxide (SO_2), however, both absorbs and fluoresces in the same spectral regions as does OH, as illustrated in Fig. 4, where the emission spectrum of SO_2 under 282 nm excitation is shown.³⁶⁻³⁹ The signal level in SO_2 at 2.5 torr was found to be sufficient for this purpose.

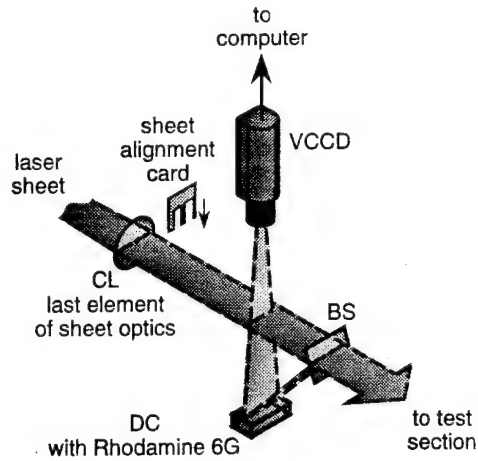


Figure 6: Schematic of equipment used for laser sheet monitoring. Abbreviations are defined in Fig. 3.

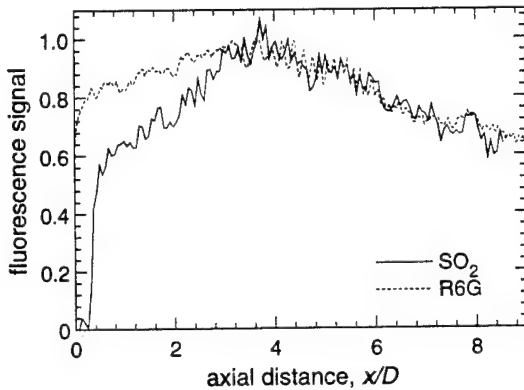


Figure 7: Frame-averaged sheet intensity profile along test section centerline in PLIF image field of view from SO_2 signal and from a corresponding dye cell image.

although frame-averaging over 200 laser pulses was necessary to achieve a signal-to-noise ratio (S/N) in the images of at least 10. The absorption coefficient was estimated from Stern-Volmer plots to be $\leq 1 \times 10^{-5} \text{ torr}^{-1} \text{ mm}^{-1}$ at wavelengths near 282 nm, leading to negligible laser attenuation across the images.

The relative collection efficiency in each camera's field of view (η_c in Eqn. 1) was evaluated by comparing the SO_2 signal with a corresponding sheet image constructed from a frame-averaged VCCD image for the laser sheet. The alignment tool shown in Fig. 6 was used in indexing each point in the laser sheet profile from the video image to the location of the laser sheet in the corresponding image acquired with the ICCD.⁸ Figure 7 shows a comparison between the normalized sheet profile extracted from a 25 frame-averaged image of the prompt laser sheet striking a cell filled with Rhodamine 6G dye and that observed in a 200 frame-averaged SO_2 image, acquired a short time later. The profiles, which were evaluated along the centerline of the test section, show a discrepancy near the nozzle exit caused by a decrease in η_c , as the PLIF signal was obstructed by the edge of the window through which the ICCD camera viewed the flowfield. The sharp drop in the SO_2 signal at $x/D = 0.4$ represents the edge of the laser sheet in the ICCD image.

The region of the flowfield imaged in the PLIF experiments was $8.95 \times 5.95 D$ in size and centered about the jet axis. After correction, the images were binned 4×4 to improve their signal-to-noise ratio and trimmed. The resulting images were 139×95 pixels in size, representing an area in the flowfield $8.61 \times 5.89 D$. Each pixel then corresponded to a region $0.31 \times 0.31 \text{ mm}$ in area and 0.35 mm thick (the

approximate thickness of the laser sheets as they passed through the jet). Some blurring of the signal due to the bulk motion of the flow took place inside the jet core, where the fluorescence decay significantly exceeded the gating period of the intensifiers. Only a small systematic error toward higher temperature in these regions is expected, however, because of the sensitivity of the signal ratio at low temperatures.

D. Pulsed Spectrum Analyzer

The arrangement shown in the upper right corner of Fig. 3 was used to monitor the lineshape and detuning of the individual laser pulse used in each PLIF measurement. A small portion of the laser pulse energy was diverted from the main optical axis prior to sheet formation, as indicated in Fig. 3, for this purpose. The monitor beam was split into two parts, one of which repeatedly passed just above a flat flame methane-air burner, where an OH concentration sufficient to significantly absorb the beam existed. It was then re-directed to propagate nearly co-linearly with the unperturbed portion of the beam. The beams diverged following passage through a negative cylindrical lens (focal length, $f = -10 \text{ mm}$) and were transmitted as distinct peaks or fringes by an air-spaced Fabry-Perot etalon with a free spectral range of 2 cm^{-1} and a finesse of 20. A spherical lens (nominal $f = 140 \text{ mm}$) imaged the light directly onto a 508×240 pixel UV-sensitive VCCD array with a total area of $8.8 \times 6.6 \text{ mm}$. Adjacent linear fringe patterns, spatially separated due to a small angle between the two incoming beams, were recorded. The fringe patterns were observed live on a video monitor or laboratory computer and/or stored for later analysis.

Frame-averaging was required when acquiring attenuated fringe patterns because of beam steering and the broadening of the OH absorption in the flame, which greatly suppressed the fringe pattern. Consequently, several frame-averaged fringe patterns were collected with varying laser wavelength, prior to a series of shock tunnel runs. From the total signal in each bleached fringe pattern and an analysis of the unbleached pattern to determine the laser peak wavelength,²³ a measurement of the laser transmission through the flame as a function of frequency was obtained. Comparison of a single-shot unattenuated fringe pattern acquired with the flame extinguished and the other beam blocked with the frame-averaged pattern acquired at the laser frequency where minimum transmission occurred then yielded the single-shot laser detuning from the un-Doppler-shifted absorption and the laser lineshape.²³ Pressure shifts of the OH absorption⁴⁰ in the flame were small with respect to the overall uncertainty in the peak wavelengths and

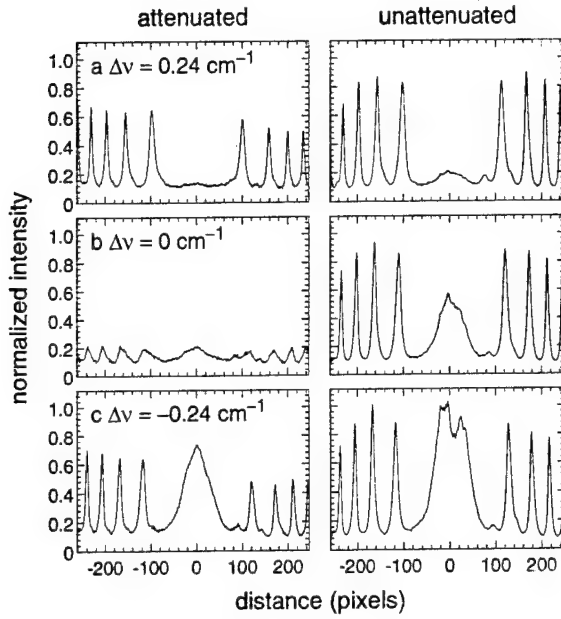


Figure 8: Fringe patterns with and without OH absorption (attenuated, left, and unattenuated, right) for three amounts of laser detuning from the absorption linecenter in an atmospheric, methane-air flame.

were ignored when determining the laser detuning. Figure 8 shows three examples of fringe patterns extracted from 25 frame-averaged images acquired in this manner. In each case, the laser detuning from the OH absorption linecenter ($\Delta v = v_l - v_a$) is listed. The fringes in a and c represent cases in which the laser was tuned far from the $Q_1(5)$ absorption linecenter. When the fringes displayed in b were acquired, the transmission was at its minimum and the laser was tuned close to the absorption linecenter.

V. Results and Discussion

A. OH PLIF Images

Figure 9 shows three single-shot OH PLIF images acquired by pumping different $A^2\Sigma^+ \leftarrow X^2\Pi(1,0)$ transitions. Each image has been normalized by the maximum signal in the $Q_1(5)$ image (c). The scale located to the right of the images shows the relationship between PLIF signal level and gray tone. Axial and radial distances are scaled by the nozzle throat diameter $D = 5$ mm. No OH PLIF signal was recorded in the upper left portion of the images, as that region was beyond the edges of the laser sheets. Each image represents a sum of images acquired simultaneously with the laser detuned from the given absorption line by an amount that, for the delayed laser sheet, approximately compensated for the Doppler shift of the absorption due to the axial velocity in the jet ($v_l - v_a \approx v_a V_x \cos\beta/c \approx -0.12 \text{ cm}^{-1}$, with $V_x \approx 2 \text{ km/s}$ and $\beta = -121^\circ$). Since the axial velocity was relatively constant along the axis and the radial Doppler shifts were equal, but opposite in direction, the resulting signals were nearly symmetric about the jet axis. In this case, the contribution to each summed image from the prompt laser sheet ($\beta = 59^\circ$) was relatively small.

A comparison of the images in Fig. 9 illustrates the rotational temperature sensitivity of the two-line PLIF technique and the difficulty in acquiring adequate signals near the Mach disk with the two higher- J' lines. Inside the jet core, the S/N for the $P_1(1)$ image was fairly uniform at 12-15:1, while the $R_1(4)$ and $Q_1(5)$ images had a maximum S/N of ~15-20:1 near the nozzle exit and a minimum of ~3-5:1 near the Mach disk. A thresholding operation was performed on the images before temperature extraction to eliminate the small OH signal levels in the ambient region of the flowfield.

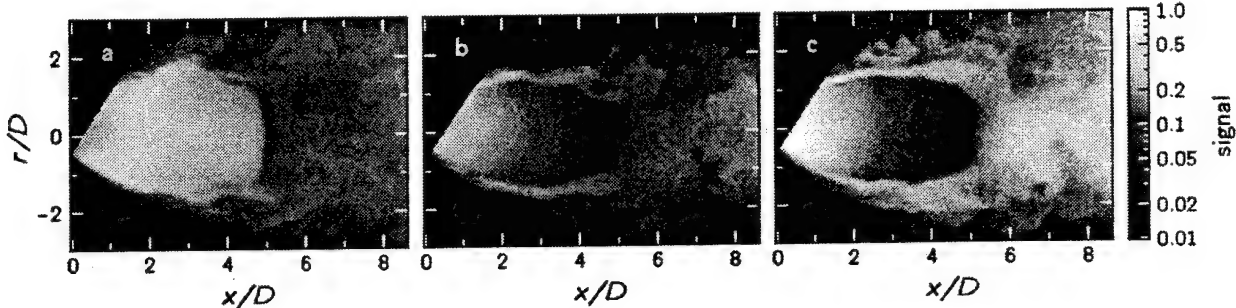


Figure 9: Single-shot PLIF images obtained by pumping different OH transitions: a $P_1(1)$, b $R_1(4)$, and c $Q_1(5)$. The images were matched according to their excitation characteristics. In each case, the laser was detuned from the absorption linecenter by $\sim -0.12 \text{ cm}^{-1}$ and its linewidth was $\sim 0.37 \text{ cm}^{-1}$. The images are $8.61 \times 5.89 D$ (139 \times 95 pixels) in size. The conditions of the free jet were: $T_s = 3350 \text{ K}$, $P_s = 3.2 \text{ atm}$, $P_s/P_a = 61$, with 1.9% OH in Ar and $D = 5 \text{ mm}$.

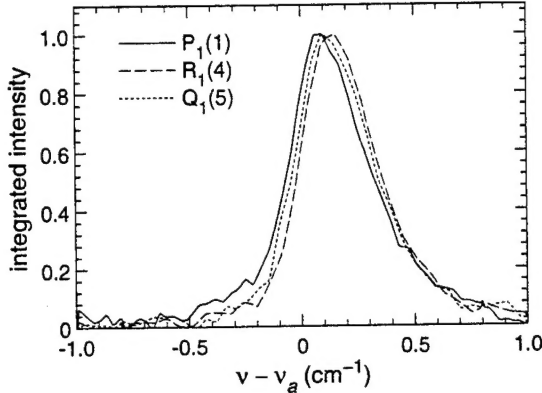


Figure 10: Laser spectral lineshapes for individually acquired PLIF images, matched according to their linewidth and detuning from the unshifted absorption linecenter. In each case, the laser was detuned from the absorption linecenter by $\sim 0.12 \text{ cm}^{-1}$ and its linewidth was $\sim 0.37 \text{ cm}^{-1}$.

Figure 10 shows the lineshape for the laser pulse used in creating each image. The three images were grouped on the basis of the similarity of their lineshapes and tuning characteristics. The systematic error in the signal ratio of any two of the images caused by differences in the spectral convolution (Eqn. 4) may be estimated from a direct comparison of the laser lineshapes. However, the smoothing effect of the convolution of the laser and absorption lines lessens its severity. The error in signal ratio is estimated to be $< 10\%$ for the example shown here, leading to errors in an inferred temperature field of $< 5\%$, depending on the temperature.

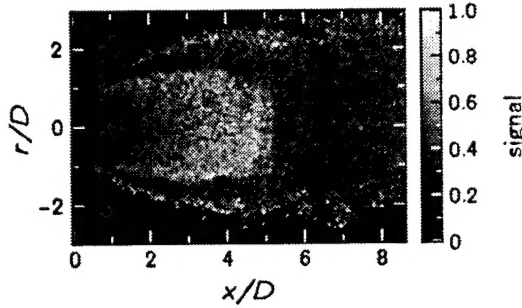


Figure 11: Signal in image 2 contributed by laser sheet 1 relative to that in image 1. The average of six frames is displayed; the fractional signal level corresponding to the gray tones in the image is given by the scale to the right. The image is $8.61 \times 5.89 D$ (139 \times 95 pixels) in size. The conditions of the free jet were: $T_s = 3350 \text{ K}$, $P_s = 3.2 \text{ atm}$, $P_s/P_a = 61$, with 1.9% OH in Ar and $D = 5 \text{ mm}$.

B. Fluorescence Lifetime Measurement

Figure 11 shows the result of a series of PLIF experiments in which only the prompt laser sheet was used. It induced a fluorescence burst from the OH in the test gas which lasted well beyond the gating period of the first intensifier and into the second in most parts of the flowfield. The displayed image represents the signal collected during the second gating period, relative to that during the first, as described in Sect. III.B. The scale to the right of the image indicates the relationship between the fractional signal level and the displayed gray tone. Shown is an average of six ratios of single-shot images acquired simultaneously in this manner. The laser tuning relative to the absorption linecenter varied, but in each case, the fractional signal was symmetric about the axis, as would be expected from the axisymmetry of the jet. The similarity of the signal level contours in this image to those of the temperature images described in the next section demonstrates that the observed fractional signal is purely a function of the local flow conditions.

As shown in Fig. 12, the observed variation in the fluorescence lifetime, as represented by the fractional signal for the second gating period,⁴¹ is independent of the transition used. Hence, it is independent of the upper rotational state J' . Measurements are shown here only for the $P_1(1)$ and $R_1(4)$ transitions, although since $J' = 5.5$ for both $R_1(4)$ and $Q_1(5)$, the result is equally valid for all three transitions. Consequently, when inferring temperature from ratios of the images obtained here, differences in photon yield need not be considered. In the ratio, Φ cancels, leaving the simplified relationship between signal ratio and rotational temperature given in Eqn. 5.

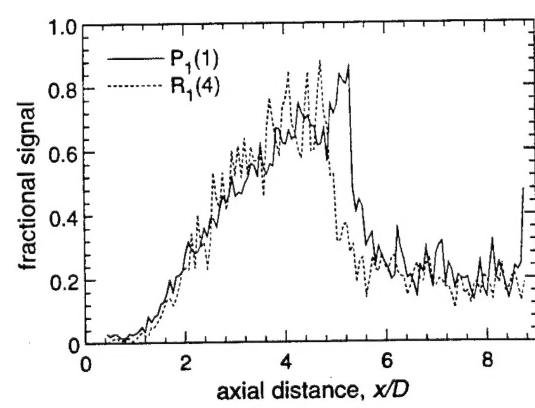


Figure 12: Signal in image 2 contributed by laser sheet 1 relative to that in image 1 for single-shot images obtained by pumping the $P_1(1)$ and $R_1(4)$ transitions.

The low S/N and the shift in the location of the Mach disk apparent in Fig. 12 are consequences of the fact that the signals shown are from single image pairs acquired during two runs of the shock tunnel facility. The image displayed in Fig. 11 was constructed from four image pairs acquired with $P_1(1)$ excitation and two with $R_1(4)$ pumping.

A measurement of the fluorescence lifetime $(A+Q)^{-1}$ throughout the flowfield may be obtained from the fractional signal, using the data displayed in Fig. 5 for the temporal characteristics of the intensifier gates. For instance, the observed signal during the second gate divided by that during the first was 0.5 ± 0.05 at $x/D = 3$ on the jet axis. Using a five level rate equation model of the fluorescence,³⁴ one finds that this value corresponds to a fluorescence lifetime of 220 ns, which yields $Q = 3.2 \times 10^6 \text{ s}^{-1}$ for $A = 1.27 \times 10^6 \text{ s}^{-1}$ (based on the assumption that the fluorescence occurs from the directly excited vibrational level).⁴² Estimating the electronic quenching rate for the conditions at $x/D = 3$ (0.0044 atm, 275 K, with the composition computed for the stagnation zone) from a recently published model⁴³ yields $Q = 4.8 \times 10^6 \text{ s}^{-1}$. The discrepancy between the measured and calculated values is likely the result of errors in the gas composition used in predicting the quenching rate and the low temperature at which it was evaluated.⁴³

C. Thermometry

Rotational temperature fields inferred from the single-shot images displayed in Fig. 9 are shown in

frames a and c of Fig. 13. Also shown are frame-averaged fields (b and d) obtained by evaluating the temperature from 40 individual image ratios and then averaging the results. The images in a and b of Fig. 13 are from combinations of images with $P_1(1)$ and $R_1(4)$ excitation; while those in c and d are from images with $P_1(1)$ and $Q_1(5)$ excitation. Also shown is the MOC prediction of the temperature field (e), with a white line placed at the location of the edges of the laser sheets in the PLIF images. The scale to the far right of Fig. 13 indicates the temperature corresponding to a given gray tone in the images.

The measured signal ratio fields were scaled to the value of R from Eqn. 5, based on the MOC prediction on the jet axis at $x/D = 1$, before conversion to T . The normalization constant C_{12} ranged from 0.92 to 1.15 in these evaluations. The symmetry of the single-shot temperature fields, expected because the flowfield is axisymmetric, demonstrates the similarity of the laser pulses used in acquiring each image, as shown in Fig. 10. Likewise, the frame-averaged images were constructed with temperature fields obtained from pairs of single-shot images having excitation characteristics similar to each other.

In Fig. 14, the rotational temperature from the frame-averaged images shown in Fig. 13 is plotted along the jet axis. The agreement between the measured and calculated fields is good throughout the free jet flowfield. Blurring of the shock structure caused by differences in its position in the single-shot images is evident. Large fluctuations in the

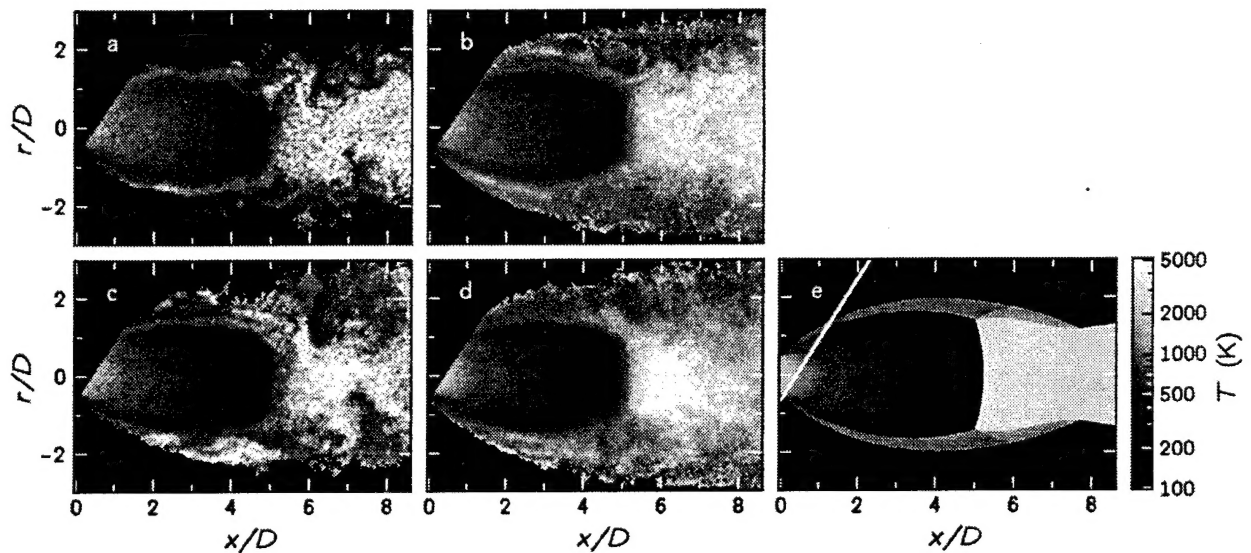


Figure 13: Single-shot and frame-averaged temperature images, inferred from ratios of $R_1(4):P_1(1)$ (a and b) and $Q_1(5):P_1(1)$ images (c and d). Also shown is the temperature field predicted by the MOC (e). The images are $8.61 \times 5.89 D$ (139×95 pixels) in size. The conditions of the free jet were: $T_s = 3350 \text{ K}$, $P_s = 3.2 \text{ atm}$, $P_s/P_a = 61$, with 1.9% OH in Ar and $D = 5 \text{ mm}$.

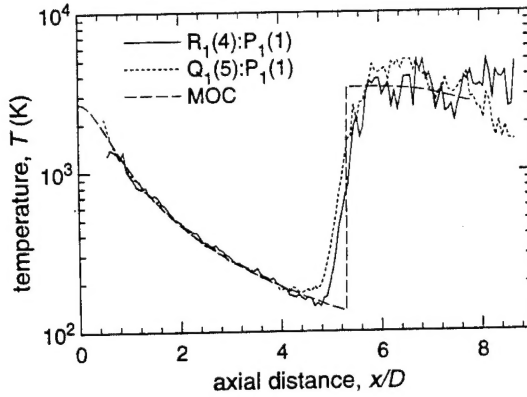


Figure 14: Measured and predicted rotational temperature along the jet axis.

temperature field downstream of the Mach disk resulted from shot-to-shot changes in that portion of the flowfield and the relatively small lower level energy separation of the lines pumped compared with the temperature (2500-3400 K).²⁴ In the turbulent flow downstream of the Mach disk, any systematic bias caused by the nonlinear dependence of the temperature on signal ratio and the fact that the signals were obtained nonsimultaneously appears slight.⁴⁴ Inside the jet core, the signal-to-noise of the inferred temperature varied, depending on the temperature. In the single-shot images, it ranged from a low of 5-6:1 near the Mach disk to 10-15:1 at moderate temperatures (300-700 K), then decreased again near the nozzle exit, where kT was much larger than the energy separation of the lower states of the transitions.

VI. Summary and Conclusions

The results of this investigation included single-shot PLIF images of OH in a reacting, supersonic free jet, images from which the electronic quenching of the OH $A^2\Sigma^+$ state could be inferred, and rotational temperature fields derived from combinations of individual, instantaneous images. Laser monitoring and data correction procedures were implemented which enabled quantitative results to be obtained. The measured fluorescence lifetime for signals acquired by pumping different ro-vibrational lines was found to be independent of the excited rotational state. Thus, a simplified analysis of the PLIF image ratios could be used to measure the rotational temperature.

The temperature field was not acquired instantaneously, although the demonstrated single-shot technique would allow such a measurement if two laser systems were used. However, in the free jet's inviscid core, where the flow was steady, the single-shot temperature agreed favorably with that predicted numerically. Frame-averaged images, obtained by

evaluating the mean temperature from many single-shot experiments, showed good agreement with the simulation throughout the flowfield, including the turbulent portion downstream of the Mach disk.

Acknowledgment

The authors gratefully acknowledge the contributions of Drs. J.M. Seitzman and B.K. McMillin to the experimental effort. The work was supported by the U.S. Air Force Office of Scientific Research, Aerospace Sciences Directorate, with Dr. J. Tishkoff as Technical Monitor.

References

1. R.L. McKenzie, "Progress in Laser Spectroscopic Techniques for Aerodynamic Measurements: an Overview," *AIAA J.*, Vol. 31, 1993, pp. 465-477.
2. R.K. Hanson, J.M. Seitzman, and P.H. Paul, "Planar Laser-Fluorescence Imaging of Combustion Gases," *Appl. Phys. B*, Vol. B50, 1990, pp. 441-454.
3. P. Desgroux and M.J. Cottreau, "Local OH Concentration Measurements in Atmospheric Pressure Flames by a Laser-Saturated Fluorescence Method: Two-Optical Path Laser-Induced Fluorescence," *Appl. Opt.*, Vol. 30, 1991, pp. 90-97.
4. M.D. Smooke, Y. Xu, R.M. Zurn, P. Lin, J.H. Frank, and M.B. Long, "Computational and Experimental Study of OH and CH Radicals in Axisymmetric Laminar Diffusion Flames," *24th Comb. Symp.*, The Comb. Inst., Pittsburgh, PA, 1992, pp. 813-821.
5. A. Arnold, B. Lange, T. Bouche, F. Heitzmann, G. Schiff, W. Ketterle, P. Monkhouse, and J. Wolfrum, "Absolute Temperature Fields in Flames by 2D-LIF of OH Using Excimer Lasers and CARS Spectroscopy," *24th Comb. Symp.*, The Comb. Inst., Pittsburgh, PA, 1992.
6. J.M. Seitzman and R.K. Hanson, "Two-Line Planar Fluorescence for Temporally Resolved Temperature Imaging in a Reacting Supersonic Flow over a Body," *Appl. Phys. B*, Vol. B57, 1993, pp. 384-391.
7. B.K. McMillin, J.M. Seitzman, and R.K. Hanson, "Comparison of NO and OH Planar Laser-Induced Fluorescence Temperature Measurements in Scramjet Model Flowfields," *AIAA J.*, Vol. 32, 1994, pp. 1945-1952.
8. J.M. Seitzman, R.K. Hanson, P.A. DeBarber, and C.F. Hess, "Application of Quantitative Two-Line OH Planar Laser-Induced Fluorescence for Temporally Resolved Planar Thermometry in Reacting Flows," *Appl. Opt.*, Vol. 33, 1994, pp. 4000-4012.
9. K.G. Klavuhn, G. Gauba, and J.C. McDaniel, "High Resolution OH LIF Velocity Measurement Technique for High-Speed Reacting Flows," *AIAA-92-3422*, 1992.
10. M.G. Allen, S.J. Davis, W.J. Kessler, H. Legner, K. McManus, P. Mulhall, T. Parker, and D.M. Sonnenfroh, "Nonintrusive Multipoint Velocity Measurements in High-Pressure Combustion Flows," *AIAA-93-2032*, 1993.
11. J.L. Palmer and R.K. Hanson, "PLIF Measurements of Temperature and Velocity in a Reacting Supersonic Free Jet with OH," *AIAA-94-0618*, 1994.
12. R. Suntz, H. Becker, P. Monkhouse, and J. Wolfrum, "Two-Dimensional Visualization of the Flame

Front in an Internal Combustion Engine by Laser-Induced Fluorescence of OH Radicals," *Appl. Phys. B*, Vol. B47, 1988, pp. 287-293.

13. B.K. McMillin, M.P. Lee, P.H. Paul, and R.K. Hanson, "Planar Laser-Induced Fluorescence Imaging of Shock-Induced Ignition," *23rd Comb. Symp.*, The Comb. Inst., Pittsburgh, PA, 1990, pp. 1901-1914.
14. S.H. Starner, R.W. Bilger, R.W. Dibble, R.S. Barlow, D.C. Fourquette, and M.B. Long, "Joint Planar CH and OH LIF Imaging in Piloted Turbulent Jet Diffusion Flames Near Extinction," *24th Comb. Symp.*, The Comb. Inst., Pittsburgh, PA, 1992, pp. 341-349.
15. W.L. Roberts, J.T. Driscoll, M.C. Drake, and J.W. Ratcliffe, "OH Fluorescence Images of the Quenching of a Premixed Flame During an Interaction with a Vortex," *24th Comb. Symp.*, The Comb. Inst., Pittsburgh, PA, 1992, pp. 169-176.
16. M.D. Moser, J.J. Merenich, S. Pal, and R.J. Santoro, "OH-Radical Imaging and Velocity Field Measurements in a Gaseous Hydrogen/Oxygen Rocket," AIAA-93-2036, 1993.
17. B. Yip, M.F. Miller, A. Lozano, and R.K. Hanson, "A Combined OH/Acetone Planar Laser-Induced Fluorescence Imaging Technique for Visualizing Combusting Flows," *Exp. Fluids*, Vol. 17, 1994, pp. 330-336.
18. J.L. Palmer and R.K. Hanson, "Shock Tunnel Flow Visualization Using Planar Laser-Induced Fluorescence Imaging of NO and OH," *Shock Waves*, 1995, in press.
19. C.D. Carter, J.T. Salmon, G.B. King, and N.M. Laurendeau, "Feasibility of Hydroxyl Measurements by Laser-Saturated Fluorescence in High-Pressure Flames," *Appl. Opt.*, Vol. 26, 1987, pp. 4551-4562.
20. R.S. Barlow, R.W. Dibble, and R.P. Lucht, "Simultaneous Measurements of Raman Scattering and Laser-Induced OH Fluorescence in Nonpremixed Turbulent Jet Flames," *Opt. Lett.*, Vol. 14, 1989, pp. 263-265.
21. R.S. Barlow and A. Collignon, "Linear LIF Measurements of OH in Nonpremixed Methane-Air Flames: When Are Quenching Corrections Unnecessary," AIAA-91-0179, 1991.
22. J.L. Palmer and R.K. Hanson, "Planar Laser-Induced Fluorescence Imaging in Free Jet Flows with Vibrational Nonequilibrium," AIAA-93-0046, 1993.
23. J.L. Palmer and R.K. Hanson, "Single-Shot Velocimetry Using Planar Laser-Induced Fluorescence Imaging of Nitric Oxide," AIAA-93-2020, 1993.
24. B.K. McMillin, J.L. Palmer, and R.K. Hanson, "Temporally Resolved, Two Line Fluorescence Imaging of NO Temperature in a Transverse Jet in a Supersonic Crossflow," *Appl. Opt.*, Vol. 32, 1993, pp. 7532-7545.
25. J.L. Palmer, B.K. McMillin, and R.K. Hanson, "Planar Laser-Induced Fluorescence Imaging of Underexpanded Free Jet Flow in a Shock Tunnel Facility," AIAA-91-1687, 1991.
26. C.B. Cleveland, J.R. Wiesenfeld, "Electronic Quenching of Highly Rotationally Excited OH ($A^2\Sigma^+, v'=0,1$) by H₂O," *Chem. Phys. Lett.*, Vol. 144, 1988, pp. 479-485.
27. R.J. Cattolica and T.G. Mataga, "Rotational-Level-Dependent Quenching of OH $A^2\Sigma^+(v'=1)$ by Collisions with H₂O in a Low-Pressure Flame," *Chem. Phys. Lett.*, Vol. 182, 1991, pp. 623-631.
28. J.L. Palmer, B.K. McMillin, and R.K. Hanson, "Planar Laser-Induced Fluorescence Imaging of Velocity and Temperature in Shock Tunnel Free Jet Flow," AIAA-92-0762, 1992.
29. R.J. Kee, F.M. Rupley, and J.A. Miller, "Chemkin-II: A Fortran Chemical Kinetics Package for the Analysis of Gas-Phase Chemical Kinetics," Sandia Rept. No. SAND89-8009 UC-4001, Sandia Natl. Lab., Livermore, CA, 1989.
30. K. Radhakrishnan and D.A. Bittker, "LSENS, A General Chemical Kinetics and Sensitivity Analysis Code for Gas-Phase Reactions: User's Guide," NASA TM 105851, 1993.
31. Schott Glass Technologies, Inc., *Optical Glass Filters*, Duryea, PA, 1988.
32. D.R. Crosley and R.K. Lengel, "Relative Transition Probabilities and the Electronic Transition Moment in the A-X System of OH," *J. Quant. Spectrosc. Radiat. Transfer*, Vol. 15, 1975, pp. 579-591.
33. B.K. McMillin, "Instantaneous Two-Line PLIF Temperature Imaging of Nitric Oxide in Supersonic Mixing and Combustion Flowfields," Ph.D. Thesis, Dept. of Mech. Eng., Stanford University, Stanford, CA, May, 1993.
34. J.M. Seitzman R.K. Hanson, "Comparison of Excitation Techniques for Quantitative Fluorescence Imaging of Reacting Flows," *AIAA J.*, Vol. 31, 1993, pp. 513-519.
35. Exciton, Inc., *Laser Dyes*, Dayton, OH, 1992.
36. H.D. Mette, "Fluorescence and Phosphorescence of SO₂ Vapor," *J. of Chem. Phys.*, Vol. 49, pp. 1784-1793, 1968.
37. H. Okabe, *Photochemistry of Small Molecules*, Wiley, NY, 1978.
38. D.L. Holtermann and E.K.C. Lee, "Rates of Collision-Induced Electronic Relaxation of Single Rotational Levels of SO₂(\tilde{A}^1A_2): Quenching Mechanism by Collision Complex Formation," *J. Chem. Phys.*, Vol. 77, 1982, pp. 5327-5339.
39. S.M. Ahmed and V. Kumar, "Quantitative Photoabsorption and Fluorescence Spectroscopy of SO₂ at 188-231 and 278.7-320 nm," *J. Quant. Spectrosc. Radiat. Transfer*, Vol. 47, pp. 359-373, 1992.
40. A.Y. Chang, "Rapid-Tuning Continuous-Wave Laser Technique Applied to Nitric Oxide Spectroscopy and Flow Measurements," Ph.D. Thesis, Dept. of Mech. Eng., Stanford University, Stanford, CA, Aug., 1991.
41. A. Hirano, F. Ricoul, and M. Tsujishita, "Two-Dimensional Direct Quenching Measurement of OH in a Cross-Section of a Bunsen Burner," *Jpn. J. Appl. Phys.*, Vol. 32, 1993, pp. 3300-3307.
42. I.L. Chidsey and D.R. Crosley, "Calculated Rotational Transition Probabilities for the A-X System of OH," *J. Quant. Spectrosc. Radiat. Transfer*, Vol. 23, 1980, pp. 187-199.
43. P.H. Paul, "Model for Temperature-Dependent Collisional Quenching of OH $A^2\Sigma^+$," *J. Quant. Spectrosc. Radiat. Transfer*, Vol. 51, 1994, pp. 511-524.
44. D.G. Fletcher, "An Investigation of Nonsimultaneous Laser-Induced Fluorescence," AIAA-93-0043, 1993.